Exploring the Immune Signatures of Lung Adenocarcinoma: Examining RORγT Expression in *KRAS* and *STK11* Mutant Tumours

Richard James Buchanan

A thesis submitted to the University of Birmingham for the degree of

DOCTOR OF PHILOSOPHY

Institute of Immunology and Immunotherapy

College of Medical and Dental Sciences

University of Birmingham

May 2021

Abstract

Lung adenocarcinoma (LUAD) is a common subtype of non-small-cell lung carcinoma that is driven by somatic mutations in various cancer genes. Intratumoural immunity is linked to tumour genetics and can influence response to treatment. Examining LUAD data from The Cancer Genome Atlas (TCGA), we delineated immune gene expression signatures for tumours with mutations in 11 different key cancer genes including *KRAS* and *STK11*. Although both these groups had generally low immune gene expression, each demonstrated significantly increased *RORC* mRNA expression, which encodes the T helper 17 (Th17) transcription factor RORγT. Using a unique cohort of mutationally profiled tumour resections, we found significantly higher intratumoural RORγT$^+$ lymphocytes by immunohistochemistry in LUADs with these mutations, many of which bordered tertiary lymphoid structures. Multiplex immunohistochemistry revealed that these lymphocytes were largely Th17s, and elevated intratumoural RORγT$^+$ lymphocytes were associated with poor overall survival. We subsequently developed an *in vitro* system in which T cells were cultured in media conditioned by lung carcinoma cell lines and found suppressed or regulatory CD3$^+$/CD4$^+$/RORγT$^+$ T cells were present in conditioned media from cell lines with loss of *STK11* function. These findings show that cancer gene mutations can influence tumour immunity and have important implications for stratified immunotherapy.

Acknowledgements

First and foremost, I would like to thank my supervisors Gary and Heather for giving me this opportunity and for the invaluable guidance throughout this journey. I feel your supervision has really developed me in many aspects of my life, and I truly could not have achieved this without your support, understanding and insights. Thank you both!

I would also like to thank all the members of 'Team EBV' (past and present) for adopting me into the group and for their assistance in the lab, with special thanks to my friends from the office Ben, Sam, and Olivia. I wish I had space to name you all and I really value the time we have spent together and the fun along the way, I will miss you all!

Thanks also to the team at the HBRC for their help accessing patient samples and their IHC knowledge. Likewise, I would like to thank the pathologists who provided review for this project: Abeer Shaaban, Phillipe Taniere and Matt Pugh, as well as the Thoracic Research Team at Heartlands Hospital.

A special thank you to the patients and donors, without whom none of this work would be possible, and to my funders The British Lung Foundation.

Ευχαριστώ τη φίλη μου Αρετή, της οποίας ο ενθουσιασμός βλέποντας τις Ελληνικές λέξεις και τους χαρακτήρες σε αυτή τη διατριβή φωτίζει πάντα τη μέρα μου. Σε ευχαριστώ για την αγάπη και την υποστήριξή σου.

Thanks to my family and friends for their support and the much-needed distractions.

Finally, thank you to my parents (who I know will try to read this thesis, good luck!) for fostering my scientific intrigue, as well as for their perspective and unwavering support throughout this journey.

Contents

List of Figures

List of Tables

List of Abbreviations

4EBP1	Eukaryotic Translation Initiation 4E-Binding Protein 1
AHR	Aryl Hydrocarbon Receptor
ALK	Anaplastic Lymphoma Kinase
AMPK	5'AMP-Activated Protein Kinase
APC	Antigen-Presenting Cell
ATCC	American Type Culture Collection
ATM	ATM Serine/Threonine Kinase
ATR	Serine/Threonine-Protein Kinase ATR
BSA	Bovine Serum Albumin
CAF	Cancer Associated Fibroblast
CCL	Chemokine (C-C Motif) Ligand
CCR	C-C Chemokine Receptor Type
CD	Cluster Of Differentiation
CDKN2A	Cyclin-Dependent Kinase Inhibitor 2A
CK7	Cytokeratin 7
CNA	Copy Number Alteration
COPD	Chronic Obstructive Pulmonary Disease
CPS1	Carbamoyl Phosphate Synthetase-1
CRC	Colorectal Cancer
CREB	cAMP Response Element-Binding Protein
CRTC2	CREB Regulated Transcription Coactivator 2
CSE	Cigarette Smoke Extract
CTLA-4	Cytotoxic T-Lymphocyte-Associated Protein 4
CXCL	C-X-C Motif Chemokine Ligand
CIITA	Class II Transactivator
DC	Dendritic Cell
DMEM	Dulbecco's Modified Eagle's Medium Culture Media

DMSO	Dimethyl Sulfoxide
DSMZ	Deutsche Sammlung Von Mikroorganismen Und Zellkulturen
EAE	Experimental Autoimmune Encephalomyelitis
ECACC	European Collection Of Authenticated Cell Cultures
EGF	Epidermal Growth Factor
EGFR	Epidermal Growth Factor Receptor
EML4	Echinoderm Microtubule-Associated Protein-Like 4
EMT	Epithelial-Mesenchymal Transition
FBS	Foetal Bovine Serum
FoxP3	Forkhead Box P3
GAP	GTPase-Activating Protein
G-CSF	Granulocyte Colony-Stimulating Factor
GEF	Guanine Exchange Factor
GEO	Gene Expression Omnibus
GM-CSF	Granulocyte-Macrophage Colony-Stimulating Factor
GRB2	Growth Factor Receptor-Bound Protein 2
GSEA	Gene Set Enrichment Analysis
HSP90	Heat Shock Protein 90
HGF	Hepatocyte Growth Factor
HIER	Heat-Induced Epitope Retrieval
HIF1α	Hypoxia-Inducible Factor 1-Alpha
HLA	Human Leukocyte Antigen
HSP90	Heat Shock Protein 90
IDO	Indoleamine 2,3-Dioxygenase
IFN	Interferon
IHC	Immunohistochemistry
ILC	Innate Lymphoid Cell
IMS	Industrial Methylated Spirit

iNKT17	Invariant Natural Killer T Cell 17
IL	Interleukin
IRON	Iterative Rank-Order Normalisation
iTreg	*In Vitro*-Induced Treg
KEAP1	Kelch-Like ECH-Associated Protein 1
LAG-3	Lymphocyte-Activation Gene 3
LKB1	Liver Kinase B1
LTi	Lymphoid Tissue Inducer
LUAD	Lung Adenocarcinoma
MAIT	Mucosal Associated Invariant T Cell
MAPK	Mitogen-Activated Protein Kinase
MARK	KIN2/PAR-1/MARK Kinase
MDM2	Mouse Double Minute 2 Homolog
MDSC	Myeloid Derived Suppressor Cell
MEF	Mouse Embryonic Fibroblast
MEK	Mitogen-Activated Protein Kinase Kinase
MEM	Minimum Essential Medium Eagle Culture Media
MEMod	Marker Enrichment Modelling
MMP	Matrix Metallopeptidase
MO25	Calcium-Binding Protein 39
MSI	Microsatellite Instability
MT	Mutation
mTOR	Mechanistic Target Of Rapamycin
mTORC	Mechanistic Target Of Rapamycin Complex
NCR	Natural Cytotoxicity Receptor
NF1	Neurofibromin 1
NK	Natural Killer
Noxa	Phorbol-12-Myristate-13-Acetate-Induced Protein 1

NRF2	Nuclear Factor Erythroid 2-Releated Factor 2
NSCLC	Non-Small-Cell Lung Carcinoma
OS	Overall Survival
OXPHOS	Oxidative Phosphorylation
P21	$P21^{Cip1}$
P53	Tumour Protein P53
PAH	Polycyclic Aromatic Hydrocarbons
PBMC	Peripheral Blood Mononuclear Cell
PCA	Principle Component Analysis
PD	Programmed Cell Death Protein
PD-L	Programmed Cell Death Protein Ligand
PI3K	Phosphoinositide 3-Kinase
PMA/iono	Phorbol 12-Myristate 13-Acetate And Ionomycin
Puma	P53 Upregulated Modulatory Of Apoptosis
qPCR	Quantitative Polymerase Chain Reaction
RA	Retinoic Acid
RAF	RAF Kinase
ROR	Retinoic Acid-Related Orphan Receptor
ROS	Reactive Oxygen Species
ROS1	Proto-Oncogene Tyrosine-Protein Kinase ROS
RTK	Receptor Tyrosine Kinase
RMA	Robust Multi-Array Average
RPMI	Roswell Park Memorial Institute-1640 Culture Media
RPPA	Reverse Phase Protein Array
RT	Room Temperature
Runx1	Runt-Related Transcription Factor 1
S6K	Ribosomal Protein S6 Kinase
SIK	Salt-Inducible Kinase

SIRT1	Sirtuin 1
SMP2	Stratified Medicine Programme 2
SOS	Son Of Sevenless
SqCC	Squamous-Cell Carcinoma
ssGSEA	Single Sample Gene Set Enrichment Analysis
STAT	Signal Transducer And Activator Of Transcription
STING	Stimulator Of Interferon Genes
STRAD	Protein Kinase LYK5
TAM	Tumour Associated Macrophage
TAN	Tumour Associated Neutrophil
T-bet	T-Box Transcription Factor TBX21
TCA	Tricarboxylic Acid
TCGA	The Cancer Genome Atlas
TCM	Tumour Conditioned Media
TCR	T Cell Receptor
Tfh	T Follicular Helper
TGF	Transforming Growth Factor
Th	T Helper
Th17	T Helper 17
TIGIT	T Cell Immunoreceptor With Ig And ITIM Domains
TIM-3	T-Cell Immunoglobulin And Mucin-Domain Containing-3
TLS	Tertiary Lymphoid Structure
TMB	Tumour Mutational Burden
TME	Tumour Microenvironment
TNF	Tumour Necrosis Factor
TRACERx	Tracking Cancer Evolution Through Therapy
Treg	Regulatory T Cell
TSC	Tuberous Sclerosis Complex

VEGF	Vascular Endothelial Growth Factor
WT	Wild Type

1. Introduction

Cancers are an important group of diseases characterised by abnormal cell growth that can have poor clinical outcomes. They represent a major burden of disease globally, which provides a challenge for healthcare and research. Lung cancer is a serious yet largely preventable disease that is heavily linked with smoking history. Recent knowledge of how the immune system works in a cancerous tumour has led to promising immunotherapies which have transformed lung cancer treatment. However, these therapies do not work for all patients which is fundamentally due to variations in the genetics and immune response to a lung tumour.

This thesis will primarily explore how the immune system responds to lung cancers driven by different genetic mutations which cause different features and course of disease.

1.1 Lung Cancer

Lung cancer is one of the most common malignancies and cause of cancer related death worldwide (1). 5.6% of total deaths in all age groups in 2019 in England and Wales were due to lung cancer, more than any other cancer (2). Disease is often asymptomatic at early stages, and as the most common symptoms – coughing and breathlessness – are perceived to be minor inconveniences with many different causes, patients often seek medical advice at later stages and present with advanced disease. Patients are firstly examined by chest x-ray and CT imaging; followed by biopsy (often by endobronchial ultrasound-guided transbronchial needle aspiration) to confirm diagnosis by histopathology, and to guide lung cancer staging alongside additional investigations for metastases. Metastatic disease is common and metastases often home to the lymph nodes, bones, brain and liver. The American Joint Committee on Cancer Staging provide frequently used guidelines on lung cancer staging, which is achieved using the 'tumour, node, metastasis system', and these results are combined to give overall stages from early stage I disease to advanced stage IV disease. Late-stage lung cancer is especially difficult to treat, as such patients with this disease in England have a poor 5-year age-standardised net cancer survival (13.8% for men, 19% for women) (3). Management and palliation of lung cancer requires specialists, making it a major burden on the NHS.

1.1.1 Lung Cancer Histology

Cancers are classified by histology, which is dependent on the cell type of origin. Lung cancers originate from epithelial cells and are classified as carcinomas. The only exception to this within pulmonary cancers is the occupational cancer mesothelioma, which is caused by exposure to asbestos fibres that damage the specialised mesothelium epithelial cells that line the pleura. The two main broad histological types of lung carcinomas are small-cell lung carcinomas and non-small-cell lung carcinomas (NSCLCs), with the latter encompassing more than 85% of lung cancer diagnoses. LUADs arising from glandular epithelium are the most common subtype of NSCLC (50% of NSCLC cases), followed by squamous-cell carcinomas (SqCCs) from squamous epithelium (30% of NSCLC cases) and rarer histologic subtypes including large-cell carcinomas constitute the remaining NSCLC cases (4). There is evidence that most LUADs arise from transformed surfactant secreting alveolar type II cells which are one of the progeny of club cells (5). This thesis will focus throughout on LUAD, which is the most common NSCLC.

1.1.2 Lung Cancer Pathogenesis

Over 80% of lung carcinoma diagnoses are attributed to tobacco smoking, making smoking the most important risk factor for lung carcinomas (6). Smoke from cigarettes contains over 4000 different compounds, including some of the following carcinogens: *N*-nitrosamines, polycyclic aromatic hydrocarbons (PAHs) and benzene. These compounds are genotoxic and can directly bind onto DNA to make DNA adducts. If these are not repaired properly by DNA repair mechanisms, this can give rise to somatic mutations in

key oncogenes (7). Moreover, chronic cigarette smoke exposure can cause progressive hypermethylation of gene promoters, and these epigenetic changes can sensitise a cell to allow oncogenic transformation by events including somatic mutations (8). Chronic smoke exposure can also cause inflammatory injuries to the airways within the lung resulting in narrowings. This obstructive lung disease is called chronic obstructive pulmonary disease (COPD) and is another independent risk factor for lung carcinomas (9). Although most lung carcinomas are associated with tobacco smoke, some cancers occur in patients who have never smoked. Genome-wide association studies have identified the 5p15.33 chromosome locus which regulates telomere length as a potential familial susceptibility locus for lung cancer (10). Other suggested lung carcinoma aetiological risk factors for never smokers are a poor diet, obesity, and exposure to pollutants of which many are PAHs.

Oncogenesis is a complex process, and malignant transformation is progressive, non-linear and multifaceted. At the simplest level, transformation is a result of the dysregulation of many cellular pathways by functional genetic changes. There are two main sets of genes which are genetically altered to drive cancer, oncogenes and tumour suppressor genes. Aberrantly activated oncogenes cause cellular growth and proliferation, whereas tumour suppressor genes are inactivated, enabling abnormal cellular proliferation and survival. Tumours may become 'addicted' to the effects of particular driver oncogenes on a cellular pathway. For instance, epidermal growth factor receptor (EGFR) is a receptor tyrosine kinase (RTK) that binds extracellular growth factors; its kinase activity initiates downstream signalling resulting in proliferation. NSCLC tumours may become addicted to somatic *EGFR* mutations that cause uncontrolled cellular proliferations by constitutive

kinase activation in the absence of ligand (11). As tumours progress, they avoid normal cellular regulatory rules by evading contact inhibition and circumventing the Hayflick limit – the limited number of times a cell can divide before division ceases and apoptosis occurs – to have unlimited replicative potential (12).

Tumour formation is also an evolutionary process. Tumour clones which accumulate genetic or epigenetic alterations that cause competitive advantages over other cells including other tumour cells, expand and dominate a tumour. These alterations can be described as clonal, although tumours and metastases can also later acquire subclonal alterations which can confer further selective advantages and provide resistance to therapy. NSCLC tumours have a high degree of intratumour heterogeneity, with different tumour regions being driven by different subclones. The aforementioned *EGFR* mutations predominantly occur at an early stage of a tumour's life and are clonal, as are whole genome doubling events, whilst mutations in genes such as the *NF1* tumour suppressor are typically subclonal (13). Metastasis and tumour heterogeneity may also be driven by lung cancer stem cells, which are tumour cells that have undergone clonal evolution, have stem-like properties and are able to seed new tumours. These lung cancer stem cells may help shape the tumour microenvironment (TME) and can metastasise due to mutational interference with signalling pathways which induces epithelial-mesenchymal transition (EMT) (14).

NSCLC tumours have complex nutritional and metabolic requirements, undergoing metabolic rewiring to establish a supporting TME. An example of NSCLC metabolic reprogramming is altered glucose metabolism in tumours with certain genetic profiles,

with a switch from oxidative phosphorylation (OXPHOS) to glycolysis; these glucose metabolites are then channelled through the tricarboxylic acid (TCA) cycle (15). A shift from normoxia can also be pathological. Despite the fact that the lung is an oxygen rich environment, there is evidence that heterogeneity within a lung tumour and differential tumour cell densities may cause degrees of hypoxia which impact metabolism and growth (16). This TME heterogeneity is in part down to the heterogeneous distributions of the constitutive cells of the stroma, including endothelial cells, cancer associated fibroblasts (CAFs) and immune cells.

The stroma is instrumental in another key oncogenic mechanism, the angiogenic switch, in which quiescent endothelial cells are activated to allow them to produce new blood vessels to vascularise the tumour. NSCLC tumours can make their own angiogenic factors such as vascular endothelial growth factor (VEGF) and fibroblast growth factor to trigger this switch, and these factors are also importantly produced by CAFs. CAFs are very abundant in the tumour stroma and have a key role in remodelling the extracellular matrix to support cancer growth and to potentiate metastases (12, 17, 18).

Cells of the immune system are another important constituent of the stroma. The immune system provides a defence against a wide range of microbial pathogens and some immune cells can develop immunological memory towards these pathogens to allow enhanced protection upon subsequent exposures. The immune system not only surveys for non-self pathogens, but can recognise and kill cancerous cells (19). However, immune cells not only play a crucial role in tumour regression but can also aid cancerous growth. Chemokines secreted from CAFs can recruit myeloid lineage innate immune cells, which in turn can

promote angiogenesis, create chronic inflammation, and can suppress other anti-tumour immune cells. To continue to proliferate, the tumour can also directly evade and suppress immune cells, as well as indirectly hijack other stromal cells to help (12, 17, 18).

Malignant tumours that cannot be kept under control may metastasise. For this to occur, tumour cells gain an EMT phenotype which is governed by pathways including the Wnt/β-catenin pathway and expression of transcription factors such as Twist, Snail and Slug. Acting through a variety of mechanisms, these all result in downregulated E-cadherin expression which is needed to maintain epithelial integrity. Tight junction disruption coupled with an increased stem-like motility allows metastatic intravasation into the blood and lymph, followed by transit to a new site. The metastatic cells then undergo the reverse process called mesenchymal-epithelial transition and colonise a new site by adapting to the new environment, or by colonising an already permissible stromal environment. Cancer stem cells may drive metastasis due to their EMT phenotype and stemness (12, 20).

1.1.3 Non-Small-Cell Lung Cancer Management

Some of the historically earliest used treatments for cancer are still used in modern NSCLC management. Surgery was first successfully used to remove tumours in the 18th century and remains the standard of care in early-stage NSCLC today as it can be curative. Surgical approaches depend on tumour location and patient fitness. Targeted video-assisted resections such as wedge resections and lobectomies are preferred, but full pneumonectomy may be performed (21). Another curative approach is radiotherapy using

ionising radiation to induce cell death by dsDNA breaks. Stereotactic ablative radiotherapy is one such effective radical radiotherapy, delivering high dosages by multiple radiation beams. Approaches for late-stage NSCLCs focus on management of disease. Patients often receive surgery and palliative care including by chemotherapy or chemoradiotherapy. There are several types of chemotherapy used in NSCLC management such as: platinum-based agents to cause DNA crosslinking, the nucleoside analogue gemcitabine, the folate antimetabolite pemetrexed and taxane agents to disrupt microtubule function. These agents can be used alone or in combination (22, 23).

1.1.4 Non-Small-Cell Lung Cancer Genetics

Oncogenesis is predominantly driven by dysregulated cellular pathways controlled by altered genetics. There is great variety behind the underlying mechanisms of somatic genetic alterations in cancer, from single-nucleotide changes to gross alterations to entire chromosome loci.

Some of the most frequently observed somatic alterations in NSCLC are point mutations. Missense mutations are nonsynonymous single-nucleotide alterations in which one base is swapped for another, which results in a changed codon that encodes a different amino acid. Another type of point mutation are nonsense mutations, in which there is a premature ending of translation and often a truncation of the polypeptide product, as these single-nucleotide alterations result in an early stop codon. As with all nonsynonymous mutations, not every new polypeptide is successfully post-translationally modified to create a functional mature protein product. Nonstop mutations occur in a

stop codon and convert it into a sense codon, allowing translation into the 3' untranslated region and producing a longer altered polypeptide (24).

Frameshift mutations are caused by nucleotide insertions or deletions which either change the codon reading frame, or if the number of insertions or deletions is divisible by three, then one extra/missing amino acid will be added/removed from the polypeptide. Early DNA sequence non-triplicate frameshift mutations can have a particularly large impact on the polypeptide product. Splice site mutations refer to any of the aforementioned mutations that occur at and disrupt splice sites found at the borders of introns and exons. These mutations have a range of mRNA splicing consequences, often resulting in intron retainment and exon skipping (25).

Somatic changes in copy number are a key structural alteration to the genome in cancer. These can occur in a focal manner at the gene-level or at a certain chromosomal locus, as well as at a higher chromosomal-level in which the whole genome is duplicated. Copy number alterations (CNAs) result in amplifications or deletions of segments of genetic code, which can be caused by errors in the non-allelic homologous recombination and non-homologous recombination mechanisms of dsDNA damage repair. If a region is amplified then there are more copies of the genes found in that region compared to diploid which can lead to increased protein expression of these genes, and likewise if a region is deleted then there are less or no copies of genes in that region compared to diploid, and less or no subsequent protein expression. In NSCLC, CNAs often occur in regions home to oncogenes and tumour suppressor genes, as well as more generally when the whole genome is duplicated (26). This genome-wide polyploidy occurs early in NSCLC

and is associated with chromosomal instability (13). Epigenetic modifications can cause transcriptional changes in NSCLC. For instance, tumour suppressor genes can be directly silenced by hypermethylation of their gene promoter CpG islands, and indirectly silenced by histones remaining in a tightly packed transcriptionally inactive state by enzymatic deacetylation of histone tails (27). Finally, fusion genes are a combination of two genes that form a new gene with an oncogenic role. Rearrangements are usually by chromosomal translocations and the resultant fusion genes often act as kinases (28, 29).

1.1.5 Molecular Pathogenesis of Non-Small-Cell Lung Cancer

NSCLC cancer genes are genes associated with cancer development, acting as oncogenes and dysfunctional tumour suppressor genes after acquiring genetic alterations. These altered cancer genes impact key cellular processes including cell cycle regulation, apoptosis and cell signalling pathways. This section covers the oncogenic mechanisms of some of the key cancer genes in NSCLC, and a list of abbreviations for proteins and genes in this section can be found in Table 1.1.

Abbreviation	Full Name	Description
4EBP1	Eukaryotic Translation Initiation Factor 4E-Binding Protein 1	mTORC1 effector subunit
ALK	Anaplastic Lymphoma Kinase	Involved in oncokinase fusions
AMPK	5'AMP-Activated Protein Kinase	Protein kinase responsive to energic stress regulated by LKB1
ATM	ATM Serine/Threonine Kinase	DNA damage checkpoint protein
ATR	Serine/Threonine-Protein Kinase ATR	DNA damage checkpoint protein
CDKN2A	Cyclin-Dependent Kinase Inhibitor 2A	Cyclin-Dependent Kinase Inhibitor
EGF	Epidermal Growth Factor	Growth factor ligand for EGFR
EML4	Echinoderm Microtubule-Associated Protein-Like 4	Involved in oncokinase fusions
GAP	GTPase-Activating Protein	Regulates the KRAS GTPase
GEF	Guanine Exchange Factor	Regulates the KRAS GTPase
GRB2	Growth Factor Receptor-Bound Protein 2	Adaptor protein involved in KRAS signalling
HGF	Hepatocyte Growth Factor	Growth factor ligand for MET
HIF1α (*HIF1A*)	Hypoxia-Inducible Factor 1-Alpha	Transcriptional regulator of the hypoxia response
LKB1 (*STK11*)	Liver Kinase B1	Tumour suppressor serine/threonine kinase responsive to energic stress
MAPK	Mitogen-Activated Protein Kinase	RAF kinase member
MDM2	Mouse Double Minute 2 Homolog	Regulator of p53
MEK	Mitogen-Activated Protein Kinase Kinase	MAPK signalling kinase intermediate
MO25	Calcium-Binding Protein 39	LKB1 scaffold protein
mTOR	Mechanistic Target Of Rapamycin	Growth and proliferation pathway
NF1	Neurofibromin 1	GTPase-activating protein
Noxa	Phorbol-12-Myristate-13-Acetate-Induced Protein 1	Pro-apoptotic protein

p21	$P21^{Cip1}$	Cyclin-dependent kinase inhibitor
p53 (*TP53*)	Tumour Protein P53	An essential tumour suppressor
PI3K	Phosphoinositide 3-Kinase	RTK signal transducer
Puma	P53 Upregulated Modulator Of Apoptosis	Pro-apoptotic protein
RAF	RAF Kinase	RTK signal transducer
ROS1	Proto-Oncogene Tyrosine-Protein Kinase ROS	Involved in oncokinase fusions
S6K	Ribosomal Protein S6 Kinase	mTORC1 effector subunit
SOS	Son Of Sevenless	Guanine exchange factor
STAT	Signal Transducer And Activator Of Transcription	Transcription factor family
STRAD	Protein Kinase LYK5	Kinase that activates LKB1
TSC	Tuberous Sclerosis Complex	GTPase-activating protein and negative regulator of mTORC1

Table 1.1 Abbreviations in Chapter 1.1.5

List of abbreviations and brief descriptions for common proteins involved in cancer described in this section. Where appropriate, the abbreviation column shows the protein name and gene name in brackets if these differ. References for each protein can be found as in-text citations.

The cell cycle, which controls mitotic cell division, is frequently dysregulated by genetically altered cancer genes in NSCLC to allow uncontrolled cell division free of essential cell cycle checkpoints. *TP53* is the most commonly altered cancer gene in all human cancers and is key in controlling the cell cycle. p53 is activated upon DNA damage, oxidative stress and other stressful conditions, and halts cell cycle progression at G1/S under mild stress or initiates apoptosis under extreme stress. Mechanistically, DNA damage repair members ATM and ATR phosphorylate p53 after sensing dsDNA and ssDNA breaks respectively (30). The phosphorylated p53 dissociates from MDM2 which normally marks p53 for degradation by ubiquitination. This allows p53 to regulate a myriad of other proteins

including p21, a cyclin-dependent kinase inhibitor that binds to and inhibits cyclin/cyclin-dependent kinase complexes that signal cell cycle progression. Apoptosis is also regulated by p53 by initiating transcription of the pro-apoptotic factors Puma and Noxa. *TP53* is subject to loss of function mutations and deletions in NSCLC, which reduce the stability of the p53 protein and stops p53 post-translationally modifying other proteins (12, 31, 32). Inactivating mutations also affect the serine/threonine kinase and cancer gene ATM, found upstream of p53. In addition to its role as a DNA damage sensor, ATM has an emerging role sensing hypoxia (33). Inactivating mutations and deletions affect the *CDKN2A* gene which codes for two important cyclin-dependent kinase inhibitors p16 and p14ARF that are translated in different reading frames. p16 acts stops progression from the G1/S cell cycle checkpoint by inhibiting cyclin-dependent kinases, and p14ARF inhibits MDM2 allowing p53 mediated cell cycle arrest (34).

Two cancer genes, *ALK* and *ROS1*, are implicated in most of the fusion gene driven LUADs that occur in younger never smokers. There is a high degree of homology between ALK and ROS1, with both proteins normally functioning as RTKs that cause cell growth and anti-apoptosis signals via pathways including the mTOR pathway, acting through PI3K phosphorylation. For ALK, gene translocations usually result in the EML4-ALK fusion oncokinase, whereas ROS1 has a number of fusion partners, the most common being CD74-ROS1. Both *ALK* and *ROS1* are also subject to directly activating mutations (29, 35, 36). Figure 1.1a provides an overview of dysregulated signalling in NSCLC, focusing on mTOR complex (mTORC) 1 signalling and its intermediates.

RTKs can also act as cancer genes when subject to gain of function mutations and amplification CNAs. Activating alterations to the ErbB RTK family member EGFR commonly occur in NSCLC, and less commonly to the MET RTK. Usually, RTK activity is triggered by binding of ligands including EGF for EGFR, and HGF for MET, which causes cell signalling via Ras, PI3K and STAT family members. However, mutations can activate EGFR in a ligand-independent manner, as discussed previously (11). Sustained oncogenic MET activation can be a result of mutations to the exon 14 splice site, which cause exon 14 skipping. As this exon is the binding site for a ubiquitin ligase, these mutations cause reduced MET degradation from lower protein turnover (37).

Oncokinase fusions and genetically altering RTKs are not the only ways that tumours can dysregulate cell signalling from RTKs to cause growth, proliferation, and changes to cell energetics – downstream cell signalling proteins can also be involved. KRAS is a member of the Ras family of small GTPases which are attached to the cell membrane and are involved in the initiation of signal transduction from RTKs and G protein-coupled receptors, interacting with more than 80 downstream proteins including RAF and PI3K to cause cellular survival, proliferation, differentiation and altered metabolism. For KRAS signalling to occur, the receptor bound GRB2 firstly combines with SOS, which interacts with KRAS. SOS and other GEFs facilitate the conversion of GDP to GTP which activates KRAS. As a GTPase, KRAS is naturally self-regulatory having an intrinsic hydrolytic activity and converts GTP slowly back to GDP, which can be sped up by GAPs (Figure 1.1b). KRAS is a binary molecular switch and is either in an active ‘on’ state, or an inactive ‘off’ state. It is therefore subject to gain of function missense mutations in NSCLC which render KRAS

signalling constitutively ‘on’, moreover, chromosomal amplifications increase the number of *KRAS* copies (38, 39).

One of the main GAPs regulating KRAS activation is NF1, which can be deleted or acquire inactivating mutations to stops NF1 from negatively regulating KRAS activation, increasing the duration of KRAS activation (40). Furthermore, downstream of KRAS is another cancer gene which is mutated or amplified in a gain of function manner in NSCLC, BRAF. This serine/threonine RAF kinase member is crucial in the MAPK signalling cascade and phosphorylates MEK1/MEK2 in this pathway, which leads to growth, division and transcription of genes including *MYC* (41, 42). Downstream of RAF is LKB1, a serine/threonine kinase that works with AMPK (a heterotrimeric protein comprised of AMPKα, AMPKβ and AMPKγ subunits) to create a metabolic checkpoint. Decreased intracellular ATP and increased AMP occurs after metabolic stressors like low glucose and hypoxia. AMPKγ senses high AMP and changes confirmation allowing LKB1 access to AMPKα. For LKB1 to be active, the STRAD kinase phosphorylates it then complexes with LKB1 and the scaffold protein MO25. LKB1 then phosphorylates AMPKα at threonine 172, activating AMPK which is a key negative regulator of the mTORC1 pathway. AMPK inhibits the mTORC1 activity directly by phosphorylating the RAPTOR scaffold protein, and indirectly by phosphorylating TSC2 of the TSC1/TSC2 complex which then inhibits mTORC1 (Figure 1.1c). This mTORC1 inhibition means that its effector subunits 4EBP1 and S6K1 are unable to continue providing growth signals and translation of proteins including HIF1α, MYC and cyclin D1. Loss of function mutations and deletions of the LKB1 gene *STK11*, enable oncogenic mTORC1 signalling (43).

a)

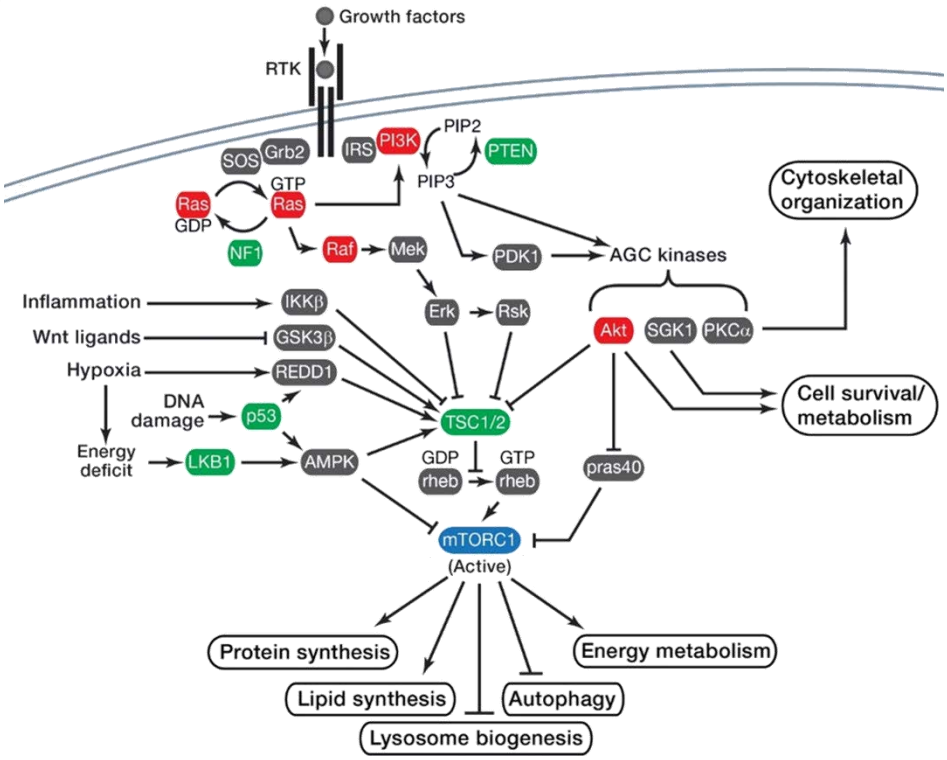
Growth factors
RTK
SOS
Grb2
IRS
PI3K
PIP2
PIP3
PTEN
GTP
Ras
GDP
Ras
NF1
Raf
Mek
PDK1
AGC kinases
Cytoskeletal organization
Inflammation
IKKβ
Wnt ligands
GSK3β
Hypoxia
REDD1
DNA damage
p53
Energy deficit
LKB1
AMPK
Erk
Rsk
Akt
SGK1
PKCα
Cell survival/ metabolism
TSC1/2
GDP
rheb
GTP
rheb
pras40
mTORC1
(Active)
Protein synthesis
Energy metabolism
Lipid synthesis
Autophagy
Lysosome biogenesis

b)

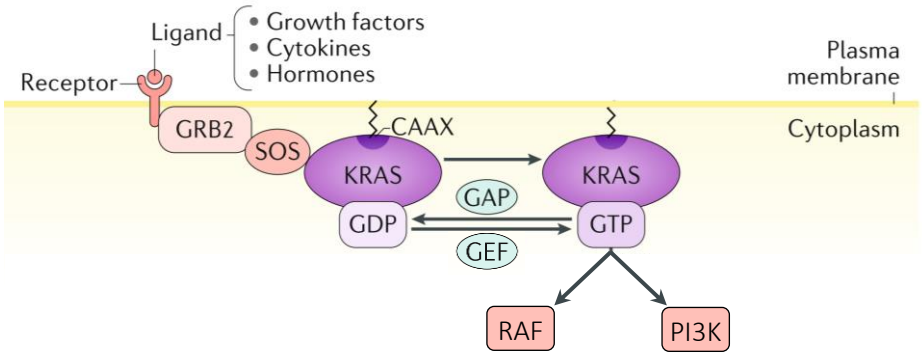
Ligand
• Growth factors
• Cytokines
• Hormones
Receptor
Plasma membrane
Cytoplasm
GRB2
SOS
CAAX
KRAS
KRAS
GAP
GDP
GTP
GEF
RAF
PI3K

c)

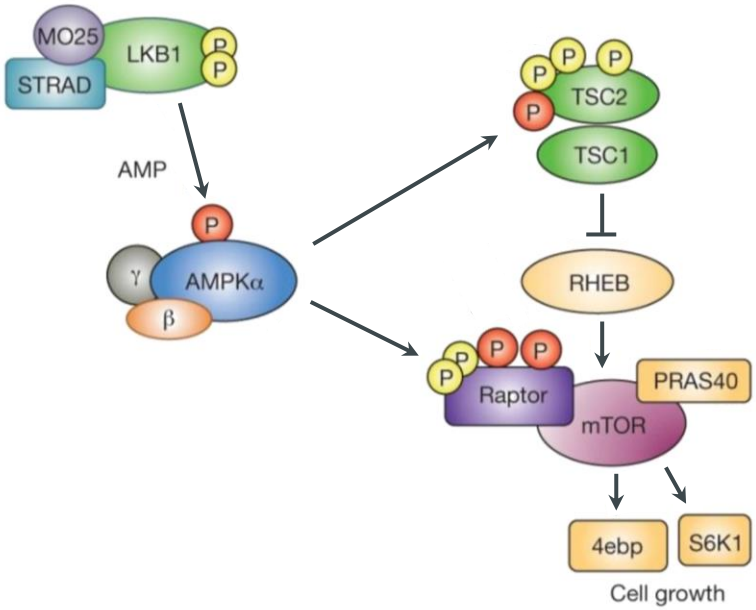
MO25
LKB1
STRAD
P
P
AMP
P
γ
AMPKα
β
P
P
P
P
TSC2
TSC1
RHEB
P
P
P
P
Raptor
PRAS40
mTOR
4ebp
S6K1
Cell growth

Figure 1.1 mTOR, KRAS and LKB1 signalling pathways

a) An overview of signalling from RTK to mTORC1, showing key signalling intermediates and providing a broad context for the Ras and LKB1 pathways. Figure adapted from Laplante and Sabatini (44). **b)** The KRAS GTPase. GTP activated KRAS signals to RAF and PI3K. Figure adapted from Buscail, Bournet and Cordelier (38). **c)** LKB1 regulation of AMPK under conditions of high AMP and downstream regulation of mTOR (mTORC1). Figure adapted from Mihaylova and Shaw (45).

1.1.6 Novel Treatments for Non-Small-Cell Lung Cancer

In recent years, oncology has sought to go beyond the traditional strategies for cancer management, developing rational treatments based on knowledge of the cancer to treat disease more effectively with less associated toxicities. Precision medicine uses knowledge of cancer genetics to select appropriate treatments. Small molecule inhibitors gefitinib and afatinib inhibit signalling from the EGFR tyrosine kinase intracellular domain, whilst cetuximab binds to the EGFR extracellular domain (11). Cetuximab is only appropriate for use in patients with activating *EGFR* mutations but without *KRAS* mutations. NSCLC tumours driven by *ALK* and *ROS1* fusion oncokinases are effectively inhibited by the tyrosine kinase inhibitors crizotinib, resulting in longer overall survival (OS) for patients with these fusions. However, activating *ALK* and *ROS1* mutations can cause crizotinib resistance, though these mutations do not affect second generation ALK inhibitors like ceritinib to the same extent (29, 35, 36). Furthermore, crizotinib also works to inhibit the MET RTK and patients with *MET* amplifications also benefit (46).

Not all genetic alterations however can currently be targeted by precision medicine. For instance, as they are inactivating, p53 mutations are difficult to target. Compounds against p53 attempt to destabilise the mutant protein or change mutant p53 to the wild type (WT)

conformation (47). LKB1 altered NSCLC is also difficult to target due to the diversity of *STK11* somatic alteration and the plethora of roles for LKB1 in the cell. Research has therefore focused on targeting the various pathways controlled by LKB1. As LKB1 has an important role as a negative regulator of mTOR signalling, mTORC1 inhibitors have been examined and are especially effective in NSCLC in combination with mTORC2 inhibitors to reverse tumour metabolic rewiring (48). Heat shock protein 90 (HSP90) can regulate LKB1 stability and inhibition marks LKB1 for degradation but also causes a short-term increase in LKB1 kinase activity, potentially helping patients with inactivating mutations. However, HSP90 inhibitors are not selective for mutant LKB1 and may also degrade WT LKB1, so there is a need to stratify patients by mutational status (47, 49).

In contrast to *STK11*, *KRAS* mutations lack diversity and frequently substitute glycine at codon 12. One such common substitution at codon 12 is a change from glycine to cysteine (G12C), which can be targeted by G12C inhibitors that stop KRAS cycling. Early data suggest these inhibitors are effective, but not in all patients (50, 51). Some patients partially respond before adaptations to mutant G12C which restarts KRAS cycling (52). Other patients with G12C mutations do not respond, which may be because these patients are not addicted to KRAS G12C signalling and are instead reliant on signals from another altered cancer gene (53). Precision medicine has benefited a great number of previously untreatable patients, yet some patients remain insensitive to rational treatments. Additional understanding cancer genetics and the TME will allow for correct treatment stratifications.

Further recent knowledge of tumour immunology has led to the advent of immunotherapy drugs which target immune cells to improve the immune response to cancer. Many immunotherapies target T cells, which are a type of lymphocyte involved in the adaptive arm of the immune system. The first impactful immunotherapy drugs in the field of cancer immunotherapy are immune checkpoint inhibitors, which block immune regulatory checkpoints. Ipilimumab is an immune checkpoint inhibitor which binds onto the cytotoxic T-lymphocyte-associated protein 4 (CTLA-4) receptor on T cells, and stops interactions with B7 family members that causes suppressive signalling propagating from this receptor. Though monovalent ipilimumab was the first approved checkpoint inhibitor drug, it has had limited clinical success in treating NSCLC.

The first truly successful checkpoint inhibitors target the programmed cell death protein (PD)-1/PD-ligand (PD-L)1 axis. Mechanistically, tumour cells can express PD-L1 or PD-L2, these bind to PD-1 expressed on the surface of activated T cells causing inactivation. Thus, the tumour can directly inhibit T cell mediated cytotoxicity, and antibodies that block this interaction prevent T cell inactivation (22). In 2016 the FDA approved the PD-1 inhibitor pembrolizumab as a first-line treatment following promising results from the KEYNOTE-024 and KEYNOTE-010 trials (54, 55). This approval was based on measuring the level of PD-L1 expression for the NSCLC tumour, but recent studies show that PD-L1 inhibitors may work in patients with low or negative PD-L1 expression (22). Moreover, treating NSCLC patients with a combination of ipilimumab and another PD-1 inhibitor nivolumab resulted in longer OS compared to treating with nivolumab alone or chemotherapy alone, and this was not dependent on the level of PD-L1 expression (56).

Following the success of PD-1/PD-L1 inhibitors there has been great interest in investigating blocking novel lymphocyte expressed checkpoint receptors such as lymphocyte-activation gene 3 (LAG-3), T cell immunoreceptor with Ig and ITIM domains (TIGIT) and T-cell immunoglobulin and mucin-domain containing-3 (TIM-3). LAG-3 binds stable peptide/human leukocyte antigen (HLA) class II complexes and transduces inhibitory signals to cluster of differentiation (CD)4^+ T cells, whereas TIGIT and TIM-3 have a variety of ligands. TIM-3 triggering causes intracellular calcium influx and consequential T cell apoptosis, whilst TIGIT outcompetes co-stimulatory receptors for CD155 ligand binding causing direct T cells suppression by signal transduction, or indirect suppression by paracrine interleukin (IL)-10 release. There are several ongoing trials investigating blocking these novel checkpoint receptors (57).

Vaccinating against cancer is a long touted immunotherapeutic option to aid cytotoxic tumour infiltrating lymphocytes (TILs) or prophylactically establish cancer immunity before oncogenesis. Target antigens for vaccination include tumour-associated antigens which are aberrantly expressed by the tumour but are also present in normal cells, or tumour-specific neoantigens arising from somatic mutations. Vaccines can be delivered in several ways, for instance long peptides with adjuvant can be injected directly into the tumour, or autologous patient dendritic cells can be pulsed *ex vivo* with peptides or mRNA and are adoptively transferred into the NSCLC tumour (58, 59).

Adoptive cell transfer therapy uses autologous TILs which are expanded *ex vivo* before re-infusion. A particularly interesting technique in NSCLC combines vaccination and adoptive cell therapy. A tumour biopsy and blood samples are firstly taken from the patient, the

tumour is sequenced to identify clonal neoantigens and these are synthesised in the laboratory. TILs from the tumour are cultured with dendritic cells from the blood which have been loaded with peptides corresponding to the neoantigens, and TILs that recognise these neoantigens are selectively expanded before adoptive transfer back into the patient (60). Autologous T cells can also be engineered to express chimeric antigen receptors with distinct domains, one such domain recognises tumour antigens such as EGFR which is overexpressed in NSCLC (61). Most adoptive transfer and vaccination strategies use autologous T cells to avoid HLA mismatches and graft versus host disease. However, using allogenic cells potentially allows the graft versus host response to augment the anti-tumour response, which could be made safe by blocking lymphocyte egress from the tumour (62). There are currently a great number of challenges for cellular therapies for NSCLC, including a difficulty for cells to infiltrate solid tumours, the suppressive role of the TME, a lack of a universal target antigen, as well as the fact that these therapies are difficult and expensive to manufacture in the laboratory.

1.2 *KRAS* and *STK11* Alterations in Non-Small-Cell Lung Cancer

This thesis predominantly concentrates on somatically altered *KRAS* and *STK11* LUADs. These cancer genes are currently very interesting as they are often found concomitantly in patients and work together to metabolically reprogram the tumour to aid oncogenesis. Alone, *KRAS* mutations and *STK11* mutations are associated with reduced survival, but together this lower survival is particularly pronounced. Moreover, at the time of writing there are no FDA approved drugs for *KRAS* or *STK11* mutations; PD-1/PD-L1 checkpoint blockade is effective for patients with *KRAS* mutations, but not for patients with *STK11* mutations or concomitant *KRAS/STK11* mutations. Therefore, these patients are a therapeutically underrepresented subgroup with lower survival and there is great clinical need for research into their underlying cancer immunology.

1.2.1 Constitutively Active *KRAS*

The Ras family of small GTPases were one of the first proto-oncogenes identified by scientists, with the most important members of this family in oncology being: HRAS, KRAS and NRAS. All Ras family members are closely related, highly homologous proteins with hydrolase enzymatic activity and acquire gain of function mutations at the same codons in cancer. Despite this similarity, somatically altered different Ras family members do result in distinct biological consequences (63). KRAS is the most frequently mutated Ras family member in NSCLC, with alterations occurring in 20–40% of LUAD patients often at an early stage of disease (13, 64, 65).

The KRAS GTPase and *KRAS* Mutations

The KRAS G domain, in which GTPase activity takes place encompasses over 80% of the protein. Importantly, within this large region a phosphate binding P-loop can be found between codons 10–17, as well as two switch regions between codons 30–40 and codons 58–72 which bind GEFs and GAPs. The phosphate groups from GDP or GTP bind onto the P-loop, and the conversion of GDP to GTP and hydrolysis back to GDP are regulated by the GEFs and GAPs. After the G domain towards the C-terminus is hypervariable region which is post-translationally modified to allow anchorage to the cell membrane close to RTKs (66, 67).

Typically, mutated KRAS has a 97-99% reduction in GAP-mediated GTP hydrolysis compared to the WT protein, but this happens by a variety of different mechanisms (68). Over 90% of *KRAS* mutations occur at codons 12 and 13 in the KRAS P-loop and these have

the highest transformation potential (63). Work by Zhang *et al* (69) showed that *KRAS* G12 mutations are transformative and can effectively activate MEK signalling. MEK signalling has also been suggested to be a dominant form of proliferative mTORC1 activation in cells with G12V mutations, taking preference over KRAS signalling via PI3K/AKT (70, 71). Different *KRAS* mutations have varying GDP/GTP affinities and kinetics of nucleotide exchange. One experiment established isogenic MCF10A breast epithelium cells in which KRAS G12C, G12D, G12V, G13C and G13D were overexpressed, found higher GTP affinities in cells expressing KRAS G12C, G12V and G13C compared to empty vector or WT MCF10A cells. Furthermore, KRAS G12D overexpressing MCF10A gained EMT-like features, and G12D or G12V overexpression caused increased MCF10A migration (72). Another study showed that KRAS G12V can activate other small GTPases from RHO family to regulate cellular motility and polarity (73).

The second most important site for *KRAS* mutations is glutamine 61, which is located in the regulatory Switch II region that controls GTP hydrolysis. Q61H and Q61L mutations were found to significantly decrease GTP hydrolysis speed compared to WT KRAS (68). Like *KRAS* G12V mutations, Q61H mutations preferentially activate MEK signalling relative to PI3K signalling via enhanced interactions with RAF1 (74). Mutations at *KRAS* codons such as 19 and 146 are deemed non-canonical as they are not located within the P-loop or switches, yet are still in the G domain. Whilst the oncogenic potential of position 19 mutations is subject to debate (75, 76), *KRAS* A146T mutations are transformative. GDP/GTP can bind at position 146, and A146T mutations have a GDP dissociation rate that is 12-fold higher than cells with WT KRAS. This dissociation rate was further increased in the presence of the GEF SOS1 suggesting that A146T tumour formation may be assisted by

increased nucleotide exchange instead of reduced GTP hydrolysis (76, 77). A phosphoproteomic comparison of KRAS A146T and KRAS WT cells suggests that A146T mediated signalling is via MEK (77). To compare the transcriptional signatures associated with canonical and non-canonical *KRAS* mutations, researchers performed an mRNA microarray on mouse embryonic fibroblasts (MEFs) transfected with both types of mutations. Hierarchical clustering showed that despite both being found in the P-loop, codon 12 mutations cluster together and codon 13 mutations cluster separately. Non-canonical mutations clustered with codon 13 mutations, which were linked with a reduced transformation potential (76).

Findings from studies assessing the prognostic impact of different *KRAS* mutations are unclear. Patients with treatment resistant NSCLC with *KRAS* G12C or G12V mutations have a lower time from end of treatment until disease progression (progression free survival), compared to patients without *KRAS* mutations or those with G12D mutations (70). Another study agreed that *KRAS* G12C mutations were associated with a reduced time to progression (not including death as an outcome) compared to G12D mutations, but found that patients treated with chemotherapy who have G12V mutations had a longer time to progression compared to those with G12C mutations (78). Patients with G12V mutations had better response rates to taxane chemotherapy compared to patients with G12V mutations treated with gemcitabine or pemetrexed, but this was not significantly associated with a longer progression free survival or OS (79).

KRAS Driven Epigenetic and Metabolic Changes

Epigenetic regulation of the KRAS pathway appears to play an important role in KRAS mediated oncogenesis. Vaz *et al* (8) exposed human bronchial epithelial cells to chronic cigarette smoke or DMSO over a period of 15 months and performed chromatin immunoprecipitation. They found a progressive silencing by hypermethylation of a transforming growth factor (TGF)β family member gene and repressor of Ras/MEK signalling, as well as the development of an EMT-like phenotype in these cells. KRAS G12V was then overexpressed in these smoke exposed bronchial epithelial cells and they were injected into immunodeficient mice. The mice injected with smoke conditioned KRAS G12V overexpressing cells developed tumours and not the control mice injected with dimethyl sulfoxide (DMSO) treated KRAS G12V overexpressing cells, suggesting that these epigenetic changes sensitise lung epithelial cells to mutant *KRAS* transformation. Furthermore, analysis of TCGA found that lower methylation of chronic smoke methylated genes in patients with *EGFR* mutations – which are less associated with smoking status – compared to patients with *KRAS* or *TP53* mutations (8). To compliment this effect on the KRAS pathway, other studies show that exposure of cigarette smoke products to pulmonary cells causes increased phosphorylation and thereby activation of MAPK, amplifying any existing KRAS mediated MEK pathway activity (80-82).

As KRAS driven LUAD is highly proliferative, these tumours undergo metabolic reprogramming to support their high energetic and anabolic requirements. Generally, tumours undergo a glycolytic switch termed the 'Warburg effect' in which cells switch from predominantly utilising OXPHOS – which is an efficient method of producing ATP

from glucose – to mainly using aerobic glycolysis which yields around 1-fold less ATP per glucose molecule. As aerobic glycolysis is a quicker process than OXPHOS, this change in glucose metabolism helps support rapidly growing tumour cells by synthesising lipids, nucleotides, and proteins (83, 84). Although there is a shift away from OXPHOS, the TCA cycle is still utilised by cancer cells with a key change in how pyruvate is metabolised. NSCLCs have high levels of pyruvate carboxylase activity which irreversibly carboxylates pyruvate to oxaloacetate. Replenished oxaloacetate is a TCA cycle intermediate and allows TCA cycling in a manner that is not completely dependent on acetyl-CoA to generate glucose-derived metabolites including citrate and succinate (85). Figure 1.2 provides an overview of the metabolic pathways subject to oncogenic rewiring.

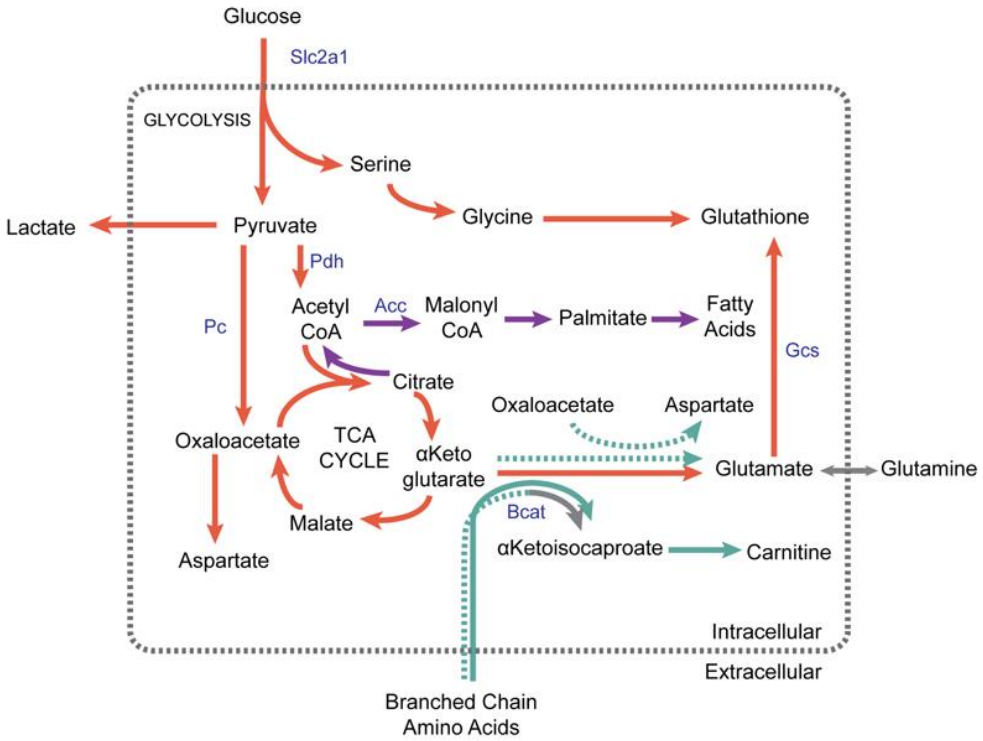

Figure 1.2 Glucose metabolic rewiring

An overview of the key metabolic pathways involved in glucose rewiring discussed in this thesis: glycolysis, TCA cycle and channelling towards glutathione production. Figure from Kerr and Martin (83).

Glycolytic KRAS driven tumours also require the TCA cycling to develop tumours, by using pyruvate carboxylase to replenish TCA intermediates (39). This work also showed that most of the glucose in *in vitro* KRAS driven NSCLC is used to generate lactate which can aid NAD^+ regeneration, allowing the cell to generate ATP by OXPHOS in low oxygen settings. *In vivo*, KRAS driven NSCLC uses glucose more evenly to generate lactate and provide a path to replenish TCA intermediates by both pyruvate carboxylase and also by pyruvate dehydrogenase which is the canonical link between glycolysis and the TCA cycle (39). The *KRAS* G12D mutation has been particularly associated with a glycolytic phenotype and its allelic content has been suggested to alter glucose metabolism. A study by Kerr *et al* (15) generated MEFs with different zygosities and found that profiling $KRAS^{G12D/G12D}$

homozygous MEFs by microarray showed a transcriptional upregulation of glycolytic genes compared to heterozygous $KRAS^{G12D/WT}$ and WT $KRAS^{WT/WT}$ MEFs. This was supported by increased secretion from $KRAS^{G12D/G12D}$ MEFs compared to the other two types of MEFs. This study showed that glucose metabolism was directed towards glycolysis and TCA cycle mediated glutathione production which is an important antioxidant for reactive oxygen species (ROS) (15).

The role of ROS in KRAS driven NSCLC is controversial, with some researchers suggesting that KRAS signalling in lung cancer induces mitochondrial ROS generation to control proliferation (86). However, the previously described study by Kerr *et al* (15) suggests that KRAS has a role in reducing oxidative stress. This is supported by research from the Tuveson group who showed that oncogenic KRAS increased transcription of nuclear factor erythroid 2-related factor 2 (NRF2), a transcription factor responsible for inducing an antioxidant transcriptional programme (87). It has been postulated that by having an antioxidant capability, tumour cells with *KRAS* mutations will be able to survive during metastasis and seed in areas with high oxidative stress (88). Conversely, high oxidative stress has been associated with metastasis (89).

To aid antioxidative glutathione production, NSCLCs with *KRAS* mutations take up high levels of essential branched-chain amino acids such as valine and leucine from their environment. These can be used as a nitrogen source to support production of the glutathione precursor glutamine using TCA cycle metabolites (90).

In summary, the literature around *KRAS* mutations in lung cancer show that smoking induced epigenetic changes can make epithelial cells permissible to *KRAS* mediated

transformation and that KRAS can signal via a multitude of different pathways to assist oncogenesis, although there is a tendency for signalling to MEK from RAF. Although they initially appear very similar, *KRAS* mutations function differently and there is a metabolic rewiring of glucose metabolism which is particularly associated with *KRAS* G12D mutations. The shift towards aerobic glycolysis to allow rapid growth is not the only metabolic fate for KRAS driven NSCLC, and the TCA cycle helps enable an antioxidant phenotype. These metabolic observations are particularly interesting considering that in LUAD KRAS alterations are linked to alterations in the important metabolic sensor LKB1.

1.2.2 Loss of LKB1/*STK11* Function

LKB1 acts with AMPK to provide a key metabolic checkpoint in cells sensing high intracellular AMP in response to metabolic stress. Dysregulation of this axis results in altered metabolism and proliferative mTORC1 signalling. Like *KRAS* alterations, *STK11* (the gene name for LKB1) alterations occur relatively early in LUAD, but the frequency of patients with *STK11* mutations is lower at 10–35% (4, 13, 65, 91). Although *STK11* mutations appear less common, in fact most NSCLC patients have loss of the *STK11* chromosomal locus at 19p13.3. *STK11* chromogenic *in situ* hybridization and 19p microsatellite analysis revealed that 62% of NSCLCs tested had hemizygous *STK11* loss and 28% had homozygous loss akin to a deletion. Together, 90% of NSCLC patients tested had some loss of LKB1 function (92).

Germline *STK11* mutations are the cause of the polyposis syndrome Peutz-Jeghers Syndrome which can be inherited. This syndrome is not just as a result of mutations, as

murine studies show that biallelic *STK11*$^{-/-}$ deletions are embryonically lethal, but that hemizygous *STK11*$^{+/-}$ loss also results in Peutz-Jeghers Syndrome. Peutz-Jeghers patients have an increased risk of a variety of cancers, especially breast and gastrointestinal cancers (93, 94). *STK11* alterations in non-Peutz-Jeghers cancer patients arise during oncogenesis alongside other drive alterations and are extremely heterogeneous. Furthermore, most *STK11* mutations are predicted to cause some loss of LKB1 function (92).

The main structural feature of LKB1 is a large functional protein kinase domain which is over 250 amino acids in length. At the start of this domain is a regulatory region – called the deacetylation region – which is post-translationally modified to allow for LKB1 to complex with other proteins to exert its kinase function. Deacetylation is performed by the sirtuin 1 (SIRT1) enzyme, which is activated by abnormal high intracellular NAD^+ under conditions of energic stress such as calorie restriction. SIRT1 mediated deacetylation is linked to LKB1 being phosphorylated by and complexing with STRAD, which then potentiates nuclear export, further complexing and phosphorylation of LKB1 target proteins (95).

Loss of LKB1 alone is unable to initiate NSCLC (64). However, experiments treating LKB1 proficient and deficient mice with a chemical carcinogen was able to induce SqCC. Carcinogen treated LKB1 deficient mice with hemizygous *STK11*$^{+/-}$ loss were shown to have significantly decreased tumour free survival compared to their *STK11*$^{+/+}$ littermates. This study also showed that despite the presence of a WT allele, *STK11*$^{+/-}$ mice did not express *STK11* mRNA or LKB1 protein (96). LKB1 protein loss or loss of function mutations are

thought to signify insufficient AMPK-mediated mTORC1 inhibition. As such, cell lines from LKB1 deficient mice have high phosphorylated S6K with no change in mTORC1 levels, and reintroducing WT LKB1 caused a reduction in phosphorylated S6K in these cells (96). LKB1 deficiency therefore reduces the inhibitory signals on mTORC1 allowing for proliferative signalling.

Metabolic Rewiring in LKB1/*STK11* Deficient Lung Cancers

Metabolic reprogramming of glucose utilisation also occurs in LKB1 deficient NSCLC, characterised by a similar switch towards aerobic glycolysis as observed in KRAS driven NSCLC. An important transcription factor that is regulated by mTORC1 signalling as proven by inhibiting mTORC1 using rapamycin is HIF1α. HIF1α normally controls the cellular response to hypoxia and is associated with a glycolytic switch under both hypoxic and normoxic conditions, including by regulating glucose transporter 1 and the angiogenic factor VEGF-A (97). mTORC1 can regulate HIF1α at a transcriptional level by phosphorylating STAT3 which then promotes transcription, as well as at a translational level through 4EBP1 and S6K (98). Correspondingly, Faubert *et al* (99) generated LKB1 deficient MEFs and used two NSCLC cell lines with *STK11* alterations (A549 and A427) to show high HIF1α protein expression in LKB1 null cells, which is reduced upon reintroduction of WT LKB1. They also found that HIF1α drives expression of genes involved with glucose metabolism including pyruvate dehydrogenase kinase 1 and lactate dehydrogenase A. Faubert *et al* (99) agrees with findings from Dodd *et al* (98) showing that HIF1α is regulated by mTORC1 and that cell lines with *STK11* alterations were

dependent on HIF1α to survive in a glucose and oxygen limited environment (99). These studies suggest that LKB1 deficient cells shift towards a glycolytic phenotype that is driven by HIF1α expression.

In addition to altered glucose utilisation, deletion of LKB1 results in increased glucose uptake helping these tumour cells competing with others in the TME for nutrients (100). This is coupled with a raise in the available intracellular glucose by increased gluconeogenesis as shown in a LKB1 knockout murine hepatocyte model (101). Like KRAS driven NSCLC which uses glutamine to enhance the supply of antioxidative glutathione, the growth of LKB1 deficient cell lines is sensitive to glutamine withdrawal (102). Moreover, NRF2 activity is directly regulated by LKB1 loss causing the transcription of antioxidant genes (102).

The Impact of LKB1/*STK11* Loss on Related Kinases

AMPK is not just an important intermediary in LKB1 signalling to mTOR but is itself intrinsically linked to the phenotype of NSCLC cells with loss of LKB1 function. An abrogation of AMPK signals can result in a loss of epithelial polarity in NSCLC (47). In addition to its role as an inhibitor of mTOR, AMPK can also induce cell cycle arrest and p53-dependent apoptosis by phosphorylating p53 (103). Likewise, LKB1 can also directly interact with p53 and induce apoptosis, as well as halt cell cycling by targeting p21, p27 and cyclin D1 (104-107). Interestingly, DNA damage activated ATM and ATR can induce LKB1-dependent AMPK phosphorylation, suggesting that DNA damage repair pathway can regulate mTOR growth signals, inhibit cell cycle progression and stimulate p53-mediated

apoptosis all via LKB1/AMPK signalling (47, 108, 109). AMPK also plays a direct role in stress management as a regulator of autophagy and loss of LKB1 reduces the energic outputs of AMPK-mediated autophagy and mitophagy (110).

AMPK is not the only target for LKB1, as it also interacts with at least 12 other kinases called the AMPK-related kinases. These include members from the KIN2/PAR-1/MARK kinase (MARK) and salt-inducible kinase (SIK) families of protein kinases, and dysregulation of some of these is association with poor cancer prognosis (93). Like AMPK, normal signalling to MARK family members is associated with cellular polarity as the MARKs interact with scaffold proteins (111). Loss of polarity from nullified LKB1 signalling can also promote metastasis in an AMPK-independent manner as MARK1 and MARK4 normally repress Snail expression and its regulation of genes involved with migration and invasion (112). By knockdown of all known human kinases Mohseni *et al* (113) discovered that loss of LKB1 is able to dysregulate growth and cell size by inducing Hippo pathway signalling through altered protein localisation regulated by MARK1, MARK3 and MARK4. Studying the SIK family of AMPK-related kinases showed that SIKs phosphorylate the CREB regulated transcription coactivator 2 (CRTC2) stopping nuclear migration. CRTC2 is dephosphorylated in A549 and A427 cells, allowing binding with the transcription factor cAMP response element-binding protein (CREB) which induces transcription of genes that promote growth, survival, chemotherapy resistance and NSCLC progression (114). This is the same mechanism as described previously (101), in which AMPK phosphorylated CRTC2 to inhibit CREB-mediated gluconeogenic gene expression.

To summarise, LKB1 is unable to transform cells alone, but if LKB1 is altered in an established NSCLC tumour it can have substantial pleiotropic effects. Loss of LKB1 switches metabolism towards aerobic glycolysis to aid fast growth in a nutrient limited environment which is accompanied by enhanced glucose uptake and *de novo* synthesis. LKB1 deficient cells also have antioxidant properties to detoxify ROS. As a stress sensor, LKB1 is normally linked to other stress responses including the response to DNA damage and is able to impact cell cycling and induce apoptosis in response to metabolic or genotoxic stress. LKB1 regulates AMPK and a set of related kinases which can impact polarity and metastatic potential upon dysregulation. There are similarities between *STK11* altered NSCLC and *KRAS* altered NSCLC, and the pathological phenotype of a KRAS driven tumour can be enhanced by LKB1 deficiency in a potentially synergist manner.

1.2.3 Co-occurring *KRAS* and *STK11* Alterations

LUADs driven by concomitant *KRAS* and *STK11* cancer gene alterations are associated with a significantly reduced survival compared to LUADs without any *KRAS* and *STK11* alterations, or those with just *KRAS* alterations (115). This may be evidence of KRAS gain and LKB1 loss working synergistically to dysregulate cellular processes to suit cancer progression. Concomitant *KRAS/STK11* alterations occur in approximately 50% of LUAD patients with *STK11* mutations but considering that most NSCLC patients exhibit some loss of LKB1 this number is likely to be much higher (65, 91, 92). It was previously suggested that *KRAS/STK11* alterations drove oncogenesis predominantly by hyperactive proliferative mTORC1 signalling, with positive signals from KRAS signalling and no mTORC1

inhibition from LKB1 (43). Though unrestrained mTORC1 signalling occurs in NSCLC which aids growth and the glycolytic switch, it is now clear that these co-occurrent alterations have important roles in a host of other cellular processes which may be more clinically actionable. Furthermore, *KRAS/STK11* driven NSCLC is also associated with alterations in other cancer genes, including *TP53*, kelch-like ECH-associated protein 1 (*KEAP1*) and *ATM* (49).

ATM is classically known as a sensor of DNA damage and is subject to inactivating mutations in 5–15% of LUADs and these mutations are often subclonal (13, 49, 65). A study in which a subset of patients with *KRAS* driven LUADs were subject to unsupervised clustering based on RNA-Seq data showed that inactivating *ATM* and *STK11* mutations are significantly co-occurrent with *KRAS* mutations, and that two of the main clusters were substantially enriched either with concomitant *KRAS/STK11* mutations or *KRAS/TP53* mutations. Patients with *ATM* mutations often fell into the first cluster, having *KRAS/STK11/ATM* mutations (49). Interestingly, *ATM* and *TP53* mutations were mutually exclusive. This may be because complete loss of p53 and ATM function would result in lethal levels of excess DNA damage, whereas inactivating mutations in *ATM* alone would result in a reduction in the sensitivity to DNA damage and further genomic instability but not complete insensitivity (30, 64). As ATM is a sensor of hypoxia, loss of ATM could aid glycolytic *KRAS/STK11* driven LUAD to proliferate in low oxygen (33). There is also evidence that ATM loss may phenocopy LKB1 loss. Alexander *et al* (108) found that functional activated ATM could negatively regulate mTOR signalling via LKB1/AMPK signalling. Later work by Skoulidis *et al* (49) suggested that mutations in *ATM* mimic those in *STK11* and allow unrestricted mTORC1 signalling, even in the absence of LKB1 loss.

These findings show that *ATM* inactivation in patients with *KRAS/STK11* alterations can promote tumour growth under hypoxia and copy the *KRAS/STK11* phenotype in patients with *KRAS/ATM* alterations.

Antioxidative, Metabolic and Epigenetic Rewiring in *KRAS/STK11* Driven Lung Cancer

KRAS/STK11 alterations also co-occur with *KEAP1* mutations in mice and humans, and lung tumours with this combination of alterations tend to be of a higher grade (49, 116). *KEAP1* inactivating mutations occur in 10–20% of LUADs and enhance the antioxidative profile of a cell (49, 65). Normally, KEAP1 induces turnover of antioxidative NRF2 by marking it for proteasomal degradation by ubiquitination and as KEAP1 is a key NRF2 regulation, loss of KEAP1 is associated with more available NRF2 (64). *KRAS*$^{G12D/WT}$*STK11*$^{-/-}$ mice have higher levels of ROS and lower levels of NRF2 compared to *KRAS*$^{G12D/WT}$*TP53*$^{-/-}$ mice, so concomitant *KEAP1* loss would therefore be beneficial to LKB1 deficient cells to help with detoxification (117). This is supported by clinical evidence, as patients with *KRAS/STK11/KEAP1* tumour alterations are resistant to platinum chemotherapy due to enhanced detoxification (118). This KEAP1-mediated NRF2 regulation also directly aids antioxidative glucose rewiring in *KRAS/STK11* driven NSCLC. NRF2 positively regulates a ligase that catalyses glutathione production from glutamate derived from glutamine. *KEAP1* alterations cause further metabolic perturbations and co-occurrence with *STK11* alterations causes a near complete dependency on glutamine in *KRAS* driven NSCLCs which have already undergone considerable metabolic rewiring. This heavy rewiring causes metabolic inflexibility and *in vitro* cells with *KRAS/STK11/KEAP1* alterations were

sensitive to glutaminase inhibitors and could not grow in glutamine free media (102). *KRAS/STK11/KEAP1* LUADs therefore use glutamine to metabolise glutathione directly via glutamate conversion and indirectly by feeding back into a rewired TCA cycle via α-ketoglutarate that is biased towards glutathione production, whilst also generating ATP (15, 119).

Lipid metabolism is also dysregulated by *KRAS/STK11* NSCLC to provide additional sources of energy and to help maintain tumour cell membranes. *KRAS*$^{G12D/WT}$*STK11*$^{-/-}$ mice were shown to have elevated *de novo* fatty acid synthesis as AMPK usually phosphorylates and inhibits acetyl-CoA carboxylase, an enzyme that produces the fatty acid biosynthesis precursor malonyl-CoA (120). LKB1/AMPK also regulate fatty acid, triglyceride and cholesterol biosynthesis at a transcriptional level (121, 122). Furthermore, tumours from *KRAS*$^{G12D/WT}$*STK11*$^{-/-}$ mice accumulate intracellular lipid droplets which are normally processed by autophagy to provide energy, but as LKB1 deficiency impairs AMPK-regulated autophagy, droplets may be insufficiently processed or autophagy may not be completely inhibited by LKB1 loss (123).

KRAS and *STK11* alterations are also interestingly able to process nitrogen using the urea cycle (112, 124, 125). The urea cycle is normally restricted to hepatocytes, but cells with *KRAS/STK11* alterations are also able to manipulate this pathway to favour the production of pyrimidine derived nucleotides which can provide a growth advantage. A study by Kim *et al* (125) found that human NSCLC cell lines with *KRAS/STK11* alterations abnormally express the urea cycle enzyme carbamoyl phosphate synthetase-1 (CPS1). This expression was inversely correlated with LKB1 expression and CPS1 regulation was dependent on

LKB1 kinase activity. CPS1 was shown aid synthesis of pyrimidine derived nucleotides from glutamine metabolites. The authors propose that glutamine rewiring in *KRAS/STK11* NSCLCs also occurs to increase these nucleotides to support growth (125).

Nucleotide generation in *KRAS/STK11* altered NSCLC is additionally controlled by a metabolic flux towards serine biosynthesis which also supports antioxidative NADPH production and potentiates epigenetic regulation. Intermediates from glycolysis and glutamine metabolism can be channelled into the serine-glycine-one-carbon pathway towards the methionine salvage pathway which produces s-adenosyl methionine, a substrate for DNA methylation and promotor epigenetic regulation by DNA methyltransferases (124). Epigenetic regulation in *KRAS/STK11* driven NSCLC affects numerous pathways including the cytoplasmic dsDNA sensing stimulator of interferon genes (STING) pathway. Patients with *KRAS* and *STK11* mutations had high expression of DNA methyltransferases and elevated s-adenosyl methionine and exhibited an epigenetic silencing of the STING-mediated type I interferon response (126).

Targeting *KRAS/STK11* Driven Lung Cancer

As efforts to treat *KRAS/STK11* driven LUAD have only limited success, the most important clinical question is how to treat patients with these cancer gene alterations. Investigators have sought to inhibit increased MEK signalling downstream of KRAS. MEK inhibition has proved successful for patients with *KRAS* alterations, but not for those with *KRAS/STK11* alterations (64). Another promising therapeutic strategy is to target *KRAS/STK11* LUAD epigenetic and metabolic vulnerabilities including by inhibiting glycolysis; HSP90 inhibitors

promote the degradation of HIF1α which regulates the glycolytic switch and of mutated LKB1 (47, 49). HIF1α is itself regulated by mTORC1 activation. Treating LUAD cell lines with *KRAS/STK11* alterations with an experimental dual mTORC1/mTORC2 inhibitor in combination with the mitochondrial complex I inhibitor phenformin inhibited glucose metabolism by glycolysis and OXPHOS (93). Using an mTORC1 inhibitor, like rapamycin, alone may not provide therapeutic clinical benefit as the lesser studied mTORC2 also has important roles in glucose metabolism reprogramming (127-129). Targeting nucleotide synthesis including by using nucleoside analogues like gemcitabine is another possibility for *KRAS/STK11* LUADs (64), which might be enhanced by inhibiting the serine-glycine-one-carbon pathway and CPS1/CPS2 (124, 125). Moreover, *KRAS/STK11* altered cell lines are sensitive to DNA methyltransferase inhibitors which repress negative epigenetic regulation of inflammatory pathways including STING (124, 126). Exploring novel combinations of these treatments may be key in drugging *KRAS/STK11* driven LUAD as well as potentiating renewed immune engagement in these patients.

1.3 Immune Response to Non-Small-Cell Lung Cancer

The process in which the immune system recognises and eliminates cancerous cells is called immunosurveillance. Immune cells continually perform immunosurveillance and regularly eliminate transformed cells before they can become established as a tumour. In cancer there is a failure of immune control, often precipitated by tumour cells themselves. To survive and proliferate, solid tumours like NSCLC evade the immune system and create complex TMEs depending on their needs, often manipulating immune cells to promote tumour growth. How NSCLC tumours develop is fundamentally controlled by cancer genetics. Knowledge of how the immune system interacts with established tumours driven by different underlying cancer gene alterations is key in understanding cancer progression as well as how to treat patients, including the timing and choice of immunotherapy.

1.3.1 Immunosurveillance and Tumour Immunoediting

One of the key concepts in cancer immunosurveillance is the priming and response of T cells to tumour antigens. Cancer antigens are released during tumour cell death by normal apoptosis or because of innate immune cell involvement, such as natural killer (NK) cell-mediated destruction or macrophage engulfment. Antigens are then captured by professional antigen-presenting cells (APCs) like dendritic cells (DCs) and are processed to a peptide form which is presented on HLA molecules at the cell surface. DCs then migrate from the tumour to secondary lymphoid organs including lymph nodes, where they present peptide-HLA complexes to naïve αβ T cells via their T cell receptor (TCR). This priming is accompanied by secondary co-stimulatory signals. For example DC-expressed CD80/CD86 binds to T cell CD28 which induces the expression of CD25 to produce a functional cell surface IL-2 receptor. T cells are then able to undergo clonal expansion supported by IL-2, and other cytokines in the environment may induce T cell differentiation to various T cell subsets (19, 130). The newly primed effector T cells are then able to migrate to a tumour site to perform immunosurveillance themselves, recognising and lysing tumour cells (19).

As immunocompetent people develop cancer, this suggests that immunosurveillance fails to always keep cancers in tumours in check. Immunoediting is an evolutionary escape from immunosurveillance by cancer cells, described as having three stages: elimination, equilibrium, and escape. The elimination stage represents successful immunosurveillance in which T cells can kill tumours presenting tumour-associated antigens, tumour-specific neoantigens and also viral antigens (131-134). During dynamic equilibrium, some tumour clones have escaped total elimination but are still being contained by the immune system.

This exerts a selection pressure and tumours evolve to fully escape immune regulation by further genomic instability, allowing progression into the final stage, escape (135). Immunoediting has been shown to occur in lung cancer (136-140).

There are many ways in which immunoediting can happen in tumours, including by immunosuppression. For instance, tumours may secrete factors including IL-10, TGFβ and indoleamine 2,3-dioxygenase (IDO) to directly suppress immune cells as well as indirectly suppress via induction of regulatory T cells (Tregs) (141, 142). Tumour cells can also upregulate suppressive checkpoint receptors, including PD-L1 and PD-L2 as well as B7 family members to interact with CTLA-4 (140, 143). Immune activation is also affected as tumours can express high levels of inhibitory NK ligands (144, 145). There is also plenty of evidence of tumour loss of HLA class I molecules to inhibit $CD8^+$ T cells and HLA class II to inhibit $CD4^+$ T cells by hemizygous loss of *HLA* genes (140, 146, 147). Moreover, β2-microglobulin – which is a structural component of class I – is often downregulated in NSCLC, as is the coordinator of class II expression, class II transactivator (CIITA) (146-148). Furthermore, tumours with normal HLA class I and II expression may exhibit dysfunction in peptide processing and binding, including downregulations in the transporter associated with antigen processing protein, which allows proteasomally processed peptide into the endoplasmic reticulum for association with HLA class I molecules (58). Interestingly, neoantigens from mutated peptides are associated with particular HLA types and poorly presented on HLA. Tumours may select against mutated peptides with high HLA affinities (149, 150). Whilst there is heterogeneity in the mechanisms causing loss of immune recognition, the endpoint of immune escape is crucial for the establishment of a malignant NSCLC tumour and its microenvironment.

1.3.2 The Non-Small-Cell Lung Cancer Immune Microenvironment

To respond to an established lung tumour, leukocytes are recruited to the tumour site and can migrate inside the tumour bulk. Large numbers of adaptive and innate infiltrating immune cells are found in both the LUAD and SqCC histological subtypes of lung cancer relative to other solid tumours. However, there is heterogeneity and certain lung tumours have higher leukocytes numbers – known as immunologically 'hot' – whilst others have lower leukocyte numbers and are called immunologically 'cold' (151). Leukocytes are recruited from secondary lymphoid organs or the blood (142). Migrant leukocytes then move in response to chemokine gradients to execute their roles within the tumour (152).

Most intratumour lymphocytes are organised into ectopic tertiary lymphoid structures (TLSs) to cultivate adaptive immunity (Figure 1.3). Like secondary lymphoid structures, these lymphoid aggregates have distinct T and B cell areas, and germinal centres may form in the most mature TLSs (153). The majority of tumour infiltrating B cells are found in B cell follicles, alongside follicular DCs, macrophages and T follicular helper (Tfh) cells. TLS-organised T cells can be found in T cell zones with mature DCs (154). These structures are surrounded by high endothelial venules which allows extravasation potentially directly into TLSs. Naïve and memory T cells can be activated in TLSs, then enter the stromal environment to exert anti-tumour functions (155).

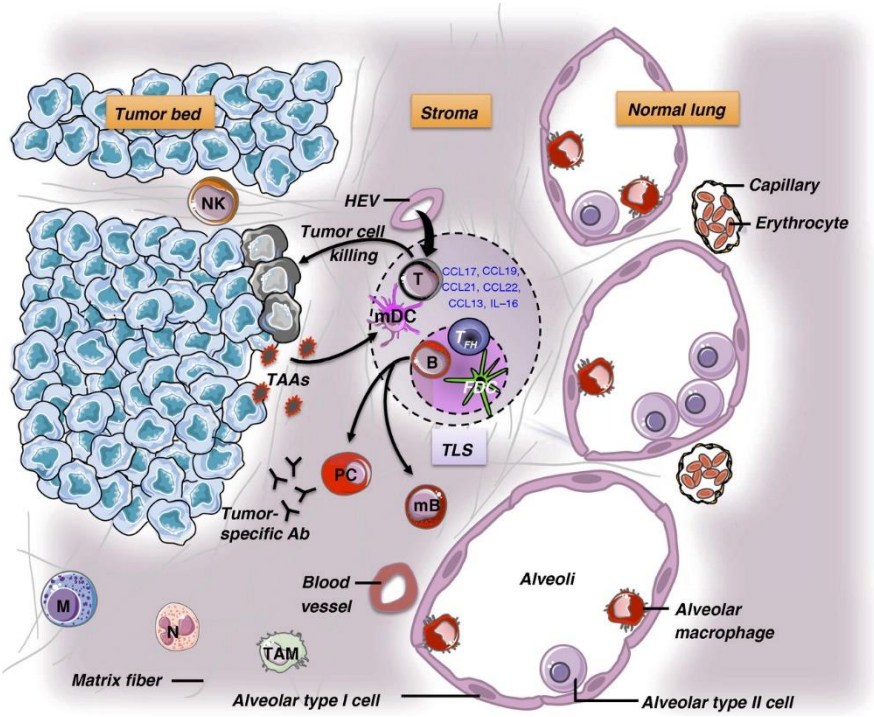

Figure 1.3 NSCLC immune contexture

The NSCLC intratumoural immune response, orchestrated by interactions within a TLS. Figure from Remark *et al* (142).

The Lymphoid Environment

The most abundant CD45$^+$ leukocyte in LUAD tumours are T cells with CD4$^+$ T cells being more common than CD8$^+$ T cells (156). CD4$^+$ T cells differentiate into various T cell subsets dependent on activation factors including TCR and co-stimulatory signal strength, and the cytokine milieu. These cells are not entirely lineage-committed however and can exhibit phenotypic plasticity post-polarisation (157). One of the two classical CD4$^+$ T cell subsets are T helper (Th)1 polarised CD4$^+$ T cells which are involved in helping cell-mediated immunity including cytotoxic CD8$^+$ T cell responses. Th1 cells are predominantly found within TLSs but can also act as TILs in the stroma. Other major CD4$^+$ T cell subsets including Th2, Th17, Tfh and Treg have all been observed within lung tumours (155, 158). Most CD4$^+$ and CD8$^+$ T cells from NSCLC tumours were shown to express CD69 and CD103, markers of

tissue retention which are characteristic of resident memory T cells (159). Interestingly, there is evidence that many LUAD resident memory $CD8^+$ T cells are specific for viral antigens rather than tumour antigens and act as bystander T cells, although it is not yet established as to whether these cells can contribute to anti-tumour responses (133, 160). Cytotoxic $CD8^+$ effector memory TILs are activated inside TLSs but are predominantly found in the NSCLC stroma and are key players in the adaptive immune response against the tumour (142, 147, 161-164). Isolating $CD4^+$ and $CD8^+$ TILs then co-culturing with lung tumour digests showed that subsets of TILs were tumour reactive, polyfunctionally secreting interferon (IFN)γ with IL-2 or tumour necrosis factor (TNF)α (165). Although there is evidence of cytotoxicity and response to tumour antigens, chronic exposure to clonal neoantigens derived from NSCLC cancer gene mutations results in $CD4^+$ and $CD8^+$ T cell exhaustion and dysfunction (166).

NK cells are innate lymphocytes that can lyse stressed cells and tumours by several approaches including using cytolytic granules. However in NSCLC, there are lower numbers of intratumoural NK cells from early stages of disease and their cytotoxicity is inhibited (139, 144, 145, 156, 167). Another small innate lymphocyte population are the HLA-unrestricted γδ T cells which respond to non-peptide antigens. Lung resident γδ T cells in the lung are likely to be of the Vγ9Vδ1 or Vγ9Vδ2 subsets and there is mixed evidence for their roles in NSCLC, with some studies suggesting that γδ T cells are pro-angiogenic and others suggesting that they induce tumour lysis via NKG2D, Fas receptor/Fas ligand and granule secretion (168, 169).

It has been proposed another innate lymphocyte cell (ILC) subset called lymphoid tissue inducer cells (LTi) cells may a have a role in constructing intratumoural TLSs. LTi cells are known to form secondary lymphoid tissues during gestation, and the interaction of LTi membrane lymphotoxin (LT) α and LTβ with their receptor can induce expression of chemokines such as chemokine (C-C motif) ligand (CCL)19 and CCL21 that can recruit lymphocytes into TLSs (155, 170). This process is aided by IL-7 which helps humoural immunity develop in the B cell follicle and maintains T cell homeostasis (155, 171). However, it is not entirely clear whether LTis are the sole cell responsible for ectopic adult lymphoid structure development in the lung and in lung tumours (172, 173). LTi cells are similar to the lineage$^-$ ILC3 subset, as both depend on the expression of the transcription factor retinoic acid-related orphan receptor (ROR)γT and secrete IL-17 (172, 174). Furthermore, natural cytotoxicity receptor (NCR)$^+$ ILC3s have their own LTi-like properties and have been found at the edges of NSCLC TLSs (172).

DCs can originate from either the common myeloid or lymphoid progenitors. Mature DCs in T cell TLS zones prime an effector Th1 anti-tumour immune response which can also protect from metastatic NSCLC. Whilst follicular DCs and Tfhs in B cell zones interact with B cells and promotes class switching, affinity maturation as well as differentiation into prognostically favourable plasma cells (142, 155, 161, 164, 175). Presence of plasma cells suggests a functional antibody response, potentially with antibodies specific for tumour antigens, but this has been difficult to characterise. Nevertheless, a study by Germain *et al* (154) expanded B cells from NSCLC tumours *ex vivo* and described antibodies reactive for tumour antigens including P53, which they suggested was generated by antigen exposure inside the TLS germinal centre (154).

The Myeloid Environment

In contrast with immune cells of lymphoid origin, immune cells of myeloid origin are largely associated with the suppression of anti-tumour immunity. Tumour associated macrophages (TAMs) have a dichotomy between 'M1' pro-inflammatory/anti-tumour TAMs and 'M2' anti-inflammatory/pro-angiogenic TAMs, although this is likely to in fact be a continuum (176, 177). TAMs differently use lipids available in the NSCLC TME, with M2 TAMs taking up higher levels of lipids compared to M1 TAMs. This also indirectly suppresses resident memory $CD8^+$ which require lipids for maintenance within the tumour (177). TAMs also directly affect T cells by expressing PD-L1 to induce T cell exhaustion, secreting IL-10 to suppress T cell function and releasing TGFβ which can polarise T cells to Tregs (139, 178). CAFs can also polarise $CD4^+$ Tregs driven by the transcription factor forkhead box P3 (FoxP3) in a TGFβ dependent and independent manner (179, 180). In normal conditions Tregs are important in the regulation of autoimmunity, suppressing self-reactive lymphocytes to achieve self-tolerance. Although Tregs are of lymphoid and not myeloid origin, they contribute to a suppressive NSCLC microenvironment in a variety of ways, for instance: by utilising IL-2 in the environment without providing any IL-2 back, expressing CTLA-4, inducing IDO expression from APCs and secreting adenosine, IL-10 and TGFβ (142, 181, 182). Tregs are present both in the stroma and inside TLSs, and depletion in NSCLC causes an increase in $CD8^+$ T cells cytotoxic function with a reduction in tumour burden (164, 183, 184).

Although M2 TAMs are suppressive in the TME, the dominant myeloid lineage cells of the NSCLC immune contexture are neutrophils and myeloid derived suppressor cells (MDSCs).

MDSCs are a heterogeneous subset of suppressive immature myeloid cells resulting from disrupted myelopoiesis, which can be sub-categorised based resemblance of neutrophils or monocytes (176). MDSCs induce T cell suppression by secreting TGFβ, ROS and arginine hydrolysing enzymes, as well as prompting angiogenesis via VEGF secretion and aiding metastasis by matrix metallopeptidase (MMP)9 expression (185-188). There is great recent research interest in MDSCs and a reliable human MDSC marker has recently been described, yet the most common myeloid cells in NSCLC are neutrophils (156, 176, 189, 190). Neutrophils are important granulocytes in the body and can degranulate cytolytic granules, produce coagulative neutrophil extracellular traps from DNA and protein, and are also professional phagocytes (191). Like TAMs, tumour associated neutrophils (TANs) can also be split into N1 and N2 TANs, of which N2 can be polarised like M2 TAMs using TGFβ and have a pro-tumour effect (192). Interestingly, TANs may act as prominent APCs for T cells during early-stage NSCLC, but TANs are overall associated with a worse prognosis in LUAD, and can secrete IL-10, arginase, and pro-inflammatory IL-6 (189, 193, 194).

1.3.3 Immune Contextures and Non-Small-Cell Lung Cancer Genetics

Tumour cell oncogenic alterations in different cancer genes can be linked to particular changes in the immune microenvironment. Changes in immune cell phenotype or functionality might be preferentially linked to responses to neoantigens derived from these mutated cancer genes. Alternatively, immune cells may be directly manipulated by tumour cells. For instance, oncogenic alterations could induce tumoural cytokine

secretion, expression of immune checkpoints and changes in metabolite availability in the TME.

Links between cancer alterations and the immune system have been made in other cancers, including colorectal cancer (CRC) in which a subset of patients suffer with deficiencies in DNA mismatch repair. This repair mechanism excises erroneous base insertions or deletions then resyntheses the sequence. However, defects in this process causes microsatellite instability (MSI) in which sequence errors accumulate resulting in new repetitive short microsatellites and additive levels of genomic instability (195). MSI-high CRC tumours have increased TIL and TAM infiltrates albeit with high expression of immune checkpoints compared to microsatellite stable tumours. These TILs have been shown to be predominantly memory $CD8^+$ T cells which express IFNγ and are suggested to be responding to neoantigens, as the genomic instability in MSI-high CRC indicates a high tumour mutational burden (TMB) (195-197). Studies in CRC also demonstrate that tumour-specific immune responses are not only associated with cumulative genomic instability but are also linked with specific cancer gene alterations. For example, patients with *BRAF* mutations in CRC have high numbers of anti-tumour TILs and tumours with *BRAF* mutations are also associated with anti-tumour $CD4^+$ TILs, whilst melanoma cell lines expressing mutant BRAF secrete cytokines which can suppress DCs (197-199). Like MSI-high and *BRAF* driven tumours, mutations in DNA polymerase epsilon catalytic subunit (*POLE*) – which causes dysfunctional DNA polymerase proofreading – are associated with high TILs in CRC and endometrial cancer (197, 200).

This potential immune engagement observed in patients with the aforementioned alterations in CRC is not observed in those with *KRAS* alterations. Gene expression analyses have shown that CRC patients with *KRAS* mutations have reduced expression of immune genes including *CD4* and *HLA* class II genes, with increased expression of immune checkpoints (197). Reduced immune gene expression suggests lower TILs. This was confirmed by another study which found lower numbers of T cells expressing the Th1 transcription factor T-box transcription factor TBX21 (T-bet) in CRC tumours with *KRAS* mutations compared to MSI-high and *BRAF* mutant tumours. The investigators also examined patient prognosis and noted that T-bet – which can be expressed by $CD4^+$ and $CD8^+$ T cells – is a better biomarker for prognosis than CD8 (198). Research performed in NSCLC was initially driven by interest in heterogeneity in clinical responses to PD-1/PD-L1 blockade, as it was thought that the differential responses in patients harbouring different oncogenic mutations was fundamentally down to differences in tumour immunology. A study by Skoulidis *et al* (49) showed that LUAD patients with co-occurring *KRAS/STK11* mutations expressed lower levels of PD-1 and CTLA-4 at the transcriptional level, and lower levels of PD-L1 at the transcript and protein levels. This suggested that NSCLC mutations were associated with immune marker expression and that *KRAS/STK11* patients would be less sensitive to PD-1/PD-L1 and CTLA-4 checkpoint blockade. Unlike patients with *KRAS/STK11* mutations, those with concomitant *KRAS/TP53* mutations express immune checkpoints and should benefit from checkpoint blockade (49). Another study showed that *KRAS* driven mouse models are dependent on $FoxP3^+$ Tregs and that depletion reduced tumour burden (183).

Upregulation of PD-L1 expression has also been shown to be driven by STAT3 signalling activated in *ALK* fusion driven lymphoma (201). Whereas oncogenically activated STAT3 signalling in *MET* and *EGFR* driven cancers leads to the expression of cytokines including type I interferons, IL-6, IL-23, IL-10 as well as VEGF (202-205). Using mouse models of *EGFR* driven NSCLC, Akbay *et al* (143) showed a decrease in intratumoural $CD8^+$ T cells with an increase in $FoxP3^+$/CTLA-4^+ Tregs compared to peripheral normal lung. *EGFR* mutant tumours expressed TGFβ, IL-6 and PD-L1, whilst T cells expressed PD-1 and low levels of TIM-3 and LAG-3 which the authors argue are not the dominant markers of suppression in this model. Introducing mutated *EGFR* into human NSCLC cell lines led to an upregulation of PD-L1 expression and treating mice with a combination of anti-PD-1 and anti-CTLA-4 antibodies suggested that patients with *EGFR* mutation may benefit from this checkpoint inhibitor combination, which has subsequently shown promise in the clinic (143, 206, 207). Studies like these show that rationale stratification of patients for therapy based on the molecular properties of their tumours can impact clinical responses. Therefore, investigating immune contextures associated with other NSCLC cancer gene alterations is of great value.

1.4 RORγT Regulated Immune Cells in Non-Small-Cell Lung Cancer

One of the essences of what defines a cell is its transcriptional programme, which is regulated by a heterogenous group of proteins that control gene expression called transcription factors. All transcription factors have a DNA-binding domain which binds to a specific sequence within a promoter or enhancer region, leading to the expression of the target gene. Heterogeneity in transcription largely relates to different mechanisms of action of different transcription factors including involvement with forming preinitiation complexes for RNA polymerase by recruiting a host of other proteins (208, 209). Immune cells express different transcription factors to promote different transcriptional programmes throughout the stages of their lives, from early development to a differentiated mature cell executing its key duties (210). A common reductionist view is that T cells become completely lineage-committed and are driven by 'master transcription factors' that elicit their functions through specific transcriptional programmes (157, 211). However, whilst some transcription factors are preferentially associated with certain subsets, it is now clear that multiple transcription factors can be co-expressed dependent on environmental cues, and many $CD4^+$ T cell subsets are not terminally polarised and can exhibit phenotypic plasticity (Figure 1.4). Naïve T cells are typically polarised during priming by a combination of the strength of TCR signalling, the cytokine milieu and metabolic environment. These conditions activate transcription factors that then go on to induce and regulate transcriptional programmes. For instance in $CD4^+$ T cells, Th1 polarisation requires IL-12 and strong TCR signalling which induces T-bet activity, whereas Th2 polarisation needs IL-4 and a weaker TCR signal to prompt GATA3 (157, 211).

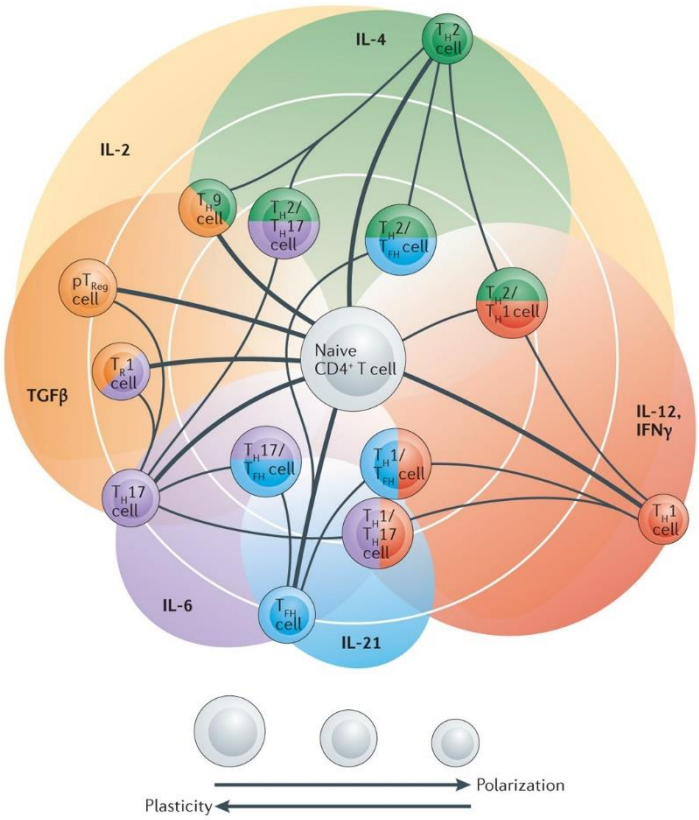

Figure 1.4 CD4⁺ T cell phenotypic plasticity

Diagram illustrating polarisation to important CD4⁺ T cell subsets and plasticity between these subsets. Figure from DuPage and Bluestone (157).

RORγT is a key transcription factor associated with type 17 inflammatory immunity, which is characterised by neutrophil recruitment and is often dysregulated in autoimmune diseases including rheumatoid arthritis, psoriasis and multiple sclerosis (212). In CD4⁺ T cell biology RORγT is best known as the canonical transcription factor for Th17 cells which secrete cytokines including the IL-17 family. Evidence from murine studies suggest that RORγT drives secretion of IL-22 in Th17s and the rarer Th22 CD4⁺ subset, albeit that RORγT is expressed at lower levels in Th22s compared to Th17s and at higher levels compared to naïve CD4⁺ T cells (213-215). It has been proposed that Th17 cells are in balance with FoxP3⁺ Tregs to regulate inflammation as these CD4⁺ T cells can transdifferentiate between each phenotype. This plasticity allows expression of RORγT and FoxP3

simultaneously during intermediary stages, and there is evidence in the colon of Tregs stably expressing RORγT alongside FoxP3 in two subsets: RORγT$^+$ Tregs, and Tr17s which also secrete IL-17 (216-224). Tregs that express RORγT have also been detected in other tissues including the lung, but it is not known whether RORγT is stably expressed with FoxP3 in these scenarios, or whether it is simply a marker of transdifferentiation, or whether this RORγT$^+$/FoxP3$^+$ phenotype is truly functional (225-227). RORγT is not only expressed in CD4$^+$ but also in CD8$^+$ T cells, called Tc17 which have effector anti-tumour properties (228). Type 17 immunity also extends to innate lymphocytes including γδ17s, which may also be cytotoxic in cancer (168, 169). Other unconventional T cells that do not recognise peptide antigens including invariant NKT17s (iNKT17s) and mucosal associated invariant T cells (MAITs) also express RORγT, both of which have been suggested to specifically lyse cancer cells (229-232). ILC3 and LTi cells also both depend on RORγT expression (172-174). From the myeloid lineages, subsets of human and mouse neutrophils express RORγT, but RORγT does not appear to be expressed in monocytes and macrophages (233-235).

Many investigations into RORγT function and patterns of immune expression have been carried out using mouse models, yet there is also a growing body of evidence of RORγT activity in the human immune system. To understand the roles of RORγT$^+$ lymphocytes in NSCLC it is important to study its underlying effects as a transcription factor and how RORγT is regulated within a cell.

1.4.1 RORγT Molecular Mechanisms and Immune Expression

RORγT is a member of the retinoic acid-related orphan receptor subfamily. Like the main family of nuclear retinoic acid (RA) receptors, RORγT has been proposed to bind the vitamin A metabolite all-*trans* RA as well as other endogenous metabolite ligands (236-239). The RORγT gene *RORC* encodes two isoforms, RORγ and RORγT, of which the shorter RORγT is missing the first 21 N-terminus amino acids and begins with three different amino acids. Variant expression is mainly controlled by two different *RORC* promoters (*RORC1* for RORγ and *RORC2* for RORγT), and cells are unable to express both RORγ and RORγT simultaneously (236, 240). RORγ is known as a regulator of circadian rhythms and can temporally induce clock gene expression. Conversely, RORγT is expressed in various immune cells as mentioned including Th17s, and can also promote the survival of double positive thymocytes during the thymic selection (241, 242). RORγT expression is regulated by cellular signals and other transcription factors including runt-related transcription factor 1 (Runx1) (241, 243, 244).

As highlighted previously, RORγT has important roles in Th17 biology. Th17s are $CD3^+/CD4^+$ T cells which often express C-C chemokine receptor type (CCR)4, CCR6, CD161, IL-6R, IL-23R and can secrete IL-22, CCL20, granulocyte-macrophage colony-stimulating factor (GM-CSF), TNFα and IL-17 family cytokines (245-248). This type 17 response is the most important function of Th17 cells. IL-17A is the best described IL-17 family cytokine alongside IL-17F, and other family members are IL-17B, IL-17C, IL-17D and IL-17E. These cytokines signal via the unique heteromeric transmembrane receptor IL-17R expressed on target cells, which normally consists of IL-17RA in complex with one of the other IL-17R subunits: IL-17RB, IL-17RC, IL-17RD or IL-17RE (243). One of the primary functions of IL-

17A signalling is to recruit neutrophils and it does this by inducing C-X-C motif chemokine ligand (CXCL)8 production from a wide range of cells including endothelial cells, fibroblasts, epithelial cells and macrophages (245). The Th17 transcriptional programme was first thought of being controlled solely by RORγT, but recent studies have shown that other transcription factors are also important in dictating and enhancing this phenotype.

Co-operation Between RORγT and Other Th17 Transcription Factors

One such complementary Th17 transcription factor is STAT3, which is also a key transcriptional regulator of MDSCs (244, 249). In Th17s, STAT3 has been shown to bind the IL-17A promotor in the presence of Th17 polarising cytokines IL-6 and IL-23. Overexpression of STAT3 results in high levels of IL-17A production, whilst a lack of STAT3 prevents IL-17A, IL-17F and RORγT expression (250). Experiments examining the human and mouse *RORC2* promoters showed that STAT3 can bind to these regions and induce RORγT expression (251). STAT3 induced RORγT expression represses T-bet transcriptional programmes and also controls the accessibility of the IL-22 promoter, working with RORγT and another transcription factor called aryl hydrocarbon receptor (AHR) to induce IL-22 expression (215, 252). As a receptor, AHR senses cytoplasmic environmental ligands such as PAHs from cigarette smoke. Upon agonist binding, AHR associates with AHR nuclear translocator to move into the nucleus and create the functional AHR transcription factor. AHR is particularly important in IL-22 production and Th17s from *AHR*$^{-/-}$ mice can produce IL-17A but not IL-22 (253). AHR agonist treatment caused mice to develop laboratory

inducible experimental autoimmune encephalomyelitis (EAE) – a Th17 driven disease used as a model for multiple sclerosis – at an earlier timepoint with increased severity (253).

Another closely related transcription factor to RORγT is RORα, which has also been associated with Th17s, particularly in mice. Like RORγ, there is some evidence for RORα and RORγT involvement in circadian rhythms, with the suggestion that a dysregulated circadian clock impacts RORγT and RORα expression, and Th17 function (241, 246). Like in tumours cells, IL-6-mediated STAT3 phosphorylation can promote transcription of HIF1α from mTORC1, which is itself another transcription factor in Th17s associated with maintenance and effector functions (98, 254, 255). Jurkat cells overexpressing HIF1α and RORγT expressed high levels of IL-17A which was increased under hypoxia. *IL17A* transcription in murine Th17s is synergistically regulated by HIF1α and RORγT, and *HIF1A*$^{-/-}$ mice are unable to mount Th17 responses and are resistant to EAE (251). These findings also provide an interesting microenvironmental link to Th17 responses, as HIF1α is a sensor of hypoxia and ROS which pushes cells towards glycolytic metabolism (43, 99, 251).

Th17 Phenotypic Plasticity

Th17 cells exhibit stem-like properties, which allows for longer self-renewal than other lineage-committed CD4^{+} T cell subsets and plasticity in polarisation. This plasticity is demonstrated by the transdifferentiation between Th17/Treg subsets (Figure 1.5), as well as by the acquisition of cytotoxic Th1 properties in cells that were previously IFNγ^{-}/IL-17A^{+} Th17s (244). These T-bet^{+} Th1-like Th17s are driven by IL-12 and have anti-tumour properties expressing IFNγ and NKG2D (228, 245, 256, 257). Other RORγT^{+} immune

subsets such as ILC3s may also display plasticity, but currently there is less known about these cells (241). Like other $CD4^+$ T cells, Th17s differentiate from naïve $CD4^+$ T cells. Temporal gene expression modelling showed that murine Th17 differentiation occurs in three phases. The first short stage is in response to polarising cytokines including IL-6 and TGFβ which stimulates expression of RORγT, AHR and other transcription factors. This leads to the second stage in which there is an onset of the Th17 transcriptional phenotype in which cytokines can be secreted, and the final stage which is a phenotypic stabilisation and maintenance that is reliant on IL-23R signalling, potentially in an autocrine manner (243, 258, 259). Human Th17 polarisation is less reliant on TGFβ – yet human Th17s may differentiate in the presence of low concentrations of TGFβ – and require IL-6 and IL-1β. Induction of IL-23R is STAT3 dependent and though this is predominantly driven by IL-6 signalling, substituting IL-6 for IL-21 can stimulate STAT3 to the same effect (244, 248, 260-262). Treating human $CD4^+$ T cells with TGFβ and IL-6 caused increased RORγT expression but not accompanying IL-17A production. This study showed that TCR stimulation was also important for IL-17A and IL-22 expression in Th17s (236).

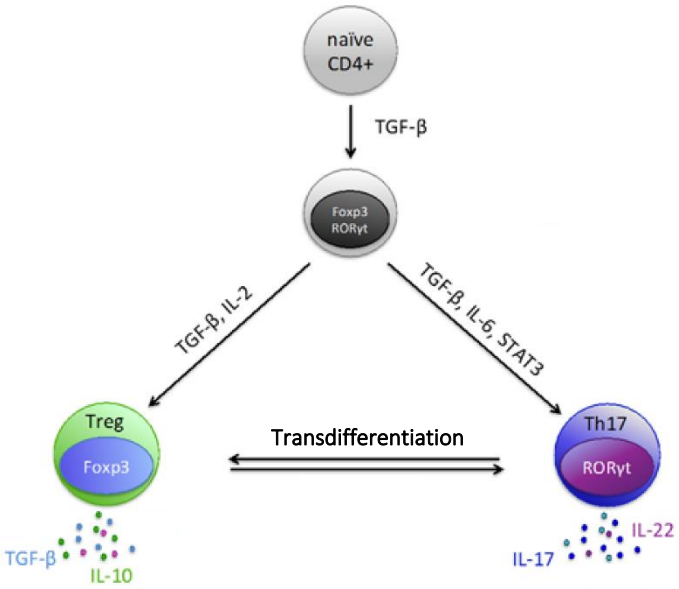

Figure 1.5 The Th17/Treg balance

Dependent on polarising conditions, naïve $CD4^+$ T cells can polarise towards Th17 or Treg phenotypes, and transdifferentiation which is also dependent on environmental conditions may occur. Figure adapted from Fasching *et al* (263).

$CD3^+/CD4^+$ Treg cells can transdifferentiate to and from Th17s, in a process in which the RORγT and FoxP3 transcription factors play important reciprocal regulatory roles. Tregs that are part of this Th17/Treg axis often express the CCR4 and CCR6 chemokine receptors like Th17 cells, and are also $CD25^+$, $TGF\beta R^+$, $CTLA\text{-}4^+$ and secrete IL-10 (245-247, 264). As suppressive Tregs express $FoxP3^+$ and heavily use environmental IL-2, they do not express the high-affinity IL-7 receptor called CD127 (265, 266). There are several different Treg subsets and because many investigations into this axis are *in vitro* studies using murine cells, Tregs in this axis are described as *in vitro*-induced Tregs (iTregs). Similar phenotype Tregs are also found *in vivo* and these iTregs arise outside of the thymus, unlike natural Tregs which differentiate from naïve T cells during thymic development (260, 267, 268). Imbalances in the Th17/iTreg axis have been associated with a variety of pathologies including in the field of oncology and in NSCLC (245, 246, 269).

Reciprocal Regulation of RORγT/FoxP3 and The Th17/iTreg Balance

Zhou *et al* (260) performed one of the first major studies on the balance between Th17s and iTregs in mice and humans, highlighting the importance of TGFβ. They found that low concentrations of TGFβ acts with IL-6 to promote IL-23R expression through RORγT, whilst higher concentrations repress IL-23R favouring iTregs. FoxP3 knockdown showed that FoxP3 is responsive to TGFβ, and co-immunoprecipitation found that FoxP3 directly interacts with and inhibits RORγT and RORα. Using mutated forms of FoxP3, the authors found that these interactions were dependent on the FoxP3 forkhead DNA binding domain and on the second exon. Despite this inhibition, RORγT can be co-expressed in T cells with FoxP3 but reduced IL-17 is produced (260). Another study in mice exploring FoxP3 interactions by Yang *et al* (270) disagreed with the Zhou *et al* (260) finding that FoxP3 did not transcriptionally regulate RORγT or RORα by DNA binding, but instead stopped RORγT and RORα complexing with necessary co-activators for their transcriptional programmes. This work also provided evidence of transient dual $RORγT^{+}/FoxP3^{+}$ expression in activated T cells, which were able to express *IL17F* transcript but not secrete protein (270). Another transcription factor shown to regulate the murine Th17/iTreg balance is Runx1 which co-operates with RORγT under Th17 polarising conditions to stimulate IL-17A expression by binding to the *IL17A* promoter and enhancers. Mutated forms of FoxP3 showed that FoxP3 can bind to Runx1 using its forkhead binding domain and Runx1-binding domain, inhibiting synergistic IL-17A secretion with RORγT (261). HIF1α also helps T cells shift to a Th17 phenotype by complexing with FoxP3 and recruiting a ubiquitin ligase to induce FoxP3 proteasomal degradation (251).

The metabolic environment can also affect the Th17/iTreg balance. Treating T cells with the putative RORγT ligand all-*trans* RA inhibited IL-17A secretion *in vitro*. Similarly, *in vivo* work showed that DCs in mouse colons can produce RA which reduces RORγT^{+} Th17s and increases FoxP3^{+}/CTLA-4^{+} iTregs (237). A comparable murine study showed that this metabolite is biphasic as physiological concentrations of all-*trans* RA promotes T cell IL-17A secretion; yet work in humans suggests that all-*trans* RA polarises to an iTreg phenotype (238, 239). Different T cell subsets and levels of activation have substantially different metabolic programmes, for example activated T cells have high energic demand – which has some parallels to tumoural glycolytic rewiring – and rely on fast glycolysis from mTOR signalling for ATP production even in normoxia, whereas quiescent T cells use OXPHOS and the TCA cycle to gradually produce ATP (271). Th17 polarising conditions induces higher levels of glycolysis which is dependent on HIF1α activity compared to iTreg polarising conditions. Like the findings from Dang *et al* (251), *HIF1A*$^{-/-}$ mice also show delayed onset EAE in the hands of Shi and colleagues (255). These knockout mice were unable to produce functional Th17s under polarising conditions and FoxP3^{+} iTregs were upregulated in this model. Furthermore, treating CD4^{+} T cells both *in vitro* and *in vivo* with rapamycin or a glucose analogue to inhibit glycolysis favoured the generation of iTregs (255). This finding of glycolysis altering the Th17/iTreg balance has been supported by other groups and there is evidence of other metabolic differences. Th17s take up and use high levels of branched-chain amino acids, and removing these from the microenvironment induces iTregs, which are themselves more reliant on oxidative metabolism of lipids than Th17s (271-273).

As the Th17/iTreg balance is non-binary – as demonstrated by the existence of RORγT$^+$/FoxP3$^+$ intermediary T cells – studies have tried to elucidate the key regulator of this transdifferentiation. Although evidence in humans remains limited and transdifferentiation is probably regulated by multiple factors, TGFβ is an important candidate for potentiating transdifferentiation in mice (236, 244, 246, 248, 260, 261, 270). Plasticity from Th17 to iTreg is most studied, yet human iTregs can transdifferentiate into RORγT$^+$ Th17s by negative epigenetic regulation of the FoxP3 locus and Th17s were best polarised using IL-1β (264). In cancer, different types of disease can skew the Th17/iTreg balance by generating an environment rich in certain polarising cytokines. Alternatively, imbalances may be because of differences in the TME metabolome affecting *in situ* polarisation and transdifferentiation (237-239, 246, 251, 255, 271-273).

1.4.2 T Helper 17 Cells in Non-Small-Cell Lung Cancer

Th17s are one of the most important CD4$^+$ T cell subsets in regulating mucosal immunity, therefore it is unsurprising that these cells can be found in the respiratory system as the lung is a large mucosal interface between the extracorporeal and intracorporeal environments. Lung Th17s are important clinically as patients with inherited *IL17RA* deficiency or inactivating *STAT3* mutations develop chronic mucocutaneous candidiasis and are susceptible to bacterial infections (212). Immunising the lungs of immunocompetent mice with heat killed *Klebsiella pneumoniae* polarised lung infiltrating CD4$^+$ T cells to tissue resident memory Th1-like Th17s, which upon rechallenge rapidly secreted IL-17A and IFNγ (274). Away from infection, Th17s are also important in

inflammatory lung disease like COPD, and a mouse model of non-typeable *Haemophilus influenzae* induced COPD-like inflammation preferentially expanded IL-17A$^+$/IL-22$^+$ Th17s and promoted high tumour burden LUAD (275).

Evidence as to whether Th17s are pro or anti-tumour and their association with prognosis appears to be cancer type, timing, and context dependent (176, 228, 244, 276, 277). This is also the case for the Th17/iTreg balance, with lung SqCC having twice as many intratumoural Tregs as Th17s and Th1s (158). The Th17/iTreg axis is more nuanced in LUAD, with evidence of imbalance in both cellular directions and a lack of detailed understanding into this heterogeneity (158, 246, 278, 279). One such explanation is that early-stage disease with lower microenvironmental TGFβ may favour an angiogenic environment driven by Th17s, whilst late-stage disease with higher TGFβ tumour cell production may prefer differentiation to iTregs to help the tumour suppress immune responses to neoantigens from higher levels of genomic instability (246). A lot of the research into Th17s in human NSCLC examines peripheral blood mononuclear cells (PBMCs) and not intratumour Th17s due to difficulties accessing tissue, though Th17s have been observed in LUAD tumours (278, 280). A study by Duan *et al* (269) found increased numbers of Th17s and Tregs – as determined by *RORC2* and *FOXP3* quantitative PCR (qPCR) and IL-17A flow cytometry staining – in PBMCs from LUAD and SqCC patients compared to healthy donor controls. They noticed that if patients had Th17s in the blood, there was an absence of Tregs and vice versa, thus supporting Th17/iTreg skewing (269). These findings contrast with comparable earlier work using PBMCs that found a preference for iTreg skewing, although both these studies observed increased levels of the Treg cytokines IL-10 and TGFβ in patient sera (269, 281). These investigations do not

elucidate whether polarisation occurs within the tumour or in the blood. Interestingly, work using healthy donor PBMCs by Hoechst *et al* (239) found that autologous co-culturing of $CD4^+$ T cells with $CD14^+$/HLA-$DR^{low/-}$ MDSCs induced iTreg differentiation by T cell interaction with membrane-bound TGFβ, whereas T cells co-culture with $CD14^+$/HLA-DR^+ monocytes induced Th17 differentiation. This suggests that this MDSC-mediated differentiation could happen entirely in the blood. Moreover, the authors polarised Th17 cells then co-cultured with MDSCs, finding a fast 12-hour transdifferentiation to iTregs and observed $FoxP3^+$/IL-$17A^+$ Tr17s in this model (239).

As most NSCLCs are associated with smoking, it is possible that Th17 differentiation is directly influenced by compounds from smoke. Exposing mice to cigarette smoke extract (CSE) increases RORγT expression and can polarise towards a Th17 phenotype, which may be due to PAHs stimulating AHR-mediated Th17 transcription (282, 283). However, exposing CSE to monocyte-derived DCs from PBMCs of COPD patients did not induce Th17 priming (284). Yet, CSE treating lung epithelial cells does show an association with Th17 biology. Exposing human bronchiole epithelial cells to CSE increased *IL17RA* and *IL17RC* expression, and subsequent IL-17A stimulation induced production of the important granulocyte and MDSC chemoattractant CXCL8 (285). IL-17A and CSE treatment induced proliferation in *ex vivo* cultured COPD bronchiole epithelium, and induced an EMT-like phenotype in murine bronchiole epithelial cells characterised by a loss of E-cadherin expression and increased vimentin expression (286-288).

Whilst Th17s in NSCLC are often associated with recruitment of suppressive myeloid cells and the induction of EMT, Th1-like Th17s have protective roles in NSCLC. Early work

focused on utilising these cells for adoptive transfer therapy as they are resistant to cellular senescence after *ex vivo* expansion (228, 289). Muranski *et al* (228) generated mouse $CD4^+$ T cells specific for a melanoma antigen which were polarised under Th17 conditions. After polarisation, these cells became effector memory Th1-like Th17s expressing IL-17A, CCL20, TNFα and IFNγ. These Th1-like Th17s could not protect their host animals from melanoma but protected other mice of a similar background following allogeneic transfer in an IFNγ-dependent manner. Unlike Th1 transfer, mice transferred with Th1-like Th17s did not relapse, which was suggested to be due to improved intratumoural persistence (228). Similar work by Martin-Orozco *et al* (257) transferring ovalbumin-specific Th17s into mouse melanomas did not result in polarisation to $IFN\gamma^+$ Th1-like Th17s. Instead, Th17s secreted IL-17A to stimulate tumour cell CCL20 release, which recruited $CCR6^+$ DCs to sample antigens and initiate a $CD8^+$ anti-tumour response. These authors propose that the Th1-like Th17 plasticity observed in the previous work occurs in lymphopenia but not in immunocompetent hosts (257). A study investigating human NSCLC patients showed that Th17s from PBMCs were $CCR7^+$ central memory cells sensitive for a cancer testis antigen, that also expressed RORγT, CCR4 and CCR6. Interestingly, one NSCLC patient had Th1-like Th17s that secreted IL-17A and IFNγ (290).

The Role of IL-17A in NSCLC

The presence of Th17s and other IL-$17A^+$ lymphocytes in NSCLC tumours is associated with bad prognosis (291-293). Furthermore, PBMCs from LUAD patients also have high frequencies of γδ17s as well as Th17s and corresponding lower Tc17s compared to healthy

donors. γδ17 and Th17 presence and Tc17 reduction was associated with advanced lung cancer stage (294). Interestingly, Th17s in NSCLC patient malignant pleural effusions were associated with good prognosis and improved survival (295). An explanation for this could be that these Th17s are not retained in the tumour and therefore cannot exert pro-tumour functions.

As NSCLCs are carcinomas, the effect of IL-17A on epithelial function is of great interest. IL-17A has been shown to activate STAT3 signalling in tumour cells and TME stroma cells. STAT3 activation can be amplified in an autocrine IL-6 signalling feedback loop, and in tumour cells can directly promote growth, aid HIF1α metabolic glycolytic reprogramming through mTOR signalling and induce angiogenic VEGF secretion (98, 254, 255, 280, 296, 297). This indicates that STAT3 is an important oncogenic facilitator of IL-17A signalling from Th17s. Moreover, IL-17A and IL-22 signalling may co-operatively allow Th17s to hyperactivate STAT3, which is associated with tumour migration, proliferation, and bad NSCLC prognosis (241, 298-302). Stimulating PBMCs with NSCLC cell line supernatant induced IL-22 production from memory Th17s and potentially Th22s. The activating cytokine in the supernatants was shown to be IL-1β which induced AHR and RORγT to make IL-22 (213). Like its angiogenic potential, IL-17 has also been linked with lymphangiogenesis in NSCLC to potentially aid metastasis (293, 303). Furthermore, treating NSCLC cell lines with IL-17A also increased expression of MMP2 and 9, which remodel the extracellular matrix to allow for metastases (304).

IL-17 also acts on myeloid cells and can directly polarise macrophages towards an M2 phenotype (305). Interestingly tumour bearing *IL17A*$^{-/-}$ mice had less MDSCs compared to

tumour bearing *IL17A*$^{+/+}$ control mice, and MDSCs from knockout mice were unable to suppress T cell proliferation *in vitro*, suggesting a developmental role for IL-17A (276). One of the key chemokines secreted by Th17s is CCL20 which potently attracts other lymphocytes including other Th17s and Tregs, that subsequently recruit TANs, TAMs and MDSCs. These suppressive myeloid cells can also be recruited by Th17s using granulocyte colony-stimulating factor (G-CSF) and GM-CSF in several cancers including NSCLC (142, 189, 244, 306, 307). Finally, there is evidence that Th17s can be directly suppressive, expressing CD39 and CD73 to convert ATP/ADP to immunosuppressive adenosine (308, 309).

In summary, Th17s have a tumour promoting role in NSCLC and the Th17/iTreg balance is dependent on cues from the microenvironment which might be a result of cancer genetics driving the TME. Though Th1-like Th17s appear to have anti-tumour properties, most Th17s support tumour progression by secreting IL-17 and IL-22 which importantly act via STAT3 to induce angiogenesis, EMT, regulate proliferation. As well as by secreting chemokines to promote an immunosuppressive myeloid-driven immune contexture.

1.5 Scope of Thesis

Patients with LUADs driven by KRAS and STK11 mutations are therapeutically underrepresented, insensitive to immunotherapy and have a poor prognostic outlook. Underlying cancer genetics controls the TME, immunological engagement and skews the immune contexture to favour certain immune subsets including Th17s or Tregs. Knowledge of the types of immune responses linked to key mutated driver cancer genes in LUAD is important for patient stratification to rationally choose an effective therapeutic or immunotherapeutic strategy.

Using data from TCGA, resections from NSCLC patients and an *in vitro* approach culturing healthy donor PBMCs in conditioned media from NSCLC cell lines with different cancer mutations, we sought to:

1. Characterise immune gene transcriptional signatures that are linked with LUAD cancer gene driver mutations.

2. Investigate the relationship between *RORC* mRNA expression and RORγT protein expression in LUADs driven by KRAS and STK11 mutations.

3. Determine which lymphocytes express RORγT, and explore spatial relationships between RORγT^{+} intratumour lymphocytes and other immune subsets in LUAD patients with KRAS and STK11 mutations.

4. Evaluate the influence of cytokines and chemokines secreted by NSCLC cell lines with KRAS and STK11 mutations on T cell phenotype.

2. Materials and Methods

2.1 Bioinformatics Methods

2.1.1 Data Acquisition and Pre-Processing

Mutation, copy number, expression and clinical data from TCGA 'LUAD TCGA 2014' (*n* = 230) and 'LUAD TCGA PanCancer' (*n* = 566) datasets were retrieved via the cBioportal tool (65, 310, 311). These data are known as 'Level 3' data which have been processed from raw data using TCGA pipeline to give data that are easily comparable by researchers without extensive bioinformatics training, such as: mutations from each mutated cancer gene (e.g. *KRAS* G12D), copy number changes as processed by the GISTIC algorithm (Chapter 2.1.5) and normalised gene-level expression data (RNA-Seq data processed and corrected for zygosity by the RSEM algorithm as RSEM gene-level abundance values, or gene-level z-scores standardised using RSEM gene-level data from all profiled tumours) (312, 313).

An R script (V3.5.2 (314, 315)) was written to tidy these data (github.com/Sithspitz/thesis/blob/master/data_processing/luadread_tcga_pancancer.R) and data were tabulated using Excel (Microsoft). Adaptations of the same method were used to acquire validation data from the diffuse large B-cell lymphoma TCGA dataset 'DLBCL TCGA PanCancer' (310).

To assess the key findings from the lung cancer TCGA cases, open access iterative rank-order normalised (IRON) microarray expression data (*n* = 422) from a publication by Schabath *et al.* (316) were downloaded from the Gene Expression Omnibus (GEO)

repository (Accession Number GSE72094) (317, 318) and tabulated by cancer gene mutation status.

2.1.2 Data Mining the Cancer Genetics of Lung Adenocarcinoma

The interactive online cBioPortal platform was used to explore general genetic features in the LUAD TCGA data. To investigate more complex genetic features such as the most common types of somatic mutations and most prevalent amino acid changes, an R script was produced (github.com/Sithspitz/thesis/blob/master/mutation_analysis/luad_pancancer_mut_analysis.R).

2.1.3 Cancer Gene Delineated Immune Gene Expression Signatures in Lung Adenocarcinoma

We reviewed the literature and used a minimum prevalence threshold of 10% in the TCGA 2014 dataset to select 11 common driver cancer genes in LUAD (65, 319, 320). As *ALK* and *ROS1* are the key cancer fusion genes in LUAD, they were also included in this analysis even though their prevalence was under 10%. 105 genes associated with immune subsets, function and recruitment were selected, including those suggested by the NSCLC literature, to create specific immunological gene expression signatures delineated by key LUAD cancer genes (132, 140, 142, 189). To produce these immune gene expression signatures from TCGA 2014 data, median mRNA expression z-scores (from RNA-Seq data) for each gene were calculated from the patient groups with mutations in the same lung

cancer gene (determined by whole-exome sequencing) and also from patients without mutations in that particular lung cancer gene. These median expression z-scores were then statistically compared using unpaired two-sample Wilcoxon tests and differences were deemed significant if *p* values were less than the Bonferroni corrected *p* value of 0.045 to stringently minimalise false discoveries. The fold change differences in the median immune gene mRNA expression (cancer gene mutation positive vs cancer gene mutation negative) were plotted as a heatmap and called an immune gene expression signature. Additional targeted exon sequencing and microarray expression data from Schabath *et al.* (316) were used as a validation dataset and cancer gene immune signatures were produced in the same way.

2.1.4 Immunological Deconvolution of TCGA Lung Adenocarcinoma

Two computational methods, CIBERSORT and MCP-counter, were used to estimate immune cell fractions from TCGA RNA-Seq RSEM normalised gene-level abundance data by algorithmic deconvolution (321, 322).

RNA-Seq data were uploaded to the CIBERSORT web tool (cibersort.stanford.edu/) and the reference leukocyte signature matrix (LM22) was applied to deconvolute the data using the CIBERSORT algorithm at 1000 permutations. The MCP-counter algorithm was run by the accompanying R package (V1.2.0), using 'HUGO_symbols' as features. The enumerated relative cell fractions from fully CIBERSORT deconvoluted TCGA patients and abundance scores from MCP-counter were compared using unpaired two-sample Wilcoxon tests.

2.1.5 Examining Copy Number Alterations

We used scores from the GISTIC 2.0 algorithm downloaded from cBioPortal to estimate genetic deletions and amplifications (312). GISTIC scores ranged from -2 to +2 at integer intervals. -2 represents a deep deletion (likely homozygous deletion), -1 represents a shallow loss (likely heterozygous deletion), 0 signifies diploid with no CNA, +1 shows a low-level gain and +2 represents a focal high-level amplification. GISTIC scores for each gene are putative, especially the +1 low-level gain which suggests that there are additional copies but that it is not necessarily an amplification of that particular gene, rather potential amplification of the locus as a whole. Samples were grouped by GISTIC scores for comparison.

2.1.6 Investigating Protein Dynamics of TCGA Lung Adenocarcinoma

To give an indication as to whether TCGA samples have gained or lost KRAS and LKB1 proteins we investigated reverse phase protein array (RPPA) z-scores from cBioPortal. We used RPPA z-scores of ± 1 (equivalent to ± 1σ) as the threshold to delineate the protein gain or loss groups.

2.1.7 *RORC* Correlation Analysis

An R script was written to correlate *RORC* expression RSEM values against RSEM values from all other genes, including those in the 1q21.3 locus (github.com/Sithspitz/thesis/tree/master/correlation_analysis/). This script uses data

from putative 1q21.3 amplified samples with *RORC* GISTIC scores of +1 or +2 and iterates the Pearson product-moment correlation test. Significant correlations were plotted.

2.1.8 Isogenic Cell Line Analysis

To investigate whether introducing genetic mutations (MTs) directly induces expression of genes, we explored the GEO repository. We came across data from Stolze *et al* (72) (Accession Number GSE60695) who established isogenic MCF10A cell lines with a range of *KRAS* mutations expressed at physiological levels and performed a microarray on these cell lines. Data was available for *KRAS* G12D and G13D isogenic cell lines, which we analysed. Unfortunately, we could not find any similar appropriate data from lung cancer isogenic cell lines with *STK11* or *KRAS/STK11* mutations. Microarray data from this study were in the form of spot intensities normalised by robust multi-array average (RMA) procedure (323). Normalised spot values were statistically compared by paired and unpaired *t*-tests.

2.1.9 *RORC* Overall Survival Analysis

Any NSCLC TCGA samples without clinical data were removed and *RORC* expression z-scores were grouped into quartiles. Samples with *RORC* z-scores between the upper quartile and maximum value were categorised into the '*RORC* High' group, samples with values between the lower quartile and minimum value were placed into the '*RORC* Low' group and the remaining samples with z-scores around the median were grouped into '*RORC* Other'. Kaplan-Meier curves were produced in GraphPad Prism (8.4.3) using

months from diagnosis to clinical outcome data and were statistically compared using Mantel-Cox tests.

2.1.10 Single Sample Gene Set Enrichment Analysis

Gene set enrichment analysis (GSEA) was performed using the single sample GSEA (ssGSEA) approach (324). The ssGSEA method calculates gene set enrichment scores on a per sample basis, from the rankings of gene set expression relative to the other genes outside of this gene set. This algorithm was run on RSEM data using the *GSVA* package and the enrichment scores were grouped then analysed using two-sample Wilcoxon tests (325). This approach was validated using a published lung cancer gene signature, comparing the TCGA DLBCL and LUAD datasets (Figure 2.1) (326).

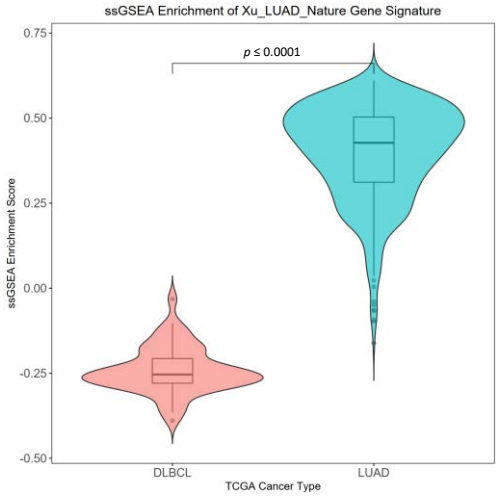

Figure 2.1 ssGSEA validation using a lung cancer gene signature

The list of genes included in the Xu *et al* (326) lung cancer gene signature was obtained. This gene list was used by the *GSVA* package to run ssGSEA and calculate ssGSEA enrichment scores from RNA-Seq RSEM data from the 'LUAD TCGA PanCancer' and 'DLBCL TCGA PanCancer' datasets. ssGSEA enrichment scores were grouped by original dataset and were compared by unpaired two-sample Wilcoxon test.

2.1.11 R Packages

Table 2.1 lists the R packages used throughout this thesis. The top of this Table shows the most commonly utilised packages and the bottom shows less used packages and some dependencies.

Package Name	Reference	Package Name	Reference
cytofkit2	(327)	*devtools*	(314)
dplyr	(328)	*ggbiplot*	(329)
ggplot2	(328)	*ggpubr*	(330)
gplots	(331)	*gsva*	(325)
MCPcounter	(322)	*MEM*	*(332)*
phenoptr	(333)	*phenoptrReports*	*(333)*
RColorBrewer	(334)	*shiny*	*(335)*
stats	(314)	*tidyverse*	*(328)*
Biobase	(336)	*car*	(337)
cowplot	(338)	*data.table*	*(339)*
e1071	(340)	*factoextra*	(341)
flowCore	(342)	*FlowSOM*	*(343)*
forcats	(328)	*genefilter*	*(344)*
graphics	(314)	*gridExtra*	*(345)*
GSEABase	(346)	*GSVAdata*	*(325)*
limma	(347)	*magrittr*	*(348)*
openxlsx	(349)	*plyr*	*(350)*
purrr	(328)	*randomForest*	*(351)*
readr	(328)	*readxl*	*(328)*
reshape2	(352)	*ROCR*	*(353)*
rtree	(354)	*Rtsne*	*(355)*
scales	(356)	*stringr*	*(328)*
tibble	(328)	*tiff*	*(357)*
utils	(314)	*uwot*	*(358)*

Table 2.1 List of R packages

R packages and dependences used throughout this thesis.

2.2 Specimen Collection and Ethics

2.2.1 Specimens for Immunohistochemical Staining

We were interested in sourcing NSCLC lung resections with and without somatic mutations in the *KRAS* and *STK11* genes. Routine molecular profiling is not performed on NSCLC biopsies or resections, therefore we collaborated with two ethically approved national NSCLC studies that have collected lung tumour resections and used next-generation sequencing to classify the cellular NSCLC mutations present. The 'Tracking Lung Cancer Evolution Through Therapy' (TRACERx) study collected tumour tissue and performed whole-exome sequencing to classify NSCLC mutations in the tumour; similarly the 'Stratified Medicine Programme 2' (SMP2) study collected tumour resections and sequenced a targeted NSCLC gene panel including *KRAS* and *STK11* (359, 360). Patient resections with mutations in genes of interest were identified and formalin-fixed paraffin-embedded slide-mounted 5µm sections were acquired nationwide via the University of Birmingham's Human Biomaterials Resource Centre. All work was performed at the University of Birmingham (ethics favourably approved by the North West Haydock Research Ethics Committee, reference 15/NW/0079). Primary tumour resections are listed in Table 2.2.

Patient ID	Age/Gender	Histology	American Joint Committee on Cancer Staging	Lung Cancer Mutation
CRUK0081	72 M	SqCC	IIA	WT
CRUK0092	76 M	SqCC	IIA	WT
CRUK0031	59 M	LUAD	IB	WT
CRUK0029	56 M	LUAD	IIIA	WT
CRUK0070	56 M	SqCC	IIA	WT
CRUK0041	72 M	LUAD	IB	WT
CRUK0032	73 M	LUAD	IB	WT
P011964	75 M	SqCC	IIIA	WT
P012745	71 F	LUAD	Staging not known	WT
CRUK0042	68 M	LUAD	IA	*KRAS* MT
CRUK0069	73 F	SqCC	IB	*KRAS* MT
CRUK0044	59 F	LUAD	IA	*KRAS* MT
CRUK0059	79 F	LUAD	IA	*KRAS* MT
CRUK0040	62 F	LUAD	IA	*KRAS* MT
CRUK0048	76 F	LUAD	IB	*KRAS* MT
CRUK0030	75 M	LUAD	IIIA	*KRAS* MT
CRUK0034	68 F	LUAD	IB	*KRAS* MT
P013778	64 F	LUAD	IIIA	*KRAS* MT
P013281	82 M	LUAD	IIB	*KRAS* MT
CRUK0008	72 M	LUAD	IA	*STK11* MT
CRUK0061	82 M	LUAD	IB	*STK11* MT
CRUK0046	61 F	LUAD	IIA	*STK11* MT
CRUK0099	77 M	Adenosquamous Carcinoma	IIIA	*STK11* MT
CRUK0050	55 M	LUAD	IIIA	*KRAS/STK11* MT
CRUK0047	72 F	LUAD	IA	*KRAS/STK11* MT
CRUK0013	67 M	LUAD	IIIA	*KRAS/STK11* MT
CRUK0024	68 M	LUAD	IB	*KRAS/STK11* MT
P014743	66 M	LUAD	IIIA	*KRAS/STK11* MT

Table 2.2 Patient lung tumour resection clinical and genetic data

Clinical and genetic data from TRACERx and SMP2 patients and their resected primary tumours.

2.2.2 Blood Specimens for Flow Cytometry Experiments

Donors were recruited in accordance with our ethical approval (favourably approved by the West Midlands Solihull Research Ethics Committee, reference 14/WM/1254). All donors provided written informed consent for venepuncture, experimentation and analysis. Age (23-28 years) and gender (female) matched postgraduates and staff from the Institute were recruited as donors. All experiments were conducted at the University of Birmingham.

2.3 Tissue Culture Methods

2.3.1 Tissue Culture Reagents

Roswell Park Memorial Institute-1640 (Sigma-Aldrich): Supplemented medium with 300mg/L L-glutamine and 2000mg/L $NaHCO_3$. Stored at 4°C.

Dulbecco's Modified Eagle's Medium (Sigma-Aldrich): Supplemented medium with 3700mg/L $NaHCO_3$ along with high amino acids at 584mg/L L-glutamine and 4500mg/L D-glucose. Stored at 4°C.

Minimum Essential Medium Eagle (Sigma-Aldrich): Supplemented medium with 292mg/L L-glutamine and 2200mg/L $NaHCO_3$. Stored at 4°C.

Penicillin-streptomycin (Gibco): Solution containing 5000IU/mL penicillin and 5000µg/mL streptomycin. Stored at 4°C.

Foetal bovine serum (FBS) (Biosera): Sterile and toxin free. Aliquoted and stored at -20°C.

EDTA (Sigma-Aldrich): Powder stored at room temperature (RT).

MEM Non-essential Amino Acid Solution (Sigma-Aldrich): 100X solution of 890mg/L L-alanine, 1500mg/L L-asparagine, 1330mg/L L-aspartic acid, 750mg/L L-glycine, 1050mg/L L-serine, 1150mg/L L-proline and 1470mg/L L-glutamic acid.

TrypLE™ Express Enzyme (Gibco): Trypsin replacement dissociation agent with 1mM EDTA and phenol red. Stored at 4°C.

DMSO (Sigma-Aldrich): Stored at RT.

PBS: Prepared by dissolving one Oxoid™ Dulbecco A PBS tablet per 100mL of type 2 pure water and autoclaved (20 mins at 121°C). Stored at 4°C.

MACS buffer: PBS solution containing 0.5% bovine serum albumin (BSA) and 2.5mM EDTA. Stored at 4°C.

Ficoll-Paque™ PLUS (GE Healthcare): Sterile centrifugation medium with a density of 1.078g/mL. Stored at RT.

2.3.2 Tissue Culture Media Preparation

Roswell Park Memorial Institute-1640 culture media (RPMI): Roswell Park Memorial Institute-1640 medium supplemented with 8% FBS and 2% penicillin-streptomycin solution (100IU/mL penicillin and 100µg/mL streptomycin).

Dulbecco's Modified Eagle's Medium culture media (DMEM): Dulbecco's Modified Eagle's Medium supplemented with 8% FBS and 2% penicillin-streptomycin solution (100IU/mL penicillin and 100µg/mL streptomycin).

Minimum Essential Medium Eagle culture media (MEM): Minimum Essential Medium Eagle supplemented with 8% FBS, 2% penicillin-streptomycin solution (100IU/mL penicillin and 100µg/mL streptomycin) and 1X MEM Non-essential Amino Acid Solution.

Freezing media: Culture media (RPMI, DMEM or MEM) supplemented with 20% FBS and 10% DMSO.

2.3.3 Adherent Human Cell Lines

The 'Catalogue of Somatic Mutations in Cancer Cell Lines Project' and the 'canSAR' databases were used alongside the literature to select appropriate NSCLC cell lines with the following lung cancer mutation (MT) genotypes: *KRAS* MT, *STK11* MT and cell lines with concomitant *KRAS* and *STK11* mutations (*KRAS/STK11* MTs) (361-365). NSCLC cell lines without *KRAS* or *STK11* MTs were called 'wild type' (WT) for these experiments. All cell lines were acquired from low passage stocks from trusted suppliers to minimise genotypic and phenotypic drift (Table 2.3). Upon cell line arrival, cells were screened for mycoplasma infection (Chapter 2.3.7) then were expanded in culture and a number of low passage stocks were cryopreserved (Chapters 2.3.4 and 2.3.5). All live cell work throughout this thesis were performed in a sterile category II tissue culture hood.

Cell Line	Description	Source	Lung Cancer Genetic Alteration	Base Medium
CALU-3	Metastatic LUAD	Professor Jo Morris, University of Birmingham	WT	MEM
H292	Metastatic lung carcinoma	American Type Culture Collection (ATCC)	WT	RPMI
HCC78	LUAD	Deutsche Sammlung von Mikroorganismen und Zellkulturen (DSMZ)	WT	RPMI
H1299	Metastatic lung carcinoma	ATCC	WT	RPMI
H2110	Metastatic lung carcinoma	ATCC	WT	RPMI
CALU-6	Pulmonary anaplastic carcinoma	Professor Jo Morris, University of Birmingham	*KRAS* Q61K	RPMI
H441	LUAD	ATCC	*KRAS* G12V	RPMI
CAL-12T	Lung carcinoma	DSMZ	*STK11* CNA loss	DMEM
H1755	Metastatic LUAD	ATCC	*STK11* P281Rfs*6	RPMI
Chago-K-1	Lung carcinoma	European Collection of Authenticated Cell Cultures (ECACC)	*STK11* G56V	RPMI
H1563	LUAD	ATCC	*STK11* G242W	RPMI
A549	Lung carcinoma	ECACC	*KRAS* G12S *STK11* Q37*	DMEM
A427	Lung carcinoma	Professor Jo Morris, University of Birmingham	*KRAS* G12D *STK11* CNA loss	MEM
H460	Lung carcinoma	ATCC	*KRAS* Q61H *STK11* Q37*	RPMI
H1734	LUAD	ATCC	*KRAS* G13C *STK11* M51Ifs*14	RPMI

HEK293T	Foetal kidney epithelium	Professor Benjamin Willcox, University of Birmingham	N/A	DMEM

Table 2.3 Cell lines

List of cell lines used in this thesis. Genetic alterations in the *KRAS* and *STK11* genes for each NSCLC cell line were confirmed from data curated by the 'Catalogue of Somatic Mutations in Cancer Cell Lines Project' database and cross-checked from data curated by the 'canSAR' database.

2.3.4 Maintenance Culture of Adherent Cell Lines

Cell lines were maintained in either 25cm^2 or 75cm^2 flasks (Corning) with 6mL or 18mL of appropriate culture media and incubated at 37°C/5% CO_2. Media were changed every 2-3 days and cells were passaged every 3-5 days (cell line dependent) once deemed to be >70% confluent by light microscopy. Before passaging using enzymatic dissociation, media were removed and cells were briefly washed with PBS. 4mL or 8mL (for 25cm^2 and 75cm^2 flasks respectively) of TrypLE^{TM} Express Enzyme was subsequently added and the cells were incubated at 37°C/5% CO_2 for 1-5 minutes dependent on cell line. After detachment from the polystyrene flask, the enzyme was removed by centrifugation and the cells were split and reseeded as required.

2.3.5 Cryopreservation

Cells to be preserved in liquid nitrogen were pelleted by centrifugation then resuspended in 1mL of appropriate freezing media and transferred to CryoTube^{TM} vials (Nunc). Vials were placed into Mr. Frosty^{TM} Freezing Containers (Nalgene) filled with isopropanol (Sigma-Aldrich), which were used to achieve a gradual cooling rate of -1°C/minute to -

80°C. Vials were transferred to liquid nitrogen freezers (approximately -200°C) the following day.

2.3.6 Revival After Cryopreservation

Cells in CryoTubes™ were thawed quickly in a 37°C water bath and washed with the appropriate culture media. Cells were counted by light microscopy before use.

2.3.7 Mycoplasma Testing

Cell lines were tested for mycoplasma infection upon arrival in the lab and routinely thereafter using a MycoAlert™ Kit (Cambrex) according to the manufacturer's protocol.

2.3.8 Isolation of Peripheral Blood Mononuclear Cells

Peripheral blood was collected into lithium heparin vacutainers (BD) by venepuncture from consenting donors. The heparinised blood was diluted 1:1 with RPMI (with penicillin/streptomycin but without FBS) and layered onto Ficoll-Paque (ratio of 2:1 blood:Ficoll-Paque) then centrifuged at 600 x *g* for 30 mins (without brake). The PBMC layer at the interface of the plasma and Ficoll was aspirated and the cells were resuspended in RPMI without FBS. PBMCs were washed twice, firstly at 800 x *g* for 10 mins (low brake) and secondly washed in RPMI with FBS at 400 x *g* for 7 mins (default high brake). The isolated PBMCs were counted and cryopreserved as previously described.

2.3.9 Collecting Conditioned Media

Conditioned media were collected from all adherent cell lines. Those cell lines not using RPMI as a base culture medium (Table 2.3) were sequentially weaned onto RPMI as follows: passage 1 using 75% base medium and 25% RPMI, passage 2 using 50% base medium and 50% RPMI and passage 3 using 100% RPMI. Once all cell lines were adapted to RPMI, conditioned media were collected when cell lines appeared 70% confluent (or after a maximum of three days culture). The conditioned media were filtered through a 0.45µm membrane and frozen at -80°C. Tumour conditioned media (TCM) or HEK293T conditioned media were used within 6 months of freezing.

2.3.10 Stimulating Peripheral Blood Mononuclear Cells for Cytokine Release

$3x10^5$ to $1x10^6$ PBMCs (depending on experiment) were seeded into 5mL flow cytometry test tubes (Falcon). PBMCs were either un-specifically stimulated by the addition of a phorbol 12-myristate 13-acetate and ionomycin (PMA/iono) solution (500X Cell Stimulation Cocktail, eBioscience™) to the RPMI or left without stimulation. Brefeldin A Solution (1000X, eBioscience™) was added to both treatments immediately after the PMA/iono and PBMCs were incubated at 37°C/5% CO_2 for 4 hours, with gentle resuspensions every hour.

2.3.11 Culturing Peripheral Blood Mononuclear Cells in Conditioned Media

$1x10^6$ PBMCs were seeded into wells of a 48 well plate in 500µL of TCM, control conditioned media (HEK293T cells) or fresh RPMI. The PBMCs were stimulated with

soluble 0.5µg anti-CD3 (clone OKT3, eBioscience™) and 1µg anti-CD28 (clone CD28.2, BioLegend) overnight at 37°C/5% CO_2. The following day PBMCs were aspirated and washed twice with PBS to remove the CD3/CD28 stimulation antibodies and then re-seeded in the same media into unused wells to avoid further stimulation by any antibodies that had become plate-bound. After two days culturing at 37°C/5% CO_2, the PBMCs were removed and split between two tubes. Half the PBMCs from each well were stimulated by PMA/iono as previously described and the other half were left without stimulation. Cellular phenotypes and cytokine production were examined by flow cytometry (Chapter 2.6.4).

2.4 Molecular Techniques

2.4.1 *RORC* Construct Design

A mammalian expression vector for the *RORC2* variant of the *RORC* gene was designed and produced by Sino Biological. *RORC2* (2223bp open reading frame) cDNA was under the control of an enhanced cytomegalovirus promotor. This plasmid also contained a kanamycin resistance gene and produced proteins tagged with C-terminus GFPSpark.

2.4.2 Transformation and DNA Sequencing

Plasmids were reconstituted as per manufacturer's instructions. Reagents from the NEB® 5-α Competent *E. coli* (High Efficiency) kit (New England BioLabs) were used to perform a heat shock transformation into competent *E. coli* following the manufacturer's protocol and bacteria were cultured overnight at 37°C on kanamycin selection plates. Antibiotic resistant colonies were taken from the plates and inoculated into lysogeny broths spiked with 50μg/mL kanamycin then incubated overnight in a shaker at 37°C. The following day, *E. coli* from the broths were pelleted and plasmid DNA were purified using a QIAprep® Spin Miniprep Kit (Qiagen) following the manufacturer's instructions. DNA were sequenced by the University of Birmingham DNA Sequencing Service using T7 forward primers and BGH reverse primers to confirm the amplified plasmids had retained the corrected sequence.

2.4.3 Transfection and Preparation for Confirmatory Analyses

For each expression vector, a transfection mix of 16µg of plasmid and 100µL polyethylenimine solution (Polysciences) was prepared in 1mL of DMEM. This transfection mix was added in a dropwise fashion to HEK293Ts growing in 10cm width petri dishes (Nunc). The cells were then incubated overnight at 37°C/5% CO_2 to enable the cationic polymer-based transfection to occur. The following day, the HEK293T cells were split by enzymatic dissociation (Chapter 2.3.4). After a PBS wash, one third of the total cells were taken for RNA extraction for a PCR confirmation (Chapter 2.4.4) and the second third were processed for confirmatory $GFP^+/ROR\gamma T^+$ flow cytometry staining (Chapter 2.6.2). The final third of cells were pelleted in 1mL of 10% neutral buffered formalin (Leica) and this pellet was taken to the Royal Orthopaedic Hospital NHS Foundation Trust's Department of Musculoskeletal Pathology for paraffin embedding into a tissue block and generation of 5µm slide-mounted sections.

2.4.4 RNA Extraction and cDNA Synthesis

$1x10^6$ cells were pelleted into an 1.5mL Eppendorf tube and RNA extraction with DNase step was carried out using the Nucleospin RNA Purification Kit (Machery-Nagel) as per manufacturer's instructions. To ensure DNA removal, the extracted RNA were subject to a second DNase 1 digestion step using the DNA-*free*™ DNA Removal Kit (Ambion). The DNA-free RNA were subsequently reverse transcribed using random hexamer primers to cDNA using the iScript™ cDNA Synthesis Kit (Bio-Rad) and cDNA were diluted 1:5 in DEPC-H_2O to

lower concentrations. This method was initially validated with no-reverse transcriptase controls. A NanoDrop™ spectrophotometer (Thermo Scientific) was used prior to the second DNase digestion to assess RNA quantity as well as quality by measuring the A260/A280 ratio. cDNA were stored at -20°C.

2.4.5 Quantitative PCR

Multiplex qPCR reactions were set up using the following TaqMan® assay primers: *RORC* FAM (Hs01076112_m1, Thermo Scientific) and *GAPDH* VIC (Hs02786624_g1, Thermo Scientific). Test DNA were run in triplicate and the qPCR master mix was prepared as Table 2.4 (total volume of 20µL/well in a 96 well plate):

After addition of the samples, the plate was sealed and subject to a brief centrifugation pulse. The plate was run on an Applied Biosystems™ 7500 Real-Time PCR machine (Thermo Scientific) using the thermal cycling conditions shown in Table 2.5 (the two cycling stages were repeated 40 times), and data were analysed using the 7500 System Software (V1.4, Thermo Scientific). No amplification occurred in the no reverse transcription control and no template control samples. Relative quantification analysis was performed by the $2^{-\Delta\Delta CT}$ method using an automatic C_T (366).

Reagent	1X Master Mix
2X TaqMan® Universal Master Mix II (Thermo Scientific)	10µL
20X *RORC* FAM primers	1µL
20X *GAPDH* VIC primers	0.5µL (validated at half concentration)
DEPC-H_2O	3.5µL
Sample (DNA, no reverse transcription control, no template control of DEPC-H_2O)	5µL

Table 2.4 qPCR master mix

1X master mix for qPCR reactions.

Stage	Temperature	Duration
Pre-PCR	50°C	2 mins
Holding	95°C	10 mins
$Cycling_1$	95°C	15 seconds
$Cycling_2$	60°C	1 min

Table 2.5 qPCR thermal cycling programming

The thermal cycling protocol used by the Applied Biosystems™ 7500 Real-Time PCR machine.

2.5 Immunohistochemistry Methods

2.5.1 Chromogenic Immunohistochemistry of Fixed Human Tissue

The method described below is our standard immunohistochemistry (IHC) protocol, though different IHC antibodies required modifications to this protocol to work optimally as outlined in Table 2.6.

Sample slides were dewaxed by being submerged in Histo-Clear II (National Diagnostics) for 10 mins and then were progressively rehydrated in industrial methylated spirit (IMS) (Fisher Scientific) (100% IMS for 10 mins, 50% IMS for 5 mins, 25% IMS for 2 mins). Rehydration was completed by submerging the slides in running water from a tap for 10 mins. This was followed by a submersion in 0.3% H_2O_2 (diluted in type 2 water, Sigma-Aldrich) for 15 mins to block endogenous peroxidases. Slides were washed again under the tap for 15 mins, and a heat-induced epitope retrieval (HIER) was performed by placing the slides into pre-heated 10mM sodium citrate buffer (pH adjusted to pH 6.0) or 10mM Tris/1mM EDTA buffer (pH adjusted to pH 9.0) (see Table 2.6 for specific antibodies) in a water bath set to 96°C and were submerged for 20 mins. After being left to cool in the epitope retrieval buffer for an hour, the buffer was washed off under the tap for 5 mins followed by 15 mins in a glass staining trough containing TBST (25mM Tris, 0.15M NaCl, 0.05% Tween-20, pH 7.5, Thermo Scientific) with constant stirring. A hydrophobic barrier was drawn around the tissue using an ImmEdge® PAP pen (Vector Laboratories). Drops of 2.5% normal horse serum (Vector Laboratories) were added to the tissue as per manufacturer's instructions and the slides were incubated in a humidified chamber for 30 mins at RT. After this blocking step, the horse serum was tipped off and 250µL of diluted

primary antibody (Table 2.6) was added to each of the sections, which were incubated at 4°C overnight in a humidified chamber (with the exception of the cytokeratin 7 (CK7)) antibody which was incubated for 1 hour at RT in a humidified chamber). The following day, the primary antibody was washed off by stirring in TBST for 30 mins. Drops of the relevant HRP conjugated secondary IgG (ImmPRESS® Polymer kits, Vector Laboratories) were added following the manufacturer's recommendations and the slides were incubated at RT for 45 mins in a humidified chamber. Unbound secondary antibody was then washed off by stirring in TBST for 30 mins. ImmPACT™ DAB (Vector Laboratories) was diluted and added in a dropwise fashion as per manufacturer's protocol and left to develop (Table 2.6) at RT. Slides were washed under a running tap for 5 mins, counterstained with 100% Mayer's Haematoxylin (Sigma-Aldrich) for 30 seconds then washed under water from a cold tap for 2 mins, a warm tap for 2 mins and a cold tap for 2 mins. Slides were then dehydrated by submerging as follows: 50% IMS for 5 mins, 100% IMS for 10 mins and Histo-Clear II for 10 mins. Appropriately sized coverslips were mounted using drops of DPX (Sigma-Aldrich) and the slides were left to dry overnight in a fume cupboard. Slides were either whole slide scanned at 10X using the Vectra 3 system (PerkinElmer) or regions of tissue were photographed using a Nikon Eclipse E400 microscope. All the staining was assessed by a pathologist.

Marker	Supplier	Clone	Host Species & Isotype	Epitope Retrieval Buffer	Antibody Dilution in PBS	DAB Development Time
Bcl-2	Cell Signalling Technology	15071	Mouse IgG1	EDTA pH 9	1:400	5 mins
CK7	Leica (IVD)	OV-TL 12/30	Mouse IgG1	Citrate pH 6	Pre-diluted, ready to use	1 min
IL-17A	R&D	AF-317-NA	Goat IgG	Citrate pH 6	1:80	90 seconds
RORγT	Novus Biologicals	NLS5188	Rabbit IgG	Citrate pH 6	1:200	90 seconds
RORγT	Merck	6F3.1	Mouse IgG2a	EDTA pH 9	1:700	1 min
RORγT	eBioscience™	AFKJS-9	Rat IgG2a	EDTA pH 9	1:125	90 seconds

Table 2.6 IHC antibodies with information on the variable IHC protocol steps

Modifications to the standard IHC protocol (Chapter 2.5.1) are listed by each IHC antibody in this table.

2.5.2 Designing Digital Pathology Algorithms for Chromogenic Staining

To quantify RORγT 6F3.1 IHC staining, two supervised machine learning algorithms were designed using inForm analysis software (V2.4.9, Akoya Biosciences) (github.com/Sithspitz/thesis/tree/master/digital_pathology/ihc_algorithms/). The first algorithm was trained to recognise 10X scanned lung regions with at least 70% cell coverage (tissue), therefore excluding large areas of wight space which are likely to be characteristic of normal alveolar histology. This inForm algorithm was run in the digital pathology viewing software Phenochart (V1.0.12, Akoya Biosciences) and the total number of 10X lung resection regions after white space removal were calculated. After this calculation, regions containing other normal structures including connective tissue, cartilage, bronchioles and blood vessels were manually removed, and the edges of the

tissue were also excluded as these often contained IHC staining artefacts. 30% of the total number of lung resection regions were randomly sampled from the remaining regions and were pushed to inForm for analysis. This 30% random coverage is better than many other investigators in the literature with many digital pathology publications quantifying from only 3 to 15 representative images, not taking into account tissue size and risking manual selection bias (367-370).

To quantify RORγT$^+$ DAB staining, an analysis algorithm was trained using inForm. The basic settings regarding image preparation, cellular segmentation and phenotyping were kept the same between sections, but due to histological heterogeneity amongst NSCLC cases the tissue segmentation was trained on a case-by-case basis (broad tissue segmentation categories are: 'Tumour', 'Stroma', 'Lymphoid Aggregates', 'Necrosis', 'White Space'). A notable strength in the design of this quantification algorithm is its ability to exclude false DAB positives resulting from anthracotic pigment in the lung, thereby only quantifying genuine DAB staining found in lymphocyte nuclei.

R scripts were written to merge, tidy and quantify the inForm export data (github.com/Sithspitz/thesis/tree/master/digital_pathology/ihc/). The abundance of total and spatially resolved (by tissue segmentation category) RORγT$^+$ lymphocytes (RORγT$^+$ lymphocytes/10,000 total counted cells) were compared using unpaired two-sample Wilcoxon tests.

2.5.3 RORγT Overall Survival Analysis

This survival analysis was performed in a similar way as described previously (Chapter 2.1.9). To group the NSCLC samples, divided the cases into quartiles based on the number of RORγT^{+} lymphocytes/10,000 cells. Resections with a RORγT^{+} abundance between the upper quartile and maximum value were categorised into the 'RORγT High' group, resections with data between the lower quartile and minimum value were placed into the 'RORγT Low' group and the remaining samples with data around the median were grouped into 'RORγT Other'. Kaplan-Meier curves were produced in GraphPad Prism using months from resection to clinical outcome data and were statistically compared using Mantel-Cox tests.

2.5.4 Multiplex Fluorescent Immunohistochemistry of Fixed Human Tissue

The multiplex panel staining was validated and optimised by colleagues at the University of Birmingham's Human Bioresources Centre using a Leica BOND RX autostainer to ensure quality and consistent staining. The BOND RX used proprietary Leica reagents to perform the IHC staining and was programmed using a modified version of the tyramide signal amplification protocol, which is a similar principle to the singleplex IHC method described in Chapter 2.5.1, but with some key differences. To multiplex we used an Opal IHC Kit (PerkinElmer) with a sequential pH 9.0 HIER strategy for both epitope retrieval and antibody removal followed by a final DAPI counterstain. Details of the multiplex panel and BOND RX protocol can be found in Table 2.7. All the staining was assessed by a

pathologist. After checking the quality of staining manually, slides were whole slide scanned at 10X using the Vectra 3 system (PerkinElmer); then regions with RORγT^{+} cells were highlighted using Phenochart software for 20X imaging, concentrating on selecting putative lymphoid aggregates with RORγT^{+} cells and tumour/stroma infiltrating RORγT^{+} cells.

Antibody Incubation Sequence	Marker	Supplier	Clone	Host Species & Isotype	HIER Incubation Time	Antibody Dilution	Opal	Opal Dilution
1	**RORγT**	Merck	6F3.1	Mouse IgG2a	20 mins	1:700	520	1:150
2	**CA9**	Leica (IVD)	TH22	Mouse IgG2a	10 mins	1:100	650	1:150
3	**CD20**	Dako (IVD)	L26	Mouse IgG2a	20 mins	1:200	690	1:150
4	**CD3**	Leica (IVD)	LN10	Mouse IgG1	20 mins	1:200	620	1:200
5	**CD4**	Abcam	EPR6855	Rabbit IgG	20 mins	1:50	570	1:150

Table 2.7 BOND RX sequential multiplex IHC staining protocol

Details of the antibodies and Opal fluorophores used the multiplex IHC protocol and of the antibody incubation sequence used to programme the BOND RX autostainer.

2.5.5 Designing Digital Pathology Algorithms for Fluorescent Staining

To phenotype the stained cells within the 20X scanned Opal stained regions, two types of supervised machine learning algorithms were designed using inForm (github.com/Sithspitz/thesis/tree/master/digital_pathology/vectra_algorithms/). The first algorithm ('Full_Pheno_Algorithm.ifp') assigns phenotypes based on expert knowledge of possible marker co-expression; whereas the second type of algorithm (suffix: '_Single_Algorithm.ifp') are trained to only recognise one marker at a time (e.g. $CD4^+$ cells vs $CD4^-$ cells), then resultant marker expression data were merged using cell segmentation XY positional data to consolidate the phenotyping to the correct cell. This second approach allows unbiased marker co-expression phenotyping.

The ‘Full_Pheno_Algorithm.ifp’ removed lung image autofluorescence, segmented tissues and cells then assigned user defined and trained cellular phenotypes. The images were batch processed and scripts was created to merge and tidy the data (github.com/Sithspitz/thesis/tree/master/digital_pathology/vectra_tidy/). Cell phenotype data were collated (github.com/Sithspitz/thesis/blob/master/digital_pathology/vectra_collation/CD4_collation_script.R) and analysed using unpaired two-sample Wilcoxon tests (github.com/Sithspitz/thesis/blob/master/digital_pathology/vectra_collation/CD4_collation_analysis_script.R).

The base settings from ‘Full_Pheno_Algorithm.ifp’ were taken and applied to each of the five ‘_Single_Algorithm.ifp’, with the only change being a revised phenotyping step which was optimised to phenotype one marker per algorithm. Batch processing and merging were done using inForm, whilst consolidation and analysis – including co-expression, count within and nearest neighbour analyses – were performed using the *phenoptr* package (V0.2.7) (333).

To ensure consistency between RORγT phenotyping approaches we compared the exported results from the two fluorescent digital pathology algorithms described above and the chromogenic quantification algorithm (Chapter 2.5.2). Encouragingly we found high similarity between the approaches with regard to the number of RORγT^{+} lymphocytes/10,000 cells, albeit with some differences in the higher cases (Figure 2.2a). Both fluorescent algorithms were similarly compared using CD20 as a different marker and again showed good concordance (Figure 2.2b). As the chromogenic algorithm quantified

from considerably more images per resection, it was considered the most accurate method of quantification.

a)

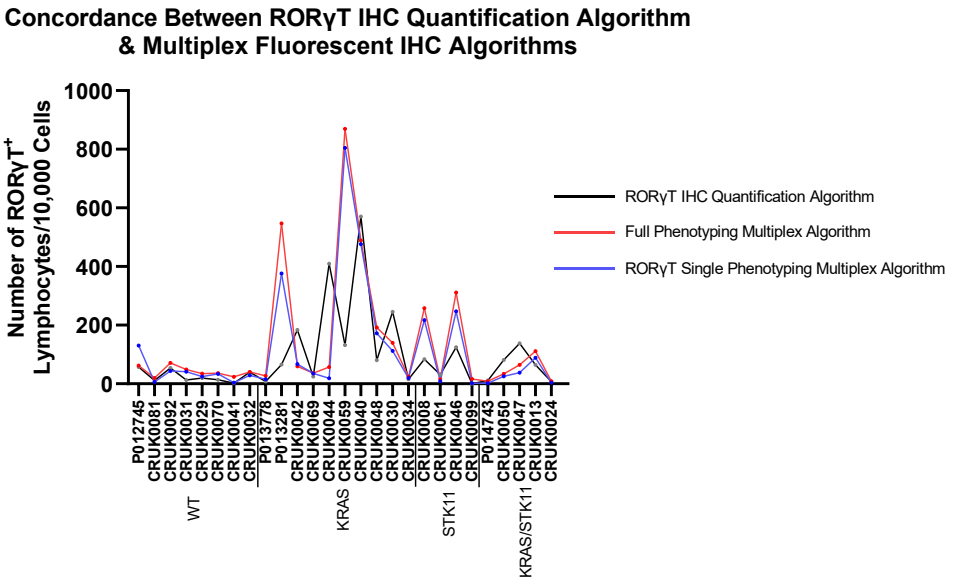

b)

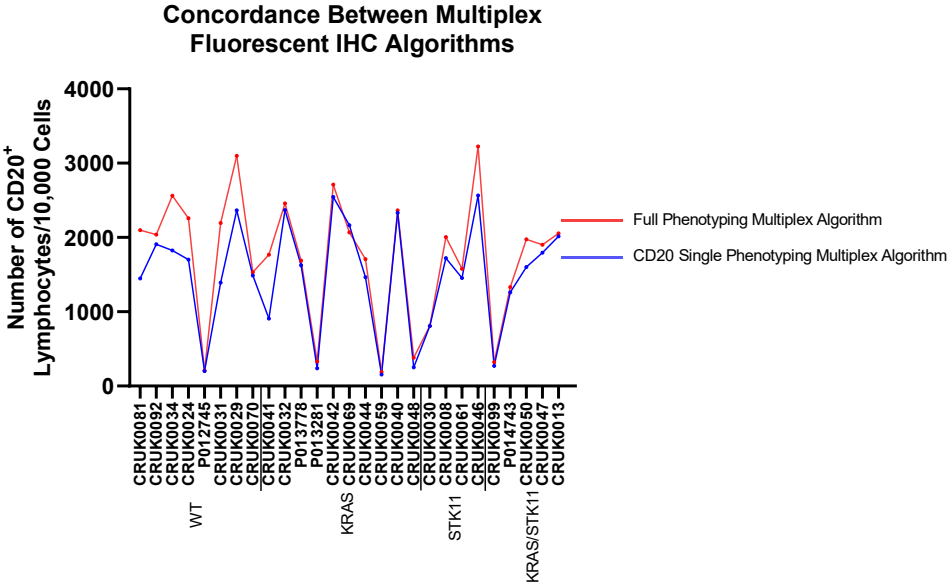

Figure 2.2 Concordance between IHC algorithms

a) The total abundance of RORγT$^+$ lymphocytes/10,000 cells were calculated for each patient resection using the three algorithms. Due to its design, the 'RORγT IHC Quantification Algorithm' calculated this abundance from more regions (median of 41 10X scanned regions examined per tumour) than the multiplex algorithms (≤ 8 20X scanned regions examined per tumour). **b)** The total abundance of CD20$^+$ lymphocytes/10,000 cells were calculated for each patient resection by the two multiplex algorithms.

2.6 Flow Cytometry Methods

2.6.1 Conjugating Merck RORγT 6F3.1 for Flow Cytometry

10µg of purified RORγT IHC monoclonal antibody clone 6F3.1 (Merck) was conjugated to the fluorophore AF647 using and following the instructions from the APEX™ Alexa Fluor™ 647 Antibody Labelling Kit (Thermo Scientific).

The manufacturer recommended to conjugate fresh aliquots of antibody every 2 weeks to ensure there is no false negative detection caused by fluorophore dissociation. We followed these recommendations, and each new conjugation was tested by flow cytometry staining of *ex vivo* PBMCs (Chapter 2.6.4). For standardisation, each newly conjugated RORγT-AF647 batch was titrated and compared against the previously conjugated RORγT-AF647 to determine the best dilution for use.

2.6.2 Flow Cytometry of *RORC2* Transfected HEK293T Cells

RORC2 transfected and untransfected HEK293Ts, prepared as described in Chapter 2.4.3, were passed through 0.70µm cell strainers to remove aggregates and then washed in PBS. Cells were fixed and permeabilised using the Foxp3 Transcription Factor Staining kit (eBioscience™) and then incubated with the pre-determined dilution of RORγT-AF647 (Chapter 2.6.1) for 30 mins at RT in the dark. Unbound RORγT-AF647 was removed by washing with the kit's Permeabilization Buffer and cells were resuspended in MACS buffer for flow cytometric acquisition. OneComp eBeads™ Compensation Beads (Thermo Scientific) were prepared in parallel as per manufacturer's instructions with one RORγT-AF647 stained tube to compensate for the AF647 staining and one CD25-FITC (1:50, clone

M-A251, BioLegend) stained tube to compensate for GFP positivity as a result of a successful transfection.

2.6.3 T Helper 17 Flow Cytometry Antibody Panel

A multiplex flow cytometry panel of extracellular and intracellular antibodies to detect Th17 cells, shown in Table 2.8, was designed and optimised. The antibody master mixes are added at different stages of the staining and a full protocol can be found in Chapter 2.6.4. The APC-Cy7 conjugated antibodies and amine binding viability dye allowed APC-Cy7 to act as a dump channel to exclude cells which are dead or, of B cell or myeloid cell lineage. Most antibodies listed had previously been validated and optimised by the laboratory, though CD127-PE, CCR6-AF488, IL-17A-PE-Cy7 and RORγT-AF647 were new for this panel. New antibodies were titrated by doubling dilutions as shown in Figure 2.3 to determine the optimal concentration for use. RORγT-AF647 validations and optimisations are described in Chapter 2.6.1. The final panel was validated by two 'fluorescence minus one' (FMO) experiments, one experiment using PBMCs stimulated for cytokine release and the other using unstimulated PBMCs.

Marker	Supplier	Clone	Fluorophore	Dilution	Master Mix
Viability Dye	eBioscience™	N/A Catalogue: 65-0865-14	APC-Cy7	1:100	Extracellular
CD14	BioLegend	HCD14	APC-Cy7	1:100	Extracellular
CD19	BioLegend	HIB19	APC-Cy7	1:100	Extracellular
CD3	BD	SK7 (Leu-4)	AmCyan	1:50	Extracellular
CD4	BioLegend	RPA-T4	BV421	1:20	Extracellular
CD127	BioLegend	A019D5	PE	1:20	Extracellular
CCR6	BioLegend	G034E3	AF488	1:33	Extracellular
RORγT	Merck	6F3.1	AF647	Variable (Chapter 2.6.1)	Intracellular
IFNγ	BioLegend	4S.B3	AF700	1:200	Intracellular
IL-17A	eBioscience™	eBio64DEC17	PE-Cy7	1:100	Intracellular
TNFα	BioLegend	MAb11	PE-Dazzle	1:400	Intracellular

Table 2.8 Th17 flow cytometry panel antibodies

Extracellular and intracellular fluorophore conjugated antibodies and their dilutions.

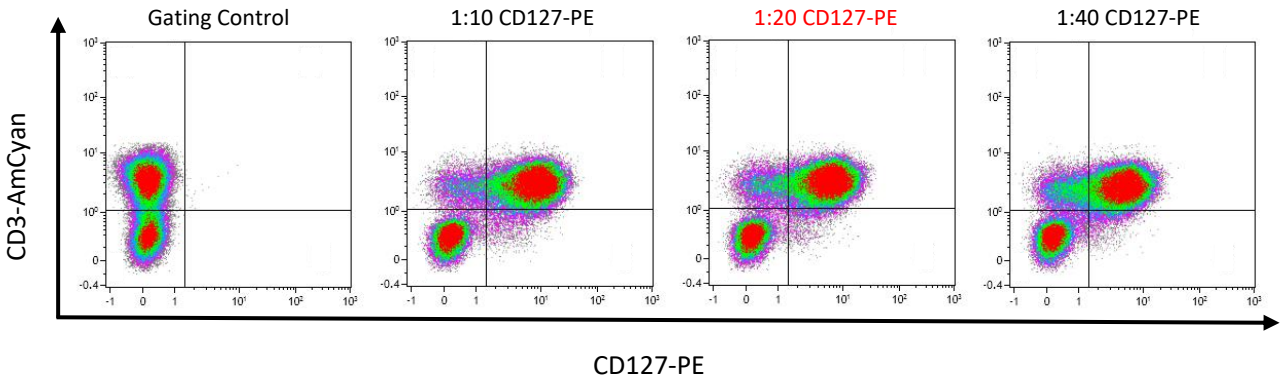

Figure 2.3 CD127-PE flow cytometry antibody titration

PBMCs were flow cytometry stained as described in Chapter 2.6.4 using Viability Dye-APC-Cy7, CD3-AmCyan and CD127-PE. The Gating Control is PBMCs stained with Viability Dye and CD3, but not CD127. Other plots show titrations of CD127 in a doubling dilution series, the red titled plot was used in this panel as it gave maximum staining at the lowest dilution.

2.6.4 Flow Cytometry Staining Peripheral Blood Mononuclear Cells

PBMCs (stimulated for cytokine release and unstimulated) were washed twice with cold PBS and were stained with an extracellular master mix of fluorescent antibodies and a viability dye (Chapter 2.6.3, Table 2.8) for 30 mins on ice in the dark. After this surface antibody incubation, PBMCs were washed with PBS then fixed and permeabilised using reagents from the Foxp3 kit following manufacturer's instructions. Once the cells had been permeabilised they were incubated with the intracellular master mix of antibodies (Chapter 2.6.3, Table 2.8) staining for 30 mins at RT in the dark. The PBMCs were subsequently washed with Permabilization Buffer and resuspended in MACS buffer before analysis. OneComp Compensation Bead tubes for each fluorophore were also prepared in parallel according to manufacturer's instructions.

2.6.5 Flow Cytometry Acquisition and Analysis

Cells and beads were acquired using a LSR II (BD) flow cytometer. All events were recorded but acquisition was stopped using the gates in Figure 2.4, at 40,000 stoppage gate events for the tubes containing HEK293Ts (Chapter 2.6.2) (Figure 2.4a), at 20,000 stoppage gate events for TCM or control mediate cultured PBMCs (Chapters 2.3.11 and 2.6.4) (Figure 2.4b), and at 50,000 stoppage gate events for all other experiments using PBMCs (Figure 2.4b). Data were analysed using FlowJo 10.6.2 (BD) and Kaluza 1.2 (Beckman Coulter).

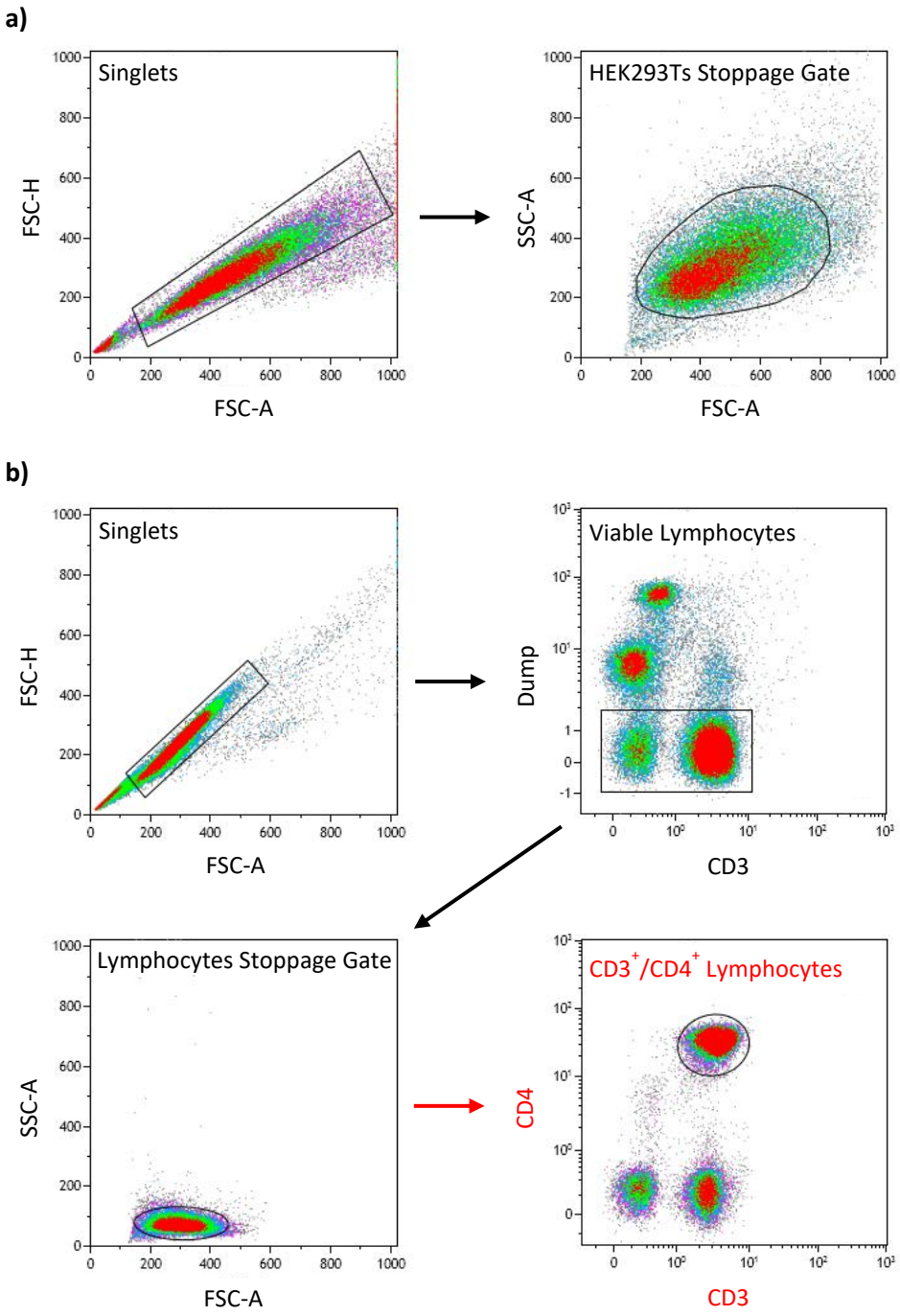

Figure 2.4 Flow cytometry gating strategies for HEK293T cells and PBMCs

a) HEK293T gating strategy. Single cells were gated using forward-scatter height (FSC-H) vs forward-scatter area (FSC-A), then appropriately sized HEK293Ts were gated using side-scatter area (SSC-A) vs FSC-A and this gate acted as a stoppage gate for LSR II acquisition. **b)** PBMC gating strategy. Single cells were first gated using FSC-H vs FSC-A. This was followed by gating of a 'Dump' APC-Cy7 channel vs CD3-AmCyan. This gate removed $CD14^{+}$, $CD19^{+}$ and dead cells, leaving viable $CD14^{-}/CD19^{-}/CD3^{+/-}$ cells. Appropriately sized viable lymphocytes were gated using SSC-A vs FSC-A and this gate acted as a stoppage gate for LSR II acquisition. The final gate, highlighted in red, gates viable $CD3^{+}/CD4^{+}$ lymphocytes which was used in downstream analysis after acquisition.

2.6.6 High Dimension Flow Cytometry Data Analysis

This workflow was based on previously published work with the packages used in this section (371-373). Firstly, $CD3^+/CD4^+$ lymphocytes were gated after the lymphocyte stoppage gate as shown in red in Figure 2.4b and all gated events in '.fcs' files from similar conditions were concatenated. This concatenation was dependent on the experimental comparison as described in Chapter 5 (e.g. all T cells cultured in TCM from the A549 cell line from our 4 donors were concatenated). The concatenated files were then downsampled (at 10,000 $CD3^+/CD4^+$ T cells) using a FlowJo plugin to ensure that the same number of cells from each comparison were processed.

Downsampled concatenations were subsequently imported into the *cytofkit2* package (V2.0.1) and were subject to logicle transformation (327). This package was then used to perform UMAP dimension reduction and FlowSOM clustering (typically at k = 40 after experimentation for each dimension reduction run, using all markers except the APC-Cy7 dump) (343, 374). To help define clusters and their phenotypes, marker enrichment modelling (MEMod) was performed using the *cytofkit2* export data. UMAP XY axes data, FlowSOM clusters and logicle marker expression data were merged and the *MEM* package (V2.0.0) was used to run the algorithm using all channels except for CD3-AmCyan, CD4-BV421 and the APC-Cy7 dump (332). The MEMod analysis and *cytofkit2* marker expression heatmaps aided manual annotation of the defining features of different UMAP regions. We gated on different UMAP regions to obtain population percentages and MFI values for comparison.

2.7 Analyte Profiling Using Luminex

2.7.1 Luminex Assay Design

We designed a custom multiplex Luminex® chemokine and cytokine panel which was mixed and produced by R&D Systems. The 21 multiplex analytes are as follows, antibodies against each were bound to magnetic beads: CCL2, CCL4, CCL20, CXCL1, CXCL2, CXCL8, G-CSF, GM-CSF, IFNγ, TNFα, IL-1β, IL-2, IL-6, IL-10, IL-12 p70, IL-17A, IL-21, IL-22, IL-23, VEGF-A, VEGF-D.

2.7.2 Luminex Experiment and Analysis

Samples for the Luminex® assay were different cell culture supernatants as described in Chapter 5. All conditioned media from Chapter 2.3.9 were profiled, as well as a kit Calibrator Diluent blank, an RPMI only control and cytokine controls from PBMCs. The PBMC controls were either stimulated or not as per Chapter 2.3.10 (except without Brefeldin A addition).

The Luminex® experiment was conducted following instructions from the kit and each of the following steps were performed using polypropylene plasticware to prevent unwanted protein adhesion. Briefly, all samples except the blank were diluted 1:1 in Calibrator Diluent, and the kit reagents and standards were prepared as instructed. 50µL of sample or standard (examined in duplicate) were added to a 96 well plate alongside 50µL of analyte capture antibody coated magnetic bead cocktail. The plate was shaken for 2 hours at RT. The 96 well plate was subsequently left on an appropriate magnetic plate for 1 min and the beads in each well were washed 3 times by adding 100µL of Wash Buffer then

inverting without blotting. 50µL of a biotinylated analyte specific antibody cocktail was then added and the plate was shaken for 1 hour at RT. The beads were washed as described previously before 50µL of a streptavidin-PE conjugate was added and shaken for 30 mins at RT. Lastly the beads were washed and resuspended in 100µL of Wash Buffer, then the plate was read using a Bio-Plex® 200 (Bio-Rad) that had been programmed as per the R&D instructions.

All the acquired sample fluorescent intensities were multiplied by 2 to account for the initial dilution in Calibrator Diluent and MFIs for each analyte were calculated. The blank MFI value for each analyte was then subtracted to give MFIs for analysis. If MFI values were higher than the highest standard for a particular analyte, then they were assigned the value of the highest standard. Likewise, if they were below the lowest standard, they were called 0. Concentrations in pg/mL were read off analyte standard curves. As all samples had been cultured in FBS supplemented RPMI, the RPMI only control acted to detect background analytes in the media, so true analyte positivity was only defined if an observed concentration was above 2σ RPMI. This control was in fact only important for IL-2, adjusting the true positive value to greater than 68.67pg/mL. Results were compared in GraphPad Prism and principal component analysis (PCA) was performed on analyte concentrations using R.

3. Analysis of Mutation Associated Immune Signatures in Lung Cancer

3.1 Introduction

Recent work has shown interesting links between cancer genetics and intratumoural immune contextures in several different cancers. With regard to NSCLC the most in-depth previous work in this area focused on understanding the heterogeneity in clinical responses to immune checkpoint blockade in relation to the cellular mutations present. However, a detailed description of immune gene transcriptional signatures in these genetically characterised tumours was not performed (49).

We therefore set out to examine patterns of intratumoural immune gene expression related to key LUAD driver cancer genes using open access data from TCGA, a large North American cancer genomics collaboration (65, 311). To describe these immune signatures, we used TCGA mutation data determined by whole exome sequencing to establish the mutational profile of each patient tumour, and RNA-Seq data to profile immune gene mRNA expression within each patient tumour.

3.2 Results

3.2.1 Lung Adenocarcinoma Cancer Gene Mutation Delineated Immune Gene Expression Signatures

We were firstly interested in identifying whether LUADs that had acquired driver mutations in different cancer genes were associated with different patterns of immune gene expression, called an immune signature throughout this thesis. To understand which key cancer genes to choose for our immunological analysis, we reviewed the literature and selected cancer genes that drive LUAD with a prevalence of over 10% in the TCGA dataset (65, 319, 320). We also included *ALK* and *ROS1*, despite prevalences of below 10% as these are the two key LUAD fusion genes. The list of LUAD cancer genes in Table 3.1 were taken forward for examination. Likewise, we used the literature to select 105 immune genes related to different immune subsets, functions, recruitment, and engagement (132, 140, 142, 189). Canonical subset genes regulating cell surface marker expression included *CD4*, *CD8A* and *CD19*, whilst functional genes included cytokines such as *IL6*, *IFNG* and *TNF*. Regulatory and exhaustion markers of clinical interest like *CTLA4*, *LAG3* along with the genes coding PD-1 and its ligand were also investigated. Moreover, markers of recruitment as well as the full repertoire of HLA class I and II genes were also included.

Cancer Gene	Mutation Prevalence in TCGA 2014	Number of Patients with Mutation in TCGA 2014
ALK	7.8%	18
ATM	11.7%	27
BRAF	11.3%	26
CDKN2A	23.9%	55
EGFR	17.4%	40
KRAS	35.7%	82
MET	11.7%	27
NF1	12.2%	28
ROS1	5.7%	13
STK11	18.7%	43
TP53	45.7%	105

Table 3.1 Frequency of cancer gene mutations in TCGA 2014

Data from TCGA 2014 dataset. Percentages calculated from the total number of patients in the series.

To investigate immune signatures in relation to LUAD cancer genes from TCGA data, we sequentially compared median immune gene mRNA expression z-scores from cancer gene mutation positive cases against all other cases that were negative for that particular cancer gene mutation. The mRNA expression fold change differences between the cancer gene mutation positive and negative groups for each immune gene made up the immune signatures, as plotted in Figure 3.1.

Markedly different immune gene signatures were observed for different cancer gene mutation groups. TCGA patients with mutations in *MET* had immunologically 'hot' signatures with increased immune gene expression of almost every gene investigated; though some of the significantly increased genes, such as *FOXP3* (p = 0.0153), *LAG3* (p =

0.0262) and *PDCD1* (p = 0.0066), are suppressive in nature. *RORC* was one of the significantly downregulated immune genes in the *MET* cancer gene mutation immune signature (p = 0.0409). The *STK11* and *ATM* immune signatures contrast the immunologically 'hot' *MET* signature, appearing as immunologically 'cold'. 52/105 immune genes in the *STK11* immune signature and 17/105 immune genes in *ATM* immune signature were significantly downregulated in the cancer gene mutation positive groups in comparison to the cancer gene mutation negative groups. These two cold signatures were 78% similar in regard to the direction of fold changes and 100% similar when comparing only shared significant results (n = 16). This low universal immune expression in the patients with *STK11* mutations interestingly also included no increase in markers of exhaustion and immunosuppression. For instance, the *CD274* and *PDCD1LG2* genes encoding PD-L1 and PD-L2 respectively, showed significant downregulations in patients with *STK11* mutations ($p \leq 0.0001$ and p = 0.0006 respectively). PD-L1 and PD-L2 are not downregulated in every immune signature. Patients with *TP53* cancer gene mutations, which are very prevalent in LUAD, show significantly increased *CD274* and *PDCD1LG2* gene expression compared to patients without *TP53* mutations (p = 0.0101 and p = 0.0244 respectively). Overall, the *STK11* immune signature gave 55 significant results, the most from this analysis. Strikingly, only 3 of these were immune gene upregulations: *STAT3* (p = 0.001), *CSF3* (p = 0.02) and *RORC* ($p \leq 0.0001$). The only other cancer gene mutation group with a significant *RORC* expression increase (p = 0.0016) was the *KRAS* immune signature. Like *ATM* and *STK11*, this signature exhibited general immune gene downregulations and was 63% similar with direction of fold changes to the *STK11* signature. This increased to 100% similar when comparing only mutually significant results (n = 9).

Another striking feature of Figure 3.1 are the differences in patterns of HLA family gene expression across the cancer gene mutation groups. HLA class II genes and their transcriptional regulator *CIITA* are increased in the *BRAF* cancer gene mutation group immune signature whilst class I are decreased, though not significantly. The opposite is true of the *CDKN2A* signature in which class I genes are increased, and class II are decreased. The *MET*, *ROS1* and *EGFR* immune signatures appear to have ubiquitously upregulated HLA class I and II. Patients with *EGFR* cancer gene mutations have significantly increased expression of 6/19 *HLA* genes (all $p \leq 0.0434$) compared to patients without *EGFR* cancer gene mutations. This contrasts with ubiquitous HLA downregulations in 5/19 *HLA* genes in the *KRAS* cancer gene mutation group (all $p \leq 0.0378$) and in 18/19 *HLA* genes in the *STK11* cancer gene mutation group (all $p \leq 0.0322$), with the only non-significant *HLA* gene downregulation in patients with *STK11* mutations being the non-classical *HLA-G*.

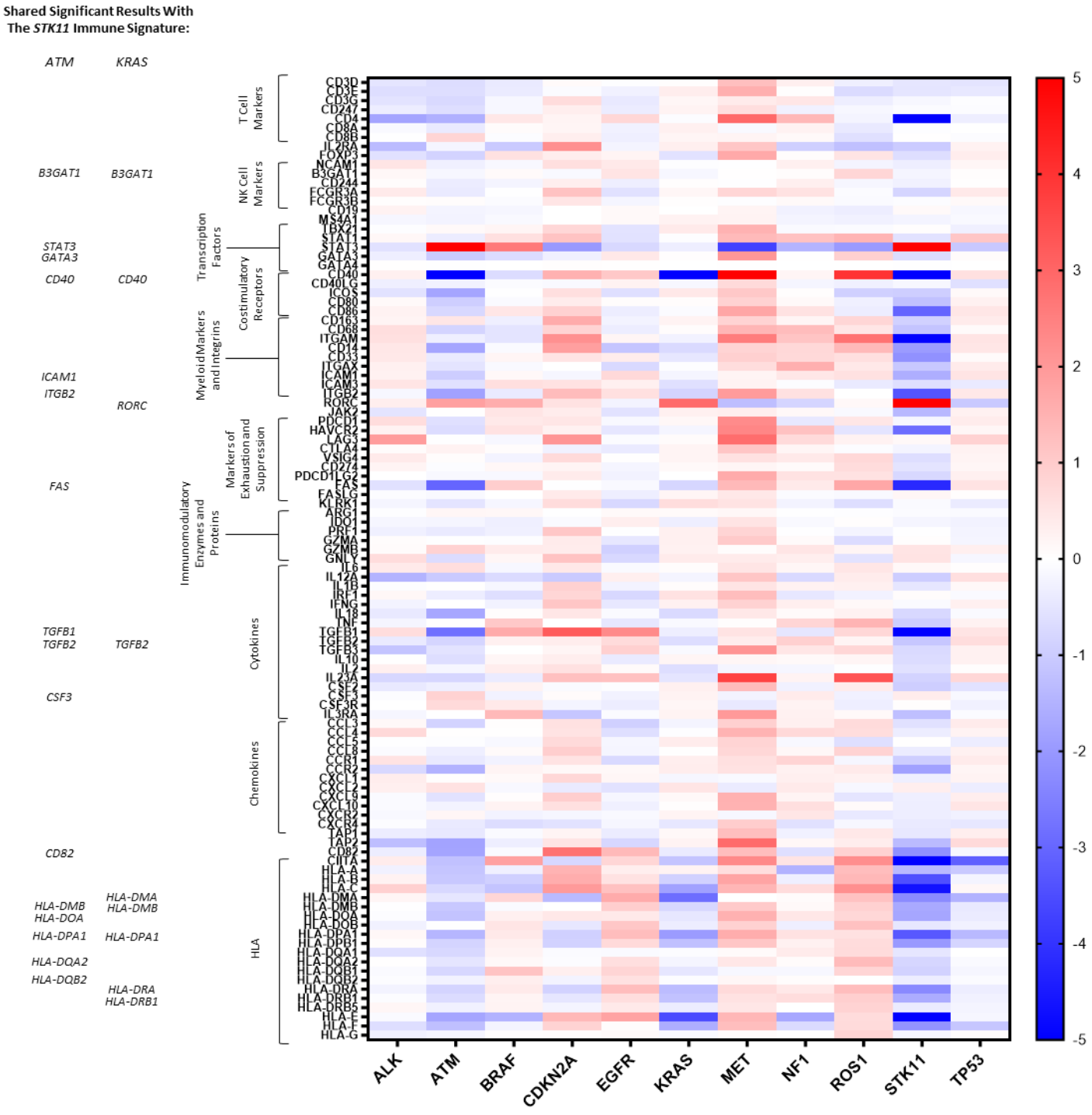

Figure 3.1 LUAD cancer gene immune signatures

Full method available in Chapter 2.1.3. Median expression z-scores for each immune gene were calculated in patients with mutations in the cancer gene in question and compared to the remaining patients without mutations in the same cancer gene. Fold changes were calculated between the mutation positive group median and the mutation negative group median and plotted. Fold change values above +5 and below -5 are called +5 and -5 respectively. Immune genes which are significantly expressed (assessed by unpaired-two sample Wilcoxon tests and deemed significant if *p* values were below the Bonferroni corrected *p* value) in both the *STK11* immune signature and *ATM* immune signature, and the *STK11* immune signature and *KRAS* immune signature are shown on the left of this Figure. TCGA 2014 dataset *n* = 230.

After interrogating these immune signatures, we were particularly interested in significant and similar patterns of general immune suppression in the *STK11* and *KRAS* cancer gene mutation groups. The *ATM* immune signature also showed similarities but we chose to focus on patients with *KRAS* mutations, *STK11* mutations and patients with concomitant *KRAS* and *STK11* mutations (called *KRAS/STK11* mutations for the purpose of this thesis), which are of particular clinical interest. *KRAS* mutations and *STK11* mutations alone are able to drive disease; yet LUAD outcomes are often worse when patients have concomitant *KRAS/STK11* mutations (115, 375, 376).

To confirm our findings of suppressed immune gene expression in TCGA patients with *KRAS* and *STK11* mutations, we used another independent comparable open access dataset to TCGA collected by Schabath *et al* (316). In their study, the authors performed gene expression microarrays and targeted sequencing to identify mutations in *KRAS* and *STK11*. We chose a reduced set of 20 significantly differentially regulated genes from the TCGA derived *STK11* immune signature for validation (Figure 3.2).

Although gene expression fold changes in the Schabath *et al* data were less pronounced than those observed in TCGA data, similarities remained. Comparing the directions of the fold changes in immune genes in the Schabath data showed that the *KRAS* mutation group immune gene fold change directions are 65% similar and that the *STK11* group expression is 95% similar to TCGA data. When comparing the direction of fold change in only shared significant results in both datasets, the Schabath and TCGA directions of immune gene expression are 100% similar for the *KRAS* mutation groups and *STK11* mutation groups.

The immune gene expression was also similar within the Schabath dataset, as the *KRAS* mutation group and *STK11* mutation group were 85% similar in fold change direction, and 100% similar when comparing the 6 genes with shared significant results. In summary, these results from a different set of patients analysed using different molecular techniques confirm our findings from TCGA, that *STK11* mutations are linked with immune gene expression downregulations and that there is similarity in immune gene expression in patient tumours with *KRAS* and *STK11* mutations.

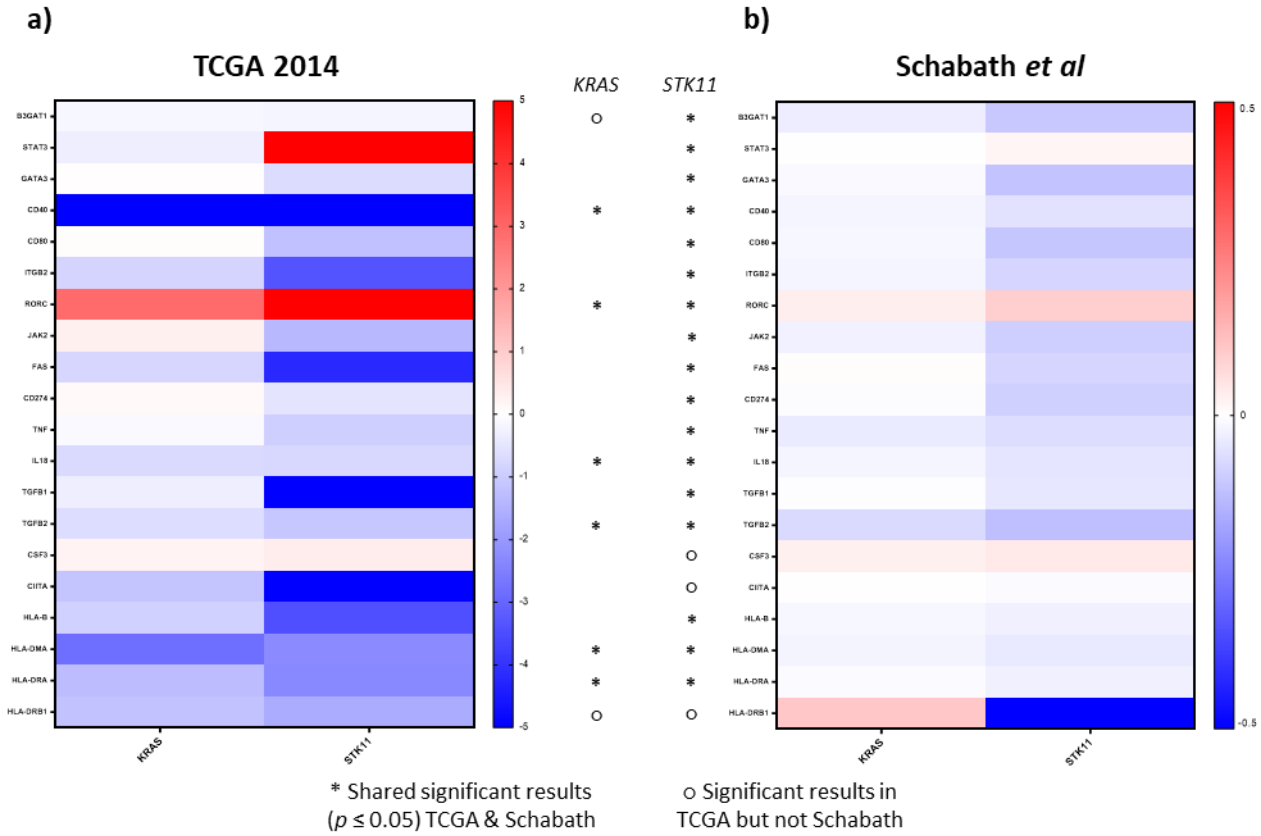

Figure 3.2 Immune gene expression validations with Schabath *et al* and TCGA 2014 data

a) The plotted fold changes were calculated, and significance assessed as described in Figure 3.1. TCGA 2014 dataset *n* = 230. **b)** Median IRON expression scores for each immune gene were calculated in Schabath *et al* (316) patients with mutations in the cancer gene in question and patients without mutations in the same cancer gene. Fold changes were calculated between the mutation positive group median and the mutation negative group median and plotted. Fold change values above +0.5 and below -0.5 are called +0.5 and -0.5 respectively. Significance was assessed by unpaired-two sample Wilcoxon tests. Schabath *et al* (316) dataset *n* = 422.

After uncovering interesting findings in the immune signatures from TCGA patients with *KRAS* and *STK11* mutations, we were next interested in computationally profiling tumour infiltrating leukocytes in the TCGA resections using immune subtype specific gene signatures. We were particularly intrigued to investigate whether patients with these clinically important concomitant *KRAS/STK11* mutations exhibited synergistic increases/decreases of specific immune phenotypes. As TCGA performed transcriptomics on heterogeneous bulk tumours, the resultant data are complex gene expression profiles

from a mixture of different cell types, which causes high non-immunological background. We therefore used the gene expression deconvolution algorithms CIBERSORT and MCP-counter to estimate the immune composition of TCGA tumours (321, 322). CIBERSORT is able to enumerate the proportion of different immune subsets per tumour (relative fraction), whilst MCP-counter can estimate the abundance of immune populations per tumour.

From the 22 CIBERSORT subsets which cover all key leukocyte subsets, we found only 4 subsets with significant changes in mean group relative fraction of the total leukocytes enumerated (Figure 3.3). TCGA cases with *KRAS/STK11* mutations had reduced M1 macrophage and resting DC relative fractions compared to cases without mutations in either of the *STK11* or *KRAS* cancer genes, defined as 'wild type' (WT) for the purpose of this thesis. Comparing the *KRAS* and *KRAS/STK11* mutation groups M1 macrophage mean relative fraction showed a near significant reduced relative fraction size in the *KRAS/STK11* mutations group ($p = 0.0783$). However, the *KRAS/STK11* mutation group had a significantly reduced M1 macrophage mean relative fraction size compared to the WT group ($p = 0.0038$). Resting DCs also had significantly reduced mean relative fractions in patients with *STK11* and *KRAS/STK11* mutations compared to the WT and *KRAS* mutation groups. The only B lineage cell with significant differences were plasma cells, which had increased mean relative fractions in patients with *STK11* and *KRAS/STK11* mutations compared to WT ($p = 0.0078$ and $p = 0.0003$ respectively). Lastly, the *KRAS/STK11* mutation group had a larger mean relative fraction of neutrophils compared to the WT group ($p = 0.0472$).

Neutrophil abundance as predicted by MCP-counter was similarly significantly higher in patients with *KRAS/STK11* mutations compared to WT patients (p = 0.0006) (Figure 3.3d). The *KRAS/STK11* group had a lower monocyte lineage abundance (encompassing monocytes and macrophages) compared to WT (p = 0.0432). The *STK11* and *KRAS/STK11* groups had significantly lower monocytic-DCs abundances compared to the WT and *KRAS* groups. These findings from MCP-counter are similar to the CIBERSORT findings for reduced M1 macrophage and resting DC relative fractions. MCP-counter analysis also showed lower T cell abundances (encompassing $CD4^+$, $CD8^+$ and γδ T cells) in TCGA patients in the *KRAS/STK11* mutation group compared to the WT group (p = 0.0009). These findings from CIBERSORT and MCP-counter show that *STK11* mutant tumours and especially those with concurrent *KRAS/STK11* mutations often have reduced leukocyte infiltrates compared to WT.

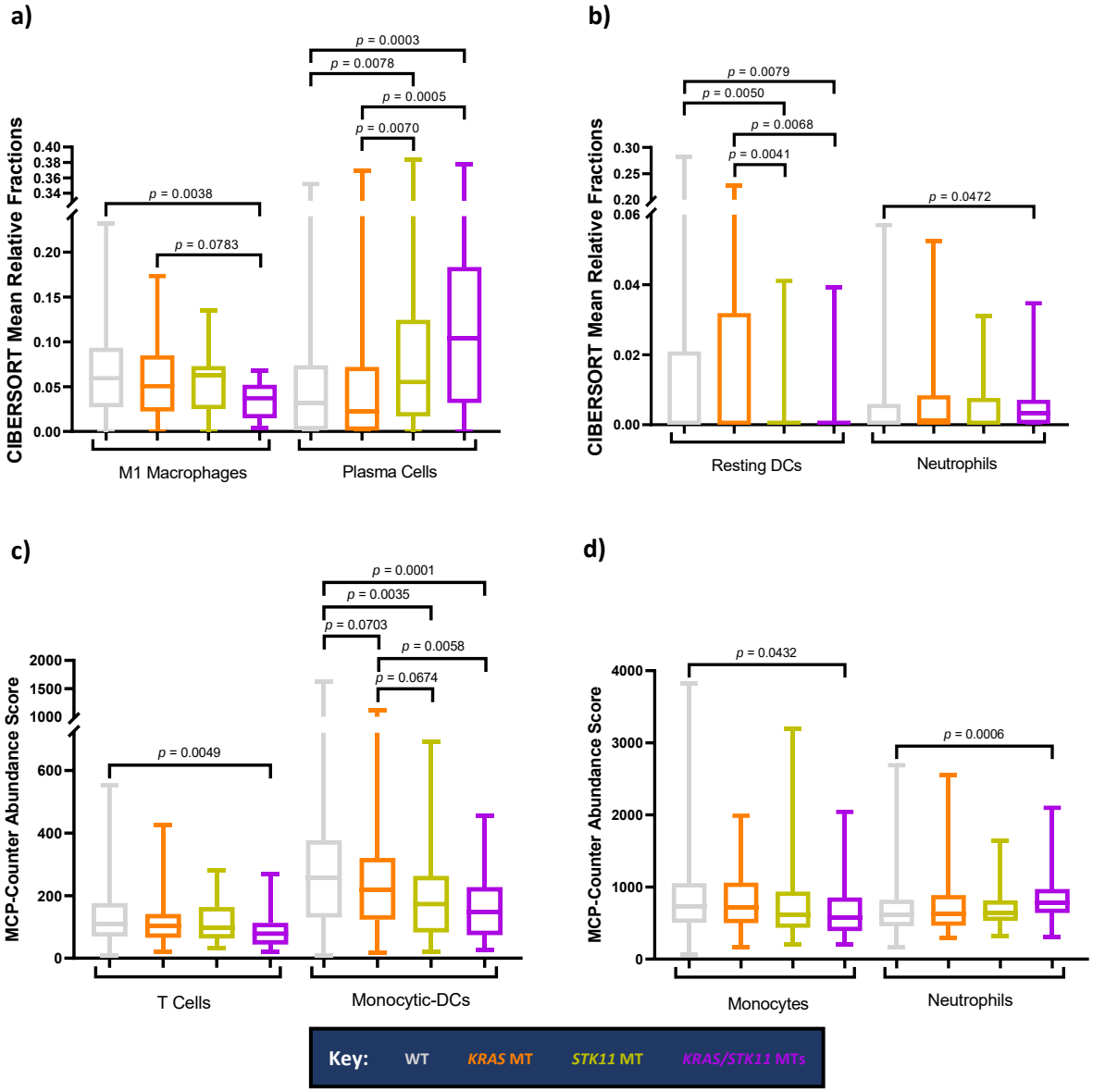

Figure 3.3 Significant results from CIBERSORT and MCP-counter immune deconvolutions

a) b) CIBERSORT mean relative fractions (using only fully deconvoluted TCGA samples at $p \leq 0.05$ as recommended by CIBERSORT) were grouped by mutation (MT). **c) d)** MCP-counter abundance scores were grouped by MT. All statistical comparisons by unpaired two-sample Wilcoxon tests.

3.2.2 The Relationship Between *KRAS* and *STK11* Alterations and *RORC* Expression

In the context of the overall immune suppression already highlighted, the only conserved significantly upregulated immune gene examined in patients with *KRAS* mutations and *STK11* mutations was *RORC* (Figures 3.1 and 3.2). Interestingly, *RORC* expression was also significantly higher in the *KRAS/STK11* mutation group compared to the WT group ($p \leq$

0.0001), and this upregulation was enhanced compared to both the *KRAS* and *STK11* mutation groups (Figure 3.4a).

RORC has two closely related major transcriptional variants *RORC1* and *RORC2* which differ in their N-terminus sequences and result in the protein products RORγ and RORγT respectively. RORγT is of particular interest in studies of the tumour immune microenvironment as it is expressed in immune subsets including Th17 cells, a type of $CD4^+$ T cell. The cBioPortal mRNA expression data from TCGA unfortunately does not describe which variant has been profiled. We therefore further investigated this by interrogating the Schabath *et al* (316) dataset.

This dataset reports *RORC2* but not *RORC1*, so we were able to verify that *RORC2* expression is upregulated in patients with these mutations (Figure 3.4b). We also validated our *RORC* findings from TCGA 2014 dataset (*n* = 230) with a larger LUAD dataset called TCGA PanCancer (*n* = 566) (310). Again, we found that *RORC* was significantly increased in the *KRAS* mutation group, *STK11* mutation group and *KRAS/STK11* mutation group in comparison to the WT group (Figure 3.4c).

The waterfall plot created from data from TCGA PanCancer (Figure 3.4d) shows the distribution of *RORC* mRNA expression z-scores in patients with or without our cancer gene mutations of interest. The coloured bars representing patients with *KRAS*, *STK11* and *KRAS/STK11* mutations are clearly more highly distributed towards the right side of the plot, mostly falling into the top two z-score quartiles. Most of the patients with our mutations of interest were in the first *RORC* expression z-score quartile (33.9% of *KRAS* mutation group patients, 43.2% of *STK11* mutation group patients and 50% of *KRAS/STK11*

mutation group patients), and a minority of patients with mutations of interest were in the fourth quartile (12.7% of *KRAS* mutation patients, 16.2% of *STK11* mutation patients and 11.1% of *KRAS/STK11* mutation patients). 28% of patients with *KRAS/STK11* mutations and 27% of patients with *STK11* mutations have high z-scores of over 3. These observations demonstrate that *RORC* expression in patients with *STK11* and *KRAS/STK11* mutations is much higher than the overall LUAD population and emphasise the importance of dual *KRAS/STK11* mutations.

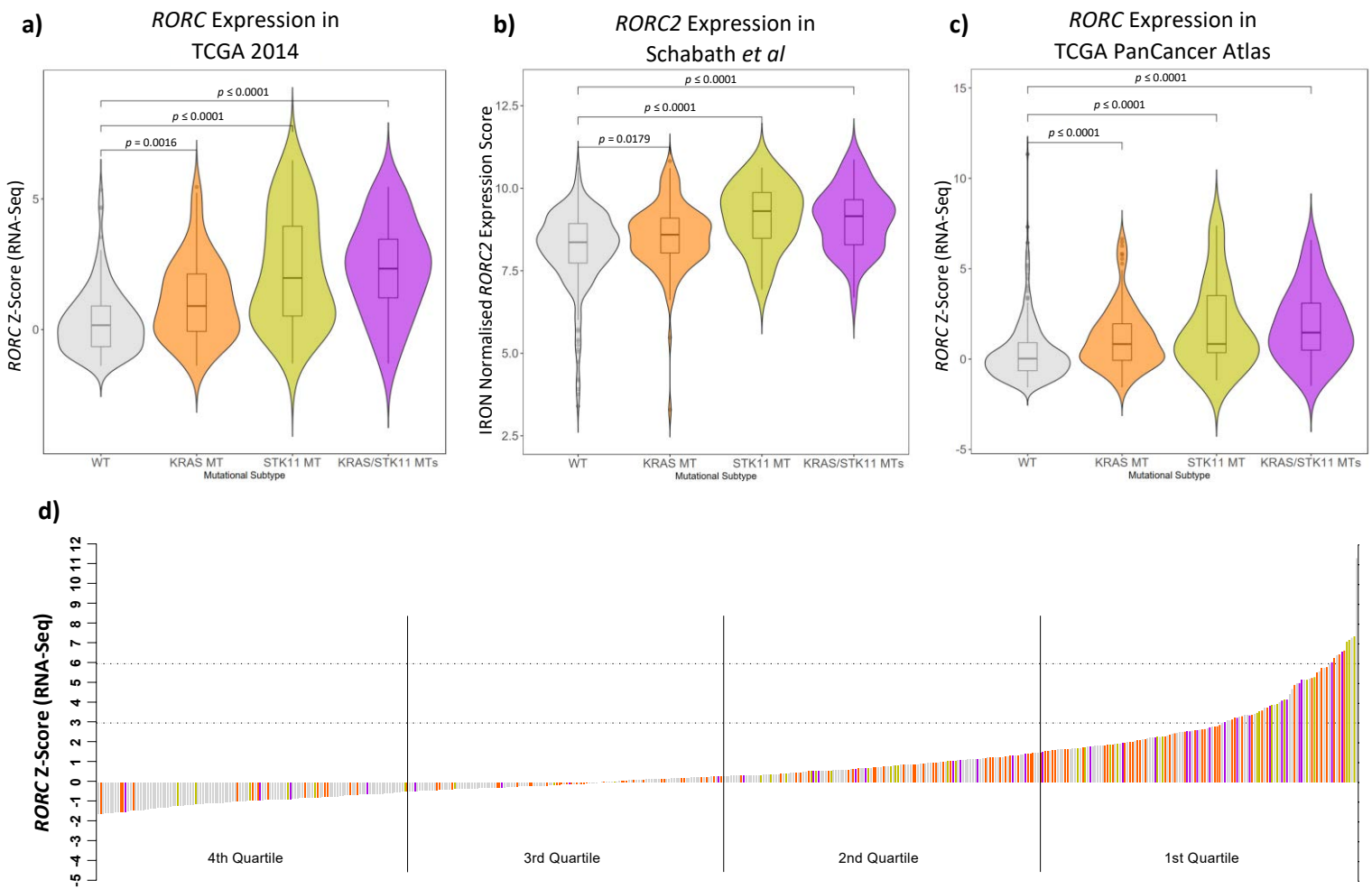
a)
RORC Expression in TCGA 2014
RORC Z-Score (RNA-Seq)
p ≤ 0.0001
p ≤ 0.0001
p = 0.0016
WT
KRAS MT
STK11 MT
KRAS/STK11 MTs
Mutational Subtype
b)
RORC2 Expression in Schabath et al
IRON Normalised RORC2 Expression Score
p ≤ 0.0001
p ≤ 0.0001
p = 0.0179
WT
KRAS MT
STK11 MT
KRAS/STK11 MTs
Mutational Subtype
c)
RORC Expression in TCGA PanCancer Atlas
RORC Z-Score (RNA-Seq)
p ≤ 0.0001
p ≤ 0.0001
p ≤ 0.0001
WT
KRAS MT
STK11 MT
KRAS/STK11 MTs
Mutational Subtype
d)
RORC Z-Score (RNA-Seq)
4th Quartile
3rd Quartile
2nd Quartile
1st Quartile

Figure 3.4 *RORC* expression upregulation in patient tumours with *KRAS* and *STK11* MTs in TCGA and Schabath *et al* datasets

a) *RORC* expression z-scores from TCGA 2014 patients were grouped by MT. **b)** *RORC2* IRON expression scores from Schabath patients were grouped by MT. **c)** *RORC* expression z-scores from TCGA PanCancer Atlas patients were grouped by MT. **d)** *RORC* expression z-scores from TCGA PanCancer patients were plotted in a waterfall style and coloured by MT (grey = WT, orange = *KRAS* MT, gold = *STK11* MT and purple = *KRAS/STK11* MT). All statistical comparisons by unpaired two-sample Wilcoxon tests.

We were next interested in investigating whether raised *RORC* expression is linked to *KRAS* and *STK11* CNAs, as well as to KRAS and LKB1 protein changes. *KRAS* mutations tend to result in a gain of function, as such *KRAS* can be subject to chromosomal amplification which may result in increased protein expression. In contrast *STK11* mutations tend to cause of loss of function in its encoded protein, LKB1. Therefore, *STK11* CNAs tend to be deleterious and the LKB1 protein may be lost via copy number loss or by epigenetic silencing (376). Using TCGA data we assessed protein changes by RPPA z-scores and putative CNAs scored by the GISTIC algorithm. As outlined in Chapters 2.1.5 and 2.1.6, we defined an RPPA z-score cut off for protein changes and used the GISTIC scoring range from -2 to +2 at integer intervals. -2 GISTIC scores represent deep deletions (likely homozygous deletions), -1 represents a shallow loss (likely heterozygous deletion), 0 signifies diploid with no CNA, +1 shows a low-level gain and +2 represents a focal high-level amplification.

None of TCGA patients had high-level *STK11* amplification GISTIC scores of +2, as expected as *STK11* alterations are associated with loss of function, and many had GISTIC scores of <0. We found that *RORC* gene expression was significantly increased in TCGA patients with *STK11* GISTIC scores of -1, compared to samples with no *STK11* loss (*STK11* GISTIC scores

0/+1) (Figure 3.5a). There were no differences in *RORC* in the *STK11* GISTIC -2 group alone, but this only contained 3 TCGA patients. *RORC* is also associated with protein changes and is significantly increased in cases with LKB1 protein downregulation (Figure 3.5b). Both of these findings matched the previous findings in which we grouped patients by *STK11* mutations.

Similar examination of *KRAS* CNAs showed that there were no TCGA patients with deleterious -2 GISTIC scores, again as expected as *KRAS* alterations are associated with gain of function. Rather, most patients had *KRAS* amplifications. Interestingly, the results from the CNA (Figure 3.5c) and protein (Figure 3.5d) comparisons were unexpected as TCGA patients with *KRAS* GISTIC scores of +1 showed significantly decreased *RORC* gene expression in comparison to patients with no *KRAS* gain (*KRAS* GISTIC scores 0/-1). There were no differences in *RORC* expression in the *KRAS* GISTIC +2 group and the no *KRAS* gain group, despite the *KRAS* GISTIC +2 group containing 29 patients. Similarly, there were no differences in *RORC* expression between the KRAS protein upregulation group and the no KRAS change group, despite there being 28 patients in the KRAS protein upregulation group. *KRAS* mutations are clearly associated with increased *RORC* expression, but these findings suggest that *RORC* expression may not be directly linked to *KRAS* CNA or KRAS protein expression.

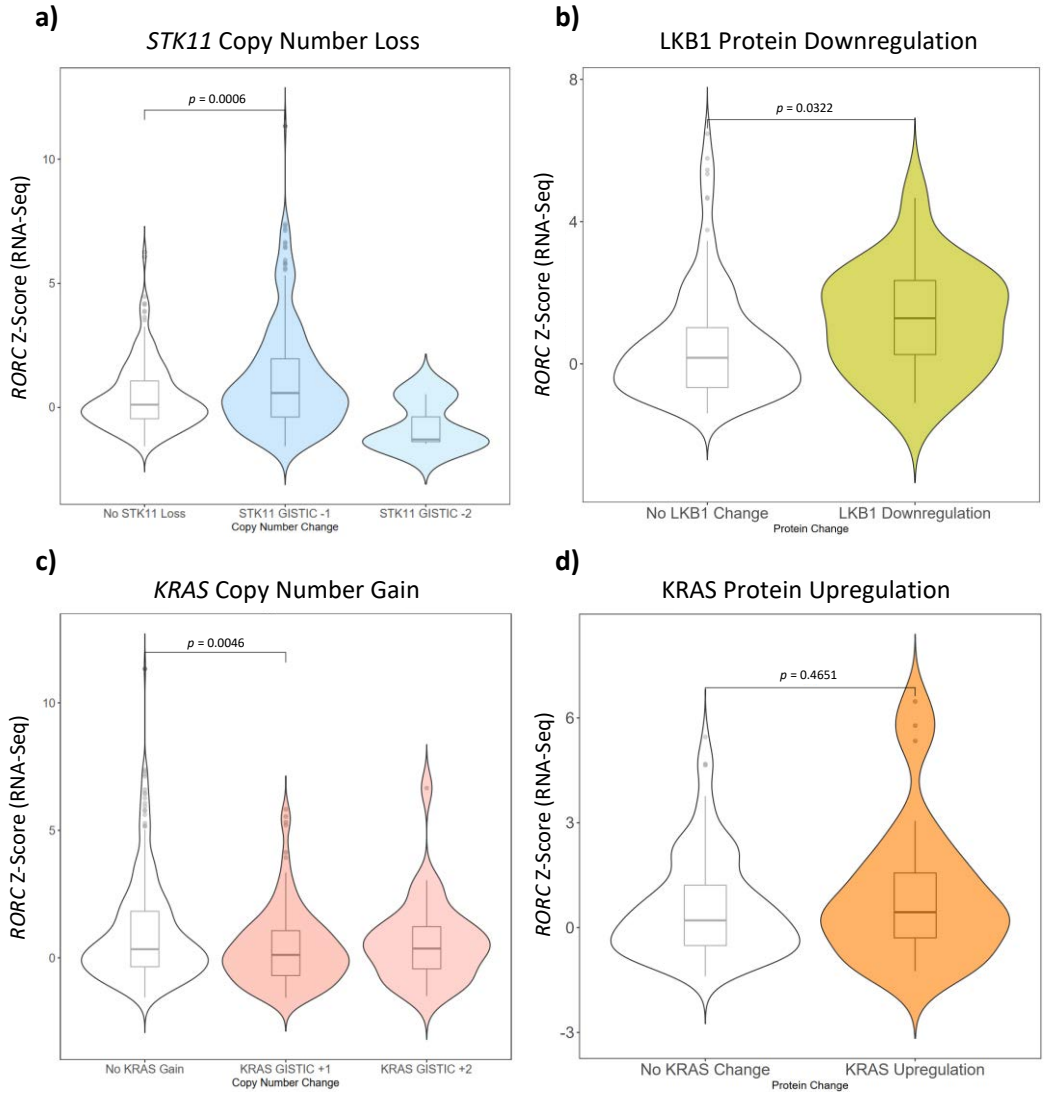

Figure 3.5 *RORC* expression in TCGA PanCancer patient tumours grouped by putative *KRAS* and *STK11* CNAs or protein change

a) *RORC* mRNA expression z-scores were grouped by *STK11* GISTIC scores. The 'no *STK11* loss' group contains *STK11* GISTIC scores of 0 and +1. **b)** *RORC* expression z-scores were grouped by LKB1 protein change. The 'no LKB1 change' group are TCGA samples with LKB1 RPPA z-scores of > -1, the 'LKB1 downregulation' group have LKB1 RPPA z-scores of ≤ -1. **c)** *RORC* expression z-scores were grouped by *KRAS* GISTIC scores. The 'no *KRAS* gain' group contains *KRAS* GISTIC scores of 0 and -1. **d)** *RORC* expression z-scores were grouped by KRAS protein change. The 'no KRAS change' group are TCGA samples with KRAS RPPA z-scores of < +1, the 'KRAS upregulation' group have KRAS RPPA z-scores of ≥ +1. All statistical comparisons by unpaired two-sample Wilcoxon tests.

We were next interested in comparing gene expression changes in patients with both CNAs and mutations impacting the same cancer gene. As both alterations should have an impact on cancer gene expression, we examined *KRAS* and *STK11* mRNA expression

alongside *RORC* mRNA expression. Figure 3.6a shows that *KRAS* gene expression is higher in patients with *KRAS* mutations (orange bars) compared to patients without *KRAS* mutations (black bars), when comparing patients without *KRAS* CNAs (*KRAS* GISTIC score 0) ($p \leq 0.0001$). Comparing patients with *KRAS* gains (*KRAS* GISTIC score of +1) again shows that those with concurrent mutations have significantly higher *KRAS* expression compared to those without *KRAS* mutations ($p = 0.0056$). Although there was no difference in *KRAS* expression in patients with or without mutations who have *KRAS* GISTIC scores of +2. Comparing the effect of CNAs on *KRAS* expression shows that increasing GISTIC scores – representing increased *KRAS* copy number – causes significantly increased *KRAS* expression in patients with *KRAS* mutations ($p = 0.0073$ for GISTIC scores 0 vs +1, $p = 0.0019$ for GISTIC scores +1 vs +2).

Figure 3.6b examines *RORC* gene expression. Similarly, *RORC* expression is increased in patients with *KRAS* mutations compared to those without *KRAS* mutations, when comparing patients with *KRAS* GISTIC scores of 0 ($p \leq 0.0001$), +1 ($p = 0.0010$) and +2 ($p = 0.0682$). Comparing the effect of *KRAS* CNAs on *RORC* expression in patients with *KRAS* mutations shows a similar finding to Figure 3.5c that *RORC* expression is significantly decreased in the *KRAS* GISTIC +1 group compared to the *KRAS* GISTIC 0 group ($p = 0.0416$). There was no difference in *RORC* expression in patients with *KRAS* mutations in the *KRAS* GISTIC +1 and +2 groups.

For patient tumours with *STK11* mutations (gold bars), significantly lower *STK11* gene expression was seen compared to patients without *STK11* mutations (black bars) in both groups of *STK11* CNAs ($p = 0.0054$ for the *STK11* GISTIC score 0 comparison, $p = 0.0005$ for

the *STK11* GISTIC score -1 comparison) (Figure 3.6c). Comparing the effect of CNAs on *STK11* expression showed that patients with concurrent mutations in the *STK11* GISTIC -1 group had significantly lower *STK11* expression than patients with mutations in the *STK11* GISTIC 0 group ($p = 0.0305$).

Figure 3.6d shows that *RORC* gene expression is increased in patients with *STK11* mutations compared to those without *STK11* mutations, when comparing patients with *STK11* GISTIC scores of 0 ($p = 0.0019$) and patients with *STK11* GISTIC scores of -1 ($p = 0.0019$). Although, there was no difference in *RORC* expression in patients with *STK11* mutations in the *STK11* GISTIC 0 and -1 groups.

These data show that *KRAS* and *STK11* cancer gene mutations have an additional effect on the expression of *KRAS*, *STK11* and *RORC*, above CNAs alone. Presence or absence of *KRAS* and *STK11* mutations is of a greater importance to *RORC* expression levels than CNAs.

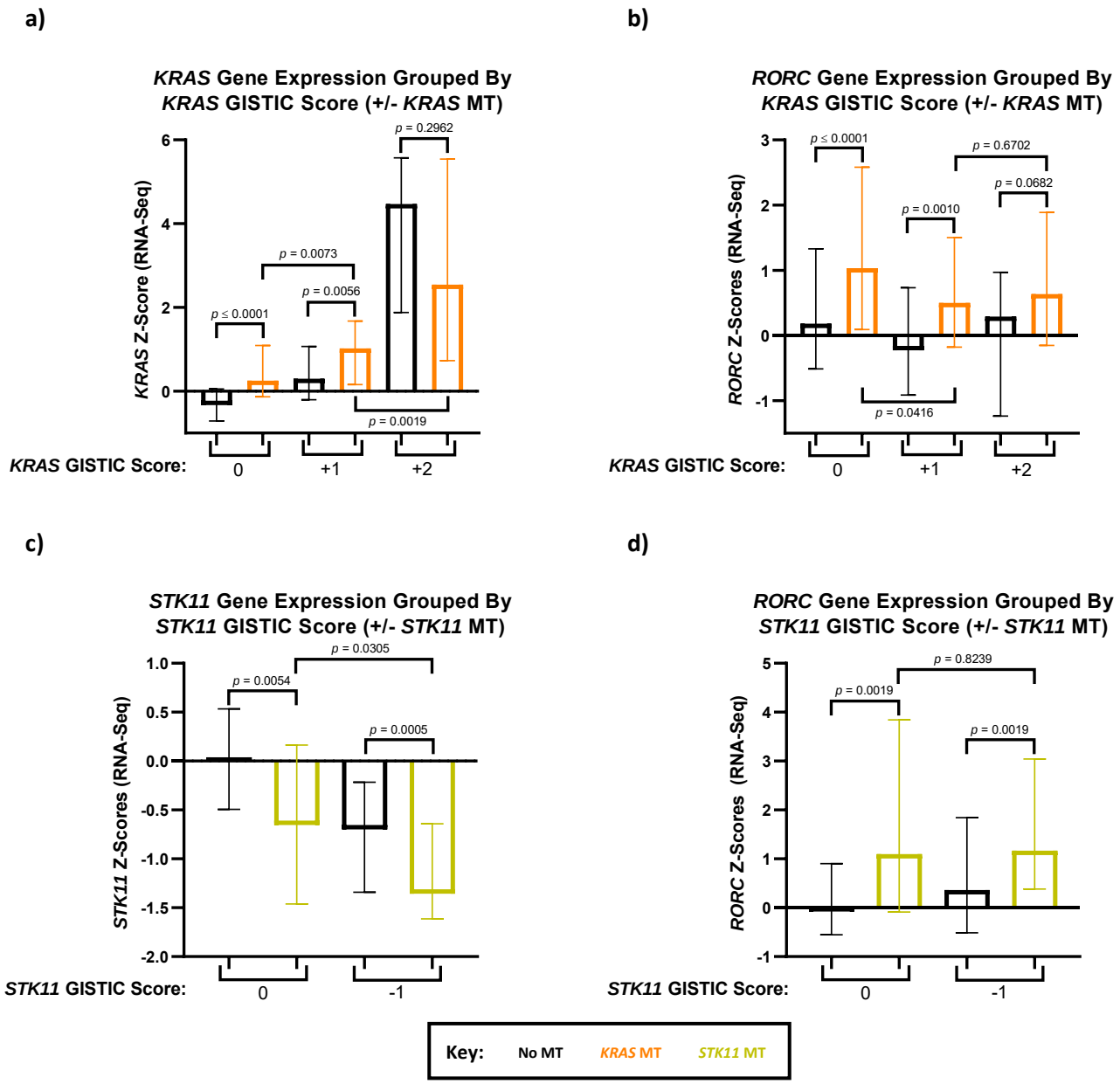

Figure 3.6 Impact of *KRAS* and *STK11* CNAs and mutations on *KRAS*, *STK11* and *RORC* expression

a) Patients were grouped by *KRAS* GISTIC scores and mutations. Orange group bars signify *KRAS* mutations and black group bars signify no *KRAS* mutation. Bar charts show median *KRAS* expression z-scores, and error bars show interquartile range. **b)** same as **a)** except the bar charts show median *RORC* expression z-scores. **c)** Patients were grouped by *STK11* GISTIC scores and mutations. Gold group bars signify *STK11* mutations and black group bars signify no *STK11* mutation. Bar charts show median *STK11* expression z-scores, and error bars show interquartile range. **d)** same as **c)** except the bar charts show median *RORC* expression z-scores. All statistical comparisons by unpaired two-sample Wilcoxon tests.

3.2.3 Amplification of the *RORC* Locus Chromosome 1q21.3 in Lung Adenocarcinoma

Given our clear observation of *RORC* overexpression in *KRAS* and *STK11* mutation groups, we were interested in determining whether there were any associated genetic aberrations in the *RORC* gene itself. Out of the 566 TCGA cases, only one patient (without any *KRAS* or *STK11* mutations) was found to have a C-terminal monoallelic missense mutation (E511D) with unknown functional significance. Although *RORC* itself does not appear to be a hotspot for cancer related mutations, we learned from the literature that its chromosomal locus 1q21.3 is frequently amplified in several carcinomas including LUAD (377-380). The 1q21.3 locus is amplified in around 15-30% of LUAD cases, although this is not specific to the 1q21.3 as instability throughout the 1q long arm is extremely common (35-80% LUADs) (381-385).

We therefore examined *RORC* CNAs in TCGA (Table 3.2), finding that *RORC* GISTIC +1 low-level gains are very common (63.3% cases) and *RORC* GISTIC +2 focal amplifications are also present in 9.9% of cases. Figure 3.7 demonstrates that *RORC* gains and amplifications have a significant functional effect on the level of *RORC* mRNA expression, with a particularly pronounced increased *RORC* z-scores in the *RORC* +2 GISTIC score group compared to the 'No *RORC* Gain' group (*RORC* GISTIC scores of 0 and -1).

To establish whether *RORC* CNAs are representative of focal 1q21.3 amplifications, we assessed the degree of correlation between *RORC* expression and expression of other 1q21.3 genes and non-1q21.3 genes. There was no correlation between *RORC* and *ECM1*, a gene from the 1q21.2 sub-band which is only 87,062 bases away from the start of 1q21.3 (Figure 3.8). Similarly, there were no gene expression correlations between *RORC*

and the *PDE4DIP* gene which is further away from *RORC* but is still on the same chromosome (1q21.2 but closer to 1q21.1), and no correlation with *CYP2E1* gene expression which is found on a different chromosome (10q26.3). Although, when we compared *RORC* to other 1q21.3 genes, as shown in Figure 3.8, we started to observe gene expression correlations. *SELENBP1* and *THEM4* are very close to *RORC* (433,346 bases from *RORC* start and 38,415 from *RORC* end respectively) and the levels of expression of both genes are significantly positively correlated with the level of *RORC* expression. We also found *RORC* expression to be significantly correlated with genes located at the opposite end of the sub-band including *ZBTB7B* (3,170,177 bases from *RORC* end). The correlations we have witnessed indicate a general amplification of the 1q21.3 locus rather than a specific amplification of the *RORC* gene, and allow *RORC* to be used as a potential surrogate for focal 1q21.3 amplifications and copy number gains.

RORC GISTIC Score	Percentage Frequency in TCGA PanCancer	Number of TCGA PanCancer Patients (*n* = 507)
GISTIC +2	9.9%	50
GISTIC +1	63.3%	321
GISTIC 0	25%	127
GISTIC -1	1.8%	9
GISTIC -2	0%	0

Table 3.2 Frequency of *RORC* CNAs in TCGA PanCancer data

Data from TCGA PanCancer dataset. Percentages calculated from the total number of patients in the series.

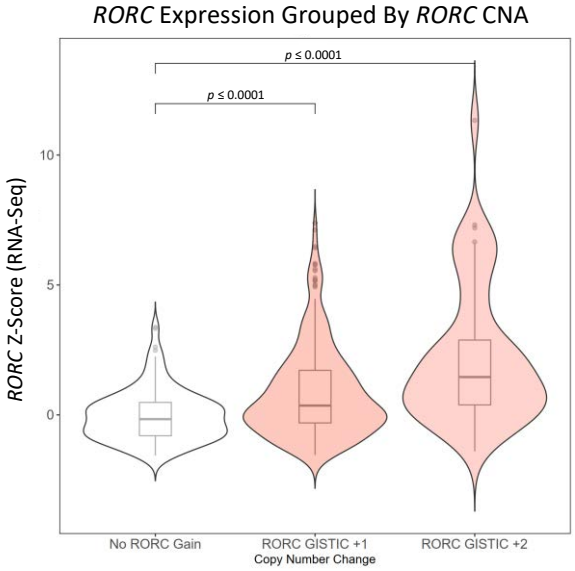

Figure 3.7 *RORC* mRNA expression grouped by *RORC* GISTIC scores

TCGA PanCancer patients grouped by GISTIC scores. The 'no *RORC* gain' group has patients with *RORC* GISTIC scores of 0 and -1. Comparisons by unpaired two-sample Wilcoxon tests.

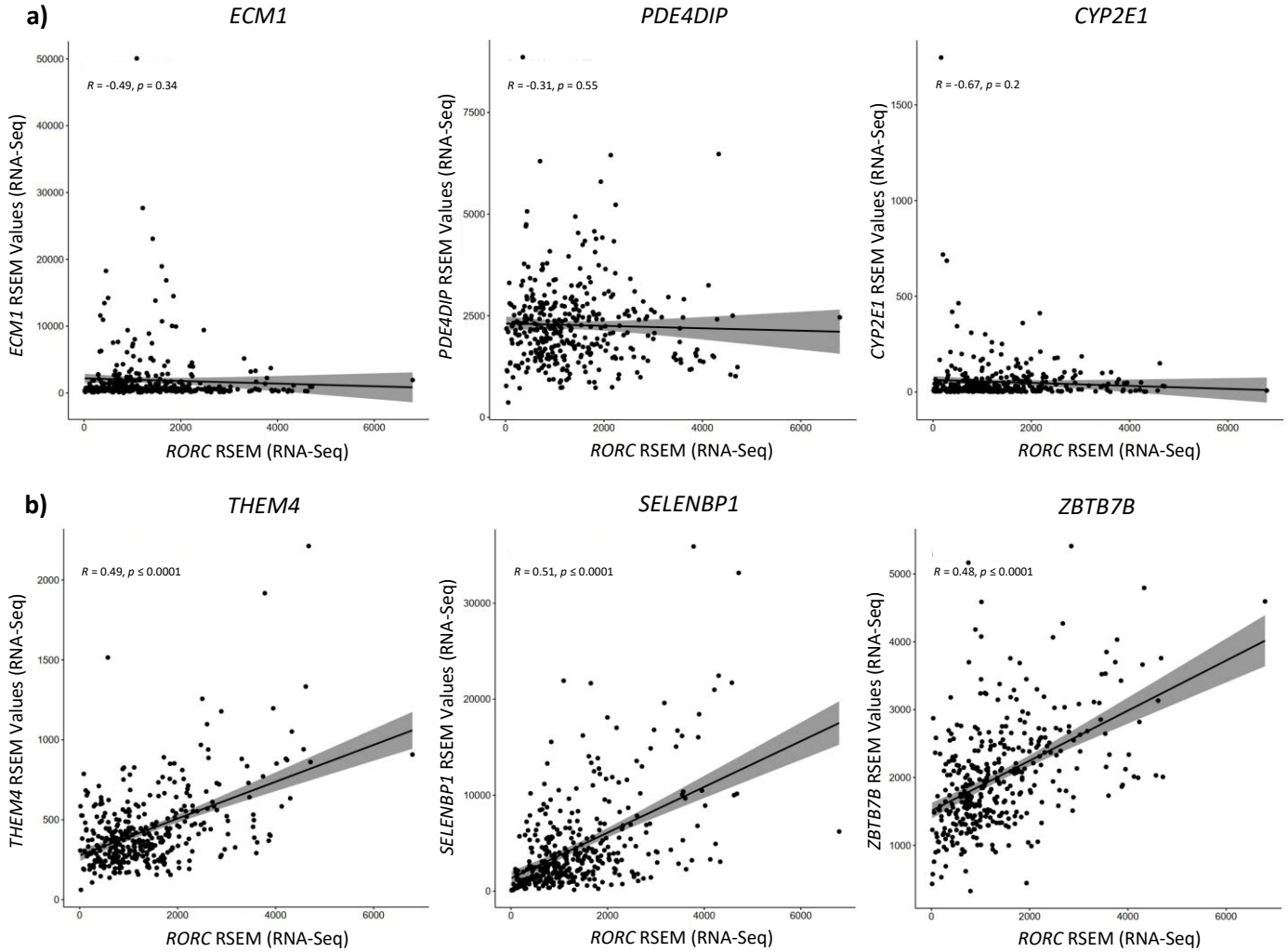

Figure 3.8 Correlation between gene expression of *RORC* and other 1q21.3 or non-1q21.3 genes

Pearson correlations using TCGA PanCancer RSEM data between *RORC* and **a)** non-1q21.3 genes, and **b)** other 1q21.3 genes.

To understand whether the increased *RORC* in patient tumours with *KRAS* and *STK11* mutations were entirely a result of 1q21.3 amplifications, we studied the association between 1q21.3 amplifications and these cancer genes using *RORC* CNAs as a marker of 1q21.3 amplifications.

We therefore investigated whether *RORC* CNAs – which can represent potential 1q21.3 amplifications – are associated with mutations in the *KRAS* and *STK11* cancer genes. Table 3.3 shows increased frequencies of *RORC* GISTIC scores of +1 and +2 in patients with these cancer gene mutations and decreased GISTIC 0 scores. Fisher's Exact tests performed on the data from Table 3.3 (H_0: *RORC* CNA GISTIC score is not associated with cancer gene mutation group, H_1: *RORC* CNA GISTIC score is associated with cancer gene mutation group), show a rejection of H_0 when comparing WT TCGA patients (no *KRAS* or *STK11* mutations) vs MT patients (with *KRAS* or *STK11* mutations) ($p = 0.0052$) and also when specifically comparing WT patients against those with concomitant mutations in *KRAS/STK11* ($p \leq 0.0001$). We failed to reject H_0 when comparing the WT vs *KRAS* groups and the WT vs *STK11* groups. This shows that *RORC* CNA GISTIC scores, potentially representing 1q21.3 amplifications, have a significant association with *KRAS* and *STK11* mutations.

Frequency by Genotype	GISTIC -1	GISTIC 0	GISTIC +1	GISTIC +2
WT: % (*n*)	2.2% (7)	29% (91)	59.9% (188)	8.9% (28)
KRAS MT: % (*n*)	0.8% (1)	24.6% (29)	65.3% (77)	9.3% (11)
STK11 MT: % (*n*)	2.6% (1)	15.8% (6)	68.4% (26)	13.2% (5)
KRAS/STK11 MTs: % (*n*)	0% (0)	2.7% (1)	81.1% (30)	16.2% (6)

Table 3.3 Frequencies of *RORC* GISTIC CNA scores by *KRAS* and/or *STK11* mutations

TCGA PanCancer patients with *RORC* GISTIC scores were grouped into presence of *KRAS*, *STK11* or concomitant *KRAS/STK11* mutations. Fisher's Exact tests were performed on the raw numeric data.

Given the association between *RORC* CNAs and mutations in the *KRAS* and *STK11* genes, we wanted to determine whether *RORC* putative gains and amplifications entirely accounted for this increased *RORC* expression in the *KRAS* and *STK11* mutation groups. We therefore removed TCGA samples with *RORC* GISTIC scores of +1/+2 or just of +2 and re-compared *RORC* expression between our mutation groups. Removing patients with all putative *RORC* gains and amplifications (GISTIC scores of +1/+2) (Figure 3.9a) resulted in non-significant increases in *RORC* expression in patients with *KRAS* mutations and *STK11* mutations compared to WT. Note that removing all the potential *RORC* gains and amplifications resulted in a *KRAS/STK11* mutation group with 1 patient which was therefore excluded and an *STK11* mutation group containing only 8 patients.

Removing only patients with *RORC* high-level amplifications (GISTIC score of +2), which are likely those with true amplifications, from these analyses (Figure 3.9b) left greater

patient numbers per group and *RORC* expression was still significantly higher for all *KRAS* and *STK11* mutation groups against WT, similar to our previous findings in Figure 3.4.

We then performed similar investigations for *KRAS* and *STK11* CNAs. Removing patients with *RORC* GISTIC scores of +1/+2 (Figure 3.9c) or just patients with *RORC* GISTIC +2 (Figure 3.9d) showed decreased *RORC* expression in the patients in the *KRAS* GISTIC +1 group compared to the no *KRAS* gain group (p = 0.0069 Figure 3.9c, p = 0.0009 Figure 3.9d). These findings are similar to the unexpected observations in Figure 3.5c.

With regard to *STK11*, removing patients with *RORC* GISTIC scores of +1/+2 resulted in no difference in *RORC* expression between the *STK11* GISTIC -1 group and the no *STK11* loss group (Figure 3.9c). Removing patients with only *RORC* GISTIC scores of +2 again left greater numbers of patients per group, and the *STK11* GISTIC -1 group had significantly increased *RORC* expression compared to the no *STK11* loss group (p = 0.0031) (Figure 3.9d). No differences were found in the *STK11* GISTIC -2 group due to low sample number (n = 3).

Together, these results show that even when patients with increased copies of *RORC* (potentially signifying patients with 1q21.3 amplifications) are removed from the analysis, *RORC* expression is still increased in patients with *KRAS* and *STK11* mutations and patients with *STK11* loss. This is not as pronounced an increase as in Figures 3.4 and 3.5, suggesting that higher *RORC* copy number boosts *RORC* expression. Nevertheless, *RORC* expression is still increased in the absence of CNAs in *RORC* itself.

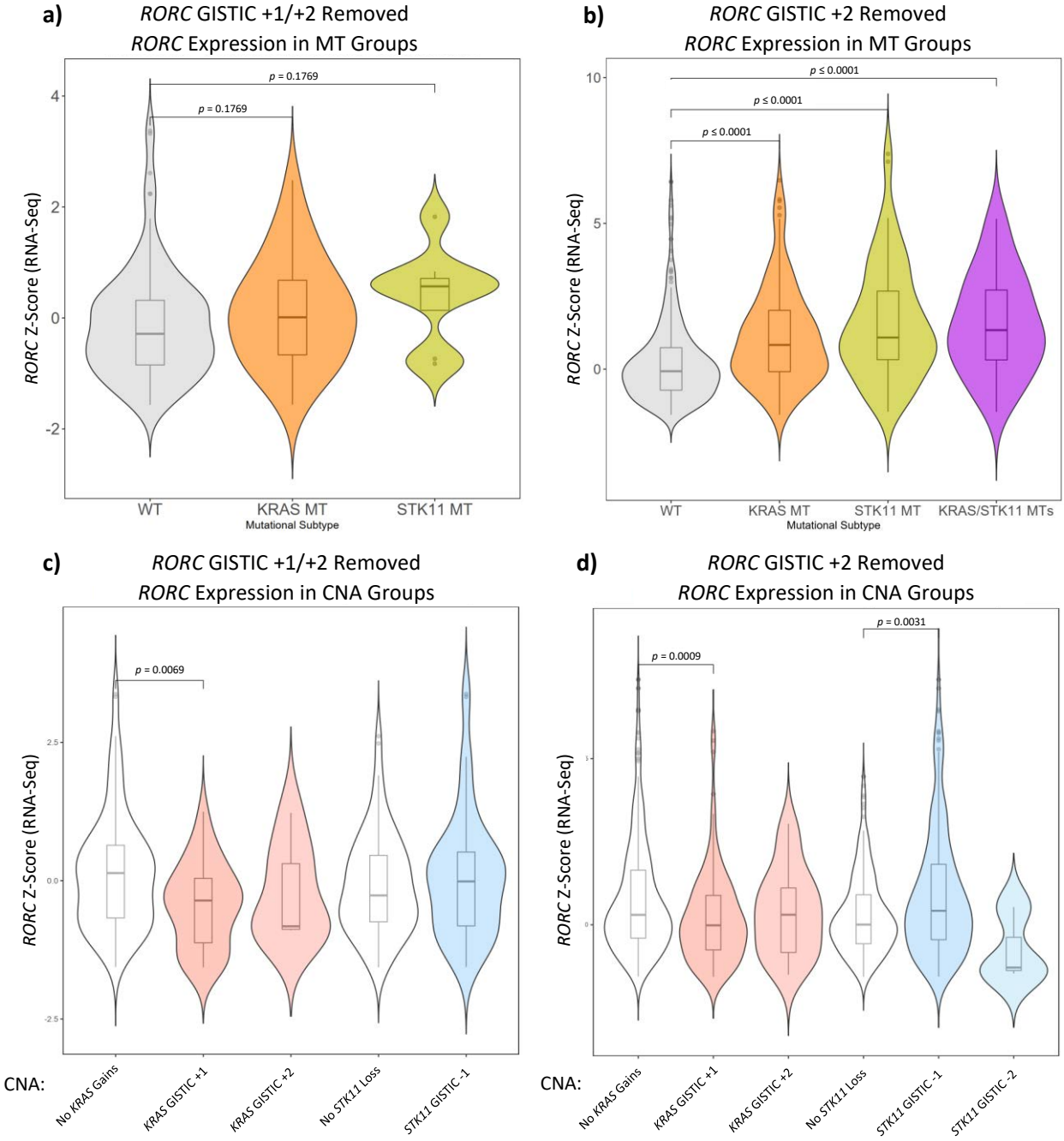

Figure 3.9 Effect of removing *RORC* CNAs on *RORC* expression delineated by *KRAS* and *STK11* MTs and CNAs

a) TCGA PanCancer patients with *RORC* GISTIC scores of +1 and +2 were omitted, then *RORC* z-scores were grouped by MT. **b)** same as **a)** except patients with *RORC* GISTIC scores of +2 were omitted. **c)** same as **a)** except *RORC* z-scores were grouped by *KRAS* and *STK11* GISTIC scores. The 'no *KRAS* gains' group consists of *KRAS* GISTIC scores of 0 and -1 and the 'no *STK11* loss' group consists of *STK11* GISTIC scores of 0 and +1. After removing *RORC* GISTIC scores of +1/+2 there

were no patients with *STK11* GISTIC scores of -2. **d)** same as **c)** except patients with *RORC* GISTIC scores of +2 were omitted. All statistical comparisons by unpaired two-sample Wilcoxon tests.

We were next interested in examining whether *RORC* gene expression had an impact on TCGA patient overall survival (OS). Patients were grouped by the *RORC* expression z-scores quartiles as shown in Figure 3.4d, and Kaplan-Meier curves were plotted to compare OS (Figure 3.10). Patients with '*RORC* Low' expression (quartile four) had a near-significant reduction OS (p = 0.0586) compared to patients in the quartiles two and three grouped as '*RORC* Other' (Figure 3.10a). Comparing all three groups ('*RORC* High', '*RORC* Other' and '*RORC* Low') showed no difference in OS, but the '*RORC* High' (quartile one) curves were very similar (Figure 3.10b).

To assess whether increased *RORC* expression through 1q21.3 amplifications impacted OS, we again removed patients with *RORC* GISTIC scores of +2. By doing this we found similar results as Figures 3.10a and 3.10b, with almost identical Kaplan-Meier curves (Figure 3.10c and 3.10d).

Removing patients with *RORC* GISTIC scores of +1/+2 again showed similar curves (Figure 3.10e and 3.10f), but the lower numbers of patients in these analyses resulted in higher p values.

Together, these data suggest that low *RORC* mRNA expression is associated with a reduced OS and that 1q21.3 mediated *RORC* gains or amplifications do not change this survival pattern.

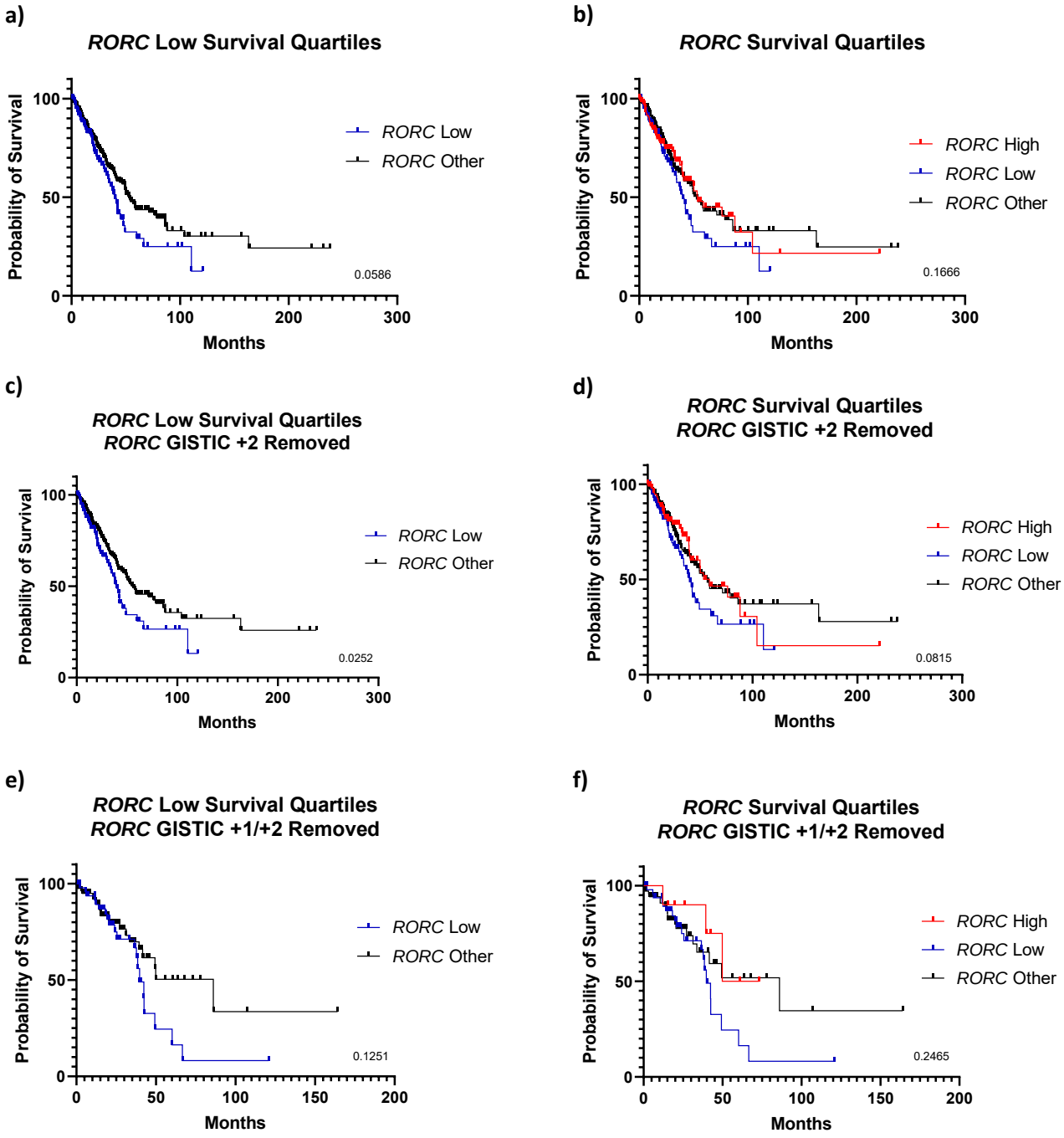

Figure 3.10 The impact of *RORC* expression on TCGA PanCancer patient survival

Kaplan-Meier curves of patients divided into the *RORC* expression quartiles from Figure 3.4d. The '*RORC* High' group represents patients in 1st quartile, the '*RORC* Other' group represents patients in the 2nd and 3rd quartiles, and the '*RORC* Low' group represents patients in the 4th quartile. OS was calculated from cancer diagnosis to death or last follow up and plotted as Kaplan-Meier curves then statistically compared using Mantel-cox tests. **a)** and **b)** show all patients, with **b)** also comparing the '*RORC* High' group. **c)** and **d)** remove patients with *RORC* CNA GISTIC scores of +2 from the analysis, with **d)** also comparing the '*RORC* High' group. **e)** and **f)** remove patients with *RORC* CNA GISTIC scores of +1 and +2, with **f)** also comparing the '*RORC* High' group.

3.2.4 Investigating *RORC* Expression in the Context of *KRAS* Isogenic Cell Lines

Having established a link between *KRAS* and *STK11* mutations and increased *RORC* expression, we looked for a system in which we could investigate whether mutations in these cancer genes directly potentiates increased *RORC* expression. For this purpose, we searched for data from isogenic cell lines coming across data from Stolze *et al* (72). This group established isogenic lines with and without *KRAS* G12D and G13D mutations from which they had compared mRNA expression by microarray. Unfortunately, we did not find any appropriate datasets investigating *STK11* isogenic cell lines.

Using the data from Stolze *et al* (72) we compared levels of gene expression in the WT and *KRAS* mutant isogenic cell lines. As expected, there was no change in the expression of the housekeeping gene *GAPDH*, and we could recreate their finding that introducing *KRAS* mutations causes increased expression of the *PYGL* gene (Figure 3.11). Interestingly, we observed no changes in *RORC1* or *RORC2* expression. However, we did find that *KRAS* mutations induced the expression of an IL-17 family member *IL17C* ($p \leq 0.0001$) (Figure 3.12a). This is particularly interesting as IL-17C and its receptor IL-17RE have been shown to support the differentiation of RORγT^{+} Th17 cells (386). As *IL17C* was not included in our exploration of LUAD cancer gene immune gene signatures, we re-examined TCGA PanCancer data and found increased expression of *IL17C* (Figure 3.12b) and its receptor *IL17RE* (Figure 3.12c) (both $p \leq 0.0001$). Although the introduction of *KRAS* mutations did not increase *RORC1* or *RORC2* in this system, *KRAS* mutations may cause regulation of the IL-17C axis.

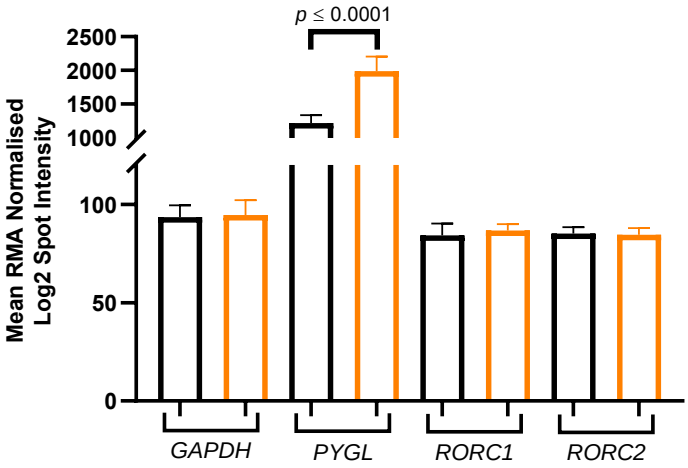

Figure 3.11 Examining the effect of *KRAS* MT isogenic introduction on gene expression

Data from Stolze *et al* (72). The black coloured bars are a control group (triplicates of WT and empty vector samples) and orange bars are a *KRAS* introduced group (triplicates of *KRAS* G12C and *KRAS* G12D samples). Microarray RMA normalised log2 spot intensity values were averaged per group and compared by paired *t* test.

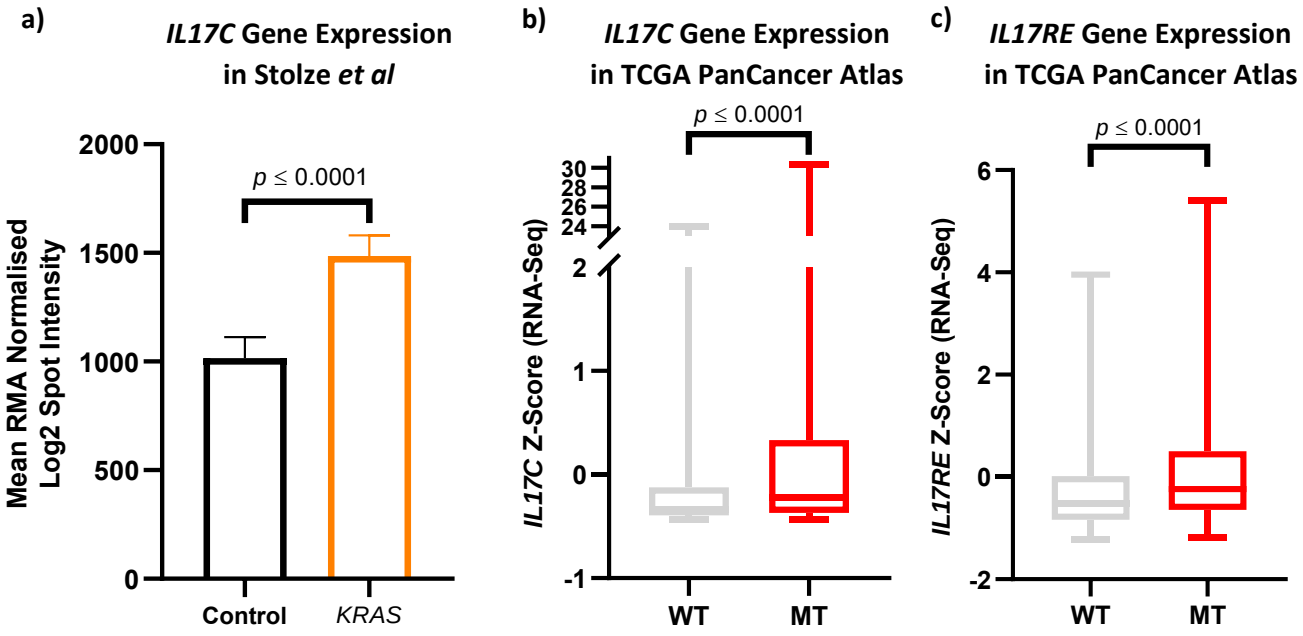

Figure 3.12 *IL17C* and *IL17RE* expression inductions in isogenic cells with *KRAS* MTs

a) *IL17C* data from Stolze *et al* (72) were grouped and compared as described in Figure 3.11. **b)** Shows *IL17C* mRNA expression z-score data from TCGA PanCancer, and **c)** shows *IL17RE* mRNA expression z-score data from TCGA PanCancer. **b) c)** compare the MT group of patients with *KRAS* and *STK11* MTs to the WT group of patients without *KRAS* and *STK11* MTs using unpaired two-sample Wilcoxon tests.

3.2.5 Exploring *KRAS* and *STK11* Somatic Mutations in Lung Adenocarcinoma and their Association with *RORC* Expression

It is known that there are a few major gain of function mutations in the *KRAS* gene that drives its oncogenic phenotype. In contrast, less is known about *STK11* mutations leading to loss of LKB1 function. To investigate whether specific mutations, types of mutations or perhaps mutated regions of the KRAS and LKB1 proteins are particularly linked to *RORC* expression, we analysed TCGA PanCancer data.

Figure 3.13a shows that 85% of all TCGA LUAD cancer gene mutations are missense mutations, with the second most common type of mutation being nonsense mutations at a considerably lower 7.1%. This is reflected by *KRAS* mutations of which 98.8% in TCGA are missense (Figure 3.13b). *KRAS* mutations lack diversity, with the vast majority functionally impacting the KRAS P-loop at codons 12 and 13 (Figure 3.13d and Table 3.4).

STK11 mutations on the other hand are considerably more heterogenous in nature with 31% being missense, 26.4% being nonsense and the remaining 42.6% being frameshift, splice site or gene fusions (Figure 3.13c). 95.4% of *STK11* mutations affect the large LKB1 protein kinase domain, and within this domain there are two major mutation hotspots (Figure 3.13e). The first is in the overlapping deacetylation region in which truncations commonly occur from frameshift insertions and deletions at position D53 and nonsense mutations and frameshift deletions at position Y60 (Figure 3.13e and Table 3.5). G56 missense mutations also occur in this hotspot, although they are annotated as of unknown biological and clinical significance by the OncoKB knowledge base through the cBioPortal portal (Figure 3.13e and Table 3.5) (387). The second LKB1 hotspot is located at the end of

the kinase domain and has oncogenic missense mutations at G242 and G251, as well as X245 splice site mutations (Figure 3.13e and Table 3.5).

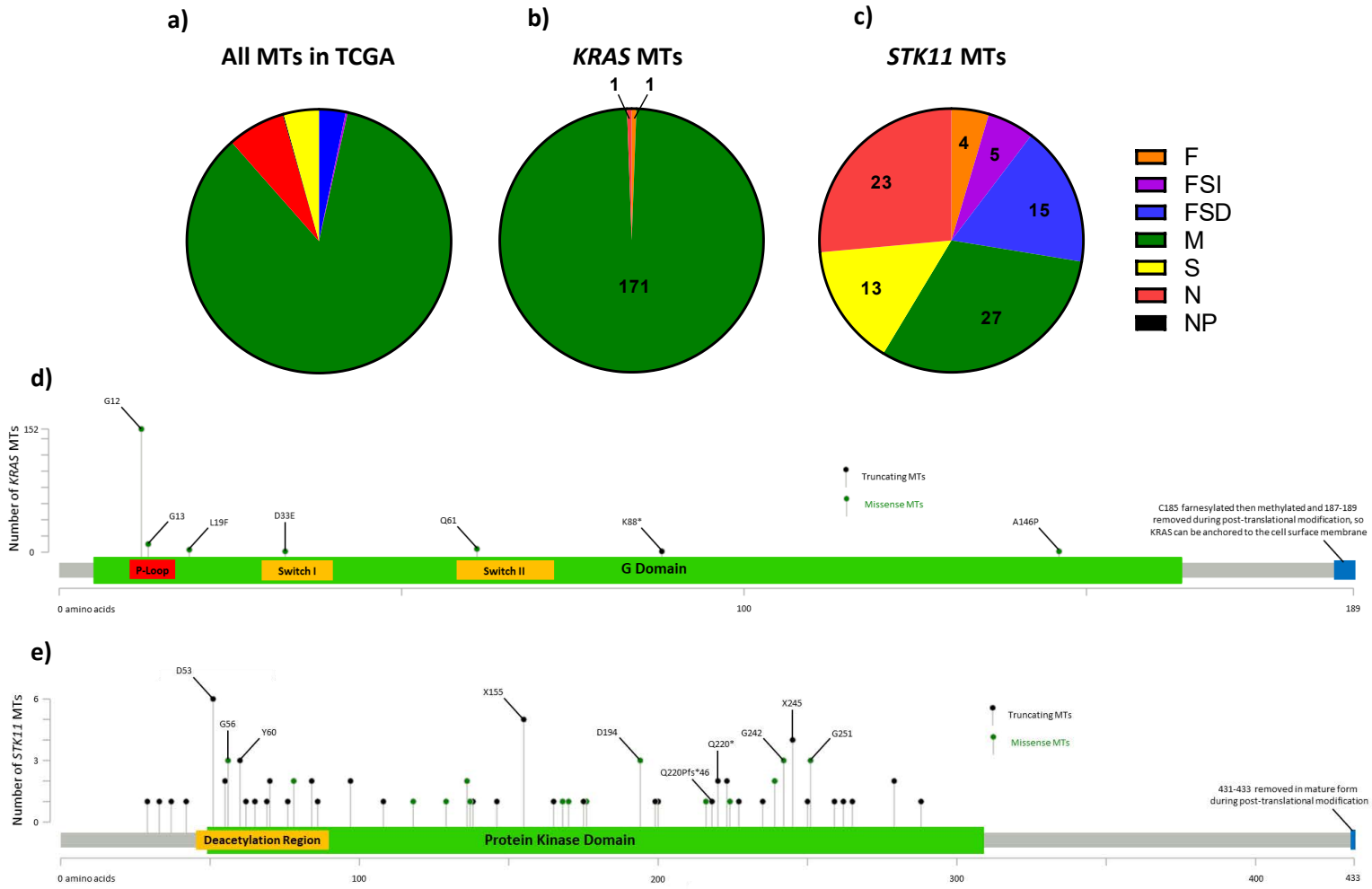
a)
All MTs in TCGA
b)
KRAS MTs
1
1
171
c)
STK11 MTs
4
5
23
15
13
27
F
FSI
FSD
M
S
N
NP
d)
Number of KRAS MTs
152
0
G12
G13
L19F
D33E
Q61
K88*
A146P
Truncating MTs
Missense MTs
C185 farnesylated then methylated and 187-189 removed during post-translational modification, so KRAS can be anchored to the cell surface membrane
P-Loop
Switch I
Switch II
G Domain
0 amino acids
100
189
e)
Number of STK11 MTs
6
3
0
D53
G56
Y60
X155
D194
Q220*
Q220Pfs*46
G242
X245
G251
Truncating MTs
Missense MTs
431-433 removed in mature form during post-translational modification
Deacetylation Region
Protein Kinase Domain
0 amino acids
100
200
300
400
433

Figure 3.13 Evaluating MTs in the TCGA PanCancer Atlas concentrating on *KRAS* and *STK11* MTs and their positions

a) All type of MTs for all cancer genes in TCGA were enumerated and plotted. **b)** All types of *KRAS* MTs in TCGA were enumerated and plotted. **c)** All types of *STK11* MTs in TCGA were enumerated and plotted. F = fusion, FSI = frameshift insertion, FSD = frameshift deletion, M = missense MT, S = splice site MT, N = nonsense MT, NP = nonstop MT. **d)** KRAS structure diagram with *KRAS* MTs annotated at their positions. Structural illustration based on entries to cBioPortal, UniProt (P01116) and a publication by Pantsar (66). **e)** LKB1 structure diagram with *STK11* MTs annotated at their positions. Structural illustration based on entries to cBioPortal and UniProt (Q15831).

KRAS MT/Position	Type of MT	Number of TCGA PanCancer Patients with MTs	OncoKB Annotation
G12	M	152	Oncogenic
G13	M	10	Oncogenic
Q61	M	4	Oncogenic
L19F	M	3	Oncogenic
K88*	N	1	Unknown
A146P	M	1	Likely Oncogenic
KRAS-SLC2A14	F	1	Unknown

Table 3.4 Common *KRAS* MTs by codon, MT type and OncoKB annotation

Data from TCGA PanCancer Atlas via cBioPortal. M = missense MT, N = nonsense MT, F = fusion.

STK11 MT/Position	Type(s) of MT	Number of TCGA PanCancer Patients with MTs	OncoKB Annotation
D53	FSI, FSD	6	Likely Oncogenic
X155_splice	S	5	Likely Oncogenic
STK11 fusions	F	4	Likely Oncogenic
D194	M	3	Likely Oncogenic
G242	M	3	Likely Oncogenic
G251	M	3	Predicted Oncogenic
G56	M	3	Unknown
Q220	N, FSI	3	Likely Oncogenic
X245_splice	S	3	Likely Oncogenic
Y60*	N	3	Likely Oncogenic

Table 3.5 Common *STK11* MTs by codon, MT type and OncoKB annotation

Data from TCGA PanCancer Atlas via cBioPortal. FSI = frameshift insertion, FSD = frameshift deletion, S = splice site MT, F = fusion, M = missense MT, N = nonsense MT.

After exploring the spectrum of *KRAS* and *STK11* mutations in LUAD, we then probed for any particularly strong associates of *RORC* mRNA expression. We started by looking at the effect of the different types of *STK11* mutations on *RORC* expression as *STK11* is not dominated by any one type of mutation.

All types of *STK11* mutations are associated with increased *RORC* expression with frameshift deletions, nonsense mutations and missense mutations being significantly increased (Figure 3.14a). We also grouped the most prevalent *STK11* mutations, as defined in Table 3.5, and found this group had the strongest link to high *RORC* expression (Figure 3.14a).

To find out whether specific *STK11* mutations were linked to *RORC* expression, we produced a detailed waterfall plot (Figure 3.14b) showing *RORC* expression with annotated *STK11* mutations and CNAs. 47% of all patients with *STK11* mutations fell into the top quartile of *RORC* expression, 27.7% into the second, 9.6% into the third and 15.7% into the fourth quartile. Although there was no dominant specific mutation or type of mutation in the first quartile, 59% of the mutations in this quartile were missense and nonsense. The second quartile however contained predominantly missense mutations (52.2%). Whilst examining specific *STK11* mutations we noted that G56 and G251 mutations (all of which are missense mutations) are all found in the top two quartiles, and the patient with the G251V mutation has the third highest *RORC* expression score and the highest score for any missense mutation. G242 missense mutations are also in the top two *RORC* quartiles, although these mutations are always found with other *STK11* mutations (S216F, M129I and a fusion of *STK11-ARHGAP45*). Nonetheless, OncoKB predicts G242 missense mutations as oncogenic, and position 242 is a known hotspot. Interestingly, all the patients with *STK11* copy number gains also had a *STK11* mutations. Finally, the two K84* mutations are both found in the bottom *RORC* expression quartile and have very similar z-scores of around -1.

We next plotted a similar waterfall plot of *RORC* expression and *KRAS* mutations (Figure 3.14c). 37.7% of patients with *KRAS* mutations fell into the first expression quartile, 26.6% in the second, 23.4% in the third and 12.3% in the last and lowest quartile. Patients with missense mutations at G12, which are the most common *KRAS* mutations in LUAD (Table 3.4), are distributed throughout Figure 3.14c with a range of *RORC* expression values. 6/9 of patients with the second most common *KRAS* gene mutations at G13 are found in the

first quartile. We could not see any other patterns from the remaining *KRAS* mutations due to the low number of patients with these mutations.

Whilst the homogeneous nature of *KRAS* gene mutations made identifying particular drivers of increased *RORC* mRNA expression difficult, differences in *RORC* expression in tumours with different *STK11* mutations suggests that the two major mutational hotspots of LKB1 are strongly associated with high *RORC* expression.

a)

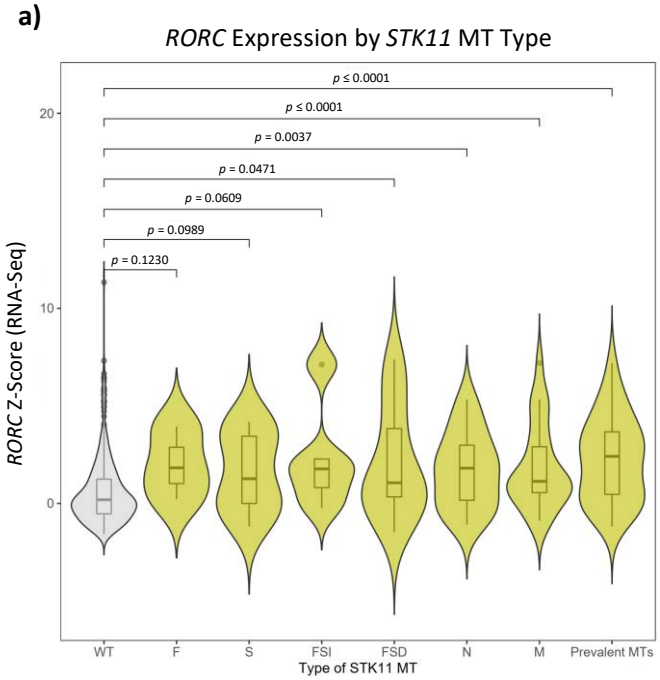
RORC Expression by *STK11* MT Type
p ≤ 0.0001
p ≤ 0.0001
p = 0.0037
p = 0.0471
p = 0.0609
p = 0.0989
p = 0.1230
20
10
0
RORC Z-Score (RNA-Seq)
WT
F
S
FSI
FSD
N
M
Prevalent MTs
Type of STK11 MT

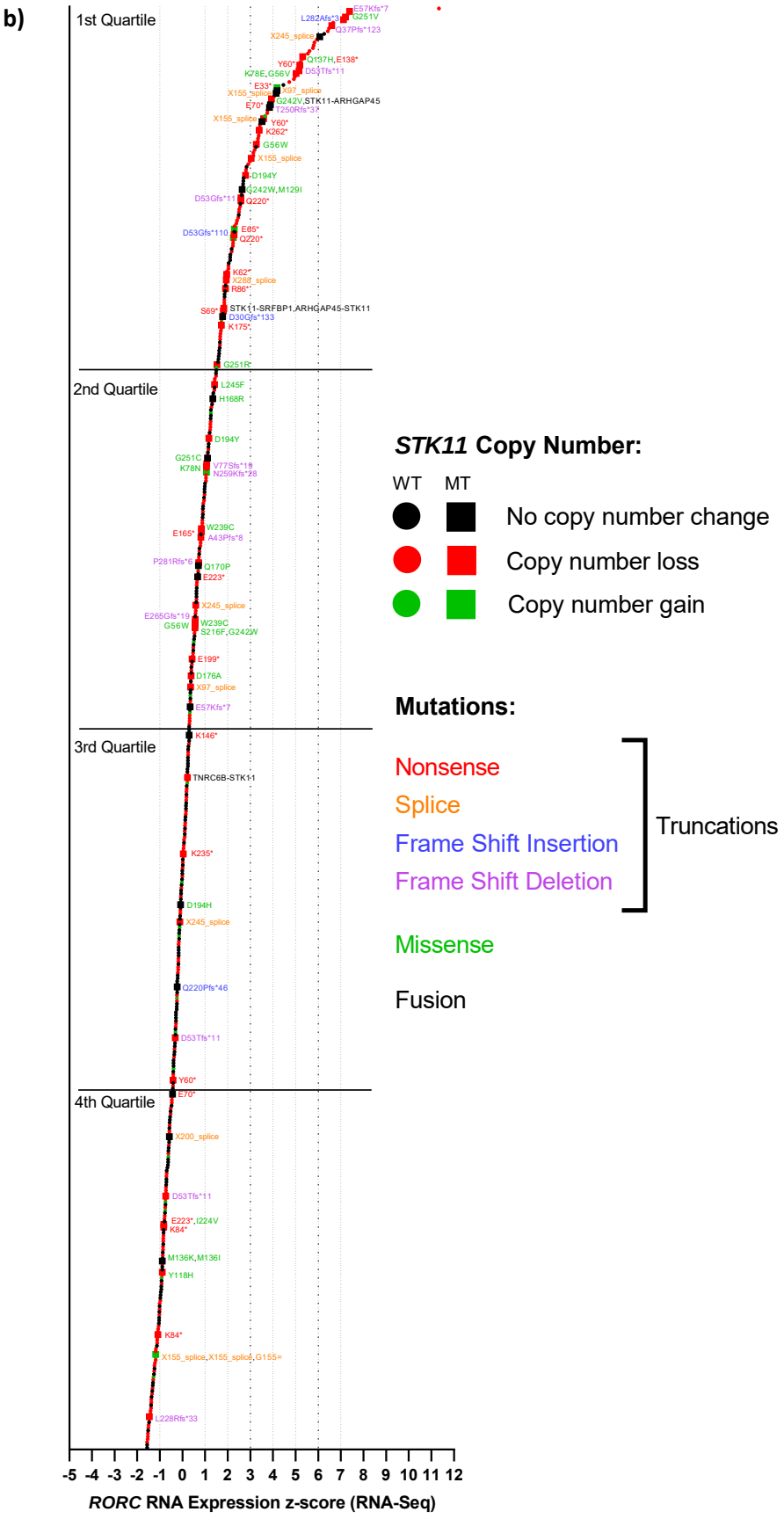
b)
1st Quartile
2nd Quartile
3rd Quartile
4th Quartile
E57Kfs*7
G251V
L282Afs*3
Q37Pfs*123
X245_splice
Q137H,E138*
Y60*
D53Tfs*11
K78E,G56V
E33*
X97_splice
X155_splice
G242V,STK11-ARHGAP45
E70*
T250Rfs*3*
X155_splice
Y60*
K262*
G56W
X155_splice
D194Y
G242W,M129I
D53Gfs*11
Q220*
D53Gfs*110
E85*
Q220*
K62*
X288_splice
R86*
S69*
STK11-SRFBP1,ARHGAP45-STK11
D300Gfs*133
K175*
G251R*
L245F
H168R
D194Y
G251C
K78N
V77Sfs*19
N259Kfs*28
E165*
W239C
A43Pfs*8
P281Rfs*8
Q170P
E223*
X245_splice
E265Gfs*19
G56W
W239C
S216F,G242W
E199*
D176A
X97_splice
E57Kfs*7
K146*
TNRC6B-STK11
K235*
D194H
X245_splice
Q220Pfs*46
D53Tfs*11
Y60*
E70*
X200_splice
D53Tfs*11
E223*,I224V
K84*
M136K,M136I
Y118H
K84*
X155_splice,X155_splice,G155=
L228Rfs*33
-5 -4 -3 -2 -1 0 1 2 3 4 5 6 7 8 9 10 11 12
RORC RNA Expression z-score (RNA-Seq)
STK11 Copy Number:
WT MT
No copy number change
Copy number loss
Copy number gain
Mutations:
Nonsense
Splice
Frame Shift Insertion
Frame Shift Deletion
Truncations
Missense
Fusion

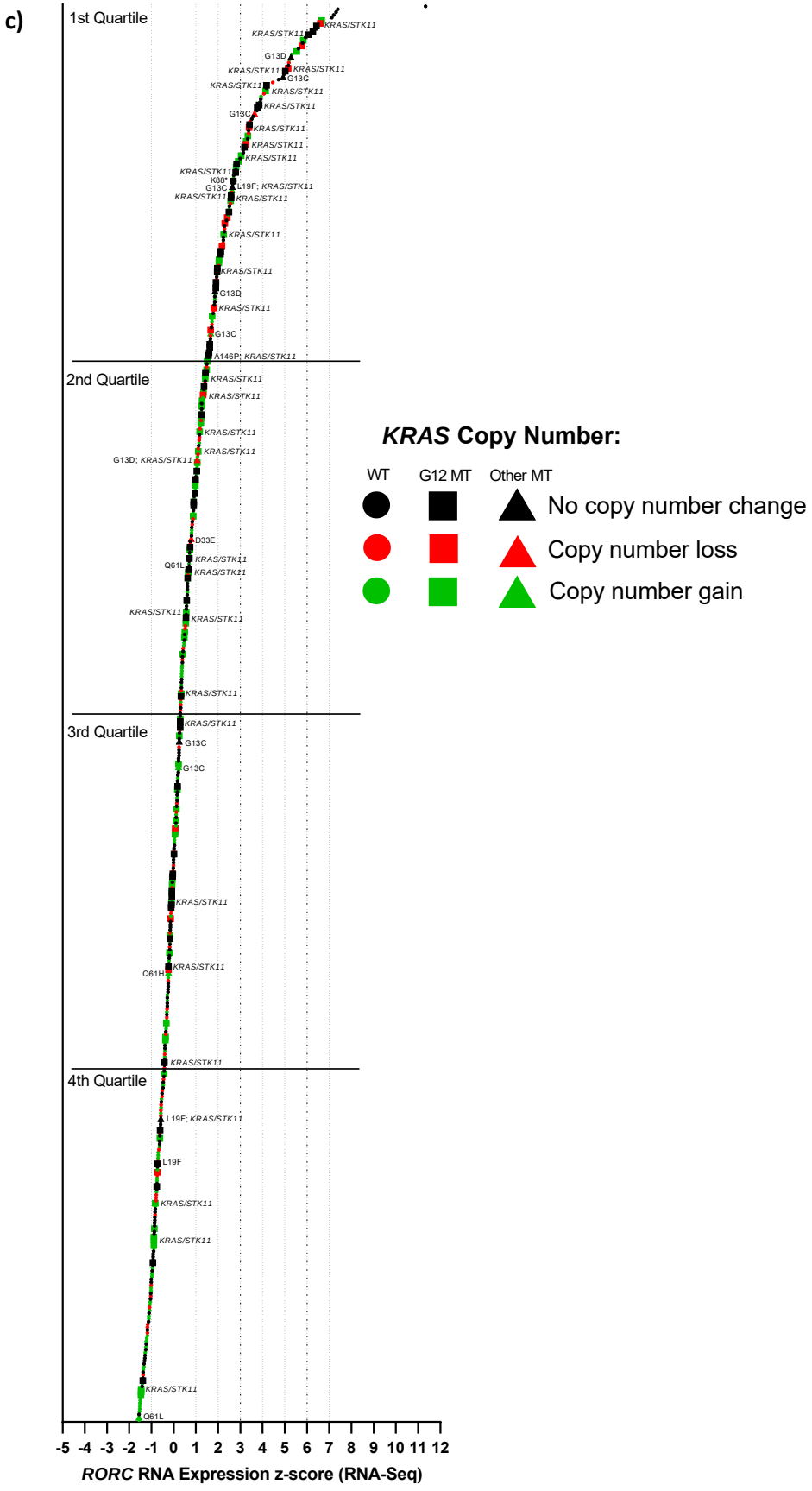
c)
1st Quartile
2nd Quartile
3rd Quartile
4th Quartile
KRAS/STK11
G13D
G13C
A146P; KRAS/STK11
G13D; KRAS/STK11
D33E
Q61L
Q61H
L19F; KRAS/STK11
L19F
KRAS Copy Number:
WT
G12 MT
Other MT
No copy number change
Copy number loss
Copy number gain
-5 -4 -3 -2 -1 0 1 2 3 4 5 6 7 8 9 10 11 12
RORC RNA Expression z-score (RNA-Seq)

Figure 3.14 *RORC* expression by MT and MT type

a) *RORC* mRNA z-scores grouped by different type of *STK11* MTs and compared using unpaired two-sample Wilcoxon tests. WT group do not have MTs in *KRAS* or *STK11*. The 'prevalent MTs' group consist of the most common *STK11* MTs in TCGA PanCancer as highlighted in Table 3.5. F = fusion, S = splice site MT, FSI = frameshift insertion, FSD = frameshift deletion, N = nonsense MT, M = missense MT. **b)** *RORC* mRNA z-scores plotted as a waterfall plot that have patients with *STK11* MTs or CNAs highlighted. The 'no copy number change' label represents patients with a *STK11* GISTIC score of 0, the 'copy number loss' label represents patients with *STK11* GISTIC scores of -1 or -2, the 'copy number gain' label represents patients with a *STK11* GISTIC score of +1. **c)** same as **b)** except plotting patients with *KRAS* MTs or CNAs highlighted. The 'no copy number change' label represents patients with a *KRAS* GISTIC score of 0, the 'copy number loss' label represents patients with a *KRAS* GISTIC score of -1, the 'copy number gain' label represents patients with *KRAS* GISTIC scores of +1 or +2. If *KRAS/STK11* is labelled next to the patient marker on the plot, this shows patients with concomitant *STK11* MTs. All data from TCGA PanCancer.

3.3 Discussion

NSCLCs are a complex group of cancers that can be driven by a range of cellular oncogenic mutations. However, little is known about the differences in the immune microenvironments of tumours with distinct driver mutations, which may impact their response to treatment. We therefore, set out to characterise the immune signatures of LUAD tumours in relation to the cancer genes mutated, using RNA-Seq data from TCGA. This work investigated a range of immune-related genes representing intratumoural immune subsets and function, key genes involved in recruitment and exploring immune checkpoint expression. This work was performed with a view to improve stratification of medicine for NSCLC patients.

3.3.1 Characterising Immune Signatures of Mutation Driven Lung Adenocarcinoma

Key strengths of this analysis were both the number of immunity-related genes analysed (*n* = 105) and the broad range of diverse LUAD cancer genes interrogated (*n* = 11), for many of which there is very little current knowledge of immunity within tumours.

For example, there is a lack of detailed intratumour immunophenotyping of *MET* driven LUAD in the literature. Our work shows that TCGA patients with *MET* mutations appear to have 'hot' immune signatures, yet some of the highly expressed immune genes like *FOXP3* are suppressive (Figure 3.1). Functionally, overexpression of MET and its ligand HGF leads to autocrine tumour growth, as well as paracrine signalling to immune cells. Mouse models show that HGF can recruit TANs and induce FoxP3^{+} Tregs, supporting our findings (388, 389). Oncogenic *MET* is also associated with PD-L1 expression, supporting our

finding of increased *PDCD1* expression in the immune signature from *MET* mutant tumours (390-393).

We also elucidated patterns of HLA class I and II expression across tumours with varied mutations, with high expression seen in the *MET*, *ROS1* and *EGFR* immune signatures and low expression in the *KRAS* and *STK11* immune signatures. This is supported in the literature by evidence of HLA protein expression in *EGFR* driven LUAD (394). HLA expression might be induced by higher levels of interferons associated with *EGFR* and *MET* mutations, though there is mixed evidence for interferon and functional T cell responses in patients with these mutations (133, 143, 202-205, 395-400). In contrast, in *KRAS* mutant tumours, profiling revealed a general immunologically 'cold' signature including low HLA class I and II expression, which is suppressed by MEK signalling downstream of KRAS, alongside epigenetic silencing of *HLA* genes (148, 401). This may provide the tumour protection from $CD4^+$ T cells in NSCLC patients that can recognise neoantigens from *KRAS* mutations (402).

3.3.2 Suppressed Immunity in *KRAS* and *STK11* Driven Lung Adenocarcinoma Tumours

Further exploring these immune signatures showed that like the *KRAS* immune signature, the overall *STK11* immune signature was also immunologically 'cold'. This was supported by several studies by other groups including the authors of the dataset we used for validation, Schabath *et al* (316), who found lower tumour TCRαβ gene expression in patients with *STK11* mutations. This was attributed to a reduced T cell tumour infiltrate (49, 115, 126, 316, 403-405).

Two of the significantly downregulated genes in the *STK11* immune signature encoded PD-L1 and PD-L2. Low PD-L1 expression in tumours with *STK11* mutations has been reported by several studies, thereby patients with tumour LKB1 loss respond poorly to PD-1/PD-L1 blockade (115, 126, 385, 400, 403, 404, 406). Work by Skoulidis *et al* (49) showed that patients with concomitant *KRAS/STK11* mutations had low PD-L1 mRNA expression, whereas patients with *KRAS/TP53* mutations had high PD-L1 mRNA expression. We also found increased expression of genes encoding PD-L1 and PD-L2 in tumours with *TP53* mutations, supporting these and other previous findings (49, 64, 189, 400, 406, 407). Moreover, the findings from Skoulidis *et al* (49) suggest roles for p53 and LKB1 in regulating PD-L1 expression in patients with *KRAS* mutations (49, 408). Thus, PD-L1 expression in KRAS-driven NSCLC is linked to increased MEK signalling and STAT3 activation, and PD-L1 expression can be increased by NF-κB activation in response to p53 loss (64, 399, 400, 409-411). Whereas the consequences of LKB1-mediated metabolic rewiring causes epigenetic silencing of STING, which reduces tumour PD-L1 expression. Interestingly, this appears to overrule the pro-PD-L1 expression signals from KRAS signalling in tumours with concomitant mutations (124, 126, 403).

The *ATM* signature also appeared immunologically 'cold' like the *STK11* signature (Figure 3.1). One of the only upregulated genes in both these signatures was *STAT3*, a transcription factor that regulates MDSCs, Th17s and is expressed in tumour cells to aid oncogenesis (98, 202-205, 241, 244, 249-251, 255, 260, 261, 270, 297-302). The only other significantly upregulated gene in the *STK11* immune signature was the canonical Th17 transcription factor gene *RORC*, which was also significantly upregulated in *KRAS* signature. Given *KRAS/STK11* concomitant mutations are known to act synergistically, we

were interested in investigating patients with *KRAS* and *STK11* mutations further (49, 115, 124, 125, 189, 316). We confirmed the raised *RORC* expression in the *KRAS* and *STK11* TCGA immune signatures using another published dataset, this time comprised of expression data from a microarray (Figure 3.2) (316).

We next used the deconvolution algorithms CIBERSORT and MCP-counter to investigate different immune cell subsets within the *KRAS*, *STK11* and *KRAS/STK11* mutant tumours, and found evidence of synergistic effects of concomitant mutations, including increased plasma cells and reduced DCs (Figure 3.3). These algorithms have key differences in output making it difficult to compare results for immune subsets between the CIBERSORT and MCP-counter runs. As MCP-counter estimates absolute immune abundances instead of relative fractions it is considered more applicable for inter-sample quantifications (322). Nevertheless, both algorithms confirmed that TCGA tumours with *KRAS/STK11* mutations had generally lower immune infiltration compared to WT tumours, reaffirming our earlier findings. This overarching finding of decreased immune cells in tumours with *KRAS* and *STK11* mutations is widely supported by other studies (132, 151, 189, 385, 406, 408, 412-414).

Plasma cells and neutrophils were the only two subsets significantly increased in TCGA patients with *KRAS/STK11* mutations compared to WT (Figure 3.3). Whilst we could not find links between *KRAS/STK11* mutations and plasma cells in the literature, there is a body of evidence connecting NSCLC patients with these mutations to the recruitment of intratumoural TANs (189, 385, 405, 406, 414). A murine study by Koyama *et al* (189) proposed a key role for LKB1 loss, finding that suppressive TANs were preferentially

recruited to *KRAS/STK11* driven tumours compared to *KRAS* driven tumours; with follow up work suggesting that IL-17A is important in this process (189, 414). Intratumoural TANs are associated with poor NSCLC clinical outcomes, and TANs exert their suppressive functions in LKB1 deficient tumours via a variety of mechanisms including cytotoxic degranulation and the secretion of IL-10 and arginase (189, 405, 414, 415).

3.3.3 Investigating the Relationship Between *KRAS* and *STK11* Alterations and *RORC* Gene Expression

We were next interested in elucidating the relationship between *KRAS* and *STK11* cancer gene mutations and increased *RORC* mRNA expression. Using data from Schabath *et al* (316) showed that the *RORC2* isoform – that specifically produces the Th17 transcription factor RORγT – is increased in patients with *KRAS* and *STK11* mutations. Furthermore, *RORC/RORC2* expression was indeed highest in patients with concomitant mutations, indicating a potential synergistic effect of double mutations (Figure 3.4). Further grouping TCGA patients by *STK11* CNA and LKB1 protein downregulation supported our finding of increased *RORC* expression in patients with LKB1 loss (Figure 3.5). However, similar analysis for *KRAS* CNA and KRAS protein upregulation did not. The reason behind this discrepancy is not entirely clear. However, comparing the impact of *KRAS* and *STK11* mutations to *KRAS* and *STK11* CNAs on *RORC* expression, showed that mutations rather than CNAs are more linked to increased *RORC* expression (Figure 3.6).

Investigating potential mechanisms for *RORC* overexpression unveiled chromosomal instability that is frequently seen throughout 1q and specifically at the *RORC* locus 1q21.3,

which is associated with recurrence (416). Whilst GISTIC +1 low-level gain scores are described as putative and may not represent true amplification, GISTIC scores of +2 likely represent 1q21.3 amplifications (312). Nevertheless, both groups showed significantly higher *RORC* expression compared to the group with GISTIC scores of 0/-1 (Figure 3.7).

1q21.3 amplifications are observed in 15-30% of LUAD cases in the literature, and using the more stringent measure we found that 9.9% of TCGA LUAD patients had *RORC* GISTIC scores of +2 (Table 3.2) (377-385, 417). As some patients with 1q21.3 amplifications may fall into the *RORC* GITIC +1 group, this is likely an underrepresentation.

We also found a significant relationship between *RORC* GISTIC scores and *KRAS/STK11* mutations (Table 3.3), suggesting that some patients with these mutations also harbour putative 1q21.3 amplifications. Studies into a rare gynaecological carcinoma and NSCLC also describe a relationship between *KRAS* mutations and 1q amplifications, and propose that these are early oncogenic lesions (381, 418-420). Mechanistically, the 1q21.3 locus also contains *IL6R*, *ARNT* and genes encoding the S100A family of proteins which activate NF-κB. Overexpression of IL-6R aids IL-6 signalling which has a role in promoting *KRAS* driven NSCLC directed by STAT3 activation (98, 205, 421-430). *ARNT* encodes for the AHR nuclear translocator which might be an initial driver of 1q21.3 amplification, as its overexpression may allow response to increased intracellular PAHs for example from cigarette smoke (7, 253, 282, 283). It has been argued that in breast cancer expression of the S100A family from 1q21.3 amplifications is important for tumour growth, and that S100A2 expression in early-stage NSCLC is associated with poor prognosis (377, 431).

To ensure that the raised *RORC* expression we had detected in *KRAS* and *STK11* mutant tumours was not entirely a result of 1q21.3 amplifications, we reanalysed the data following removal of patients with *RORC* CNA gains and amplifications. We found that whilst increased copies of *RORC* through 1q21.3 amplification boosts expression, we still observed higher *RORC* expression in patients with *KRAS*, *STK11* and *KRAS/STK11* mutations who did not have this amplification (Figure 3.9). This shows that mutations in these cancer genes are associated with raised *RORC* expression independent of *RORC* CNAs.

Survival analysis showed that low *RORC* expression was associated with reduced OS (Figure 3.10). This was surprising as RORγT^{+} Th17 cells have been shown to promote NSCLC, which contrasts with the literature (189, 276, 285-288, 291-294, 296-299, 304), but could be explained by an unknown cellular source of *RORC* which is a limitation of examining transcriptional data from bulk tumours. As *RORC* may be expressed by tumour cells or non-Th17 immune cells, it is important to establish the cellular source of *RORC* to understand these findings.

Examining published data from isogenic epithelial cell lines showed that introducing *KRAS* mutations did not change *RORC* expression. However, this did induce *IL17C* and was linked with *IL17RE* expression (Figure 3.12). Findings from the literature show that IL-17C can be expressed by Th17s but is predominantly expressed by epithelial cells (386, 432, 433). Murine studies show that IL-17C signalling through heteromeric IL-17RA/IL-17RE support polarised Th17s, though this is not necessary for earlier differentiation. Mice with *KRAS*-driven *IL17C*$^{-/-}$ lung tumours have reduced tumour cell proliferation, IL-6 concentrations and infiltrating TANs compared to *KRAS*-driven *IL17C*$^{+/+}$ tumours (386, 433). It is therefore

possible that *KRAS* mutations promote IL-17C and IL-17RE expression to assist immunosuppression in the TME, as well as to stimulate autocrine growth signalling.

Finally, we investigated whether increased *RORC* expression was associated with particular *KRAS* and *STK11* mutations affecting different functional regions of the proteins. *KRAS* mutations are extremely homogenous and G13 mutations were associated with high *RORC* expression (Figure 3.14c).

In contrast, *STK11* mutations show much greater heterogeneity, and we did not find a particular *STK11* mutation responsible for *RORC* overexpression. However, we did find that *STK11* mutations from two mutational hotspots of the LKB1 protein are linked with high *RORC* expression (Figure 3.14b). Interestingly both mutational hotspots functionally impact LKB1. *STK11* mutations affecting the deacetylation region disrupt interactions with STRAD, and truncations in this N-terminus region have large functional effects on LKB1 protein structure (43, 95). Whilst mutations in the second hotspot may impact kinase function. The G242V mutation interrupts complexing with the LKB1 scaffold protein MO25, as may the other mutations in this hotspot (43, 434). These finding support the association of functional LKB1 loss and *RORC* expression.

3.3.4 Summary

Overall, in this Chapter we characterised immune gene expression signatures linked with a range of important LUAD mutations using data from TCGA, finding that tumours harbouring *KRAS* and *STK11* mutations displayed a lack of immune gene expression and

had generally lower immune infiltrates supporting the literature (49, 115, 126, 151, 189, 316, 385, 403-406, 408, 412-414).

The only immune gene with significantly increased expression in both the 'cold' *KRAS* and *STK11* immune signatures was *RORC*, the gene encoding the key Th17 transcription factor RORγT. Our validation experiments also uncovered evidence of synergistically increased *RORC* expression in tumours with *KRAS/STK11* mutations.

After ensuring that *RORC* expression was not dependent on amplification of the *RORC* locus, we examined patient survival and found that low *RORC* expression was associated with poor OS.

We lastly deeply examined the relationship between *RORC* expression *KRAS* and *STK11* mutations and found that high *RORC* expression is linked with two mutational hotspots of the LKB1 protein with functional importance.

Work throughout this Chapter poses two key questions. The first being does this relationship between *RORC* expression tumours with *KRAS* and *STK11* mutations extend to RORγT protein expression, which was not profiled by TCGA. Whilst the second addresses the nature of performing transcriptomics on heterogeneous bulk tumours: which cells are expressing *RORC*? Work in Chapter 4 set out to answer these questions.

4. Characterising RORγT Expression in *KRAS* and *STK11* Driven Lung Cancer

4.1 Introduction

We previously found that mRNA expression of the RORγT gene (*RORC*) is increased in TCGA patient LUAD tumours with *KRAS* and *STK11* mutations and is potentially synergistically increased in *KRAS/STK11* mutant LUADs.

Whilst TCGA data is a useful resource, we were unable to determine from our analyses in Chapter 3 whether increased *RORC* mRNA expression resulted in higher RORγT protein expression in tumours harbouring these mutations. This a problem because there is a common disconnect between mRNA and protein expression, with increased expression of one not always correlated to increased expression of the other (435, 436). Furthermore, as transcriptomic data represents a combination of all cells present in tumours, we were not able to establish which cells are expressing *RORC* in the TME.

The only previous study examining *RORC*/RORγT expression in NSCLC patient tumour resections was work by Huang *et al* (437). By performing RORγT IHC on the tumour resections they found that most cells expressing RORγT were tumour cells, although this tumour cell IHC staining was weak and cytoplasmic. The authors did not examine 1q21.3 amplifications or profile these tumours for cancer gene mutations, but found a positive correlation between RORγT and IL-17A expression in NSCLC tumours and suggested that RORγT is expressed by NSCLC cell lines using western blots and flow cytometry (437).

However, one of the defining features of the different subsets of $CD4^+$ T cells is the expression of distinct transcription factors that support their differentiation from naïve T cells and drive their functionality. The transcription factor RORγT is an important transcription factor for the Th17 subset of $CD4^+$ T cells (245-248). Therefore, it is possible that raised *RORC* expression reflects greater infiltration of $ROR\gamma T^+$ immune cells.

To answer these questions surrounding RORγT protein expression, we sourced a valuable cohort of NSCLC tumour resections from patients in the TRACERx and SMP2 studies. Although tumours are not normally screened for *KRAS* or *STK11* mutations in normal clinical practice, both studies sequenced tumour cells from these resections to classify presence or absence of *KRAS* and *STK11* mutations (359, 360). By IHC staining these resections we would be able to establish which cells were expressing nuclear RORγT in NSCLC tumours; and determine whether there are increased abundances of $ROR\gamma T^+$ cells in patient tumours with *KRAS* and *STK11* mutations.

As much of the previous work profiling RORγT protein expression is focused on murine cells and human work mainly examines *RORC2* mRNA expression by PCR, not many studies have utilised monoclonal antibodies against human RORγT for IHC (221, 222, 226, 232, 248, 254, 259, 264, 269, 278, 281, 290, 438-442). We therefore purchased several RORγT monoclonal antibodies and performed a series of validations to determine which antibody could best detect RORγT protein.

4.2 Results

4.2.1 Validating and Optimising RORγT Monoclonal Antibodies for Immunohistochemistry

To be confident that a range of commercially available monoclonal RORγT antibodies could detect the RORγT protein in IHC, we firstly designed a plasmid transfection system using a plasmid expressing GFP-tagged *RORC2* encoded RORγT protein made by Sino Biological. This *RORC2* plasmid was transfected into HEK293T cells to investigate antibody sensitivity. After transforming and selecting *E. coli* colonies by antibiotic resistance we confirmed plasmid DNA sequence by Sanger sequencing. Experimental HEK293Ts were then transfected overnight and control HEK293Ts were not transfected overnight. The following day HEK293Ts were split three ways: cell for PCR confirmation, cells for flow cytometric confirmation and cells for pelleting and fixation.

Firstly, mRNA was extracted and a qPCR performed using *RORC* specific primers. Table 4.1 shows relative quantification of *RORC* in the control and transfected cell lines using the housekeeping gene *GAPDH* as reference. There was no difference in expression of *GAPDH* between Parental HEK293Ts which had not been exposed to any transfection reagents and Mock Transfected HEK293Ts which had been exposed to the 'mock transfection reagent' cocktail of DMEM, polyethylenimine and H_2O, without plasmid. As expected, no *RORC* amplification occurred in Parental or Mock cells. However, large negative changes in $\Delta\Delta C_T$ (< -20) when comparing *RORC2* Transfected HEK293Ts vs Parental HEK293Ts and vs Mock Transfected HEK293Ts indicated high positive *RORC* expression upon transfection (Table 4.1).

Cells from the same cultures used in the qPCR experiment were also processed for flow cytometry to detect GFP expression as an indicator of a successful transfection. As expected, both the Parental HEK293Ts and the Mock Transfected HEK293Ts were GFP^-, whilst 22.79% of the *RORC2* Transfected HEK293T cells were GFP^+ (Figure 4.1). The DNA sequence confirmation, detection of *RORC2* by qPCR and GFP expression by flow cytometry convinced us that the transfection model was applicable for RORγT antibody validation.

Condition	ΔC_T			
Parental HEK293Ts	16.08	$\Delta\Delta C_T$: -0.31		
Mock Transfected HEK293Ts	15.77	FC: 1.24	$\Delta\Delta C_T$: -20.41	$\Delta\Delta C_T$: -20.72
RORC2 Transfected HEK293Ts	-4.64		FC: 1.39×10^6	FC: 1.73×10^6

Table 4.1 *RORC2* qPCR relative quantification and gene expression changes between transfection conditions using $\Delta\Delta C_T$

RNA were extracted from Parental HEK293Ts, Mock Transfected HEK293Ts and *RORC* Transfected HEK293Ts and were subject to DNAse digestions before reverse transcription to cDNA (Chapter 2.4.4). After qPCR validations with no-reverse transcriptase controls which did not give any amplification, qPCR reactions (Chapter 2.4.5) were performed on the cDNA. Undetermined low C_T values were changed to C_T values of 40 for this analysis. Normalised ΔC_T values were calculated as the change between the average triplicate *RORC2* C_T and the average triplicate *GAPDH* C_T (average *RORC2* C_T – average *GAPDH* C_T). $\Delta\Delta C_T$ values were calculated as the change between ΔC_T in the two conditions being compared (e.g. ΔC_T Mock Transfected HEK293Ts – ΔC_T *RORC2* Transfected HEK293Ts). The expression fold change (FC) is $2^{-\Delta\Delta CT}$.

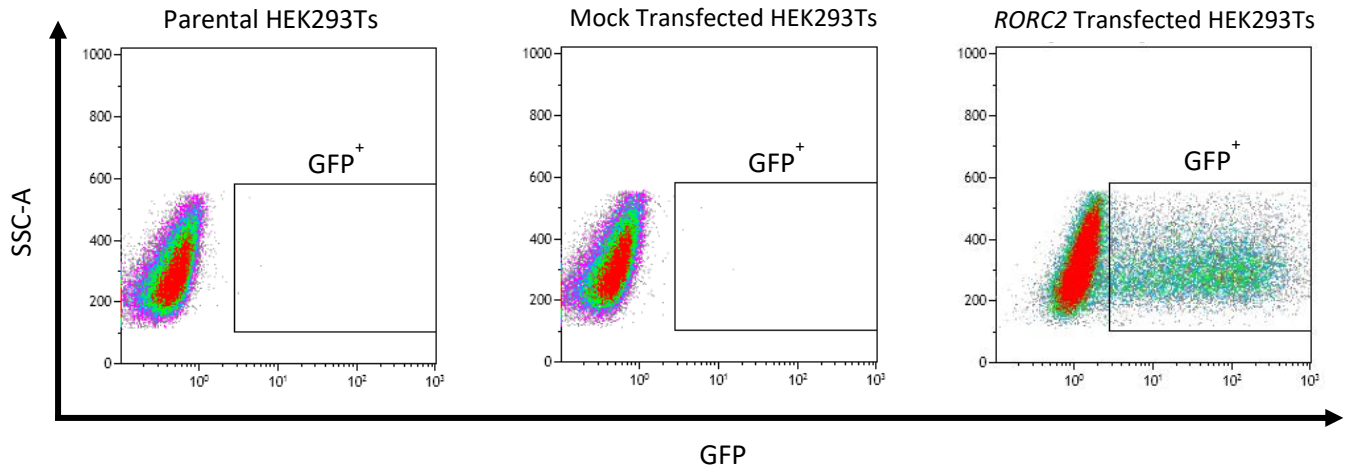

Figure 4.1 RORγT-GFP expression in transfected HEK293T cells by flow cytometry

HEK293Ts were gated to the stoppage gate as shown in Figure 2.4. The GFP^+ gate was set using the Parental HEK293T cells.

We next used the fixed HEK293T cell pellets from this transfection system to evaluate whether the three RORγT monoclonal antibodies were able to detect overexpressed RORγT protein by IHC (Figure 4.2a). The antibodies purchased from eBioscience and Merck were able to detect nuclear RORγT in the *RORC2* Transfected HEK293Ts and showed no

evidence of staining in the negative Parental and Mock HEK293T samples. In contrast, the antibody from Novus Biologicals did not detect RORγT in the *RORC2* Transfected HEK293Ts and was discarded from subsequent experiments.

Having successfully detected RORγT protein in this artificial transfection system, we then looked for evidence of nuclear RORγT staining in lymphocytes in human tissue sections. After titrating both antibodies using the HEK293T cell pellets, we IHC stained human tonsil and found that both antibodies stained the nuclei of lymphocyte sized cells located outside of the B cell dominated follicles in the interfollicular regions (Figure 4.2b). To ensure there was no non-specific staining from the anti-rat and anti-mouse secondary antibodies, we omitted the primary RORγT antibodies (eBioscience RORγT raised in rat and Merck RORγT raised in mouse) and found no evidence of non-specific secondary antibody staining. Though both antibodies worked well on human sections and detected RORγT expression in lymphocytes, we decided to take the RORγT antibody from Merck forward in our experiments due to its superior staining strength in tonsil.

a)

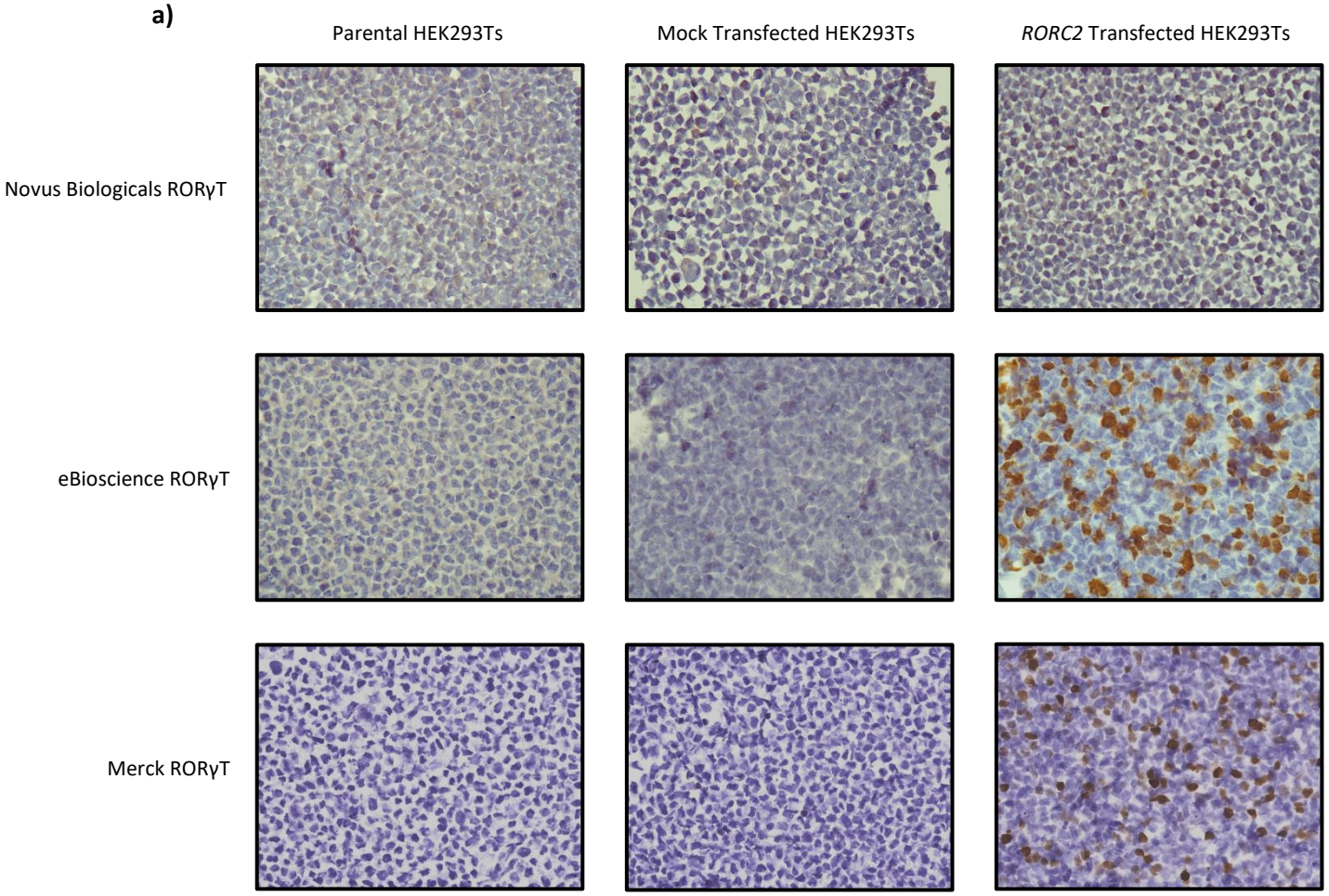
Parental HEK293Ts
Mock Transfected HEK293Ts
RORC2 Transfected HEK293Ts
Novus Biologicals RORγT
eBioscience RORγT
Merck RORγT

b)

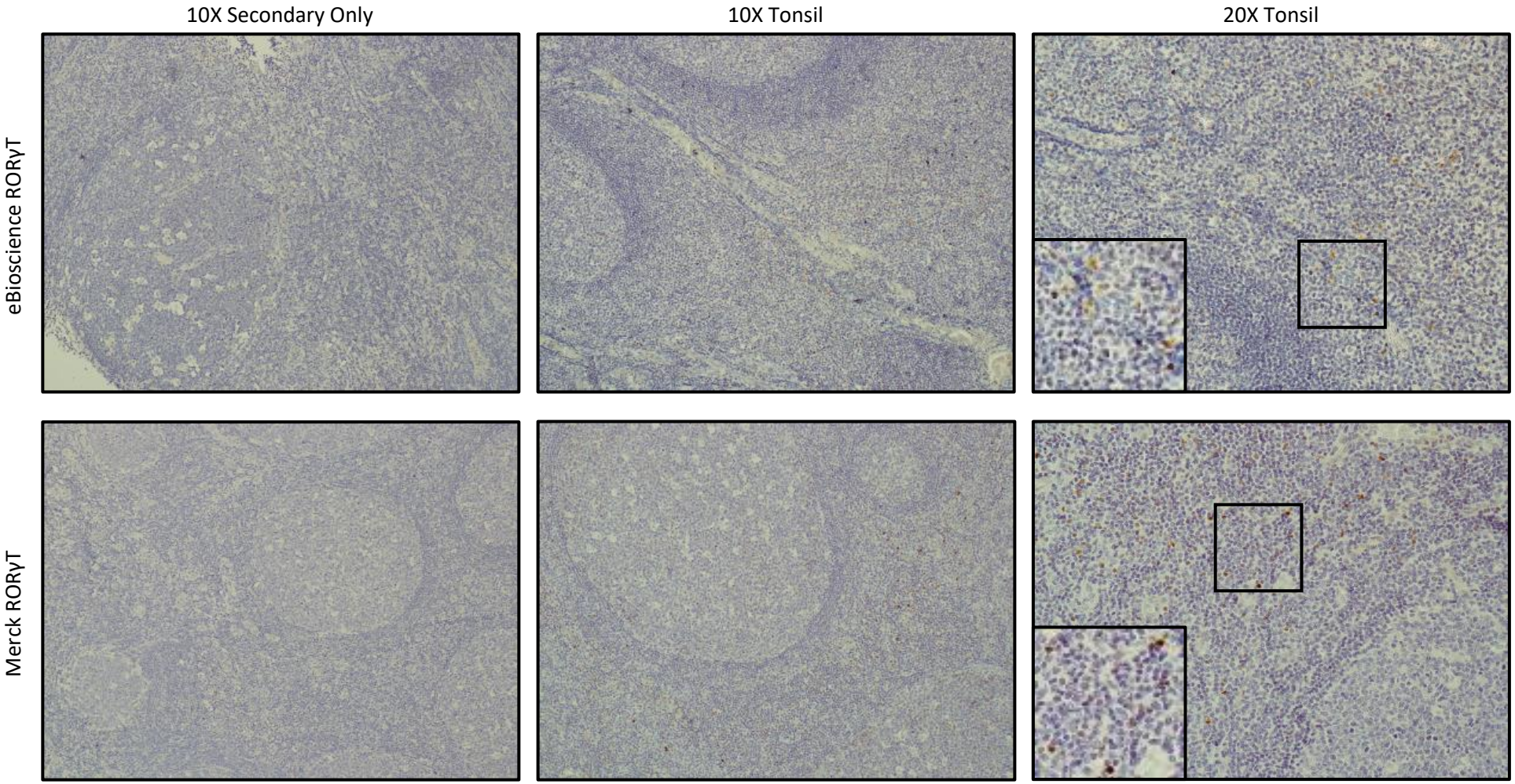
10X Secondary Only
10X Tonsil
20X Tonsil
eBioscience RORγT
Merck RORγT

Figure 4.2 RORγT expression in transfected cells and in tonsil by IHC

a) Sectioned pelleted HEK293T cells were IHC stained (Chapter 2.5.1) using three different RORγT monoclonal antibodies: 'Novus Biologicals RORγT', 'eBioscience RORγT' and 'Merck RORγT'. Images are at 40X. **b)** Sectioned tonsil were IHC stained using the eBioscience RORγT antibody and the Merck RORγT antibody. Secondary only control staining used the anti-rat secondary antibody for the eBioscience RORγT antibody and the anti-mouse secondary antibody for the Merck RORγT antibody. The 10X and 20X Tonsil images for both RORγT antibodies in this Figure were taken from different regions to show the prevalence and localisation of RORγT$^+$ cells.

Having identified a RORγT IHC antibody which can sensitively detect RORγT$^+$ lymphocytes in human tonsil sections, we were interested in testing whether this unconjugated antibody could also work in flow cytometry for future *in vitro* experiments. As the Merck RORγT is not currently available in a conjugated form for flow cytometry we therefore conjugated it to the AF647 fluorophore using a commercial kit. Figure 4.3a shows that the newly conjugated RORγT-AF647 can successfully stain *RORC2* Transfected HEK293Ts in flow cytometry, showing double positive GFP$^+$/RORγT$^+$ HEK293Ts from the *RORC2* Transfected condition with no staining in the Mock Transfected cells.

To find out if the RORγT-AF647 antibody could work outside of the transfection system, we stimulated *ex vivo* PBMCs with PMA/iono and co-stained with antibodies from a Th17 flow cytometry panel to identify Th17 cells, an IL-17 secreting T cell subset that express the RORγT transcription factor (Figure 4.3b). Using fluorescence minus one (FMO) controls we saw no positive staining in the absence of antibodies of interest. Comparing the staining with the 'RORγT-AF647 FMO' and the full panel of antibodies ('Donor 1 Staining') there was clear detection of RORγT$^+$ CD3$^+$/CD4$^+$ T cells with the addition of RORγT-AF647. Importantly, within this CD3$^+$/CD4$^+$ T cell population we could detect Th17s which express both RORγT and secrete IL-17A (0.26%).

As this AF647 fluorophore can dissociate from the RORγT antibody, we followed recommendations from the manufacturer and conjugated a fresh aliquot of antibody every two weeks. Each time this was done we repeated the staining on PBMCs to confirm successful conjugation. Broad functional populations are retained between conjugations, though the shape of the RORγT^{+}/IL-17A^{-} population varies between conjugations (Figure 4.3b 'Donor 1 Staining', 'Repeat Conjugation Donor 1 Staining' and 'Donor 2 Staining'). The frequency of RORγT^{+}/IL-17A^{+} T cells also differs between donors, as shown between Donors 1 and 2. Our flow cytometry findings show that the RORγT-AF647 conjugated Merck IHC antibody can detect RORγT^{+} Th17s from PBMCs in flow cytometry, which will be of use in this thesis but also for the wider community as a RORγT antibody for flow cytometry. We therefore decided that if this antibody could stain NSCLC sections by IHC it would be confirmed as appropriate for our study.

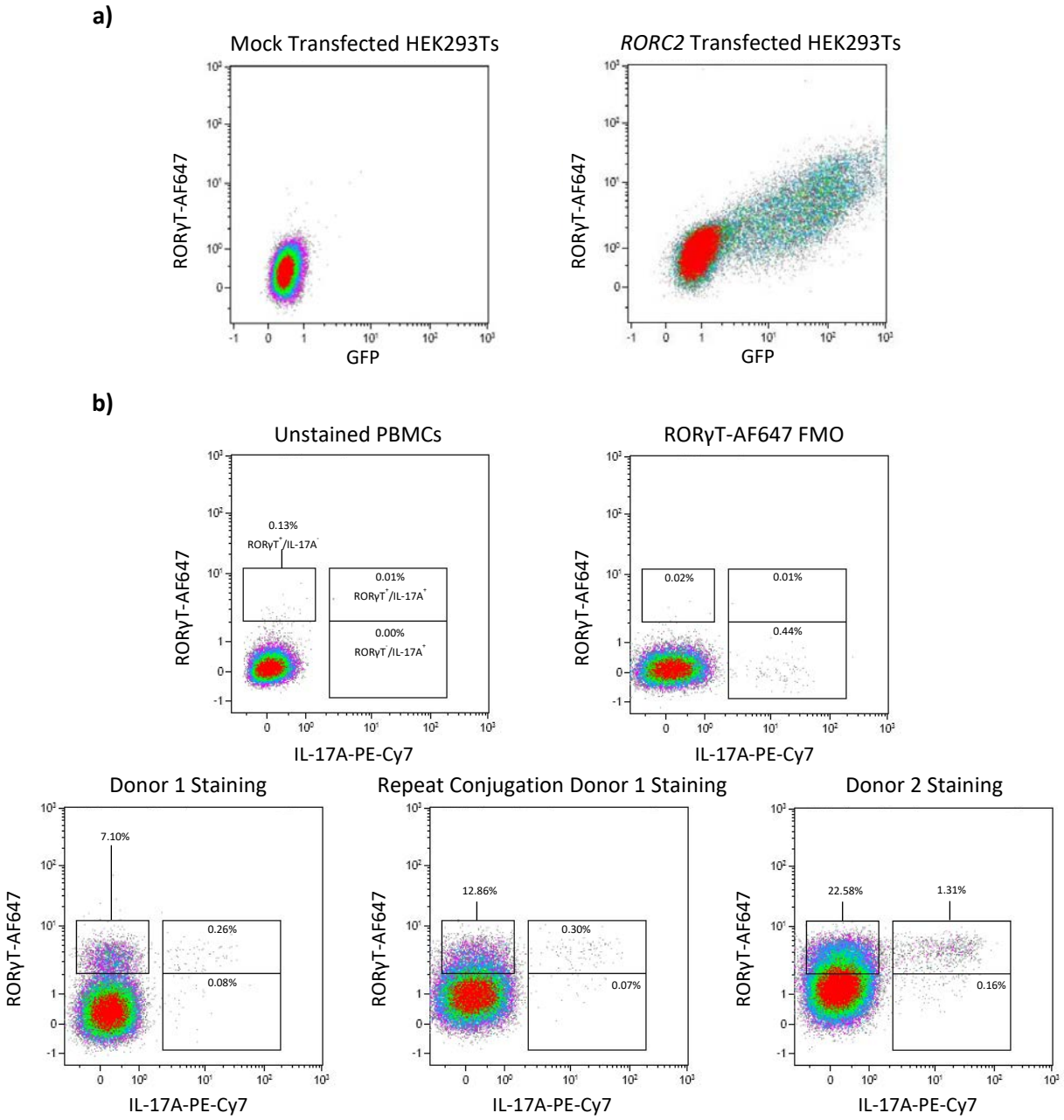

Figure 4.3 RORγT-AF647 conjugated antibody multi-colour flow cytometry validation using transfected HEK293T cells and PBMCs

a) HEK293Ts were gated to the stoppage gate (Figure 2.4). Compensation bead controls for the FITC (GFP) and APC (AF647) channels were used to compensate this experiment (Chapter 2.6.2). **b)** PBMCs were stained using the Th17 flow cytometry antibody panel (Chapters 2.6.3 and 2.6.4) and were gated to the $CD3^+/CD4^+$ lymphocytes as shown in Figure 2.4. Compensation bead controls for all the fluorophores used in the Th17 flow cytometry antibody panel were used. The $ROR\gamma T^-/IL\text{-}17A^+$ gate was set using the unstained control PBMCs. The $ROR\gamma T^+/IL\text{-}17A^-$ and $ROR\gamma T^+/IL\text{-}17A^+$ gates were set using the RORγT-AF647 FMO control PBMCs which are PBMCs stained with all Th17 antibodies except the RORγT-AF647 antibody.

The aim of the final antibody validation experiment was to check whether the Merck RORγT antibody can stain RORγT^{+} cells in human NSCLC tissue sections. After titrating the RORγT antibody by using IHC staining on NSCLC tissue in a similar fashion to the tonsil titration, we achieved the optimised staining demonstrated in Figure 4.4. The control images in the '20X Tonsil' column show expected control staining and encouragingly the images in the '10X NSCLC' and '20X NSCLC' columns show cells expressing nuclear RORγT. These RORγT^{+} cells appear as lymphocytes and are a similar size to the tonsillar lymphocytes. As the secondary only controls did not show any background staining in NSCLC, we were confident that this Merck IHC antibody was able to detect RORγT expressing cells in NSCLC without any contribution from a non-specific secondary antibody, and we decided to use this antibody in our subsequent experiments.

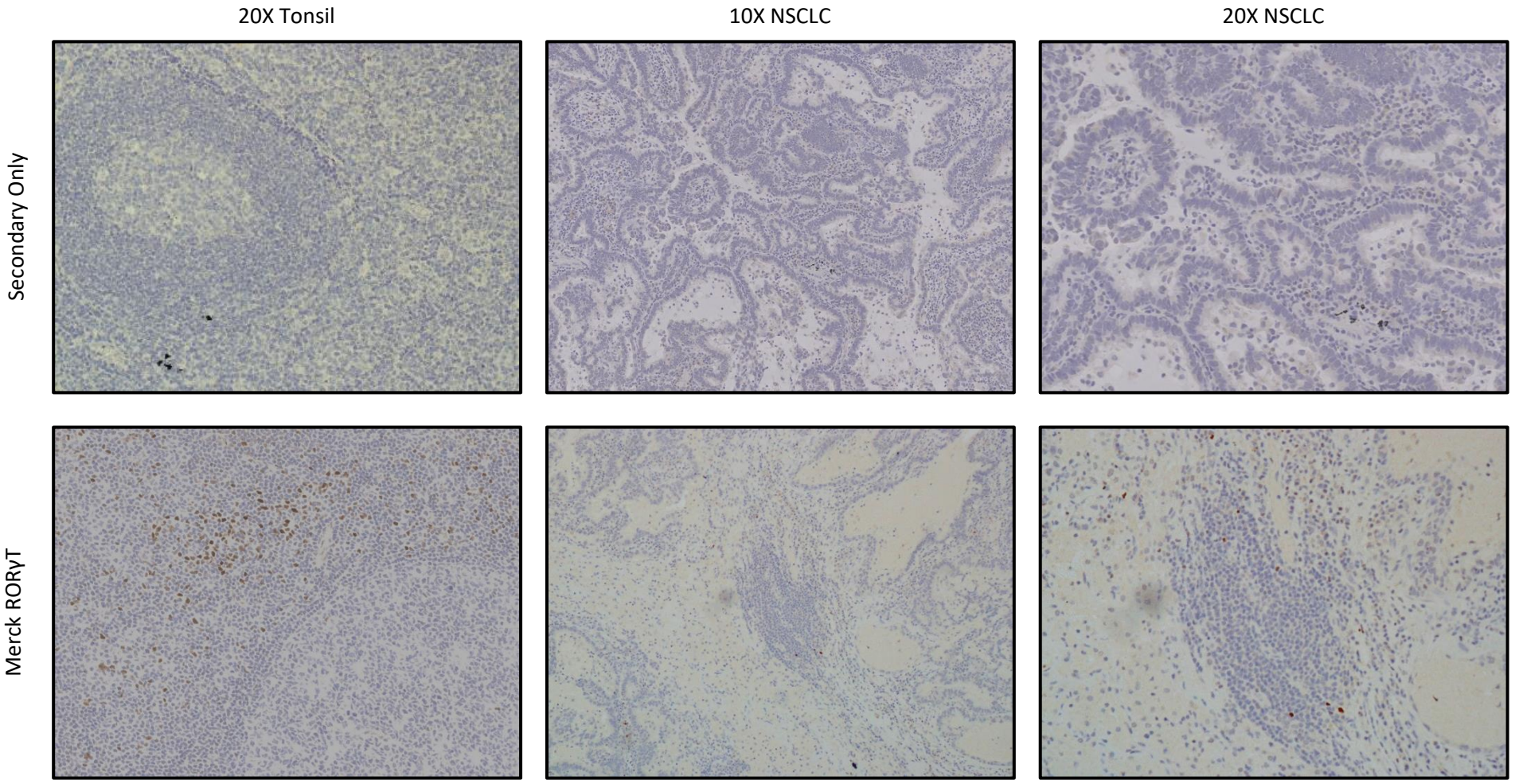

Figure 4.4 RORγT IHC staining NSCLC tumour tissue

Sectioned NSCLC tumour and tonsil were IHC stained by the Merck RORγT antibody (Chapter 2.5.1). Secondary only control staining used the anti-mouse secondary antibody.

4.2.2 Cells Expressing RORγT Protein in Non-Small-Cell Lung Cancer

Having validated and optimised a monoclonal antibody to detect RORγT expression by IHC, we sought to continue the work described in Chapter 3 and investigate whether increased *RORC* mRNA expression translates into increased RORγT protein expression in *KRAS* and *STK11* mutated tumours. Before this investigation we set out to determine which cell type in NSCLC resections are predominantly expressing the RORγT protein. We were particularly interested in interrogating the findings by Huang *et al.* (437), who reported that NSCLC tumour cells express RORγT and suggest that these tumour cells may imitate the behaviour of RORγT^{+} lymphocytes.

To assess which cells are expressing RORγT, we stained the cohort of NSCLC resections with the newly validated IHC antibody and images from four different NSCLC cases are shown in Figure 4.5. We found evidence of RORγT tumour cell expression in 25/28 cases, with the arrows on the three images labelled 'RORγT^{+} Tumour Cells LUAD' showing examples of positive tumour cell staining. This tumour cell staining was very variable between cases and was often very weak; yet pathology review by Dr Abeer Shaaban verified that this staining appeared to be genuine. The pathologist also confirmed that the majority of cells strongly expressing RORγT in NSCLC were lymphocytes, as can be seen throughout Figure 4.5.

This weak positive RORγT tumour cell staining might be as a result of 1q21.3 amplifications as described in Chapter 3. Although the SMP2 study did not profile CNAs, these data were available as part of the TRACERx study. 15/23 TRACERx cases had whole genome

duplications, however we were unable to determine whether any cases had focal 1q21.3 amplifications using the TRACERx copy number analysis methodology.

Another way of understanding the cases with RORγT^{+} tumour cells is to look at the three cases without tumour cell expression. All three of these cases were of LUAD histology as represented by the Figure 4.5 image labelled 'RORγT^{-} Tumour Cell LUAD'. However, as 22/28 cases are LUAD, histology is unlikely to be a connecting factor. It is important to note that 2/3 cases without tumour cell expression had been sectioned from the tumour blocks a few weeks prior to staining, whereas the 23 TRACERx cases with tumour cell expression had been sectioned and stored for over two years. These data suggest that many LUAD tumour cells express RORγT, although this was very weak in comparison to infiltrating lymphocytes. Nevertheless, as the majority of RORγT expression in the NSCLC sections was of lymphocyte origin, we decided to investigate this in the context of *KRAS* and *STK11* cancer gene mutations.

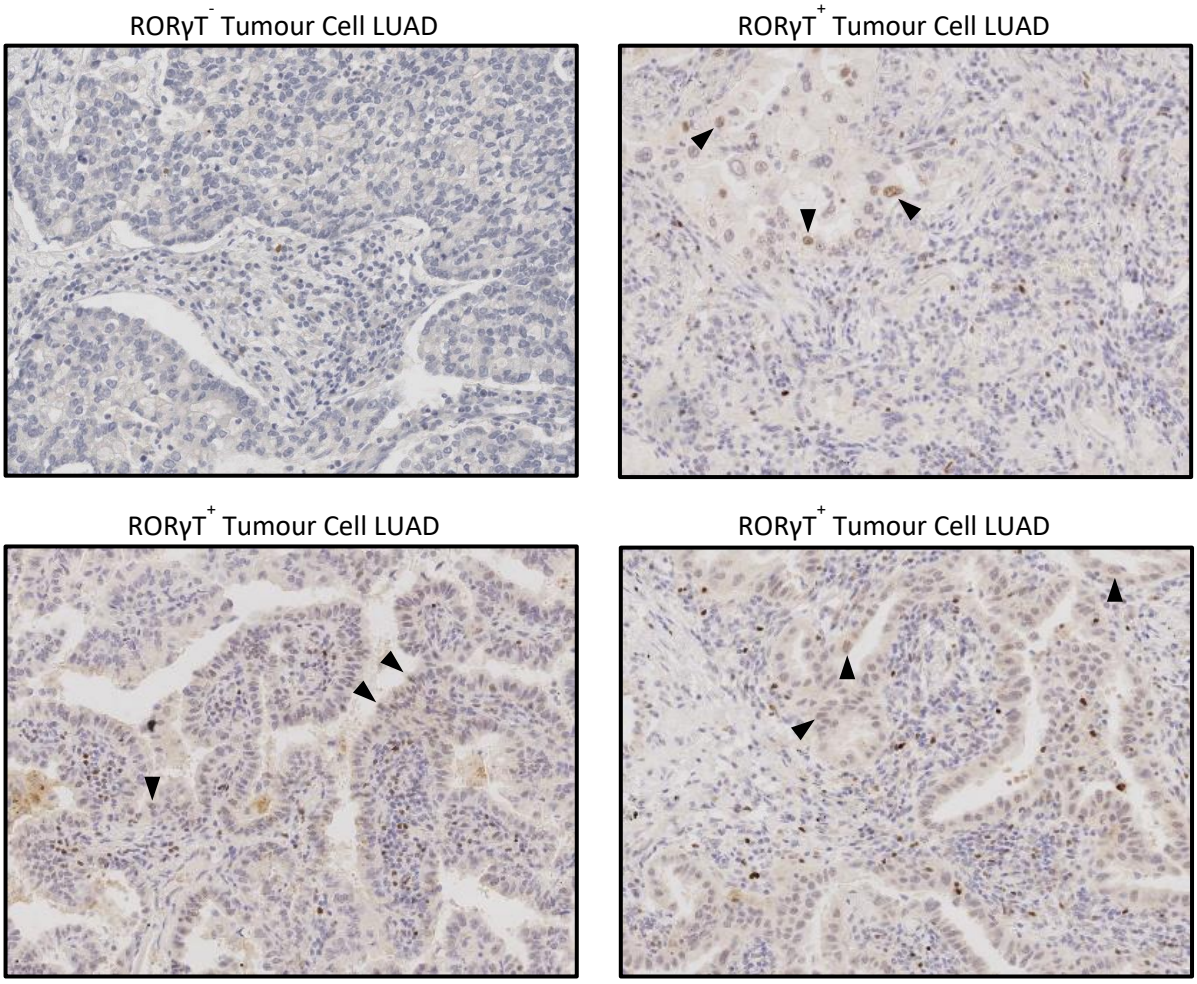

Figure 4.5 RORγT expression in tumour cells and lymphocytes

Sectioned LUAD tumour were IHC stained by RORγT antibody (Chapter 2.5.1). Each 20X image is of a different case. The black arrows highlight RORγT^{+} tumour cells.

4.2.3 Quantifying RORγT Lymphocyte Expression in Mutational Subtypes of Non-Small-Cell Lung Cancer

Our key finding from the previous Chapter was that *RORC* mRNA expression was upregulated in patients with cancer gene mutations in *KRAS* or *STK11* and patients with concomitant *KRAS/STK11* mutations. As there is not always a positive linear relationship between gene and protein expression (435, 436), we set out to quantify RORγT protein positive cells in the cohort of TRACERx and SMP2 resections, focusing on the strong lymphocyte RORγT expression seen by IHC. We collected sections from 10 patients with

KRAS mutations, 4 patients with *STK11* mutations, 5 patients with *KRAS/STK11* mutations and 9 WT patients without mutations in these two cancer genes. We used a digital pathology approach using supervised machine learning performed in the inForm software to quantify RORγT$^+$ lymphocytes.

The first challenge in this analysis was training the software algorithm to recognise the matte black anthracotic pigment which naturally accumulates in the lung from the environment and is highlighted by the box in the *KRAS/STK11* case in Figure 4.6a. Preliminary versions of this algorithm recognised this pigment as being DAB positive cells, so we successfully trained a classifier to identify this pigment and omit it from the analysis. This is shown in the phenotype maps on the right panel of each case in Figure 4.6a as white dots. The algorithm was then trained to phenotype RORγT$^+$ lymphocytes (red dots), and all other cells (green dots) which included RORγT$^+$ tumour cells. All the images in Figure 4.6a are phenotype exports from this RORγT IHC Quantification Algorithm, showing representative quantification regions from each mutation group.

Comparing RORγT$^+$ lymphocyte abundance between the WT group and the MT group (which contained all cases with *KRAS* and *STK11* mutations) showed a significantly higher abundance of RORγT$^+$ lymphocytes in the MT group (p = 0.0248) (Figure 4.6b). This appeared to be driven by the *KRAS* mutation group, which alone had a significantly higher abundance of RORγT$^+$ lymphocytes vs the WT group (p = 0.0101). Whilst having higher median RORγT$^+$ lymphocyte abundances compared to the WT group, neither the *STK11* nor *KRAS/STK11* groups reached significance. This may be due to the lower number of

resection samples in these groups (*n* = 4 and *n* = 5 respectively) compared to the *KRAS* mutation group (*n* = 10).

The groups with *KRAS* and *STK11* mutations displayed notable heterogeneity in their RORγT$^+$ lymphocyte abundances. A few highly positive samples had more than 100 RORγT$^+$ lymphocytes/10,000 cells and interestingly all these patient tumours were linked by an absence of whole genome duplications (square points on the Figure). Furthermore, cases with low RORγT$^+$ lymphocyte abundance were of non-LUAD histology (triangle points). 5/6 of these non-LUAD cases were SqCC and the last case was a mixed adenosquamous carcinoma. These data show that there is a link between *KRAS* and *STK11* cancer gene mutations and higher RORγT$^+$ lymphocyte abundance, and that intra-group heterogeneity can be explained by whole genome duplication events.

Using a similar approach to the *RORC* mRNA survival analysis in Figure 3.10, patient tumours were grouped into quartiles based on the number of RORγT$^+$ lymphocytes/10,000 cells. Patients in the 'RORγT High' group (quartile one) had a significantly reduced OS compared to patients in the quartiles two and three grouped as 'RORγT Other' (p = 0.0169) (Figure 4.6c). Moreover, there was significant difference in OS when further separating out the lowest quartile in the right-hand plot in Figure 4.6c (p = 0.0210), with the 'RORγT Low' (quartile four) group having the most favourable Kaplan-Meier curve. Altogether, there is an increased abundance of RORγT$^+$ lymphocytes in patient tumours with *KRAS* and *STK11* mutations and having high abundances of these cells is linked to a worse OS.

a)

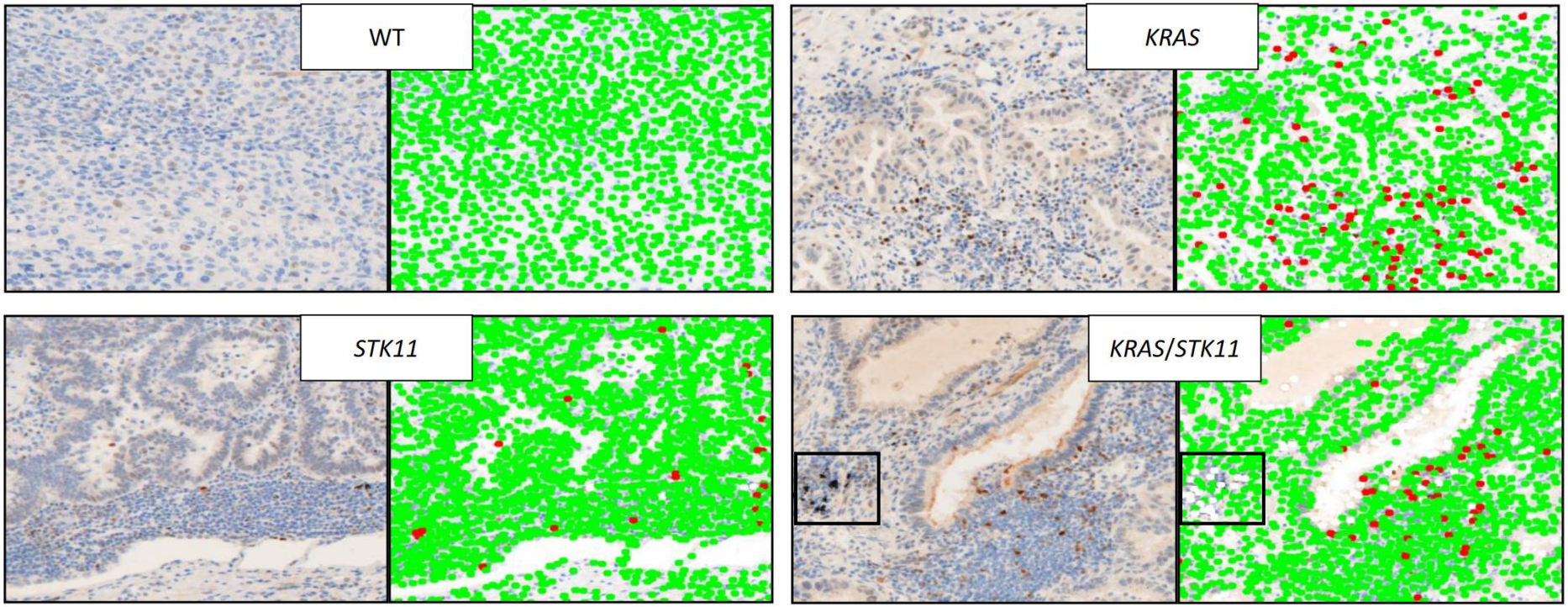

b)

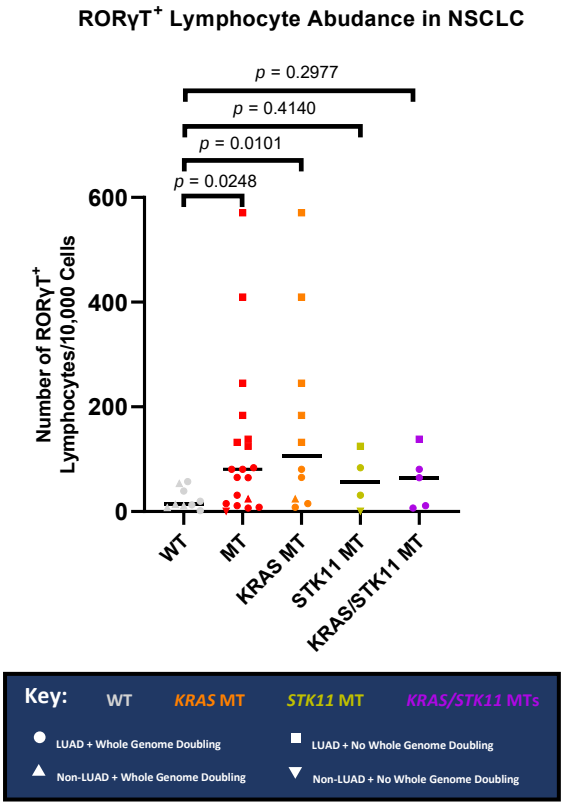

c)

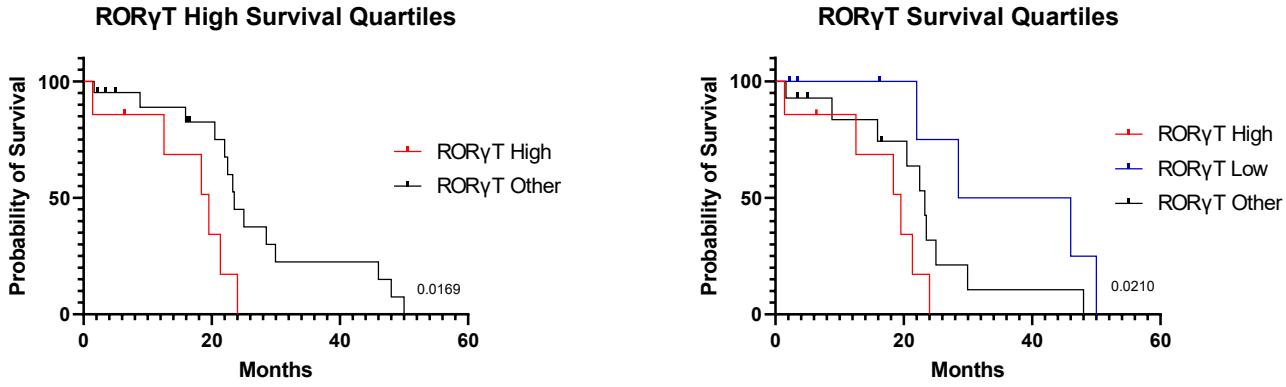

Figure 4.6 RORγT⁺ lymphocyte quantification in patient tumours with *KRAS* and *STK11* mutations and survival analysis

a) Export images from inForm software using the RORγT IHC Quantification Algorithm (Chapter 2.5.2) from four different patients of differing *KRAS* and *STK11* mutational subtypes. Left-hand images show RORγT IHC stained tumour. Right-hand images show the matched export phenotyping image in which red dots signify RORγT⁺ lymphocytes, green dots signify all other cells, and white dots signify anthracotic pigment. The box in the *KRAS/STK11* case highlights anthracotic pigment identified by the algorithm. **b)** RORγT⁺ lymphocytes from 30% of the 10X scanned regions (randomly selected) shown as RORγT⁺ lymphocytes/10,000 cells for each patient tumour. Patients are group by presence or absence of *KRAS* and *STK11* mutations (WT *n* = 9, MT *n* = 19, *KRAS* MT *n* = 10, *STK11* MT *n* = 4, *KRAS/STK11* MTs *n* = 5). The key shows the histology and whole genome doubling status of each tumour. Statistical comparisons between groups were by unpaired two-

sample Wilcoxon tests. **c)** Kaplan-Meier curves of patients divided into quartiles based on RORγT$^+$ lymphocytes/10,000 cells. The 'RORγT High' group represents patients with RORγT$^+$ lymphocytes/10,000 cells abundances in the 1st quartile, the 'RORγT Other' group represents patients in the 2nd and 3rd quartiles, and the 'RORγT Low' group represents patients in the 4th quartile. OS was calculated from cancer diagnosis to death or last follow up at relapse and plotted as Kaplan-Meier curves then statistically compared using Mantel-Cox tests.

4.2.4 Spatially Evaluating RORγT$^+$ Lymphocytes in Mutational Subtypes of Non-Small-Cell Lung Cancer

Having identified RORγT$^+$ lymphocytes in tumours, we wanted to assess whether these lymphocytes were localised in particular regions of the tumour tissue. Before training the inForm algorithm to segment and quantify within tissue segmentation categories, we performed several IHC stains under the advice of a pathologist to determine which tissue types were present in each tumour and where they were.

The H&E image in Figure 4.7a shows four major structures within NSCLC tumours. Region 1 highlights a group of stained lymphocytes. The fibrotic Region 2 contains stromal fibroblasts with their branched cytoplasm. Region 3 shows a NSCLC tumour nest with a cribriform pattern and Region 4 is a densely eosin-stained layer of connective tissue.

To further affirm the tumour nests (Region 3), we stained the sections with an *in vitro* diagnostic IHC antibody against CK7 which is used clinically to distinguish between primary NSCLC and lung metastases. No staining was observed in the negative tonsil control or in areas of resected normal lung peripheral to the bulk tumour (Figure 4.7b). As expected, the tumour compartment of our NSCLC cases stained CK7$^+$.

Effective adaptive immune responses to cancer are often generated in structures called tertiary lymphoid structures (TLS). Though B and T cell phenotyping is required to confirm

TLS presence, we firstly chose to probe for the anti-apoptotic protein Bcl-2 which can be present in both cell types in the tumour. Collectives of Bcl-2^{+} lymphocytes signify lymphoid aggregates. Running a secondary antibody only control showed no non-specific secondary antibody staining of the positive tonsil control tissue (Figure 4.7c). Furthermore, Bcl-2 staining the secondary lymphoid organ controls (tonsil and pulmonary lymph node) showed strong nuclear membrane and weak cytoplasm staining in interfollicular lymphocytes and largely negative germinal centres. The final image from Figure 4.7c shows that this antibody can stain lymphocytes in NSCLC and can effectively highlight tumour associated lymphoid aggregates.

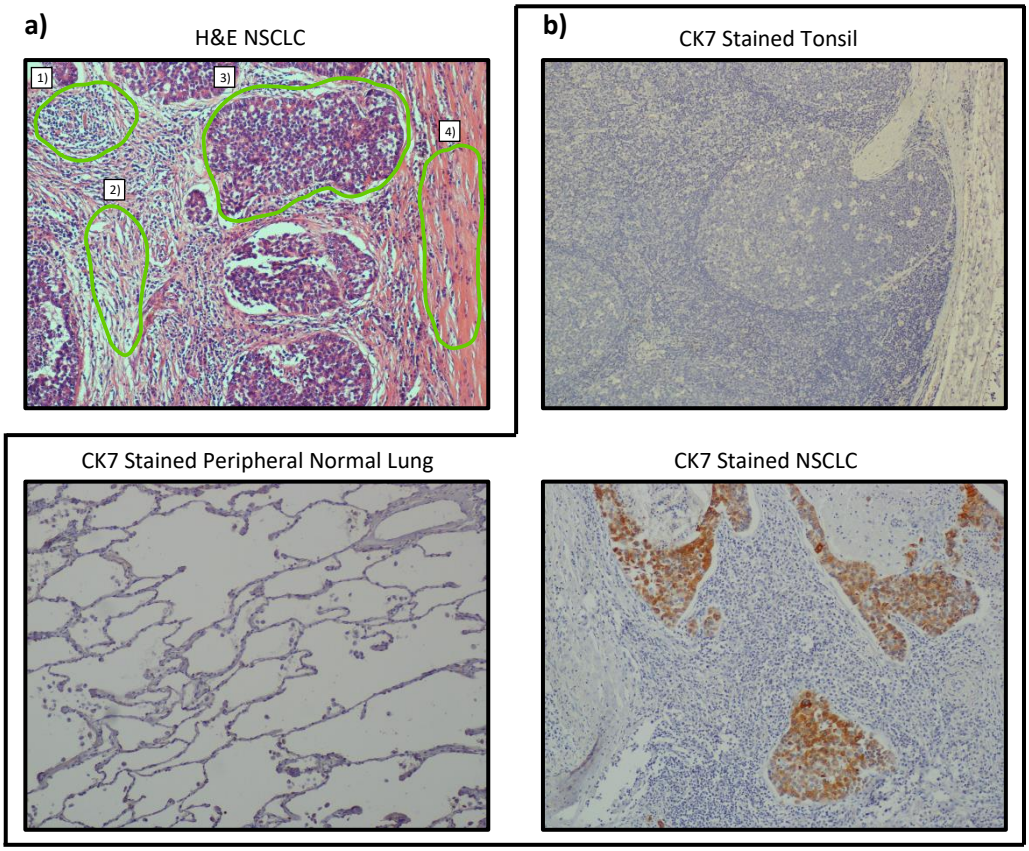
a)
H&E NSCLC
1)
2)
3)
4)
b)
CK7 Stained Tonsil
CK7 Stained Peripheral Normal Lung
CK7 Stained NSCLC

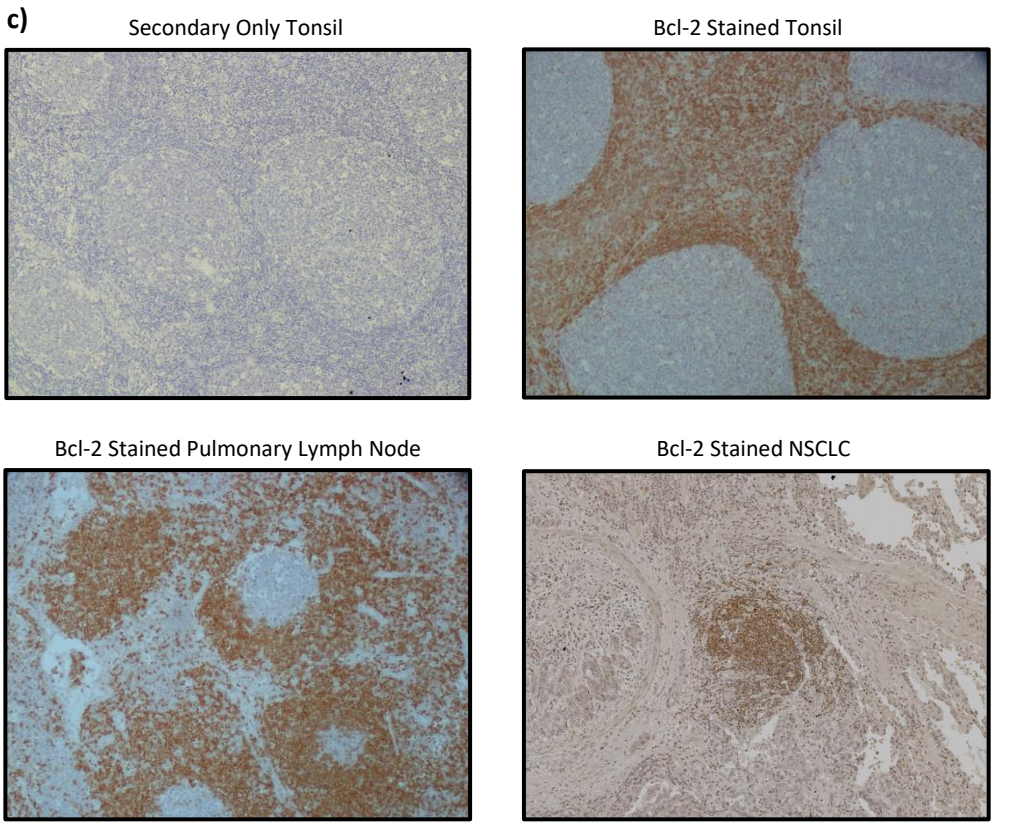
c)
Secondary Only Tonsil
Bcl-2 Stained Tonsil
Bcl-2 Stained Pulmonary Lymph Node
Bcl-2 Stained NSCLC

Figure 4.7 H&E and IHC staining structures of interest in NSCLC

a) H&E NSCLC staining was kindly performed by the Thoracic Research Team at University Hospitals Birmingham Heartlands Hospital NHS Foundation Trust. **b)** CK7 IHC staining on tonsil and NSCLC resections were performed as outlined in Chapter 2.5.1. The CK7 staining imaged in 'CK7 Stained Peripheral Normal Lung' and 'CK7 Stained NSCLC' are images from different regions of the same patient resection. **c)** Bcl-2 IHC staining on tonsil, NSCLC and lymph node resections were performed as outlined in Chapter 2.5.1. The 'Secondary Only Tonsil' is control staining using the anti-mouse secondary antibody used in the Bcl-2 IHC staining. All images are at 10X magnification.

Based on knowledge gained from the staining in Figure 4.7, we trained the RORγT IHC Quantification Algorithm with the help of a pathologist to segment the tissue into tumour nest, stroma and lymphoid aggregates, to enable the quantification of $RORγT^+$ lymphocytes in these compartments. An example tissue segmentation can be seen in Figure 4.8a, in which the red zones highlight tumour, the blue zones highlight stroma, and the yellow zones highlight lymphoid aggregates.

We proceeded to spatially quantify $RORγT^+$ lymphocyte abundances, finding near significant higher abundances in tumour, stroma and lymphoid aggregates in patients with MTs compared to WT (Figure 4.8b). When looking at specific mutation groups, the largest *KRAS* group was the only group with a significant difference (Figure 4.8c). We found a significantly higher abundance of $RORγT^+$ lymphocytes in lymphoid aggregates in patients with *KRAS* mutations compared to WT lymphoid aggregates ($p = 0.0435$), and nearly significant higher $RORγT^+$ lymphocyte abundances in the tumour and stroma compartments of *KRAS* mutant tumours compared to WT ($p = 0.0653$ and $p = 0.0503$ respectively).

Similar to Figure 4.6b, Figures 4.8b to 4.8e show that the patient samples without whole genome duplications consistently have higher RORγT$^+$ lymphocyte abundances in the three compartments examined than those with genome duplications.

Though both the *STK11* and *KRAS/STK11* groups were not significantly different to WT alone, there was a tendency for increased RORγT$^+$ lymphocyte abundances in lymphoid aggregates from these groups compared to WT lymphoid aggregates (Figures 4.8d and 4.8e). However, greater number of samples are required to confirm these findings. Overall, RORγT$^+$ lymphocytes are not localised solely to one compartment, but many of these lymphocytes in tumours with *KRAS* and *STK11* mutations can be found within lymphoid aggregates and stroma, in addition to those infiltrating into tumour nests themselves.

a)

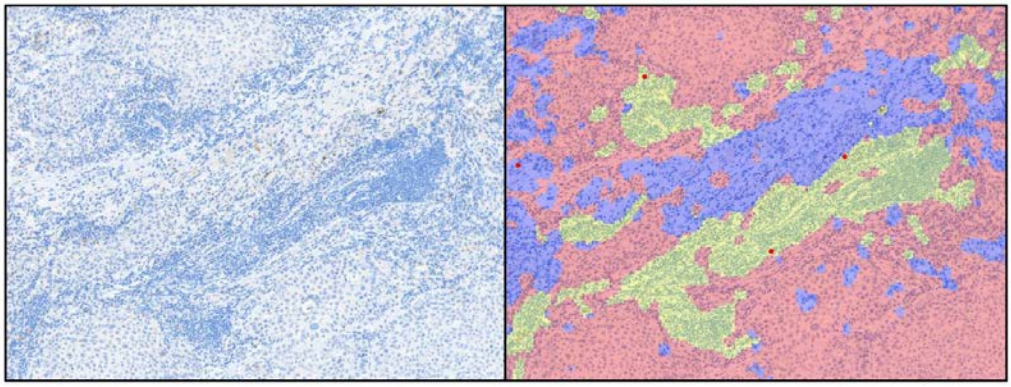

b)

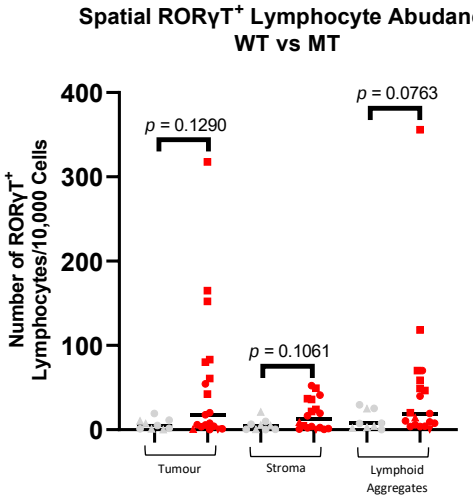
Spatial RORγT+ Lymphocyte Abudance
WT vs MT
Number of RORγT+ Lymphocytes/10,000 Cells
400
300
200
100
0
p = 0.1290
p = 0.1061
p = 0.0763
Tumour
Stroma
Lymphoid Aggregates

c)

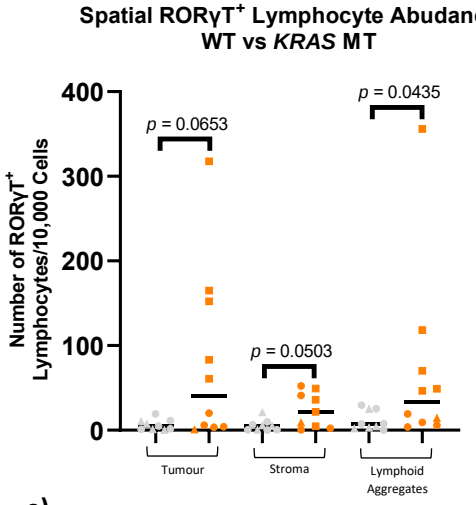
Spatial RORγT+ Lymphocyte Abudance
WT vs KRAS MT
Number of RORγT+ Lymphocytes/10,000 Cells
400
300
200
100
0
p = 0.0653
p = 0.0503
p = 0.0435
Tumour
Stroma
Lymphoid Aggregates

d)

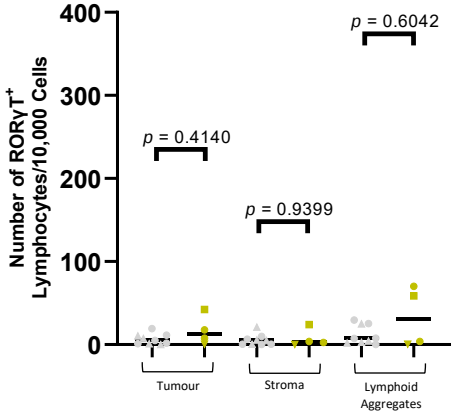
Spatial RORγT+ Lymphocyte Abudance
WT vs STK11 MT
Number of RORγT+ Lymphocytes/10,000 Cells
400
300
200
100
0
p = 0.4140
p = 0.9399
p = 0.6042
Tumour
Stroma
Lymphoid Aggregates

e)

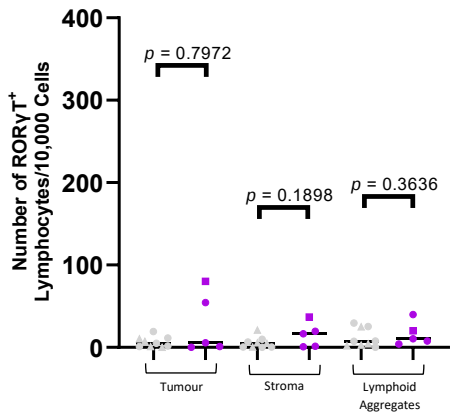
Spatial RORγT+ Lymphocyte Abudance
WT vs KRAS/STK11 MT
Number of RORγT+ Lymphocytes/10,000 Cells
400
300
200
100
0
p = 0.7972
p = 0.1898
p = 0.3636
Tumour
Stroma
Lymphoid Aggregates


Key:
WT
KRAS MT
STK11 MT
KRAS/STK11 MTs
LUAD + Whole Genome Doubling
LUAD + No Whole Genome Doubling
Non-LUAD + Whole Genome Doubling
Non-LUAD + No Whole Genome Doubling

Figure 4.8 Spatial RORγT$^+$ lymphocyte quantification in patient tumours with *KRAS* and *STK11* mutations

a) Export images from inForm software showing tissue segmentation using the RORγT IHC Quantification Algorithm, RORγT IHC (left) and matched export segmented image (right). Red regions = tumour, blue = stroma, yellow = lymphoid aggregates. The red dots on the segmentation image show RORγT$^+$ lymphocytes. **b) – e)** RORγT$^+$ lymphocytes/10,000 cells as described in Figure 4.6 except showing abundances in each segmented tissue region as described in part **a)**. RORγT+ lymphocytes/10,000 cells in each segmented region (tumour, stroma, and lymphoid aggregates) are compared between WT (grey, *n* = 9) and, **b)** MT (red, *n* = 19), **c)** *KRAS* MT (orange, *n* = 10), **d)** *STK11* MT (gold, *n* = 4), **d)** *KRAS/STK11* MT (purple, *n* = 5). Abundances in the same segmented regions were compared between mutation groups using unpaired two-sample Wilcoxon tests. The key shows the histology and whole genome doubling status of each tumour.

RORγT$^+$ lymphocytes are associated with IL-17A expression, which we previously demonstrated in Figure 4.3. We therefore decided to screen the NSCLC cases for IL-17A expression. Using tonsil sections as a positive control, IL-17A$^+$ cells were found in the interfollicular zone as expected, and the secondary only controls both on tonsil and NSCLC did not show evidence of non-specific secondary antibody staining (Figure 4.9). Staining NSCLC sections showed nuclear and cytoplasmic staining as well as secreted IL-17A surrounding cells including lymphocytes. Figure 4.9 importantly shows that IL-17A$^+$ lymphocytes are found in both stromal regions and lymphoid aggregates.

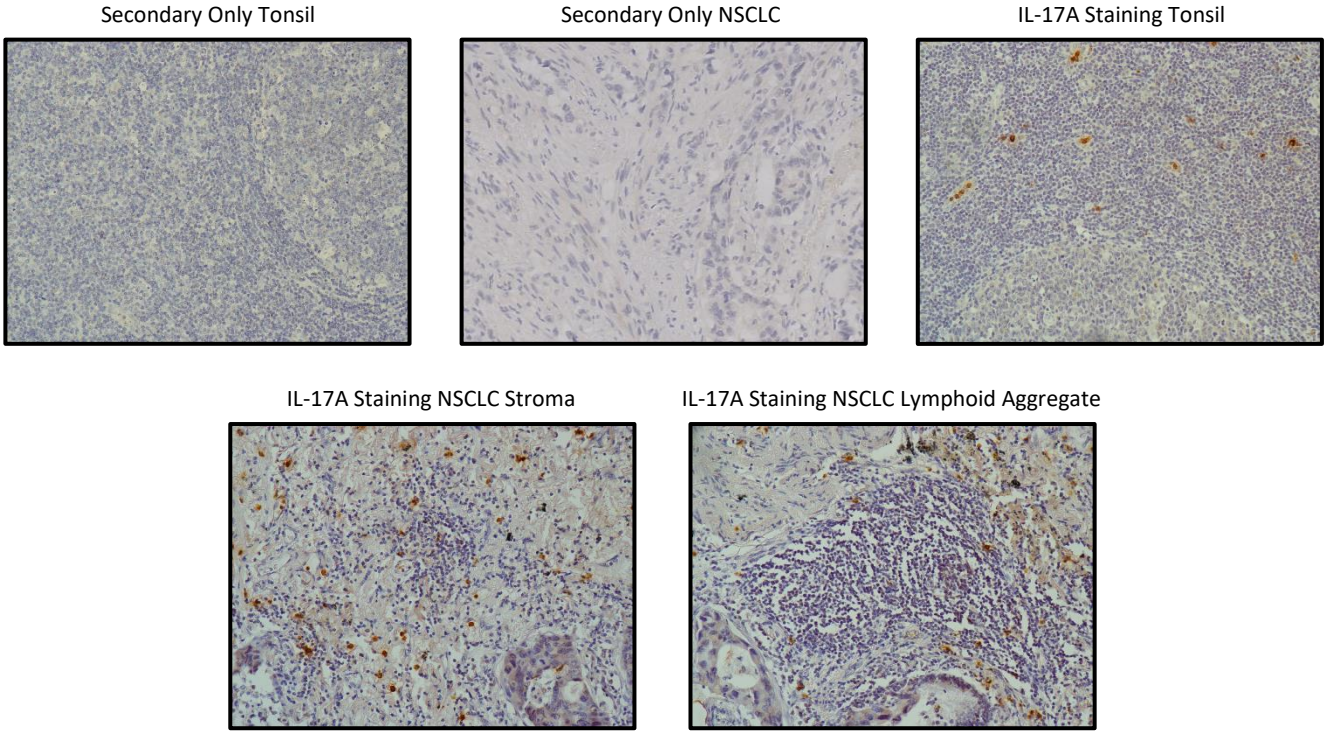

Figure 4.9 IL-17A expression in NSCLC tumours

IHC staining for IL-17A was performed as outlined in Chapter 2.5.1. The secondary only control staining on tonsil and NSCLC used the anti-goat secondary antibody for the IL-17A antibody. All images in this Figure were taken at 20X magnification.

4.2.5 Phenotyping RORγT$^+$ Lymphocytes by Multiplex Fluorescent Immunohistochemistry

We worked closely with the University of Birmingham's Human Bioresources Centre to design a lymphocyte phenotyping panel including the Merck RORγT antibody (Table 4.2). To investigate hypoxic regions, we included the hypoxia inducible gene CA9 into this panel, but only two cases expressed CA9 both showing high levels of expression.

To validate the panel, we used two known RORγT positive tissues, tonsil and CRC. The staining in Figures 4.10a and 4.10b show successful RORγT nuclear staining compatible with the multiplex panel. This nuclear RORγT staining was present in CD3$^+$/CD4$^+$ T cells, as

well as in T cell lineage marker negative cells in both tissues. After confirming the panel worked using tonsil and CRC sections we stained the NSCLC sections. Figures 4.10c and 4.10d show that RORγT^{+} lymphocytes are found around lymphoid aggregates containing T cells and CD20^{+} B cells confirming the localisation in Figure 4.8, moreover some of these lymphocytes are CD3^{+}/CD4^{+}/RORγT^{+} Th17 cells. Furthermore, RORγT^{+}/CD3^{-}/CD4^{-} lymphocytes are also present. Our initial findings with this panel therefore demonstrated that we can identify CD3^{+}/CD4^{+}/RORγT^{+} Th17s in NSCLC and that not all RORγT^{+} lymphocytes are CD3^{+}/CD4^{+} Th17s. It also demonstrated that the lymphoid aggregates found throughout the cohort of NSCLC tumours are comprised of CD20^{+} B cells and CD3^{+} T cells.

Marker	Opal Fluorophore
DAPI	N/A
RORγT	Opal 520
CD4	Opal 570
CA9	Opal 620
CD3	Opal 650
CD20	Opal 690

Table 4.2 Multiplex fluorescent IHC antibody immunophenotyping panel

Antibody panel and corresponding Opal fluorophore. DAPI was counterstaining after panel staining. See Chapter 2.5.4 and Figure 2.2 for further details on the panel antibodies and the protocol.

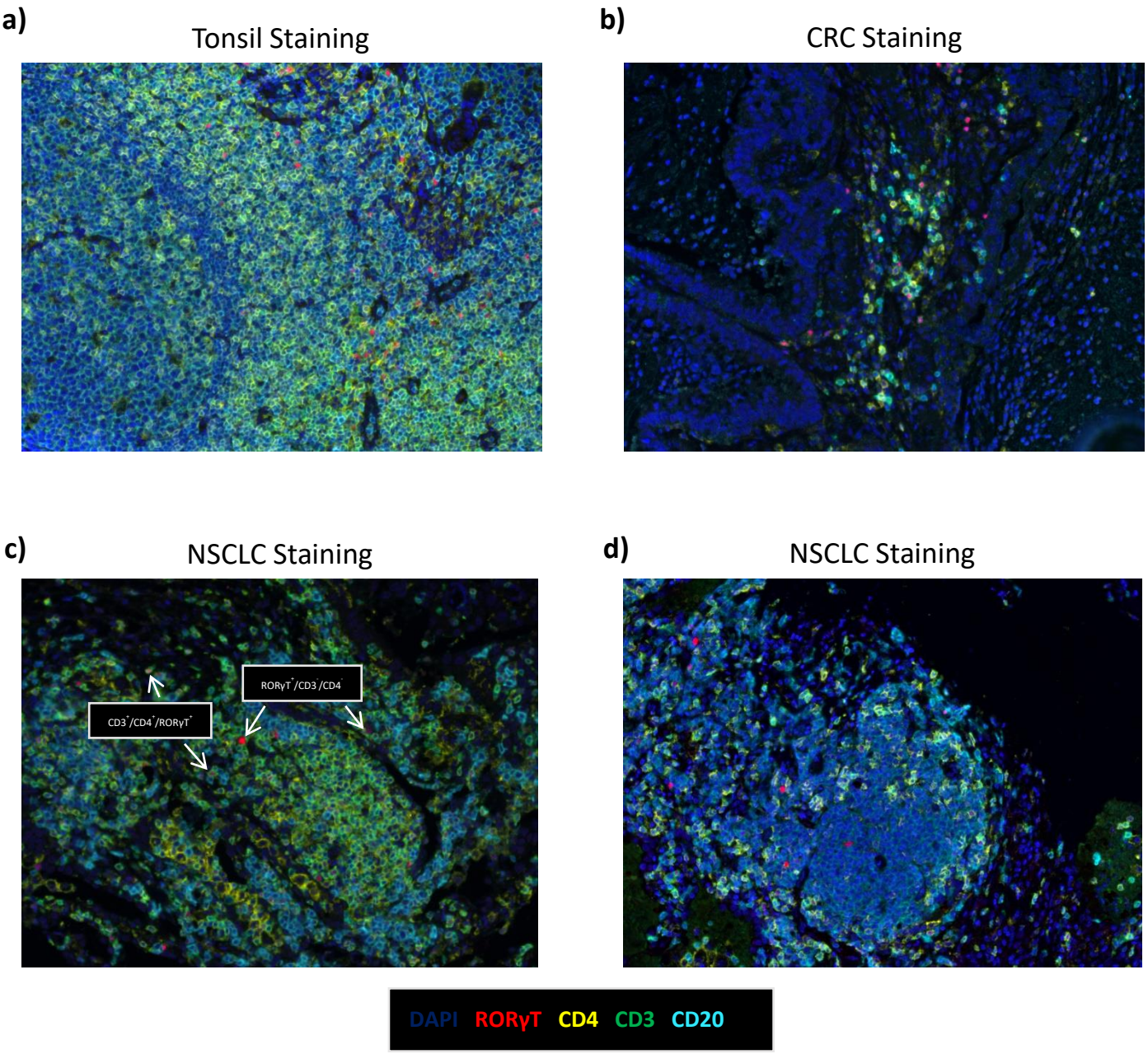

Figure 4.10 Multiplex fluorescent immunophenotyping validation staining and NSCLC staining

Positive validation control tonsil **a)**, CRC tumour **b)**, and NSCLC tumour **c) d)** sections were stained using the multiplex fluorescent immunophenotyping panel (Chapter 2.5.4). $CD3^+/CD4^+/ROR\gamma T^+$ and $ROR\gamma T^+/CD3^-/CD4^-$ lymphocytes, as confirmed by a pathologist, are highlighted. The key shows the artificial colours of the panel markers. All images are at 20X magnification.

We next wanted to establish whether the tumour associated lymphoid aggregates seen are TLSs. Though there are various definitions for what constitutes a true TLS in the literature (153, 154, 163, 164, 173), one major consistent feature is that they contain

organised B and T cells. Figure 4.11a shows that we can match Bcl-2$^+$ and multiplex stained lymphoid aggregates. The comparative 2X multiplex staining image was only available as a spectrally mixed overview image in which fluorescent spillover is still present. The yellow staining shows CD4$^+$ T cells and the red staining predominantly shows CD20$^+$ B cells. Staining from Figure 4.10c and 4.10d show that lymphoid aggregates clearly contain CD4$^+$ T cells and CD20$^+$ B cells suggesting that these are TLSs. Most TLSs in Figure 4.11a have follicular-like structures characterised by presence of CD20$^+$ B cells and Bcl-2 negativity.

Considering the data from these two stains, we enumerated all Bcl-2$^+$ TLS in the NSCLC sections and calculated TLS density. We found no significant difference in TLS density between WT and MT tumours with *KRAS* and *STK11* mutations (Figure 4.11b). This suggests that the near significant increased RORγT$^+$ lymphocyte abundance in lymphoid aggregates from patient tumours with *KRAS* and *STK11* mutations from Figure 4.8 is not because of an increased TLS burden. Rather, the differences seen are due to altered TLS composition and an increased number of RORγT$^+$ lymphocytes per TLS.

a)

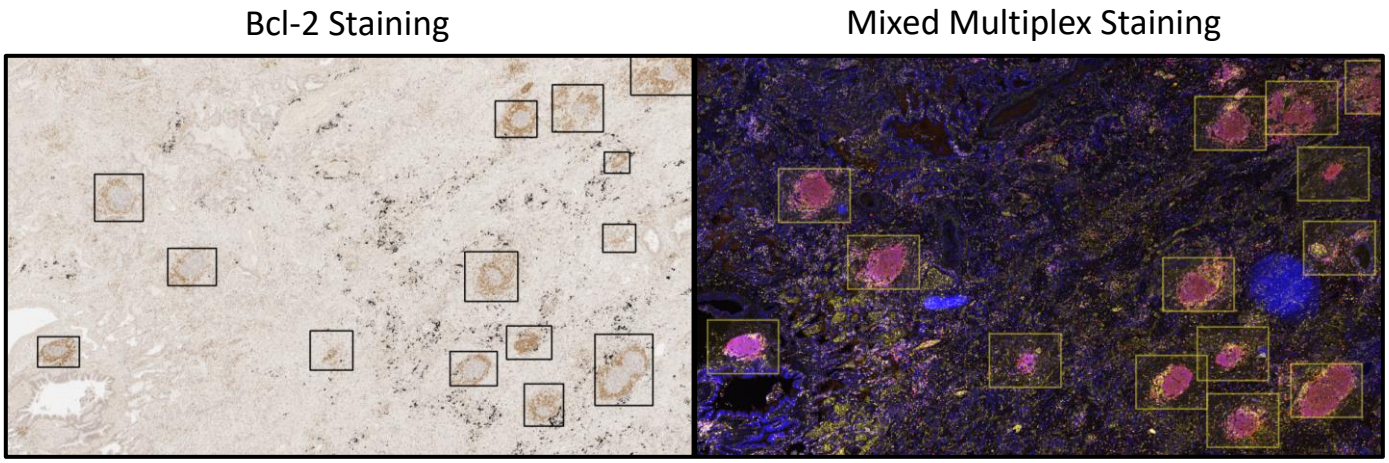

b)

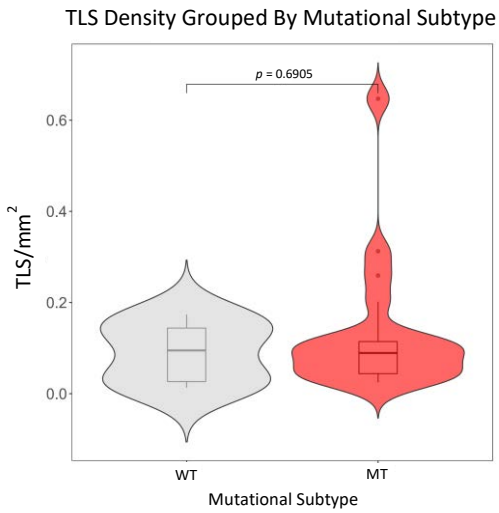

Figure 4.11 Confirmation and quantification of NSCLC TLSs

a) Both images are 2X scans from the same tumour: left-hand image shows Bcl-2 IHC staining, right-hand image shows multiplex fluorescent immunophenotyping panel staining. The 'Mixed Multiplex Staining' overview image (Phenochart software) shows the CY3 (yellow, showing $CD4^+$ cells) and CY5 (red, showing $CD20^+$ cells and some $CD3^+$ cells due to spillover from Texas Red) channels. Squares highlight examples of TLSs. **b)** TLS were defined as Bcl-2^+ structures with B and T cells and a diameter of at least 100µm. TLS in each tumour were counted and divided by the tumour area to give TLS/mm^2. Patient tumours were grouped by *KRAS* and *STK11* mutation (MT, *n* = 19) or lack of these mutations (WT, *n* = 8). TLS densities were compared by unpaired two-sample Wilcoxon test.

We were next interested in unbiasedly establishing which cells expressed RORγT in TLSs.

To do this we trained new inForm machine learning algorithms that detect cells positive

for single markers. These data were then processed by the *phenoptr* R package which also

performed an unbiased marker co-expression analysis that determined the immune phenotypes shown in Figure 4.12c.

Before training the 'Single Phenotyping' algorithms which detect only a single marker at a time, we firstly extensively trained a 'Full Phenotyping' algorithm that could recognise all possible single marker positive to triple marker positive phenotypes (e.g. from $CD3^+$ to $CD3^+/CD4^+/ROR\gamma T^+$) which is shown here as a reference for the training of the 'Single Phenotyping' algorithms (Figure 4.12a). The 'Unmixed Multiplex Staining' image shows multiplex immunophenotyping panel staining without any computationally classified cellular phenotypes from either the 'Full Phenotyping' or 'Single Phenotyping' algorithms.

We then proceeded to train five 'Single Phenotyping' algorithms to detect each marker individually. Figure 4.12a shows all the 'Single Phenotyping' algorithms of interest and how these algorithms classify cellular phenotypes within the same stroma region. For example, the 'CD3 Single Phenotyping' algorithm classified cells as either '$CD3^+$' or 'Other' ($CD3^-$). Figure 4.12b similarly profiles TLS. Spatial data exported from all images containing TLSs profiled by the 'Single Phenotyping' algorithms were used to consolidated and unbiasedly report phenotypes as shown in Figure 4.12c.

Figure 4.12c shows results from the unbiased co-expression analysis using the 'Single Phenotyping' algorithms. 'Intersection size' refers to the number of cells expressing each combination of markers, representing different cellular phenotypes. As expected, most of the cells counted by in TLSs were $CD20^+$ B cells, followed by $CD3^+$ and $CD4^+$ T cells. Moreover, CD20 and CD3 were most often expressed without any marker co-expression, indicating that B cells and $CD4^-$ T cells were of high abundance.

The most commonly co-expressed markers from our panel were CD3/CD4, which highlight $CD4^+$ T cells (Figure 4.12c). This analysis also highlights rarer phenotypes which would require further confirmation by investigating a larger number of TLSs. One such rarer potential phenotype are $CD20^+$ cells co-expressing CD3 and/or CD4.

RORγT expressing phenotypes are highlighted in Figure 4.12c by red boxes. RORγT is most frequently expressed alone in TLSs (intersection size of 2108), followed by co-expression with the T cell markers CD3 and CD4 (total intersection size of 2026 from $CD3^+/CD4^+/ROR\gamma T^+$, $CD3^+/ROR\gamma T^+$ and $CD4^+/ROR\gamma T^+$ phenotypes). These findings demonstrate that NSCLC TLSs are dominated by B and T cells, and that $ROR\gamma T^+$ cells found in these regions co-express T cell lineage markers, yet T cell lineage marker negative $ROR\gamma T^+$ cells are also present.

a)

Unmixed Multiplex Staining

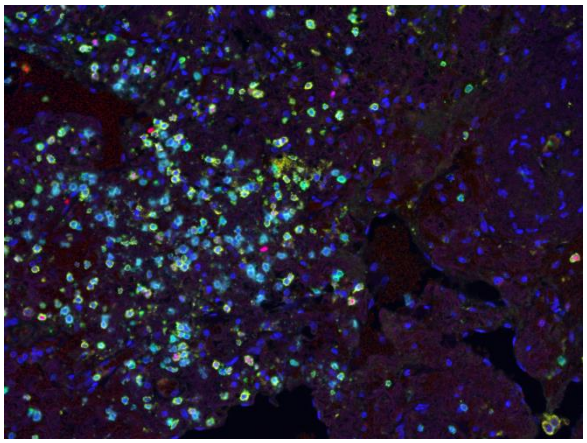

Full Phenotyping

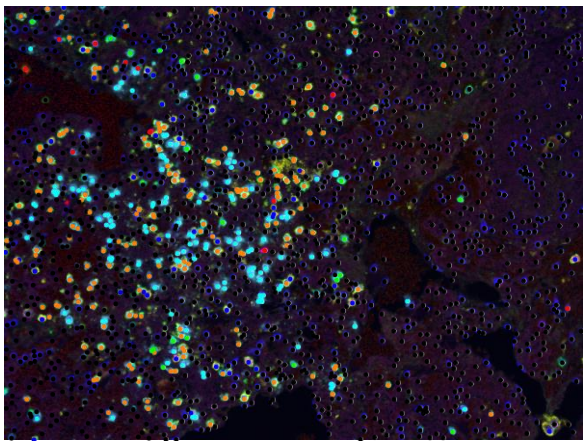

RORγT Single Phenotyping

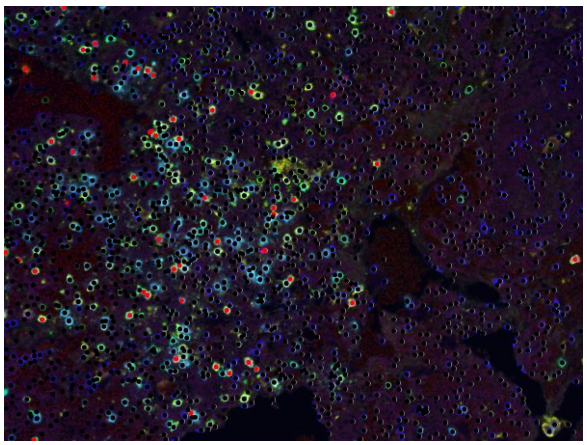

CD3 Single Phenotyping

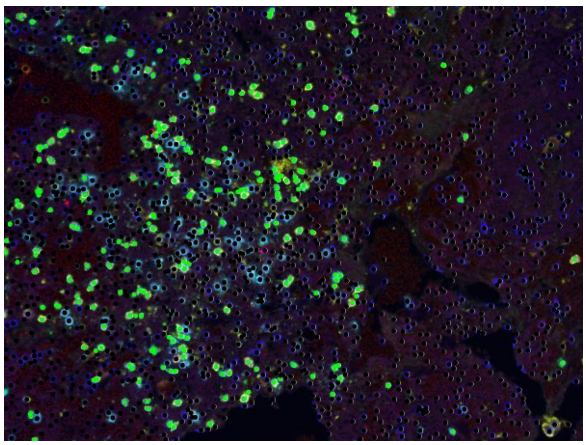

CD4 Single Phenotyping

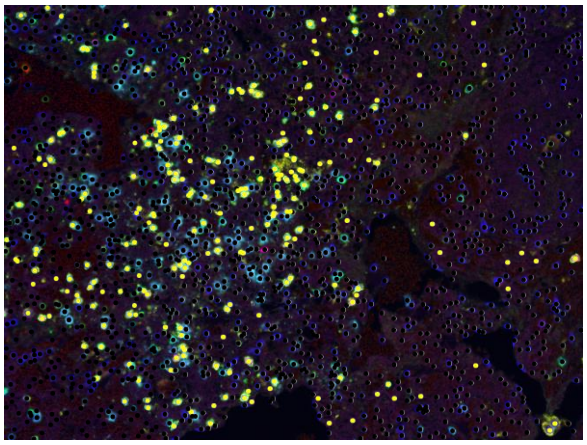

CD20 Single Phenotyping

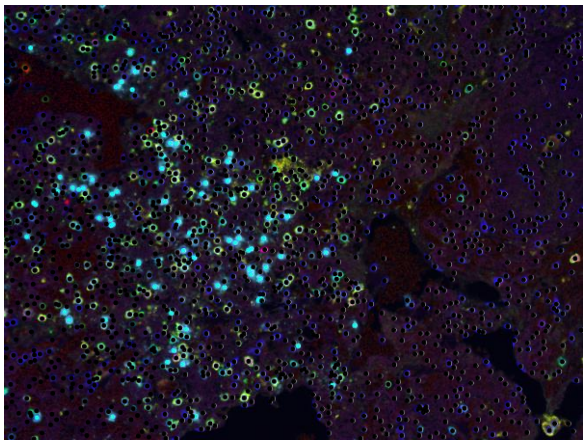

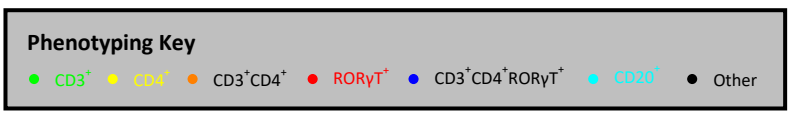

b)

Unmixed Multiplex Staining

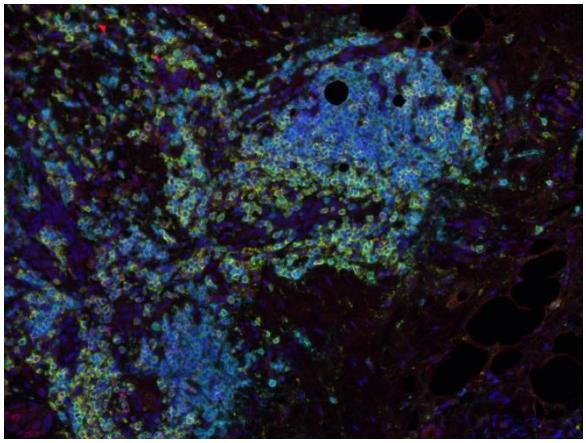

Full Phenotyping

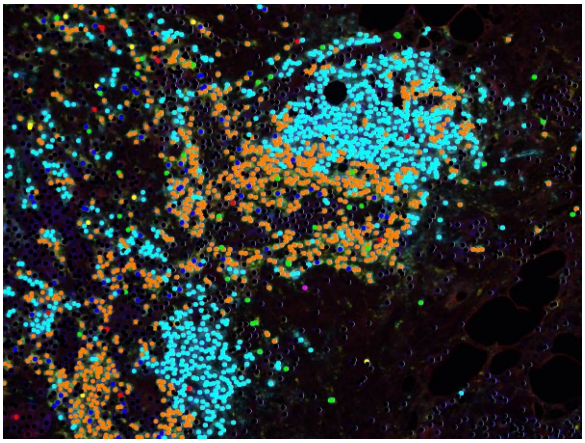

RORγT Single Phenotyping

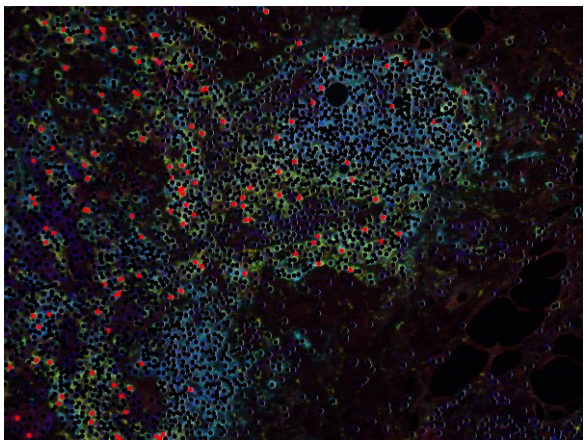

CD3 Single Phenotyping

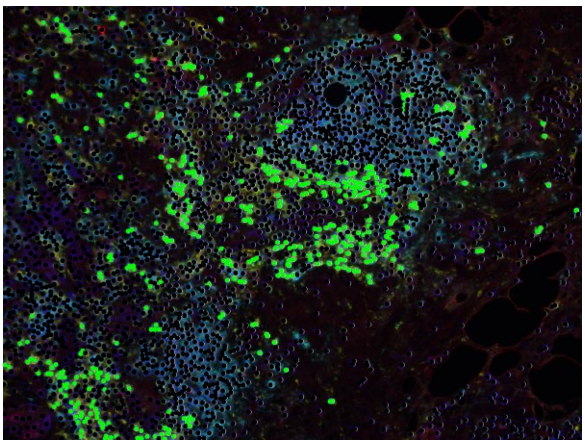

CD4 Single Phenotyping

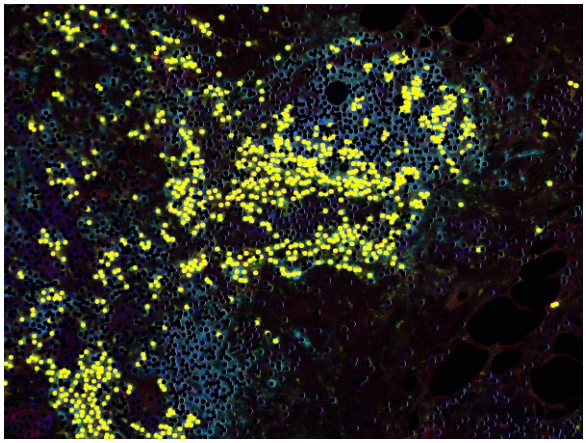

CD20 Single Phenotyping

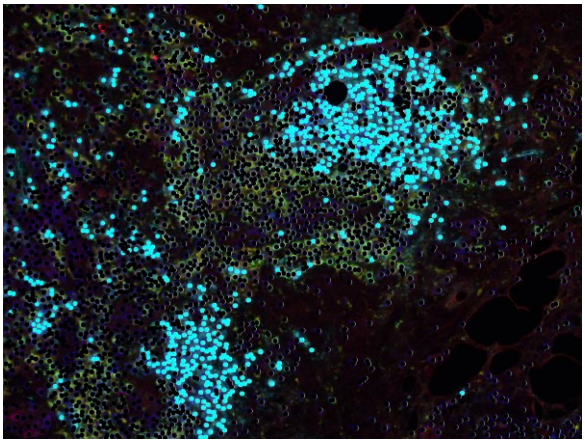

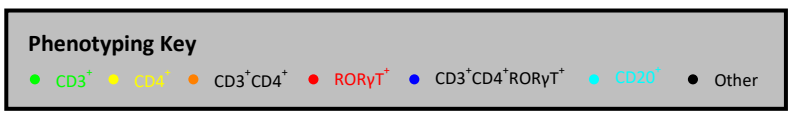

c)

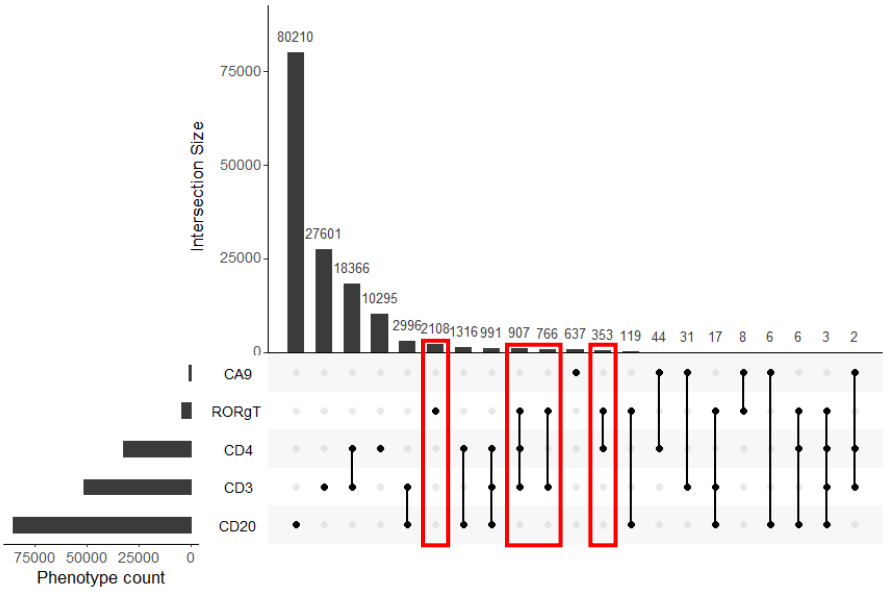

Figure 4.12 Immune phenotyping inForm algorithms and unbiased marker co-expression analysis

a) b) Images of a 20X scanned NSCLC stained by the multiplex fluorescent immunophenotyping panel (Chapter 2.5.4). The 'Unmixed Multiplex Staining' is spectrally unmixed and shows staining before application of the phenotyping algorithms. All other images are following phenotyping classification and descriptions of the different 'Phenotyping' algorithms can be found in-text and in Chapter 2.5.5. Cell phenotypes are represented by coloured dots as in the key. **a)** shows a stroma region and **b)** shows a TLS. **c)** All TLS regions (4 regions/NSCLC resection, *n* = 28 resections) were phenotyped using the 5 'Single Phenotyping Multiplex Algorithms' (including the 'CA9 Single Phenotyping Multiplex Algorithm'), then processed and analysed using the *phenoptr* R package. 'Phenotype Count' represents the total number of marker positive phenotypes classified by these algorithms. Co-expressed markers are shown by joined up dots. Red rectangles highlight the major RORγT$^+$ phenotypes.

4.2.6 Exploring the Characteristics of RORγT$^+$ Lymphocytes

Our key finding from the multiplex IHC phenotyping was that cells expressing RORγT in TLSs fell into two major categories, T cell marker positive or negative. We next sought to examine spatial relationships between RORγT$^+$ cells and other cells within a TLS to determine whether there were any positional differences between the two major subtypes of RORγT$^+$ cells: CD3$^+$/CD4$^+$/RORγT$^+$ cells (Th17s) and RORγT$^+$/CD3$^-$/CD4$^-$ cells.

To spatially quantify cells, we used 'count within' which is a measure of the number of cells within a particular radius originating from the nucleus of the cell in question. We

chose to count the phenotypes of cells within 15µm of each cell to enumerate the most proximal cells. We also examined the median distances between cellular phenotypes as a second measure of proximity.

Count within analysis in Figure 4.13a shows that Th17s have significantly higher average numbers of $CD3^+/CD4^-$ ($p \leq 0.0001$) and $CD3^+/CD4^+$ ($p \leq 0.0001$) T cells within 15µm compared to $ROR\gamma T^+/CD3^-/CD4^-$ cells. In contrast, $ROR\gamma T^+/CD3^-/CD4^-$ have significantly more $CD20^+$ B cells within 15µm compared to Th17s ($p \leq 0.0001$). These findings are corroborated by inter-phenotype distance analysis, in which Th17s have significantly lower median distances to $CD3^+/CD4^-$ ($p \leq 0.0001$) and $CD3^+/CD4^+$ ($p \leq 0.0001$) T cells compared to $ROR\gamma T^+/CD3^-/CD4^-$ cells (Figure 4.13b). Likewise, $ROR\gamma T^+/CD3^-/CD4^-$ have significantly lower distances to $CD20^+$ B cells compared to Th17s ($p = 0.0003$).

We next grouped tumours by *KRAS* and *STK11* mutation status then examined the spatial relationships between $ROR\gamma T^+$ cells of the same phenotype. There were significantly higher average numbers of other Th17s within 15µm of each Th17 in TLSs from tumours with *KRAS* mutations, *STK11* mutations and all MTs (all $p \leq 0.0001$ compared to WT group) (Figure 4.13c). Though this was not the case for patients with concomitant *KRAS/STK11* mutations, who had significantly fewer Th17s within 15µm of each Th17 in TLSs compared to groups with single *KRAS* and *STK11* mutations (both $p \leq 0.0001$) in line with the WT group.

Similarly, there were significantly higher average counts of other $ROR\gamma T^+/CD3^-/CD4^-$ cells within 15µm of each $ROR\gamma T^+/CD3^-/CD4^-$ in TLSs from tumours in the MT group and the *KRAS* mutation group (both $p \leq 0.0001$ vs WT group), and significantly fewer $ROR\gamma T^+/CD3^-$

/CD4$^-$ cells within 15µm in the *STK11* group and *KRAS/STK11* group compared to the high *KRAS* mutation group (p = 0.0008 and p = 0.0003 respectively) (Figure 4.13c).

These findings were supported by a distance analysis (Figure 4.13d). The median distances between Th17s were significantly lower in the MT, *KRAS* and *STK11* groups vs WT group (all $p \leq 0.0001$) and higher in the *KRAS/STK11* group compared to the *KRAS* and *STK11* groups (all $p \leq 0.0001$). Furthermore, the median distances between RORγT$^+$/CD3$^-$/CD4$^-$ cells in TLSs were significantly lower in the MT and *KRAS* groups compared to the WT group (p = 0.0040 and p = 0.0002 respectively), and significantly higher in the *STK11* and *KRAS/STK11* groups compared to the *KRAS* group (p = 0.0053 and p = 0.0002 respectively).

Figure 4.13e visualises these described differences in intra-phenotype distances linked with *KRAS* and *STK11* cancer gene mutations, with smaller differences between the cell types of interest in the MT vs WT groups visible.

These findings highlight that Th17s in TLSs are commonly found nearby other T cells and RORγT$^+$/CD3$^-$/CD4$^-$ are close to B cells. Groupings by *KRAS* and *STK11* mutations show that RORγT$^+$ cells of the same phenotype are nearer in patient tumours with these cancer gene mutations compared to tumours without these mutations. Phenotype proximities of below 15µm can indicate a closeness akin to cellular interaction between lymphocytes. Though these data do not directly measure membrane co-localisation, they provide some evidence that interactions between cells of these phenotypes may occur and elucidate localisation within a TLS.

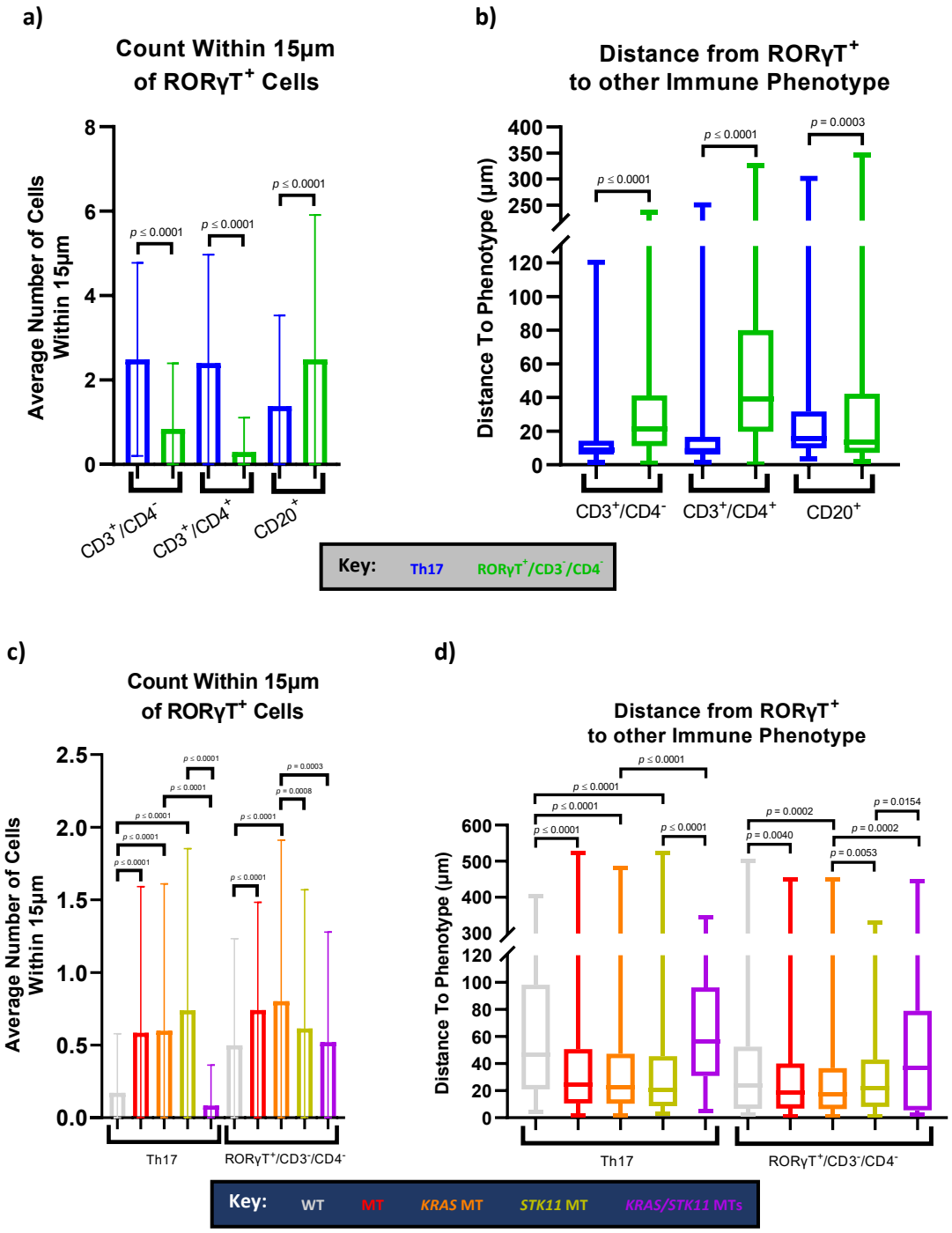
a)
Count Within 15µm of RORγT+ Cells
Average Number of Cells Within 15µm
p ≤ 0.0001
p ≤ 0.0001
p ≤ 0.0001
CD3+/CD4-
CD3+/CD4+
CD20+
b)
Distance from RORγT+ to other Immune Phenotype
Distance To Phenotype (µm)
p ≤ 0.0001
p ≤ 0.0001
p = 0.0003
CD3+/CD4-
CD3+/CD4+
CD20+
Key:
Th17
RORγT+/CD3-/CD4-
c)
Count Within 15µm of RORγT+ Cells
Average Number of Cells Within 15µm
Th17
RORγT+/CD3-/CD4-
d)
Distance from RORγT+ to other Immune Phenotype
Distance To Phenotype (µm)
Th17
RORγT+/CD3-/CD4-
Key:
WT
MT
KRAS MT
STK11 MT
KRAS/STK11 MTs

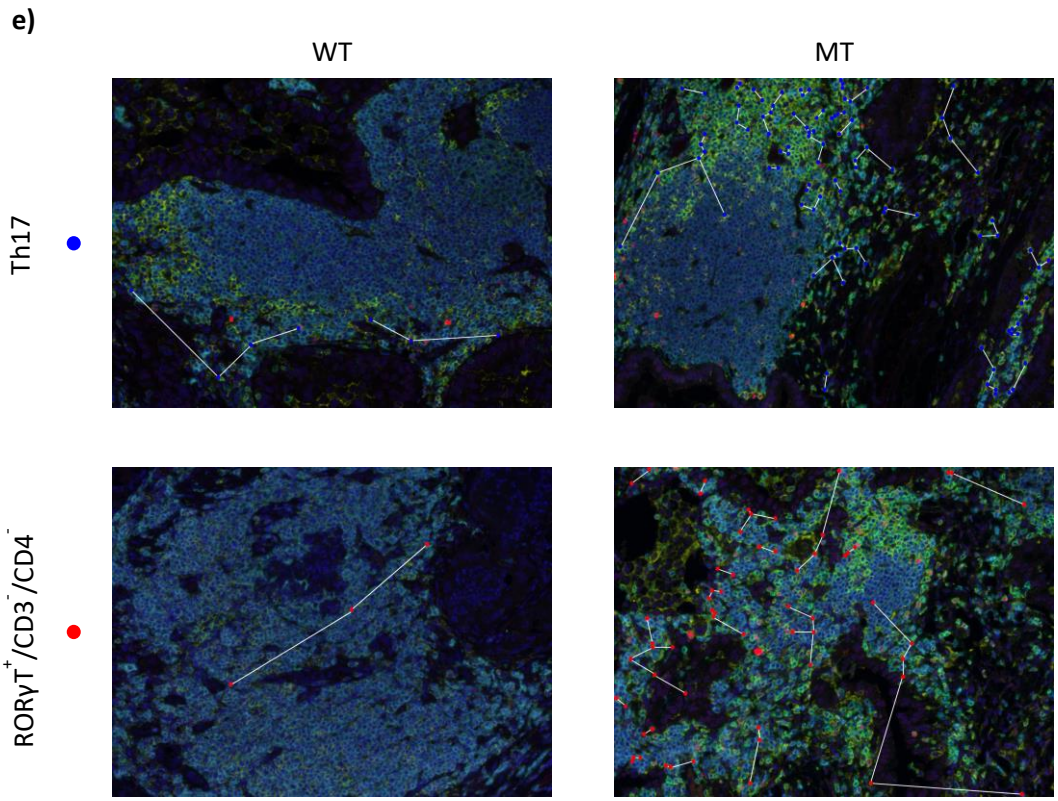

Figure 4.13 Spatial relationships between Th17 cells, RORγT$^+$/CD3$^-$/CD4$^-$ cells, CD3$^+$/CD4$^-$ cells, CD3$^+$/CD4$^+$ cells and CD20$^+$ cells

Distance analyses performed by the *phenoptr* package. **a)** The average number of CD3$^+$/CD4$^-$, CD3$^+$/CD4$^+$ and CD20$^+$ cell types within 15µm of each Th17 (blue bars) and RORγT$^+$/CD3$^-$/CD4$^-$ cell (green bars). **b)** The median distance from each Th17 (blue boxplots) and RORγT$^+$/ CD3$^-$/CD4$^-$ cell (green boxplot) to the nearest CD3$^+$/CD4$^-$, CD3$^+$/CD4$^+$ and CD20$^+$ cell. **c)** The number of Th17s within 15µm of each Th17 cell, and the number of RORγT$^+$/CD3$^-$/CD4$^-$ cells within 15µm of each RORγT$^+$/CD3$^-$/CD4$^-$ cell. Tumours were grouped/coloured by mutational subtype: WT (*n* = 9), MT (*n* = 19), *KRAS* MT (*n* = 10), *STK11* MT (*n* = 4), *KRAS/STK11* MTs (*n* = 5). **d)** The median distance from each Th17 to the nearest Th17, and from each RORγT$^+$/ CD3$^-$/CD4$^-$ cell to the nearest RORγT$^+$/ CD3$^-$/CD4$^-$ cell. Tumours were grouped/coloured by mutational subtype as shown in part **c)**. Error bars in **a)** and **c)** showed standard deviation, and statistical comparisons were by unpaired *t* tests with Welch's correction. Error bars in **b)** and **d)** show the maximum and minimum distances, and statistical comparisons were by unpaired two-sample Wilcoxon tests. **e)** 20X export images of TLSs stained by the multiplex panel with *phenoptr* next nearest phenotypes shown in WT and MT tumours. The 'Th17' row images show the nearest Th17 (blue dots) to each Th17, and the same for the 'RORγT$^+$/ CD3$^-$/CD4$^-$' row images (red dots). White lines link the next nearest cell of the same phenotype to each Th17 or RORγT$^+$/ CD3$^-$/CD4$^-$ cell. Links can be mutual.

Having identified the two main types of RORγT$^+$ cells present in NSCLC tumours and their locations within a TLS, we were interested in investigating the T cell linage marker negative RORγT$^+$ cells to establish whether they were ILCs; a group of lineage$^-$ lymphocytes

found in NSCLC tumours that may aid TLS development (172, 174). It is important to note that the multiplex immunophenotyping algorithms were trained not to recognise weak tumour cell RORγT expression. This led to the vast majority of RORγT^{+}/CD3^{-}/CD4^{-} cells phenotyped being lymphocytes, so we decided to investigate the possibility of these cells being ILCs. As we were unable to develop another multiplex IHC panel, we turned back to the wealth of TCGA data and used GSEA to interrogate the data in a more subset specific manner than can be offered by the CIBERSORT and MCP-counter approaches.

Immune subset gene sets were firstly selected from the literature. NRP1^{+} ILC3s are a subset of RORγT^{+} ILCs with LTi activity that have been described in human tissue in lymphoid structures including lung lymphoid aggregates, but not in peripheral blood by Shikhagaie *et al* (443). We therefore complied a gene set based on the markers expressed by NRP1^{+} LTi-like ILC3 identified in this paper. We also utilised gene sets for ILC1, ILC2, ILC3 and LTi cells collated and used by Suzuki *et al* (444) to profile innate immune cells in human COPD lung tissue. For Th17 GSEA, we used a gene set validated by Castro *et al* (445) who knocked down both RORγT and RORα transcription factors in Th17s to find differentially regulated genes, which we supplemented with additional IL-17 family genes including *IL17C* and *IL17RE*. Finally, we used gene sets for NK cells, CD56^{bright} NK cells, B cells, Th1 cells and macrophages described in a publication by the Galon group (446).

Positive ssGSEA enrichment scores for Th17s, NRP1^{+} LTI-like ILCs, LTis and ILC3s are observed in the MT group vs the WT group throughout Figure 4.14a. This shows that gene expression from all four gene signatures in Figure 4.14a are enriched compared to all other genes profiled by RNA-Seq by TCGA. Moreover, significantly higher median ssGSEA

enrichment scores are found in the MT group containing tumours with *KRAS* and *STK11* mutations compared to the WT group in all subsets shown in Figure 4.14a. This again confirms our finding of Th17 enrichment in *KRAS* and *STK11* mutant tumours and shows enrichment for innate immune cells with ILC3 and LTi profiles.

Importantly, this is not the case for RORγT^{-} innate immune cells (Figure 4.14b). There are no differences between the WT and MT groups in ILC1 or ILC2 enrichment scores, showing that the enrichment is specific for cells of RORγT^{+} phenotypes. Significantly lower NK cell enrichment scores are also found in the MT group compared to the WT group (p = 0.0014). Though the MT group has significantly higher enrichment scores for the suppressive CD56^{bright} NK cells compared to the WT group (p = 0.0014).

This ssGSEA approach further confirmed a pattern of immune suppression which we previously observed in tumours with *KRAS* and *STK11* mutations in Chapter 3. Figure 4.14c showed that MT tumours had significantly lower B cell, Th1, and macrophage enrichment scores compared to the WT tumour group (p = 0.0052, p = 0.0211 and p = 0.0026 respectively).

Overall, this GSEA analysis provides further evidence of RORγT^{+} lymphocyte enrichment in patient tumours with *KRAS* and *STK11* mutations, and indicates enrichment of ILC3s and LTis without enrichment of ILC1 and ILC2 cells.

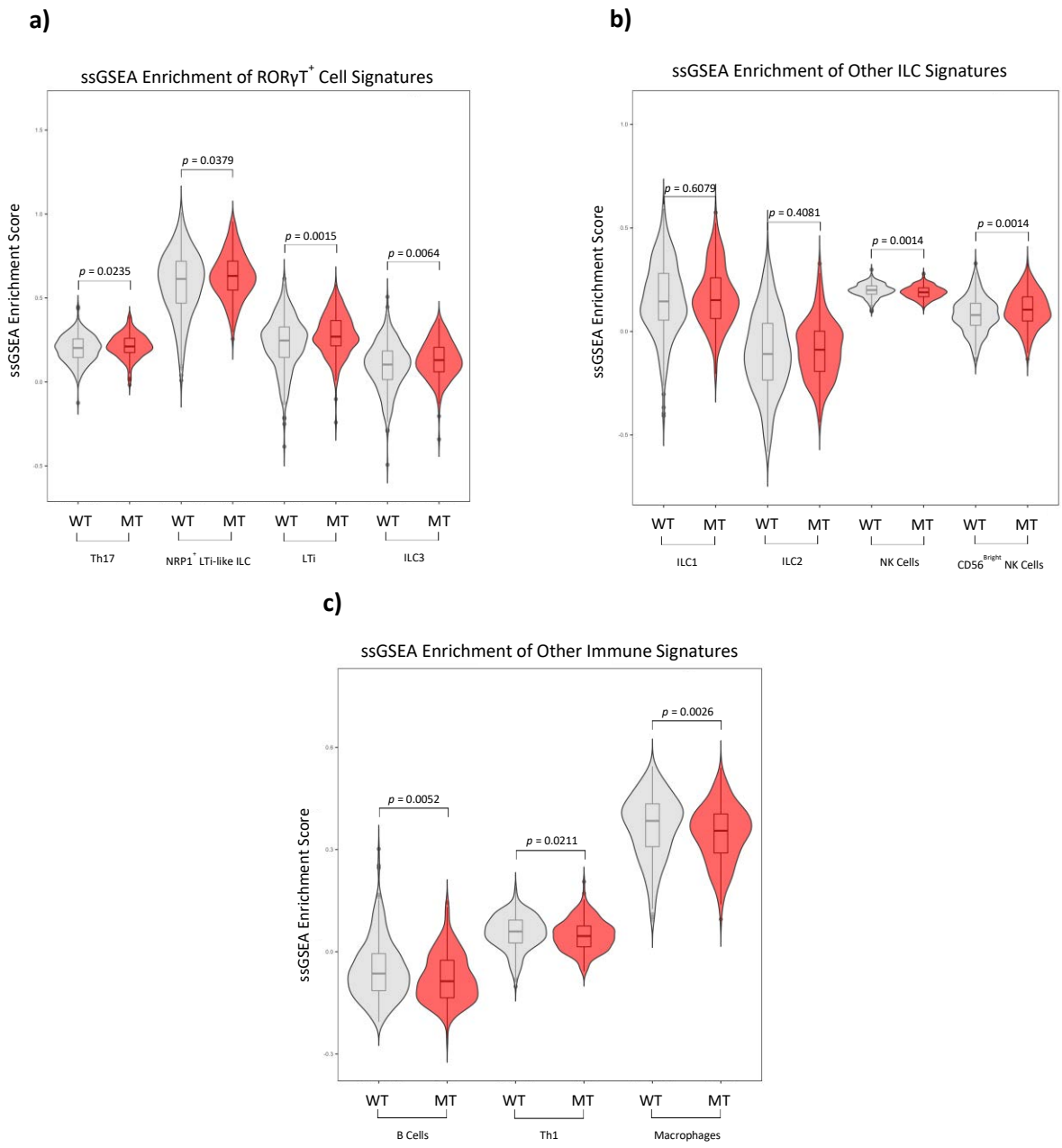

Figure 4.14 Gene set enrichment analysis of innate lymphoid cells and other immune subsets

a) b) c) Gene signature lists were obtained from the following publications: Shikhagaie *et al* (443), Suzuki *et al* (444), Castro *et al* (445) and Bindea *et al* (446). We added additional IL-17 family member genes to the Th17 gene signature from Castro *et al* (445). Gene lists were used by the *GSVA* package to calculate ssGSEA enrichment scores from TCGA PanCancer LUAD RNA-Seq RSEM data (Chapter 2.1.10). ssGSEA enrichment scores were grouped by patient tumours without *KRAS* and *STK11* mutations (WT, *n* = 315) and with *KRAS* and *STK11* mutations (MT, *n* = 191). All groups were compared by unpaired two-sample Wilcoxon tests.

4.3 Discussion

Having identified elevated *RORC* mRNA expression in TCGA cases with *KRAS* and *STK11* mutations, we wanted to investigate whether there was a relationship between mRNA and RORγT protein expression as well as establish which cells within the tumour express RORγT (435-437). To this end we sourced NSCLC resections from 28 patients from two studies which had sequenced tumours to classify *KRAS* and *STK11* mutations, which is not part of routine clinical practice (359, 360). Using this rare cohort of tumour resections, we were able to address these questions using IHC and importantly study RORγT$^+$ cells in the TME, investigating the spatial distribution of these cells in relation to other immune cells and their locations within the tumour.

4.3.1 Validating and Optimising a RORγT Monoclonal Antibody

We firstly compared several RORγT monoclonal antibodies for IHC, deciding on a Merck antibody that most clearly stained *RORC2* transfected HEK293T cells as well as lymphocytes in human tonsil and NSCLC sections (Figures 4.1, 4.2 and 4.4). This antibody has also been previously used in the literature to quantify Th17s in CRC (442), but has not been used for other applications. Additionally, we demonstrated that this antibody can be used in flow cytometry following in-house conjugation with AF647 fluorophore. We optimised its use to identify CD3$^+$/CD4$^+$/RORγT$^+$/IL-17A$^+$ Th17s from PBMCs (Figure 4.3), and integrated it into our Th17 flow cytometry antibody panel for use in Chapter 5.

We then used the optimised RORγT antibody in IHC to stain sections from 10 tumours with *KRAS* mutations, 4 tumours with *STK11* mutations, 5 tumours with *KRAS/STK11* mutations and 9 tumours without either of these mutations.

4.3.2 Identifying and Quantifying RORγT Expressing Lymphocyte in Patient Tumours

Earlier IHC by Huang *et al* (437) had shown weak staining of RORγT in NSCLC tumour cells, and the authors suggested that the majority of RORγT expression in NSCLC is tumoural. Although we also observed weak RORγT tumour cell staining, confirmed by pathologist Dr Abeer Shaaban, RORγT was predominantly expressed in lymphocytes within NSCLC tumours. One explanation for the weak RORγT staining in tumour cells may be the relatively common amplification of chromosome 1q21.3 (377-385, 417). Unfortunately, we were unable to assess 1q21.3 amplifications in our patient tumour cohort. RORγ and RORγT tumour cell expression has also been observed in other cancers and has been linked with circadian and metabolic perturbations that aid growth, and metastatic stemness (447-451).

We then designed an algorithm to identify and quantify RORγT$^+$ lymphocytes and we found a significantly higher abundance of RORγT$^+$ lymphocytes in tumours from NSCLC patients with *KRAS* and/or *STK11* mutations as well as *KRAS* mutations alone compared to WT patients (Figure 4.6). The *STK11* and *KRAS/STK11* groups were not significantly different to WT tumours, which may be due to low numbers of samples in these groups.

Interestingly, we found that SqCC resections had low RORγT$^+$ lymphocyte abundances. This agrees with findings from the literature that *RORC* expression is generally higher in

LUAD tumours than SqCC tumours, and that Th17s are more common in LUAD compared to SqCC (158, 452). In contrast, other studies have shown no difference in *RORC* expression or Th17 cell frequencies when analysing PBMCs from LUAD patients. This suggests that the increase in RORγT$^+$ cells is specifically seen inside LUAD tumours and supports findings that *KRAS/STK11* mutant NSCLC tumours with different histologies are associated with different immune infiltrates (269, 281, 453, 454).

We also observed that tumours without whole genome duplications had high RORγT$^+$ lymphocyte abundances. Genome duplications from replication fork stalling occur early during oncogenesis to protect tumours by preserving WT copies of essential genes that might be deleted during increasing genomic instability (455, 456). High genomic instability is intrinsically linked with high TMB and increased numbers of immunoreactive neoantigens. These tumours suppress TIL function by chronic neoantigen exposure-induced exhaustion, increased IL-4 and IL-10 secretion and are associated with decreased TIL numbers (158, 166, 456). Our results show that like other TILs, RORγT$^+$ lymphocytes are excluded from tumours with whole genome duplications, though the reason why is unclear. RORγT$^+$ lymphocytes therefore might be abundant before genome duplications. This is difficult to investigate as most resections are performed on early-stage NSCLC which may have already duplicated its genome; therefore, we would have to examine subclinical NSCLC tumours which is not feasible.

In contrast to our findings assessing the impact of *RORC* expression on survival of TCGA patients in Figure 3.10, in our cohort of NSCLC patient tumour sections we found that having high intratumoural RORγT$^+$ lymphocyte abundance was linked with poor OS (Figure

4.6c). These seemingly opposing findings may be explained by different methods of analysis; TCGA patients were grouped by levels of total *RORC* tumour mRNA expression, whereas the patients from whom we had sections were grouped more specifically by abundances of RORγT$^+$ lymphocytes. This latter analysis more accurately assesses OS in relation to presence of RORγT$^+$ lymphocytes and it is not influenced by RORγT expression in any other cells.

We next investigated the spatial distribution of the RORγT$^+$ lymphocytes and showed that most RORγT$^+$ lymphocytes are located within the stroma and in lymphoid aggregates (Figure 4.8). This was supported by detection of IL-17A expression in these same regions (Figure 4.9). Our findings are supported by many reports of intratumoural IL-17A mRNA and protein expression (278, 280, 288, 291, 414, 437, 457).

4.3.3 Phenotyping and Characterising RORγT Expressing Lymphocytes Within Non-Small-Cell Lung Cancer Tertiary Lymphoid Structures

To further investigate the lymphoid aggregates seen and to phenotype the RORγT$^+$ lymphocytes we designed and validated a multiplex fluorescent panel of IHC antibodies. Although this panel included the HIF1α-inducible protein CA9 to explore the relationship between Th17 cells and hypoxia (458), surprisingly only two cases showed evidence of CA9 expression, therefore this was not further investigated. This might be due to high degrees of hypoxia heterogeneity in NSCLC and could be resolved in future studies by multi-regional tumour sectioning to identify hypoxic regions (459). The remaining markers were present in multiple sections and multiplex IHC confirmed that lymphoid aggregates were

TLS consisting of $CD4^+$ T cells and $CD20^+$ B cells, in which the different proportions of $CD4^+$ T cells and $CD20^+$ B cells present represent different states of TLS maturation (Figure 4.11) (153). Many TLS had $Bcl\text{-}2^-$ B cell follicles which are likely to be mature TLS with a germinal centre. This could be confirmed by Bcl-6 staining (153, 154). Likewise, more immature NSCLC TLS lacked discrete T and B cell zones, in which all cells expressed Bcl-2 (153, 154).

When considering the mutational status of the NSCLC tumours, we found no association between TLS burden and mutations in the *KRAS* and *STK11* cancer genes. This was notably similar to studies by Cabrita *et al* (147) and Lin *et al* (460) who also both found no association of TLSs with these NSCLC mutations. This was initially surprising as we had postulated that the increased numbers of $ROR\gamma T^+$ lymphocytes in *KRAS* mutant tumours were due to higher numbers of TLSs. An alternative explanation is that tumours driven by *KRAS* mutations have different TLS compositions, which was supported by Figure 4.13c and 4.13d in which significantly greater clustering of $ROR\gamma T^+$ cells was seen.

The multiplex IHC analysis showed that RORγT is commonly expressed in $CD3^+/CD4^+$ T cells defined as Th17 cells (Figure 4.12c). Th17s are associated with a bad prognosis in NSCLC, as IL-17A signalling activates tumour STAT3 to induce proliferation and angiogenesis, as well as by controlling recruitment and activation of tumour-promoting myeloid cells (189, 276, 285-288, 291-294, 296-299, 304). RORγT is also expressed on its own and in different combinations with CD3 and CD4 (Figure 4.12c). It is possible that this unbiased computational analysis can mis-classify $CD3^+/CD4^+/ROR\gamma T^+$ Th17s as $CD3^+/ROR\gamma T^+$ or $CD4^+/ROR\gamma T^+$ T cells due to weak staining or CD3/CD4 downregulation upon T cell activation. However, it is also possible that these cells might be other immune subsets

such as γδ17s, iNKT17s or MAITs (158, 230-232, 294, 299, 303, 440, 441, 461-465). Further staining with subset-specific antibodies would be required to confirm their true identity.

Evidence from mouse models suggest that γδ17s rather than Th17s are the primary source of IL-17A and IL-22 in NSCLC, and that γδ17s are associated with *KRAS* driven pancreatic cancer and *KRAS/TP53* driven NSCLC (299, 303, 462, 465, 466). γδ17s in *KRAS/TP53* driven murine NSCLC tumours are long-lived lung resident Vγ6Vδ1 cells, which are dependent on the lung microflora for development and can promote TANs and tumour development (462). Whilst there is evidence that γδ17s are associated with worse outcomes, γδ T cells can express NKG2D and lyse NSCLC tumour cells *in vitro* (168, 169, 294, 462). iNKT17s also depend on differentiating signals from the colonic microflora in mice and can produce IL-17A, IL-22 and IL-23, though there is limited knowledge about their role in human NSCLC (230, 231). RORγT$^+$ MAITs have been shown to act like inflammatory CD8$^+$ Tc17s and lung resident MAITs can be an important source of IL-17A in paediatric pneumonia (232, 440, 441). Recent evidence has shown that non-classical MAIT-like T cells are cytotoxic and can kill a variety of cancer cell lines including NSCLC cell lines (229). RORγT$^+$ MAITs may also contribute to TLS-induction by LTβ expression (440).

The RORγT$^+$/CD3$^-$/CD4$^-$ cells seen are potentially lineage$^-$/CD127$^+$ ILC3 cells that are known to express RORγT and can secrete IL-17A. ILC3s have previously been observed in NSCLC (172, 174). This possibility is supported by GSEA of TCGA data which showed significant enrichments of both Th17s, ILC3s and LTi cells in tumours with *KRAS* and/or *STK11* mutations, but not RORγT$^-$ ILC1 or ILC2 cells (Figure 4.14).

In SqCC ILC1s can be directly converted to ILC3s in an IL-23 and RORγT dependent manner and these ILC3s can be sub-grouped by NCR expression (467). NCR^+ ILC3s secrete higher quantities of IL-17A and have more cytotoxic capacity, expressing granzyme B, granulysin and IFNγ (468-470). Work by Carrega *et al* (172) examining NSCLC tumours found that although NCR^+ ILC3s could not lyse tumour cells, tumour cell recognition induced CXCL8 release. As $NRP1^+$ ILC3s and LTi cells both express NCRs and have LTi-like activities, they may be important in inducing TLS formation (172, 443). LTi and ILC3s have been previously shown to interact with stromal cells and CAFs to remodel the microenvironment and can interact with $CD4^+$ T cells via MHC class II (172, 471-474).

In addition to their roles in TLS development, ILC3s may recruit TANs and secrete IL-22 which is linked with bad outcomes in NSCLC (155, 170, 172, 241, 298-302, 443, 467).

Examining the distances between $ROR\gamma T^+$ lymphocytes and immune cells of other phenotypes within TLSs showed that putative $ROR\gamma T^+/CD3^-/CD4^-$ ILC3s were nearby $CD20^+$ B cells, and $CD3^+/CD4^+/ROR\gamma T^+$ Th17s were close to other T cells (Figure 4.13). Whilst we did not find evidence of Th17s interacting with other T cells from the literature, it has been suggested that interactions between ILC3s and B cells can occur in secondary lymphoid organs that stimulates antibody secretion which may also occur in NSCLC TLSs (474-476).

4.3.4 Summary

Overall, in this Chapter we investigated expression of the RORγT protein and found that most nuclear RORγT staining in NSCLC tumour resections was of lymphocyte origin, disagreeing with findings by Huang *et al* (437).

Quantifying RORγT$^+$ lymphocytes using IHC staining showed that increased *RORC* mRNA translates to increased RORγT protein expression in tumours with *KRAS* and/or *STK11* mutant tumours as well as tumours with *KRAS* mutation alone. Further quantification using additional *STK11* and *KRAS/STK11* tumours might reveal an association with these mutational subtypes. Heterogeneity in the RORγT$^+$ lymphocyte quantification data was due to tumour histology and genome duplications.

Examining the specific impact of intratumoural RORγT$^+$ lymphocyte abundances on patient survival showed that a high abundance of these cells was associated with poor OS, which potentially contrasted our previous findings but supported the literature (189, 276, 285-288, 291-294, 296-299, 304).

RORγT$^+$ lymphocytes were not specifically situated in any particular region of tumour tissue but were often found in stromal regions or lymphoid aggregates. Phenotyping these lymphoid aggregates revealed that they were TLSs. As we found no difference in TLS burden between tumours of different *KRAS* and *STK11* mutational subtypes, we postulated that differences in RORγT$^+$ lymphocyte abundances were due to differences in TLS composition.

Co-expression analysis showed that RORγT is predominantly expressed in Th17 cells which were located nearby other T cells in TLSs. These analyses also highlighted a subset of

RORγT^{+}/CD3^{-}/CD4^{-} cells found near B cells which we believe from algorithmic exclusion of tumour cells, a T cell lineage^{-} nature, and evidence from GSEA to be ILC3 cells.

5. Examining the Influence of *KRAS* and *STK11* Mutant Lung Cancer Cells on T Cell Phenotype

5.1 Introduction

Plasticity of $CD4^+$ T cells allows what were previously believed to be lineage committed T cells to respond to a changing situation by adjusting their phenotypic functions dependent on microenvironmental cues. Having described raised $ROR\gamma T^+$ immune cells in NSCLC tumours with *KRAS* and *STK11* alterations, we were interested to further investigate the mechanisms that might lead to this association using *in vitro* assays. Specifically, we aimed to determine whether soluble factors released from NSCLC cell lines with these alterations could induce T cell plasticity and alter the Th17/iTreg balance. To do this we developed an *in vitro* assay in which PBMCs were cultured in media conditioned by NSCLC and control cell lines, and examined whether this led to polarisation of $CD4^+$ T cells towards Th17s.

We therefore designed a Th17 flow cytometry phenotyping panel including the following markers: CD3, CD4, CCR6, CD127, RORγT, IL-17A, IFNγ and TNFα. This enabled analysis of RORγT and IL-17A in $CD3^+/CD4^+$ T cells, and also the chemokine receptor CCR6 which is expressed on Th17s, Tregs and neutrophils, and binds the ligand CCL20 (477). CD127 is expressed on long-lasting memory cells, including Th1s and Th17s that use IL-7 over IL-2 for their maintenance, and CD127 downregulation can be used to identify Tregs (266, 478-480). Treating Th17s with IL-7 upregulates the receptor for IL-1β to aid differentiation, and IL-7 is also linked with high CCR6, TNFα secretion and surface LTα/β expression (481, 482). TNFα can be co-produced with IL-17A and has the effect of stimulating IL-1β, IL-6, CXCL8

and GM-CSF production (483, 484). Lastly, IFNγ is associated with cytotoxic Th1, Th1-like Th17 and CD8 responses and importantly upregulates cell surface HLA class I and II (228, 245, 485).

5.2 Results

5.2.1 High Dimensional Analysis of Flow Cytometry Stained *Ex Vivo* T Cells

The aim of this Chapter was to investigate whether media conditioned by NSCLC cell lines with and without *KRAS* and *STK11* mutations could induce T cell polarisation *in vitro*. As the central experiment described in this Chapter would generate complex multidimensional data from 68 conditions, we wanted to use the UMAP dimension reduction technique to identify quantifiable patterns in these data. To validate the application of high dimensional analysis for data generated by the Th17 flow cytometry panel (Table 2.8) we first examined the effect of PMA/iono stimulation on *ex vivo* $CD3^+/CD4^+$ T cells.

Ex vivo PBMCs from four age and gender matched donors were split into two test tubes. PBMCs in one tube did not receive stimulation by PMA/iono and PBMCs in the second tube received PMA/iono stimulation. At the time of stimulation, all PBMCs were treated with Brefeldin A which prevents transport through the golgi apparatus and stops extracellular cytokine secretion. The cells were then incubated at 37°C/5% CO_2 for four hours to allow cytokine accumulation. Following this, PBMCs were washed and stained with the Th17 flow cytometry panel of extracellular and intracellular fluorophore conjugated antibodies, and data were collected using a flow cytometer (full methods available: Chapters 2.6.3, 2.6.4 and 2.6.5). After flow cytometric acquisition, PBMCs from all donors were gated on single live $CD14^-/CD19^-/CD3^+/CD4^+$ lymphocytes (Figure 2.4) – henceforth referred to as $CD3^+/CD4^+$ T cells – and these gated $CD3^+/CD4^+$ T cell data from the 4 donors were concatenated based on the two PMA/iono stimulation conditions. The

two resultant concatenations were downsampled and markers were subject to a logicle transformation and UMAP dimension reduction was performed (Figure 5.1) (371-373).

The UMAP in Figure 5.1a shows the combined *ex vivo* $CD3^+/CD4^+$ T cell data from both tubes from all 4 donors, both stimulated with PMA/iono and without stimulation. Whereas Figure 5.1b shows the concatenated data from only the *ex vivo* $CD3^+/CD4^+$ T cells that did not receive PMA/iono stimulation, and Figure 5.1c shows the concatenated data from only *ex vivo* $CD3^+/CD4^+$ T cells that received PMA/iono stimulation. Overall, Figure 5.1 shows that this high dimensional approach can distinguish between $CD3^+/CD4^+$ T cells that have been treated with PMA/iono and those that have not been treated with PMA/iono. The line splitting the two islands in Figure 5.1a delineate T cells that 1) have not been stimulated with PMA/iono and 2) have been stimulated with PMA/iono. These separate islands can clearly be seen when the data is filtered to show only unstimulated (Figure 5.1b) and stimulated (Figure 5.1c) T cells. This pilot analysis confirmed that analysing flow cytometry data using a high dimensional approach can distinguish between unstimulated and PMA/iono stimulated $CD3^+/CD4^+$ T cells and was therefore suitable for analysis of the experimental data.

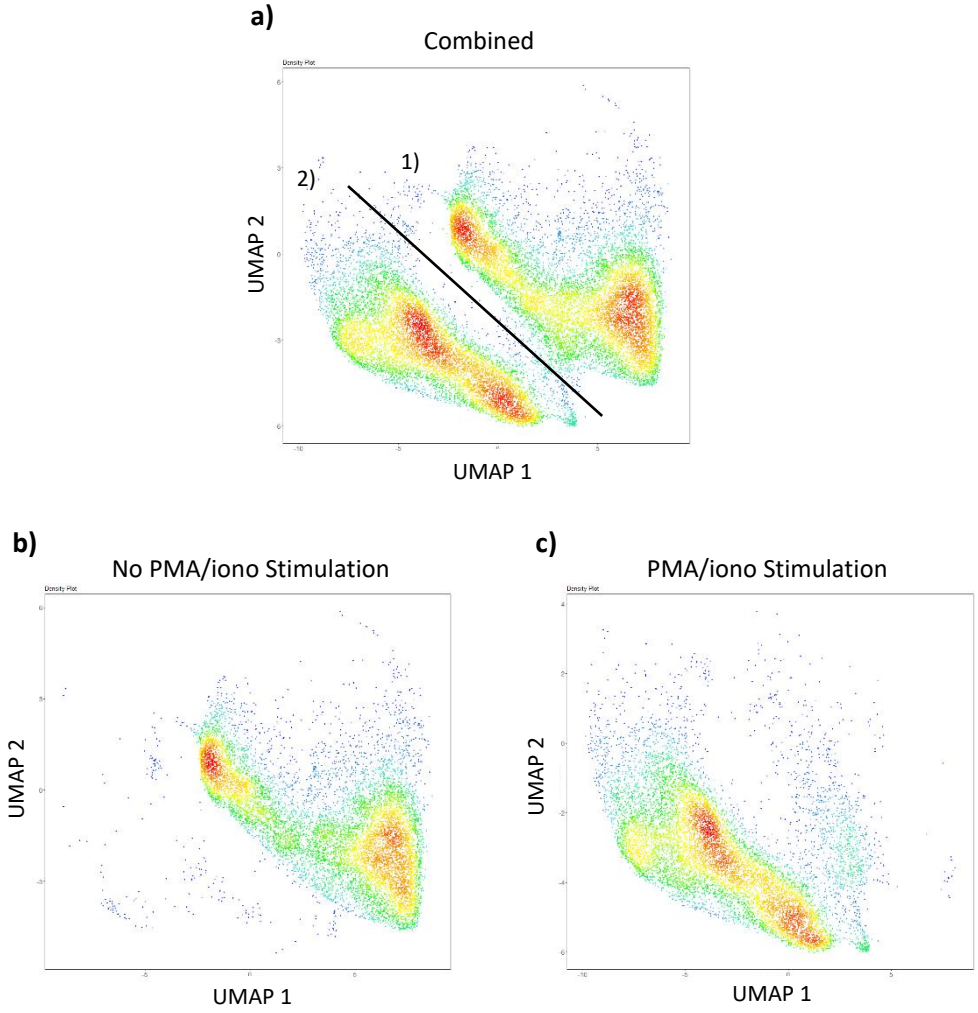

Figure 5.1 Validating a high dimensional data analysis approach by assessing the effect of PMA/iono stimulation on *ex vivo* CD3$^+$/CD4$^+$ T cells

Ex vivo PBMCs from four donors were either PMA/iono stimulated or not stimulated, stained with the Th17 flow cytometry panel and gated on CD3$^+$/CD4$^+$ T cells, as described in-text and in Chapters 2.3.10, 2.6.3, 2.6.4, 2.6.5 and 2.6.6. CD3$^+$/CD4$^+$ T cells were concatenated based on stimulation ('PMA/iono Stimulation') or not ('No PMA/iono Stimulation'). 10,000 T cells were downsampled, then transformation and UMAP dimension reduction was performed on all features except Viability Dye-APC-Cy7, CD14-APC-Cy7 and CD19-APC-Cy7 as in Chapter 2.6.6. **a)** Density UMAP showing T cells from both conditions. **b)** The same data is filtered to show only downsampled T cell concatenations that have not been stimulated by PMA/iono. **c)** The same data is filtered to show only downsampled T cell concatenations that have been stimulated by PMA/iono.

5.2.2 An Approach to Culturing Peripheral Blood Mononuclear Cells in Cell Line Conditioned Media

To investigate whether tumour conditioned media (TCM) from NSCLC cell lines with different mutations can differentially alter the phenotype of CD3$^+$/CD4$^+$ T cells, we

sourced appropriate cell lines with either *KRAS*, *STK11* or concurrent *KRAS/STK11* mutations, or with no mutations in these genes. To this end, we used *KRAS* and *STK11* mutation and CNA data from the 'Catalogue of Somatic Mutations in Cancer Cell Lines Project' and the 'canSAR' databases, alongside data from the literature, to select appropriate NSCLC cell lines for use (Table 5.1) (361-365). After purchasing these cell lines from reliable sources, cell line conditioned media were collected from low passage cells (full method in Chapter 2.3.9). All cell lines that did not usually use RPMI as a culture medium were first weaned onto RPMI for consistency, and conditioned media were collected at a low cell line passage number when cell lines were 70% confluent, or after a maximum of three days culture. All conditioned media were filtered and frozen at -80°C before use. Table 5.1 shows an overview of the different controls and NSCLC cell lines used in this experiment, as well as their *KRAS* and *STK11* mutation status. Fresh RPMI was used as a 'Culture Media Control', and conditioned media collected from non-cancerous HEK293T foetal kidney epithelial cells acted as a 'Non-NSCLC Epithelial Cell Control'.

Mutational Subtype or Control	Number of Cell Lines	Cell Lines
Culture Media Control	0	*RPMI Control*
Non-NSCLC Epithelial Cell Control	1	HEK293T
WT	5	CALU-3, H292, HCC78, H1299, H2110
KRAS MT	2	CALU-6, H441
STK11 MT	4	CAL-12T, H1755, Chago-K-1, H1563
KRAS/STK11 MTs	4	A549, A427, H460, H1734

Table 5.1 NSCLC cell lines and their *KRAS* and *STK11* mutational subtypes

Overview of the cell lines and controls from which TCM or conditioned media were collected. A detailed table with cell line sources, descriptions and specific *KRAS* and *STK11* mutations can be found in Table 2.3 in Chapter 2.3.3.

Figure 5.2a shows the laboratory workflow for this experiment and Figure 5.2b outlines how the data were processed and analysed. The dosages of anti-CD3/CD28 were not optimised before this experiment. Nor was the timing of the PMA/iono restimulation, and we did not determine whether this step was necessary following the initial anti-CD3/CD28 activation. To draw firm conclusions from future experiments it will be essential to optimise this experiment and perform time courses to determine the window of cytokine production for each cytokine investigated, as well as to optimise the downstream analysis.

Firstly, PBMCs were again isolated from the four healthy donors and cryopreserved until the day of each experiment. PBMCs were revived and seeded at $1x10^6$ PBMCs/well into 48 well plates, each resuspended in a different cell line conditioned media or RPMI control media, as shown previously in Table 5.1. At this time, a T cell activation cocktail of 0.5µg anti-CD3 and 1µg anti-CD28 antibodies was added to each experimental condition to stimulate the PBMCs. PBMC seeding and activation was performed at the end of each

working day, which was called Day 0, and plates were incubated overnight at 37°C/5% CO_2.

The following day (Day 1) PBMCs were washed to remove the anti-CD3 and anti-CD28 antibodies, then re-seeded in an unused well with fresh conditioned or control media as appropriate. PBMCs were then cultured for two days until phenotypic and functional testing on Day 3. At this time, half of the PBMCs from each condition were transferred to a 'Restimulated' test tube and the other half were transferred to a 'Not Restimulated' test tube. The 'Restimulated' condition PBMCs were stimulated, for a second time, with PMA/iono for four hours in the presence of Brefeldin A to induce cytokine production and accumulation. The 'Not Restimulated' condition PBMCs were not restimulated with PMA/iono on Day 3 and only received the initial stimulation with the T cell activation cocktail on Day 0. The PBMCs were washed then stained with the Th17 flow cytometry panel as described previously (Figure 5.1).

After flow cytometric acquisition, the data were gated on $CD3^+/CD4^+$ T cells and processed as shown in Figure 5.1b. $CD3^+/CD4^+$ T cells from the four donors that had been cultured under the same condition and subject to the same PMA/iono stimulation (either 'Restimulated' with PMA/iono or 'Not Restimulated' with PMA/iono) were concatenated together. For example, all $CD3^+/CD4^+$ T cells from PBMCs that were cultured in A549 TCM and 'Restimulated' with PMA/iono from the four donors were concatenated. Each concatenation was then downsampled to 10,000 T cells and imported into the *cytofkit2* package for dimension reduction and FlowSOM clustering. To aid cluster phenotypic definition, MEMmod was also completed.

a)

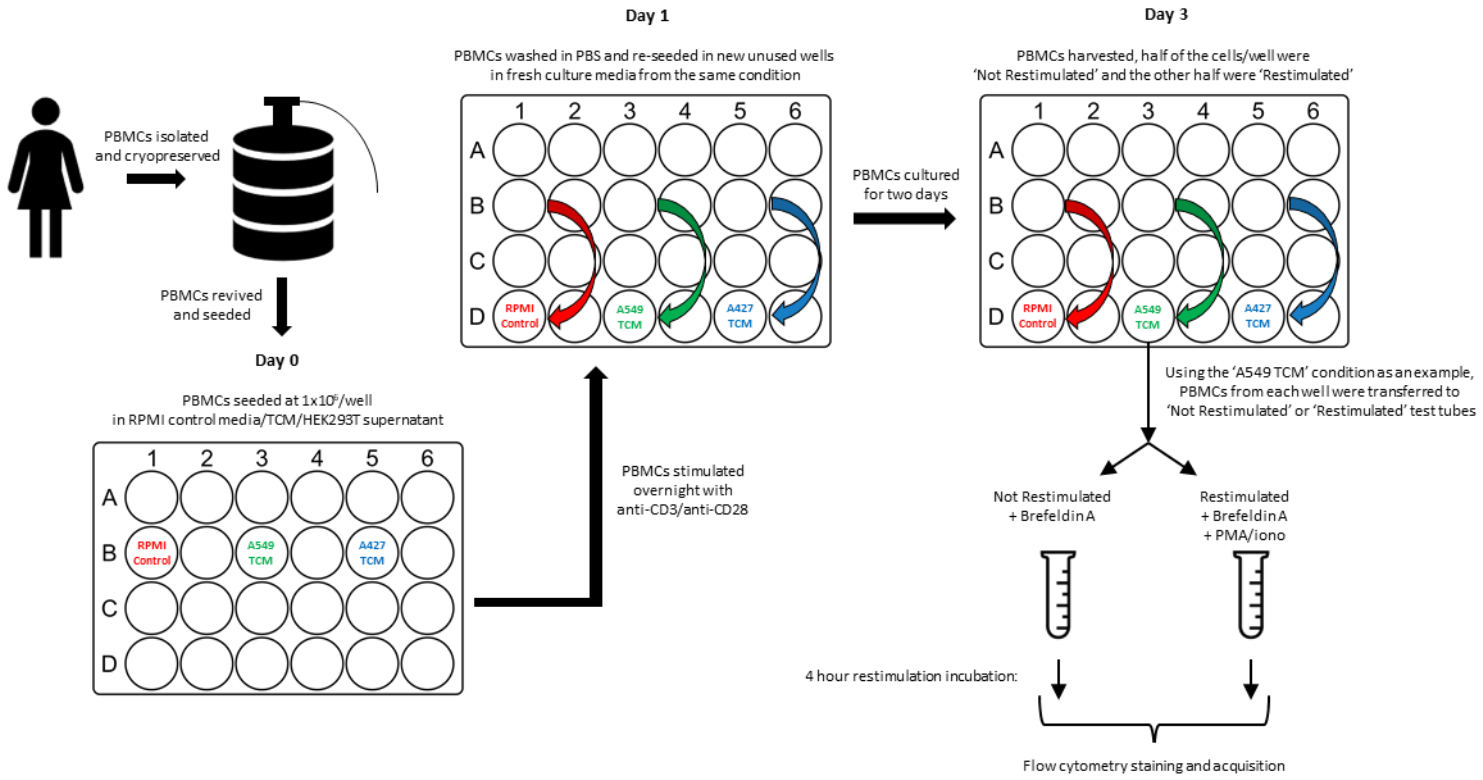
Day 1
PBMCs washed in PBS and re-seeded in new unused wells in fresh culture media from the same condition
Day 3
PBMCs harvested, half of the cells/well were 'Not Restimulated' and the other half were 'Restimulated'
PBMCs isolated and cryopreserved
PBMCs revived and seeded
Day 0
PBMCs seeded at 1x10⁶/well in RPMI control media/TCM/HEK293T supernatant
PBMCs stimulated overnight with anti-CD3/anti-CD28
PBMCs cultured for two days
RPMI Control
A549 TCM
A427 TCM
Using the 'A549 TCM' condition as an example, PBMCs from each well were transferred to 'Not Restimulated' or 'Restimulated' test tubes
Not Restimulated + Brefeldin A
Restimulated + Brefeldin A + PMA/iono
4 hour restimulation incubation:
Flow cytometry staining and acquisition

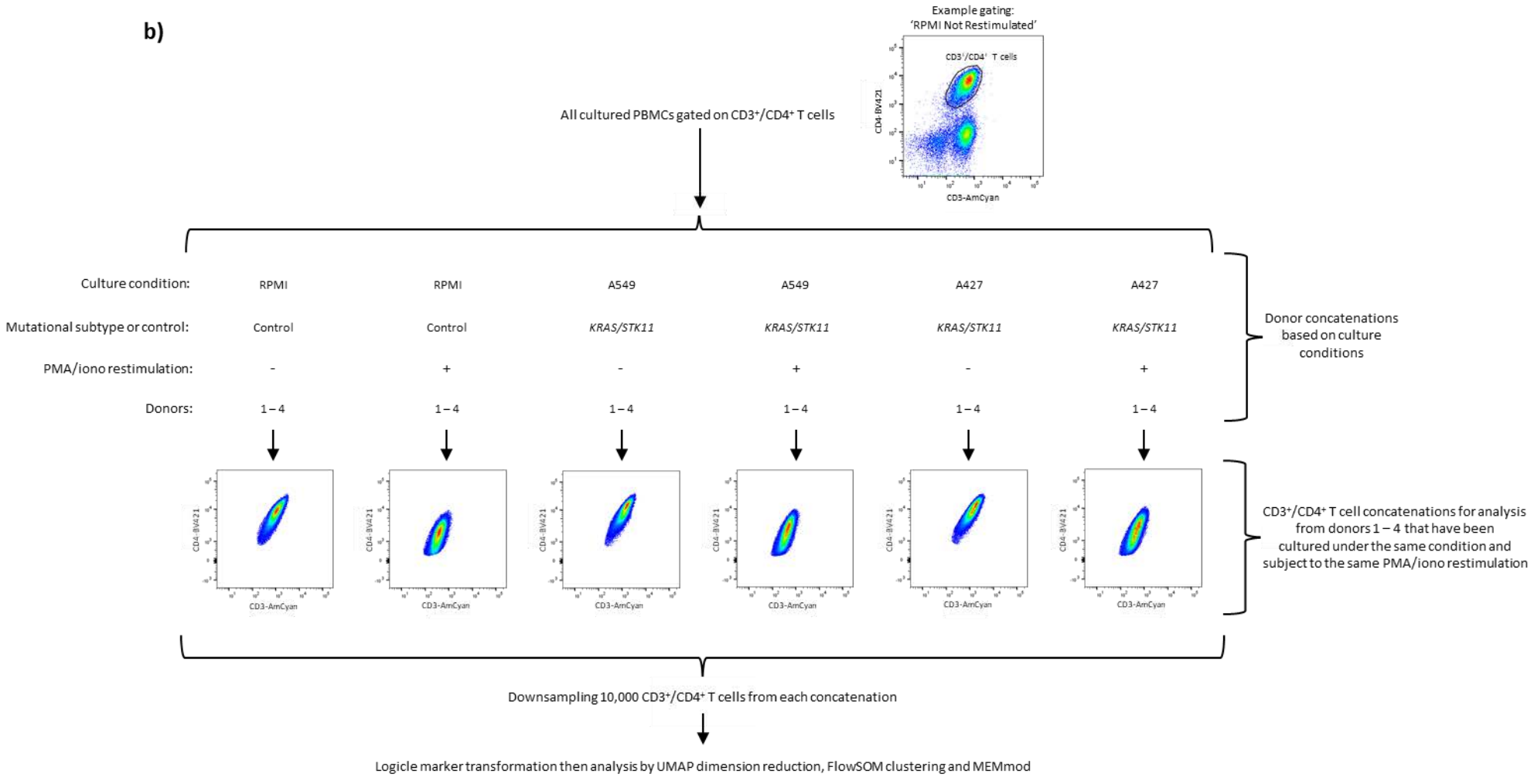
b)
Example gating:
'RPMI Not Restimulated'
CD3+/CD4+ T cells
CD4-BV421
CD3-AmCyan
All cultured PBMCs gated on CD3+/CD4+ T cells
Culture condition:
RPMI
RPMI
A549
A549
A427
A427
Mutational subtype or control:
Control
Control
KRAS/STK11
KRAS/STK11
KRAS/STK11
KRAS/STK11
PMA/iono restimulation:
-
+
-
+
-
+
Donors:
1 – 4
1 – 4
1 – 4
1 – 4
1 – 4
1 – 4
Donor concatenations based on culture conditions
CD3+/CD4+ T cell concatenations for analysis from donors 1 – 4 that have been cultured under the same condition and subject to the same PMA/iono restimulation
Downsampling 10,000 CD3+/CD4+ T cells from each concatenation
Logicle marker transformation then analysis by UMAP dimension reduction, FlowSOM clustering and MEMmod

Figure 5.2 Culturing PBMCs in conditioned media experimental and analytic workflows

a) Laboratory experiment workflow. This example workflow shows the experiment for one donor, culturing PBMCs in the 'RPMI control', 'A549 TCM' and 'A427 TCM' conditions. A full detailed method can be found in Chapter 2.3.11. A 24 well culture plate is shown here for illustrative purposes but 48 well plates were used in this experiment. **b)** Analysis workflow after data collection by flow cytometry. This example workflow shows concatenations for the 'RPMI control', 'A549 TCM' and 'A427 TCM' conditions. For the 'PMA/iono restimulation' row, '+' denotes 'Restimulated' and '-' denotes 'Not Restimulated'. Full detailed method in Chapter 2.6.6.

5.2.3 High Dimensional Analysis of Flow Cytometry Stained Cultured T Cells

Having shown that a high dimensional approach can distinguish between PMA/iono unstimulated and stimulated *ex vivo* $CD3^+/CD4^+$ T cells, we examined if this approach could distinguish between PMA/iono 'Not Restimulated' and PMA/iono 'Restimulated' $CD3^+/CD4^+$ T cells following three days of culture (Figure 5.3). The UMAPs for the $CD3^+/CD4^+$ T cells cultured in RPMI and TCM were generated in the same dimension reduction run as the *ex vivo* $CD3^+/CD4^+$ T cells in Figure 5.1, which are shown again in Figure 5.3a and 5.3b for comparison.

Similarly to the *ex vivo* $CD3^+/CD4^+$ T cell data, the cultured $CD3^+/CD4^+$ T cells shown in Figures 5.3c to 5.3f are also clearly delineated by PMA/iono as expected. The Th17 panel largely investigates cytokine release, which is low in cells that have not been recently stimulated and high in those that have. Based on visual assessment of the distribution of $CD3^+/CD4^+$ T cells in the density UMAP, the $CD3^+/CD4^+$ T cells from the RPMI and conditioned media conditions (Figures 5.3c to 5.3f) appear to be more phenotypically alike than the *ex vivo* $CD3^+/CD4^+$ T cells (Figures 5.3a and 5.3b) both with and without restimulation. There are smaller differences between the RPMI and conditioned media conditions. These data show that this approach can distinguish between PMA/iono

'Restimulated' and 'Not Restimulated' $CD3^+/CD4^+$ T cells, and also demonstrate the differences between *ex vivo* and three-day cultured $CD3^+/CD4^+$ T cells.

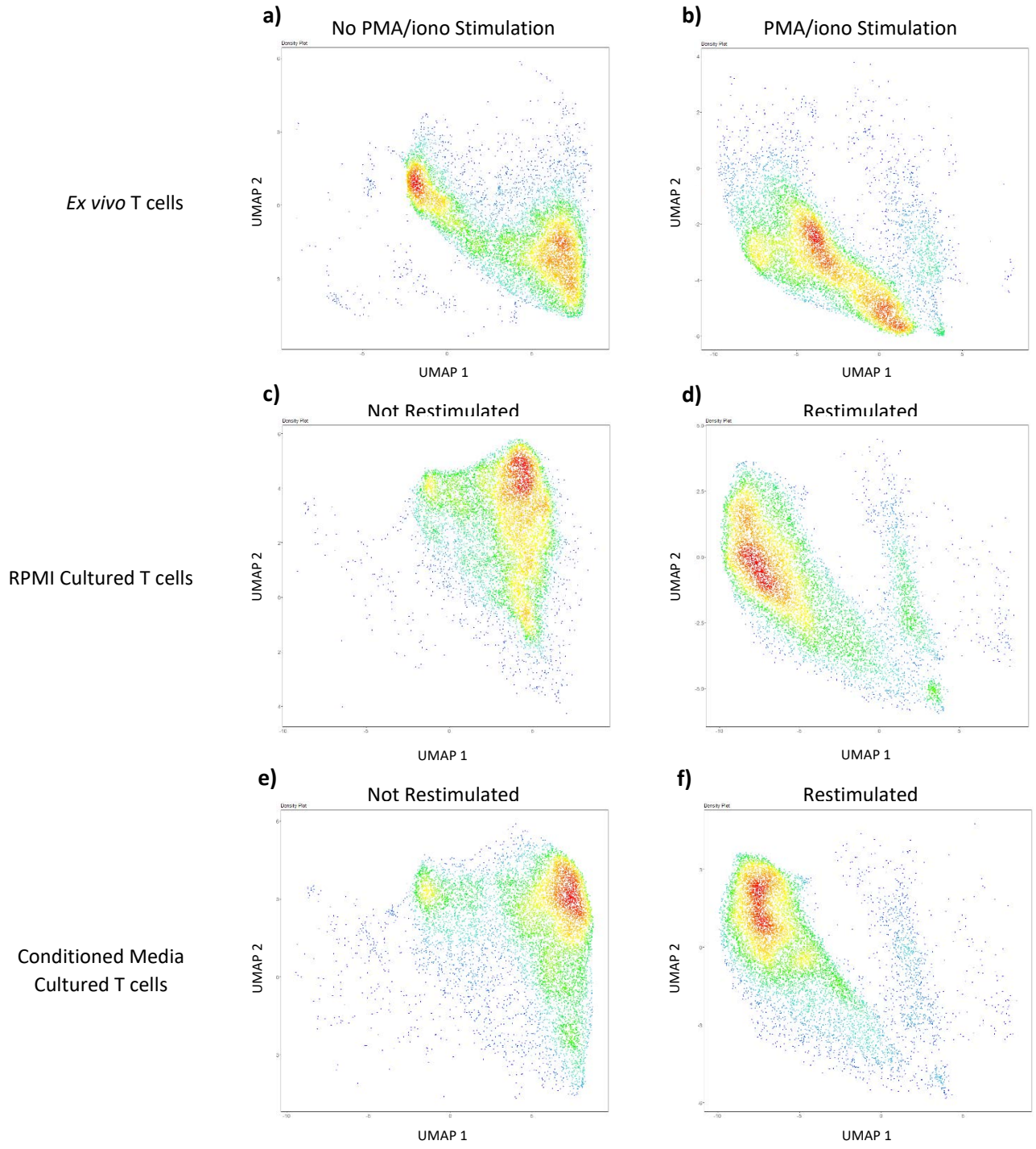

Figure 5.3 Examining differences between CD3⁺/CD4⁺ T cells from *ex vivo* PBMCs and from cultured PBMCs using a high dimensional approach

Density UMAPs of CD3⁺/CD4⁺ T cells filtered by no stimulation (left panels) or stimulation (right panels). **a) b)** Show *ex vivo* PBMC data from Figure 5.1 for comparison. **c) – e)** Show similarly filtered data from PBMCs that have been cultured for three days (Chapter 2.3.11), restimulated with PMA/iono or not (Chapter 2.3.10), then: stained, gated, concatenated, downsampled, transformed and dimension reduction performed as described in Figure 5.1. **c) d)** Show data from PBMCs cultured in RPMI control media. **e) f)** Show data from PBMCs cultured in all the different conditioned media.

We were next interested in examining our overarching experimental question, whether culturing PBMCs in TCM from NSCLC cell lines with *KRAS*, *STK11* and *KRAS/STK11* mutations led to differences in $CD3^+/CD4^+$ T cell phenotypes, with a particular interest in Th17 polarisation.

To determine whether any phenotypic differences were already apparent after three days culture or could only be seen upon PMA/iono restimulation of cultured $CD3^+/CD4^+$ T cells, we decided to examine 'Not Restimulated' and 'Restimulated' cultured $CD3^+/CD4^+$ T cells in different UMAP runs (Figures 5.4a and 5.4b respectively). These analyses used the concatenation strategy from Figure 5.2b.

All the data shown in Figure 5.4 are concatenated and downsampled based on individual conditions (e.g. 'A549 Not Restimulated' or 'A549 Restimulated') then filtered to give UMAPs showing cultured T cells grouped by TCM mutation groups. There are therefore differences in the total numbers of $CD3^+/CD4^+$ T cells per UMAP owing to the different numbers of cell lines and therefore TCM in each mutation group. The 'RPMI Control' and 'HEK293T Control' conditions only show concatenated T cells downsampled at 10,000 cells from these individual conditions.

Upon visual analysis, the 'Not Restimulated' $CD3^+/CD4^+$ T cell density UMAP plots in Figure 5.4a show clear differences in distribution of cells between the 'RPMI Control' condition and $CD3^+/CD4^+$ T cells cultured in TCM from the NSCLC cell lines. The '*KRAS* MT TCM' plot appears similar to the 'WT TCM' plot in terms of cell distribution. The '*STK11* MT TCM' and '*KRAS/STK11* MTs TCM' plots are similar to each other, and the distribution of cells shares similarities to the 'HEK293T Control'. These data suggest that there are differences in cell

phenotype following three days of culture in TCM that are apparent without restimulation of $CD3^+/CD4^+$ T cells.

As expected, the distribution of cells in the PMA/iono 'Restimulated' UMAPs shown in Figure 5.4b were generally visually different to the 'Not Restimulated' UMAPs in Figure 5.4a, as these also reflect cytokine production following restimulation. In Figure 5.4b, the '*STK11* MT TCM' and '*KRAS/STK11* MTs TCM' UMAP plots are again visually similar and are also similar to the 'HEK293T Control' and 'WT TCM' plots. The '*KRAS* MT TCM' plot is most distinct from the other plots in Figure 5.4b.

This experiment shows that culturing PBMCs in conditioned media from different cell lines influences $CD3^+/CD4^+$ T cell phenotype. It also suggests that these differences might also be linked to NSCLC tumour cell line mutation. These observations therefore warranted further investigation and quantification to allow statistical comparisons.

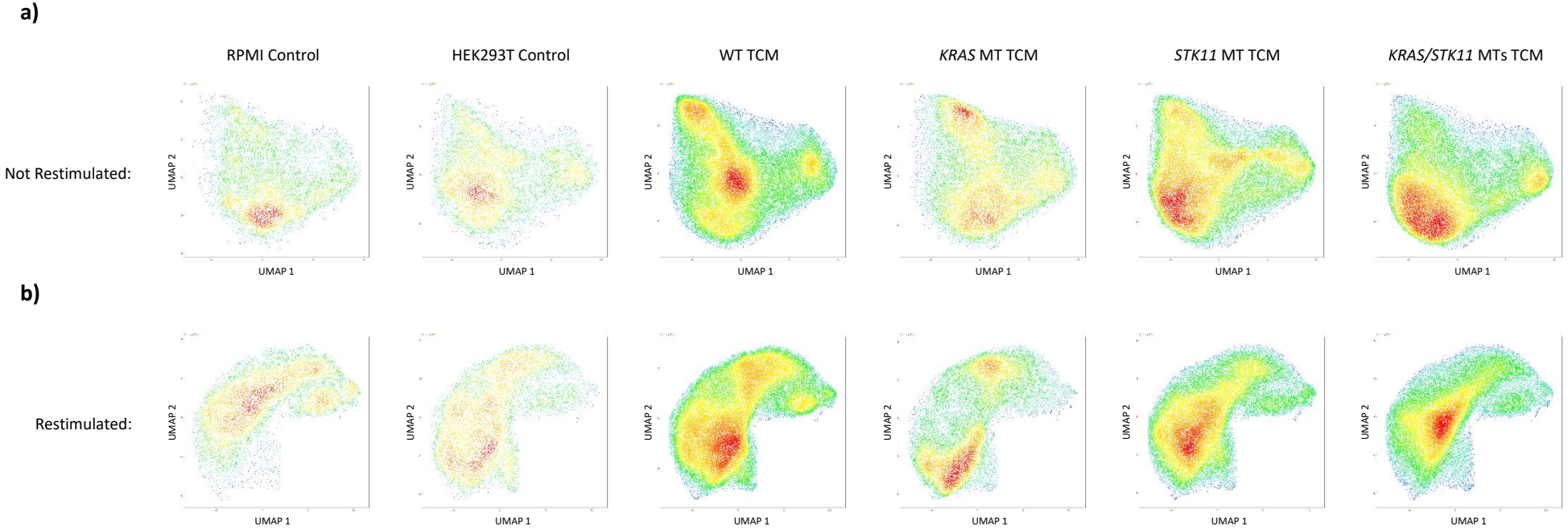

Figure 5.4 CD3⁺/CD4⁺ T cell densities filtered by *KRAS* and *STK11* mutational subtypes

PBMCs from four donors were cultured in the different conditioned media or RPMI control media from the cell lines shown in Table 5.1, using the method shown in Figure 5.2a. Cultured PBMCs were either restimulated by PMA/iono or not, then: stained using the Th17 flow cytometry panel and gated to CD3⁺/CD4⁺ T cells before concatenation, downsampling of 10,000 T cells and dimension reduction analysis using all features except Viability Dye-APC-Cy7, CD14-APC-Cy7 and CD19-APC-Cy7 as in Figure 5.2b. The UMAPs are filtered by mutational subtype (Note that 'WT TCM' are filtered on the CALU-3, H292, HCC78, H1299 and H2110 TCM, plot T cell *n* = 50,000. '*KRAS* MT TCM' are filtered on the CALU-6 and H441 TCM, plot T cell *n* = 20,000. '*STK11* MT TCM' are filtered on the CAL-12T, H1755, Chago-K-1 and H1563 TCM, plot T cell *n* = 40,000. '*KRAS/STK11* MT TCM' are filtered on the A549, A427, H460 and H1734 TCM, plot T cell *n* = 40,000). **a)** T cells in these density UMAPs were not restimulated by PMA/iono ('Not Restimulated'). **b)** T cells in these density UMAPs were restimulated by PMA/iono ('Restimulated').

5.2.4 Characterising UMAP Regions from Flow Cytometry Stained Cultured T Cells

We next sought to understand and quantify the changes seen in the $CD3^+/CD4^+$ T cells that had been cultured in different TCM, grouping by the *KRAS* and *STK11* mutation status of the cell lines. To do this we needed to understand which markers were expressed on $CD3^+/CD4^+$ T cells in the different areas of the UMAPs. To characterise the UMAP regions we used expression heatmaps of the markers included in the Th17 flow cytometry panel (locally scaled centred logicle transformed marker expression values), FlowSOM clustering, MEMmod and conventional flow cytometry gating analysis on the UMAP axes. Figure 5.5 shows these results.

To manually refine the number of FlowSOM clusters (representing different cell populations), we used the marker expression heatmaps and MEMmod. The *MEM* package was used to perform MEMmod which calculates the enrichment of each marker in each FlowSOM cluster compared to all other cells not in the cluster and gives a score from -10 (highly negatively enriched) to +10 (highly positively enriched) (332). If two clusters were within +1/-1 MEMmod score for any marker and appeared similar by heatmap examination, clusters were merged.

Figure 5.5 shows the results of the characterisation of the 'Not Restimulated' and 'Restimulated' UMAPs shown in Figure 5.4. The T cells in 'Not Restimulated UMAP 1' (Figure 5.5a) fall into two main populations delineated by CD127 expression. The CD127-PE heatmap shows higher CD127 expression in the top half of this plot compared to the bottom half. Further detail can be seen in Figure 5.5b which shows the same UMAPs

coloured by FlowSOM clusters with key MEMmod enrichments and important UMAP regions highlighted, including this 'CD127^{high}' region.

The CD3$^+$/CD4$^+$ T cells in the PMA/iono 'Restimulated UMAP 2' show cytokine driven differences between areas of the UMAP. The protruding region that is at the top right of the island is defined by CD3$^+$/CD4$^+$ T cells producing TNFα, IL-17A and IFNγ as shown in the heatmaps in Figure 5.5a and is marked as being 'Cytokine High' in Figure 5.5b. Clusters 14 to 16 have very high MEMmod enrichments scores for IL-17A, TNFα and IFNγ (Figure 5.5b), which is also visualised in Figure 5.5a. Th17 cytokine producing cells are found in clusters 15 and 16, which have MEMmod scores of +9/+10 for IL-17A, +1/+2 for RORγT and +1 for CCR6. Though IFNγ and IL-17A production were limited to this 'Cytokine High' region, cells producing TNFα and expressing CD127 were distributed throughout the top of 'Restimulated UMAP 2' (Figure 5.5a). This indicates the presence of cells producing both multiple and single cytokines.

The bottom left of 'Restimulated UMAP 2' contains 'CD127^{low}' cells, with negative MEMmod enrichments. RORγT expression is very high in the 'Cytokine High' region, matching with IL-17A production from cells in these clusters, and very low in the bottom right-hand region of the island where cytokine production is far lower (Figure 5.5b). From the heatmaps, the distributions of cells expressing RORγT and CCR6 expression are similar. Interestingly, the RORγT heatmap also shows T cells which express RORγT in the centre of the UMAP that do not produce any of the cytokines analysed.

To confirm the marker expression patterns shown by dimension reduction using FlowSOM and MEMmod analyses, we applied conventional manual test gating to different regions of

the UMAPs to analyse expression using two-dimensional dot plots (Figure 5.5c). Two regions were selected from 'Not Restimulated UMAP 1' which varied in their expression of CD127, and this was visualised in a dot plot vs the other surface marker in the Th17 panel CCR6. $CD3^+/CD4^+$ T cells falling into 'Gate 1' showed higher CD127 expression than those in 'Gate 2', confirming that the cells in the top of this UMAP express CD127.

Similarly, three regions were selected from 'Restimulated UMAP 2' which varied in RORγT and IL-17A expression. 'Gate 1' was drawn in the 'Cytokine High' region to capture $CD3^+/CD4^+$ T cells expressing IL-17A and RORγT, 'Gate 2' captured IL-$17A^-$ $CD3^+/CD4^+$ T cells with intermediate RORγT expression and 'Gate 3' captured $CD3^+/CD4^+$ T cells that did not express either IL-17A or RORγT. Dot plot visualisation in Figure 5.5c confirms that $CD3^+/CD4^+$ T cells in Gates '1' and '2' have higher RORγT expression and the $CD3^+/CD4^+$ T cells in 'Gate 1' emerge from the main population in an IL-$17A^+$ cloud. This two-dimensional analysis therefore confirms the UMAP populations identified using dimension reduction.

a)

Not Restimulated UMAP 1

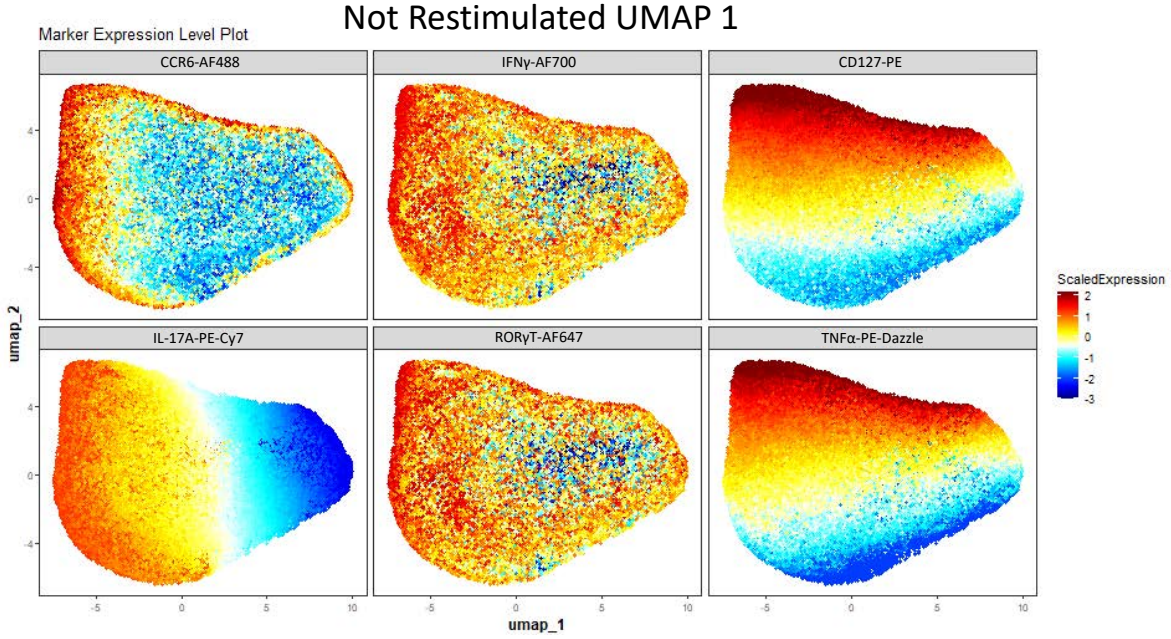

Restimulated UMAP 2

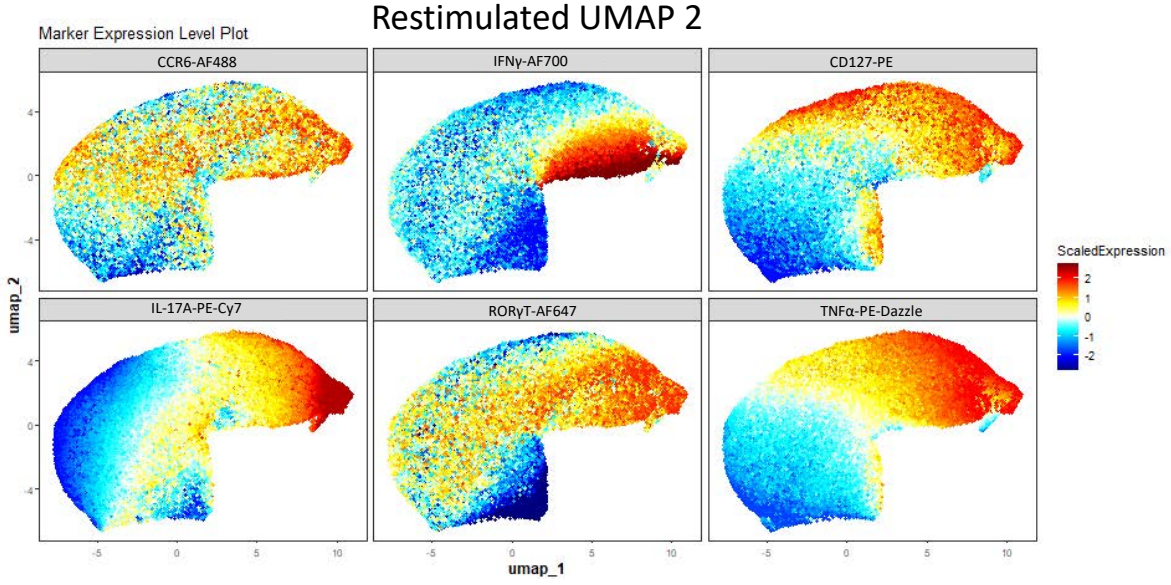

b) Not Restimulated UMAP 1

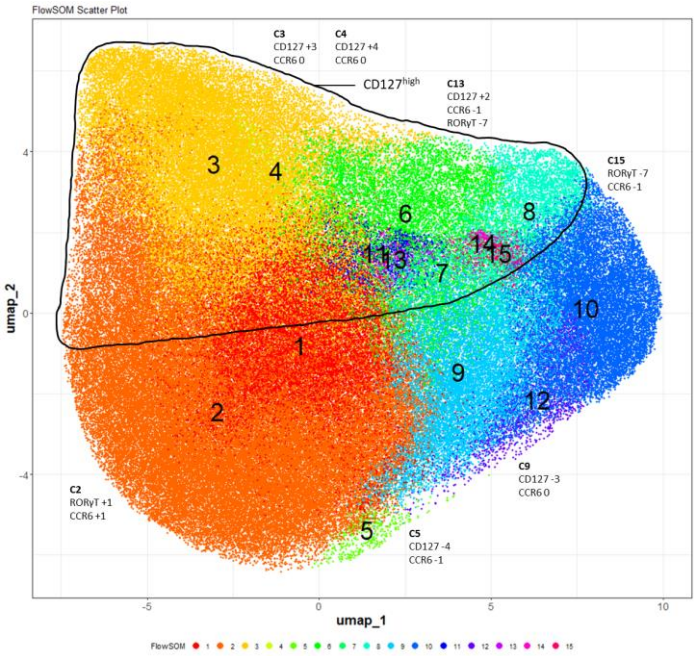

Restimulated UMAP 2

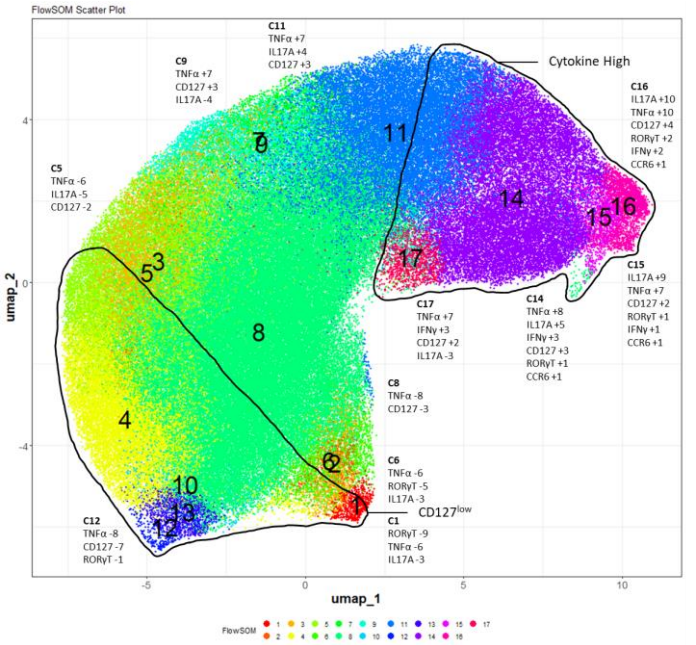

c)

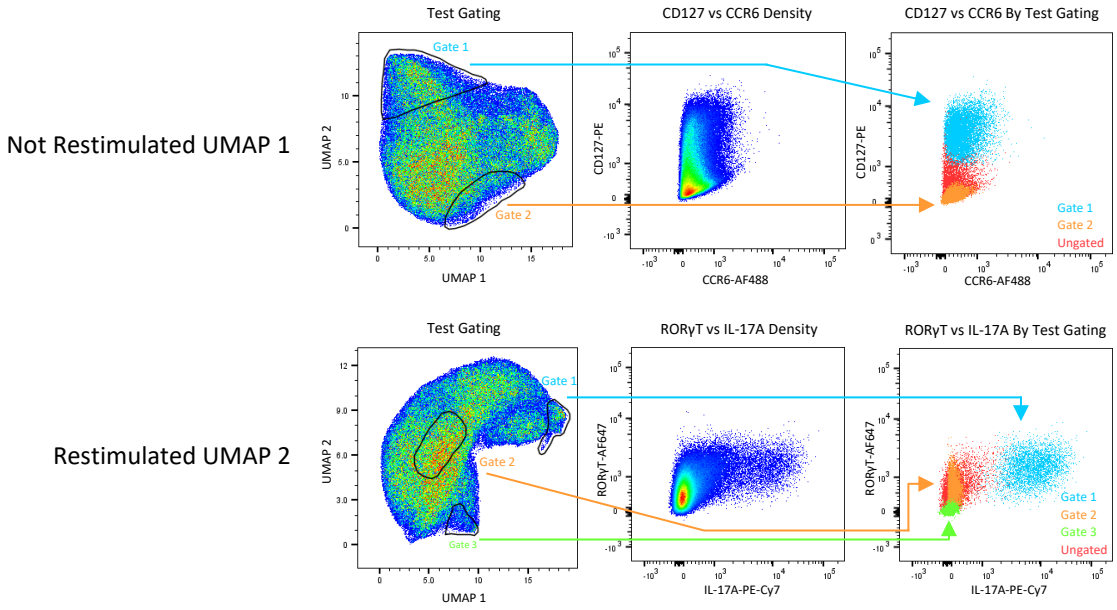

Figure 5.5 Characterising the regions of UMAPs performed on 'Not Restimulated' and 'Restimulated' CD3⁺/CD4⁺ T cells

The data for Not Restimulated UMAP 1' were processed as outlined in Figure 5.4a and the data for 'Restimulated UMAP 2' were processed as outlined in Figure 5.4b. **a)** Top UMAPs show heatmaps of Th17 flow cytometry panel marker expression without restimulation ('Not Restimulated UMAP 1'); bottom heatmaps ('Restimulated UMAP 2') show marker expression following restimulation. The logicle transformed marker expression data were scaled locally for each marker and these data were centred around 0. **b)** Data coloured by FlowSOM clusters. FlowSOM clustering was performed (Chapter 2.6.6), *k* = 15 for 'Not Restimulated UMAP 1' and *k* = 17 for 'Restimulated UMAP 2'. The *cytofkit2* export data were merged and MEMmod was performed (Chapter 2.6.6). The MEMmod enrichment scores for each cluster are annotated (e.g. 'C2' represents FlowSOM cluster 2, and 'RORγT +1' represents a positive +1 MEMmod enrichment score for RORγT). The 'CD127^{high}' ('Not Restimulated UMAP 1'), 'Cytokine High' and 'CD127^{low}' ('Restimulated UMAP 2') regions were manually annotated based expression levels. **c)** Data were imported into FlowJo. CD3⁺/CD4⁺ T cells from selected UMAP regions were analysed for their expression of CD127 vs CCR6 ('Not Restimulated UMAP 1') and RORγT vs IL-17A ('Restimulated UMAP 2') using bivariate plots to confirm the patterns of marker expression defined by the heatmap, FlowSOM and MEMmod analyses.

5.2.5 Quantifying UMAP Gated Cultured T Cells by Conditioned Media Cancer Gene Mutations

We next wanted to quantify the different phenotypes of CD3⁺/CD4⁺ T cells in the different regions of the two UMAPs. To do this we gated on different UMAP regions and analysed the percentages of CD3⁺/CD4⁺ T cells within these populations. The gates on Figure 5.6

were drawn on pseudocolour density plots but are shown on red coloured Zebra plots in Figure 5.6 for greater visibility.

In 'Not Restimulated UMAP 1' CD127 expression is a key delineating marker, so we therefore gated the 'CD127^{high}' and 'CD127^{low}' CD3^{+}/CD4^{+} T cell populations (Figure 5.6a). CD127^{low} CD3^{+}/CD4^{+} T cells may represent iTregs in this UMAP, although to confirm this we would need to expand the Th17 flow cytometry panel to also profile other Treg markers and repeat these experiments.

As CD3^{+}/CD4^{+} T cells in 'Restimulated UMAP 2' show cytokine driven differences, we gated cells falling into the previously mentioned 'Cytokine High' region (Figure 5.6b). To investigate Th17s we gated two populations based on expression of RORγT and production of IL-17A. The 'RORγT^{+}/IL-17A^{+}' population represents canonical Th17s that can produce IL-17A. A second 'RORγT^{+}/IL-17A^{-}' population represent either Th17s that are unable to produce IL-17A, or potentially a subgroup of Th17s with regulatory features that do not express CD127 (217, 220, 241, 486, 487). Like the gating in 'Not Restimulated UMAP 1', we also gated 'CD127^{high}' and 'CD127^{low}' CD3^{+}/CD4^{+} T cell populations in 'Restimulated UMAP 2' (Figure 5.6b).

We examined RORγT expression using logicle transformed MFI values to confirm the differences in RORγT expression between the two Th17 populations in the right-hand plot in Figure 5.6b. This shows that Th17s that produce IL-17A (RORγT^{+}/IL-17A^{+}) have significantly higher RORγT expression than Th17s that do not produce IL-17A (RORγT^{+}/IL-17A^{-}). CD127^{high} and Cytokine High gated T cells also have significantly higher RORγT expression compared to the RORγT^{+}/IL-17A^{-} Th17s, as the high expressing RORγT^{+}/IL-17A^{+}

Th17s are included in these gates. RORγT^{+}/IL-17A^{-} Th17s had higher RORγT expression compared to CD127^{low} putative iTregs (Figure 5.6b).

There was no difference between RORγT expression between the CD127^{high} and CD127^{low} T cells in the right-hand plot in Figure 5.6a.

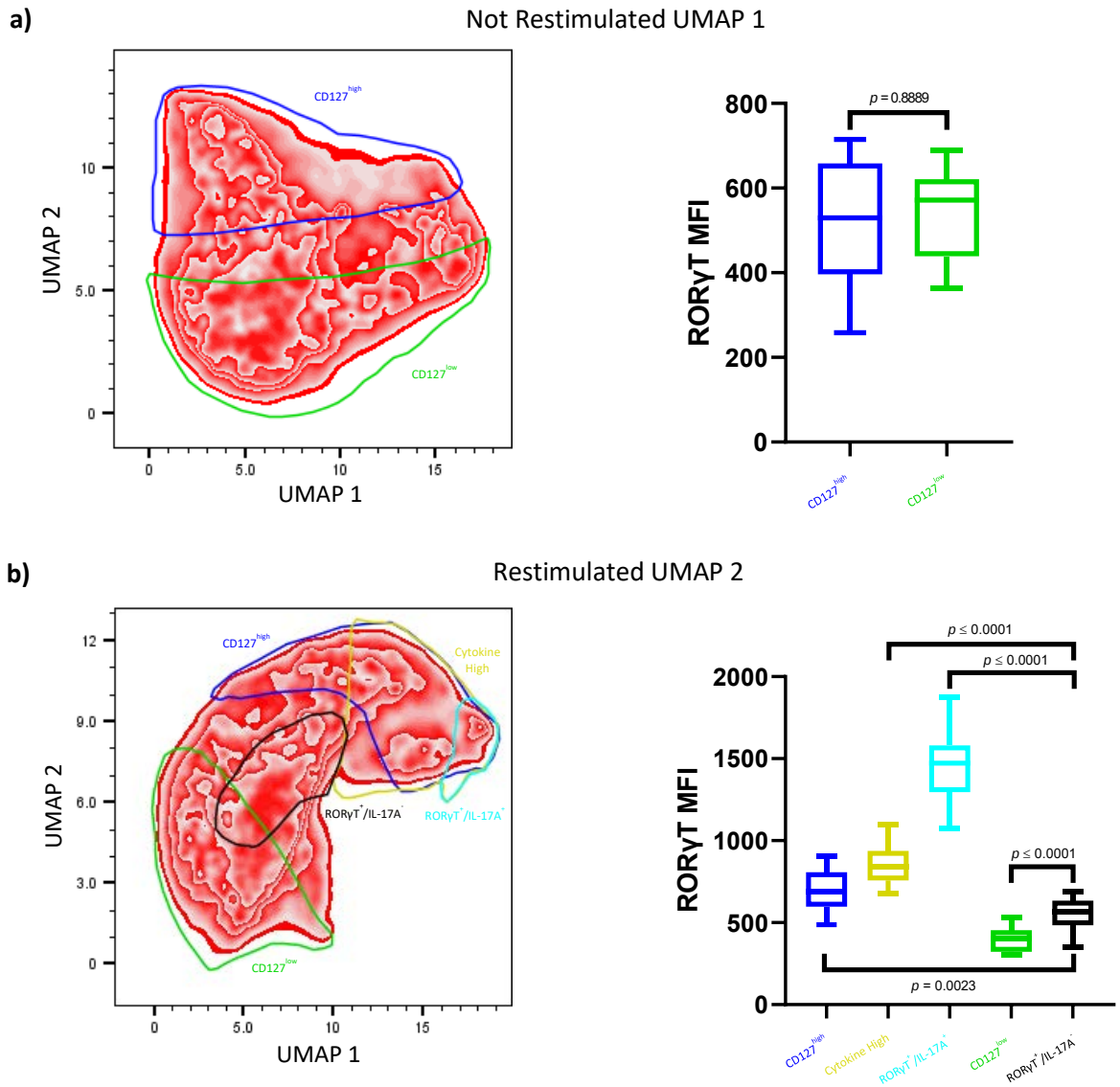

Figure 5.6 Gating UMAP populations of CD3⁺/CD4⁺ T cells

Positional and marker expression *cytofkit2* export data from all CD3⁺/CD4⁺ T cells from all conditions were imported into FlowJo, and gates were drawn (left-hand UMAP plots). These gates were copied onto the UMAPs for each individual condition concatenation except the RPMI control (e.g. 'Not Restimulated A549 TCM' or 'Not Restimulated H1563 TCM'), and logicle transformed RORγT MFI values were calculated for the T cells in each gate in each condition. These MFI values were grouped by gates (n = 16 conditions per gate group, right-hand boxplots). All statistical comparisons by unpaired two-sample Wilcoxon tests. **a)** The data for 'Not Restimulated UMAP 1' were processed as outlined in Figure 5.4a. CD127^{high} and CD127^{low} gates were drawn. **b)** The data for 'Restimulated UMAP 2' were processed as outlined in Figure 5.4b. CD127^{high}, CD127^{low}, Cytokine High, RORγT^{+}/IL-17A^{+} and RORγT^{+}/IL-17A^{-} gates were drawn.

The populations gated in 'UMAP 1' and 'UMAP 2' were subsequently quantified and compared by grouping by TCM cell line mutations to investigate whether culturing T cells

in TCM from NSCLC cell lines with *KRAS* and/or *STK11* mutations led to differences in T cell polarisation.

Figure 5.7 shows the data analysed from both the 'Not Restimulated' condition and the PMA/iono 'Restimulated' condition sub-divided into mutation subgroup. Although we did not find any significant differences with the small number of cell lines available, we did observe some interesting trends for further future investigation with a greater number of cell lines.

Figure 5.7a shows a non-significant increase in RORγT^{+}/IL-17A^{-} Th17 cells cultured for three-days in TCM from cell lines with *KRAS/STK11* mutations compared to those cultured in TCM from WT cell lines (p = 0.1905). There were no differences in the percentages of CD3^{+}/CD4^{+} T cells within the RORγT^{+}/IL-17A^{+} and Cytokine High gates between the different mutation groups.

Figure 5.7b shows a similar non-significant increase in the percentages of CD127^{low} CD3^{+}/CD4^{+} T cells, which potentially represent iTregs, cultured in TCM from cell lines with *KRAS/STK11* mutations compared to those cultured in TCM from WT (Not Restimulated). Although this was not seen following PMA/iono restimulation. Conversely, there were non-significant decreases in the percentages of CD127^{high} CD3^{+}/CD4^{+} T cells cultured in TCM from *KRAS/STK11* mutant cell lines (Not Restimulated and Restimulated) and *STK11* mutant cell lines (Restimulated) compared to culturing in WT TCM.

Overall, these findings potentially show both an increase in RORγT^{+}/IL-17A^{-} Th17s and CD127^{low} iTregs from PBMCs cultured in TCM derived from cell lines with *KRAS/STK11* mutations. However, such experiments need repeating with larger numbers of cell

lines/group to determine whether these observations are significant, and Treg markers should be incorporated into the Th17 flow cytometry phenotyping panel to verify increased iTregs.

a)

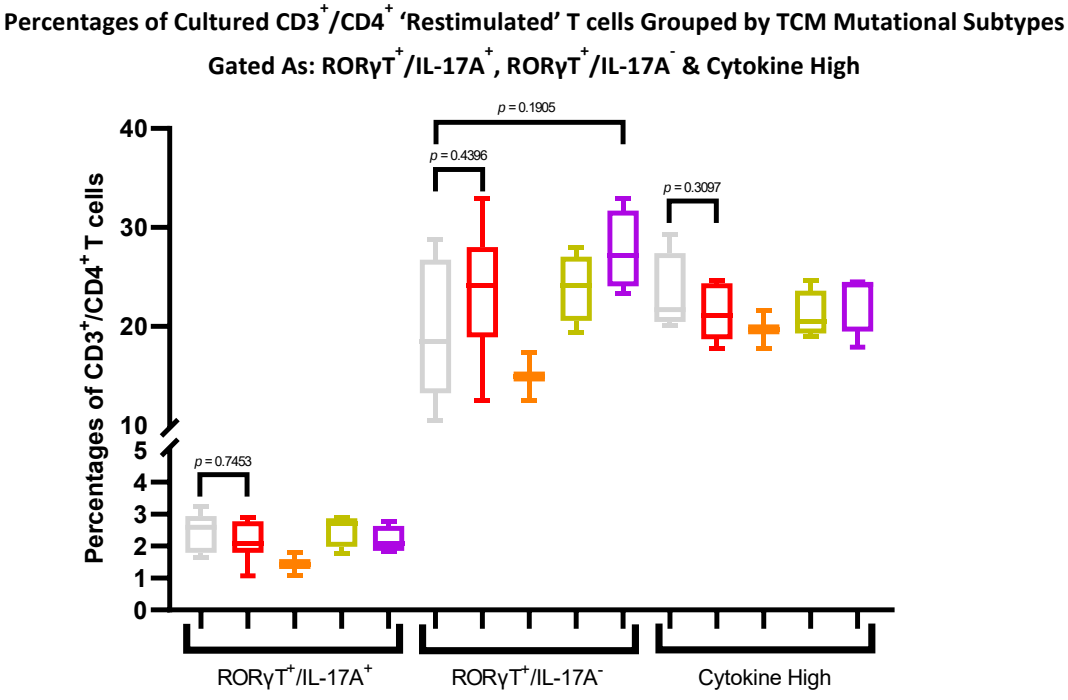

b)

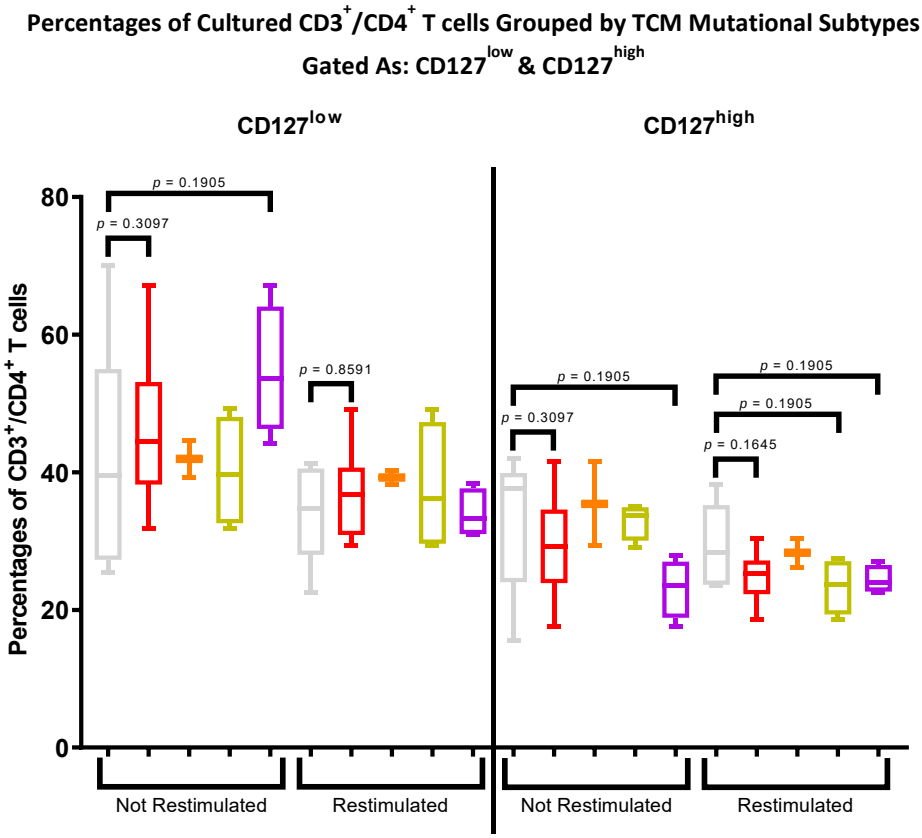

Figure 5.7 Comparing percentages of gated CD3⁺/CD4⁺ T cell populations grouped by NSCLC cell line mutational subtypes

Data were processed as outlined in Figure 5.4 and gated as described in Figure 5.6. Gates were copied onto the UMAPs for each TCM individual condition concatenation. The percentages of gated CD3⁺/CD4⁺ T cells from the individual conditions were grouped by *KRAS* and *STK11*

mutational subtypes (WT *n* = 5 grey coloured boxes, MT *n* = 10 red boxes, *KRAS* MT *n* = 2 orange boxes, *STK11* MT *n* = 4 gold boxes, *KRAS/STK11* MTs *n* = 4 purple boxes) and statistically compared by unpaired two-sample Wilcoxon tests. *p* values for WT vs MT comparisons are shown throughout this Figure, and *p* values for other comparisons are only shown if ≤ 0.2. **a)** Data from 'Restimulated UMAP 2'. **b)** Data labelled 'Not Restimulated' is from 'Not Restimulated UMAP 1', and data labelled 'Restimulated' is from 'Restimulated UMAP 2'.

5.2.6 Profiling Cell Line Conditioned Media for Type 17 Immunity Related Cytokines and Chemokines

To assess whether NSCLC cell lines with different mutations may release soluble factors such as cytokines and chemokines that may drive T cell polarisation, we designed a Luminex immunoassay multiplex panel to quantify 21 cytokines and chemokines related to different aspects of type 17 immunity. This was used to profile TCM collected from all the cell lines alongside the RPMI 'Culture Media Control', a diluent blank control and HEK293T conditioned media. As a control for cytokine detection in the Luminex assay, we also included media collected from *ex vivo* PBMCs that had been stimulated to produce cytokines.

The 'PBMC Stim' control was subject to a four-hour PMA/iono stimulation without the addition of Brefeldin A to allow for extracellular cytokine release, then the PBMCs were pelleted and the cytokine rich supernatant extracted as a positive control. The 'PBMC Unstim' control was simultaneously generated by leaving PBMCs in culture media for the four-hour incubation but without PMA/iono stimulation or Brefeldin A. To confirm that this stimulation had worked we treated two more tubes of PBMCs in parallel, this time adding Brefeldin A, and stained the cells using the Th17 flow cytometry panel to detect IFNγ, IL-17A and TNFα production. Figure 5.8a shows that this stimulation method was successful and these cytokines were clearly produced by the stimulated PBMCs.

We then performed the Luminex experiment with the TCM, control culture media and *ex vivo* PBMC media, and measured analyte concentrations against analyte standard curves. Figures 5.8b to 5.8e show the analyte quantification with each point on the plot representing a different control or conditioned media which have been grouped by cell line mutation. All analytes were successfully detected in either the controls or conditioned media, except for IL-12p70 which was only detected in the standards. IL-1β, IL-10, IL-17A, TNFα, IFNγ and IL-21 are shaded as these cytokines were only detected in the PBMC controls and were not found in any conditioned media. Although cytokines and chemokines were clearly detected in TCM, we found no associations between the presence of specific analytes and mutational groups of cell lines. Nevertheless, Figures 5.8f and 5.8g show that IL-6 and CXCL8, which are associated with Th17 polarisation and neutrophil recruitment respectively, are secreted by the majority of the NSCLC cell lines. IL-6 can be found in especially high concentrations in TCM from two cell lines with *STK11* mutations (green bars) and two with *KRAS/STK11* mutations (orange bars). The concentrations of IL-6 in TCM from these 2/4 cell lines with *STK11* mutations and 2/4 cell lines with *KRAS/STK11* mutations were higher than the highest assay standard (marked by an 'x') (Figure 5.8f). CXCL8 is found in very high concentrations in most TCM from NSCLC cell lines, and these concentrations are higher than the highest stand for 7/12 TCM with detectable CXCL8 (Figure 5.8g).

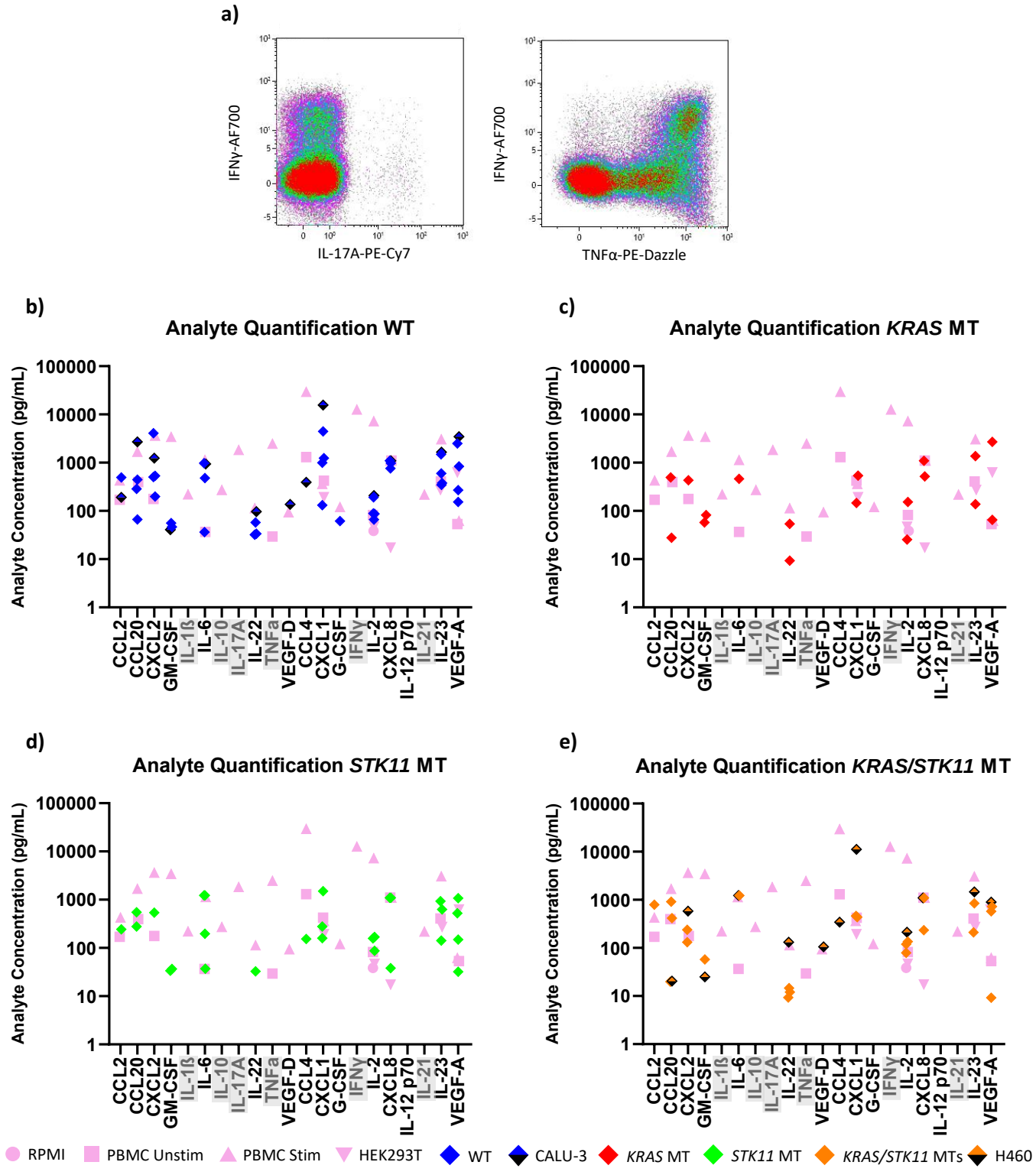
a)
IFNγ-AF700
IL-17A-PE-Cy7
IFNγ-AF700
TNFα-PE-Dazzle
b)
Analyte Quantification WT
c)
Analyte Quantification KRAS MT
d)
Analyte Quantification STK11 MT
e)
Analyte Quantification KRAS/STK11 MT
Analyte Concentration (pg/mL)
100000
10000
1000
100
10
1
CCL2
CCL20
CXCL2
GM-CSF
IL-1ß
IL-6
IL-10
IL-17A
IL-22
TNFa
VEGF-D
CCL4
CXCL1
G-CSF
IFNγ
IL-2
CXCL8
IL-12 p70
IL-21
IL-23
VEGF-A
RPMI
PBMC Unstim
PBMC Stim
HEK293T
WT
CALU-3
KRAS MT
STK11 MT
KRAS/STK11 MTs
H460

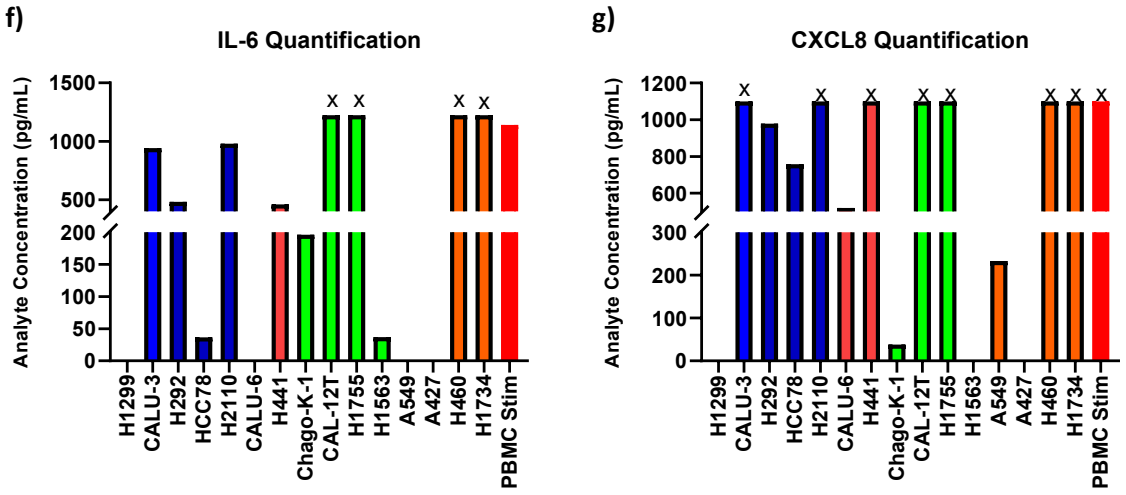

Figure 5.8 Quantifying type 17 immunity related cytokines and chemokines in TCM

a) PBMCs were stimulated for cytokine release (in parallel with the Luminex 'PBMC Stim' control), stained with the Th17 flow cytometry panel and gated to the 'Lymphocytes Gate' (Figure 2.4). **b) – e)** Luminex quantification of type 17 immunity related analytes was performed on control media (RPMI, PBMC Unstim, PBMC Stim or HEK293T) and TCM from WT **b)**, *KRAS* MT **c)**, *STK11* MT **d)**, *KRAS/STK11* MTs **e)** cell lines as described in Chapter 2.7.2. These plots show the concentrations of the different analytes which are coloured/annotated by TCM mutational status or control media. The analytes greyed out were only detected in PBMC supernatant. **f)** same as **b) – e)** except this plot shows the IL-6 concentration detected in each sample (WT = blue bars, *KRAS* MT = red bars, *STK11* MT = green bars, *KRAS/STK11* MTs = orange bars). **g)** same as **f)** except shows CXCL8 concentrations.

Although the Luminex experiment did not highlight any cytokines or chemokines that were associated with cell lines with *KRAS* and *STK11* NSCLC cancer gene mutations, we were interested in elucidating any patterns of coordinated analyte expression that could link the cell lines. We therefore performed PCA on the quantified analyte concentrations to find cell lines with similar cytokine/chemokine profiles.

The PCA plot in Figure 5.9a was generated from the conditioned media from all the NSCLC cell lines and the HEK293T cells. The PC1 and PC2 principal components accounted for the majority of variance in the dataset (all other principal components each accounted for <11% of the variance in the dataset). Of the two main principal components, PC1 accounted for 46.5% of the variance and this was ascertained to be overall analyte

concentration. The cell lines that secreted the high concentrations of most cytokines and chemokines had lower PC1 scores and those that secreted lower concentrations or less cytokines and chemokines had higher PC1 scores. We were unable to confidently determine the reason for variance in PC2. The cell line conditioned media marked on Figure 5.9a clearly associate into two groups, termed 'PCA Group 1' and 'PCA Group 2'. Interestingly, 4/5 conditioned media from the cell lines in both PCA Group 1 and PCA Group 2 have *KRAS* and *STK11* mutations. Typically, the TCM from WT cell lines were not found within these groups and only two TCM from cell lines with mutations (CALU-6 and H460 cells, *KRAS* and *KRAS/STK11* mutations, respectively) did not fall within these groups.

We then re-examined the analyte quantification data to determine which analytes were linked with PCA Group 1 and PCA Group 2. We detected CCL2 expression in 2/5 of the conditioned media in PCA Group 1 and 0/5 of the TCM in PCA Group 2, whereas we detected GM-CSF expression in 5/5 of the TCM in PCA Group 2 and 0/5 conditioned media in PCA Group 1 (Figure 5.9b). Statistical analysis in Figure 5.9b shows that the TCM in PCA Group 2 have significantly higher concentrations of GM-CSF, IL-6, CXCL8, IL-23 and CCL20, as well as CXCL1 and IL-2, compared to the conditioned media in PCA Group 1.

Having found two groups of cell lines with *KRAS* and *STK11* mutations which secrete and do not secrete type 17 immunity related cytokines and chemokines (PCA Groups 2 and 1 respectively), we were interested in whether the cytokines present in the TCM may have a greater effect on T cell polarisation than the mutational subtype of the cell lines alone. We therefore re-grouped the data from the previous experiment culturing PBMCs in

conditioned media, this time considering whether the cell lines did or did not secrete type 17 immunity related cytokines and chemokines.

Although this comparison showed no significant differences in $CD3^+/CD4^+$ T cell phenotypes between PBMCs cultured in TCM from cell lines in PCA Group 1 vs 2 (Figure 5.9c), the percentages of $CD3^+/CD4^+$ T cells in the $ROR\gamma T^+/IL\text{-}17A^-$ gate was higher in PCA Group 1 then in PCA Group 2. However, this failed to reach significance ($p = 0.1508$).

Overall, we did not see a difference in the concentrations of type 17 immunity related cytokines and chemokines present in TCM conditioned by NSCLC cell lines of different mutational subtypes. Nevertheless, PCA did uncover a potential added layer of heterogeneity with regard to cytokine/chemokine production from NSCLC cells with *KRAS* and *STK11* mutations. Thus, the cell lines grouped in PCA Group 2 secrete more type 17 immunity related cytokines and chemokines compared to those group in PCA Group 1, and these are also found at significantly higher concentrations.

a)

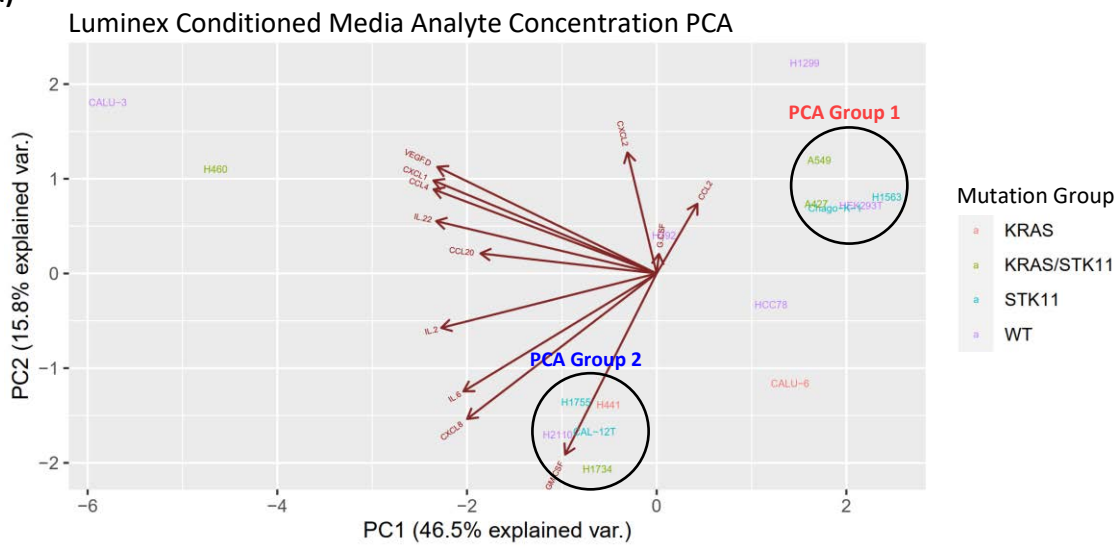
Luminex Conditioned Media Analyte Concentration PCA
PC2 (15.8% explained var.)
PC1 (46.5% explained var.)
PCA Group 1
PCA Group 2
Mutation Group
KRAS
KRAS/STK11
STK11
WT

b)

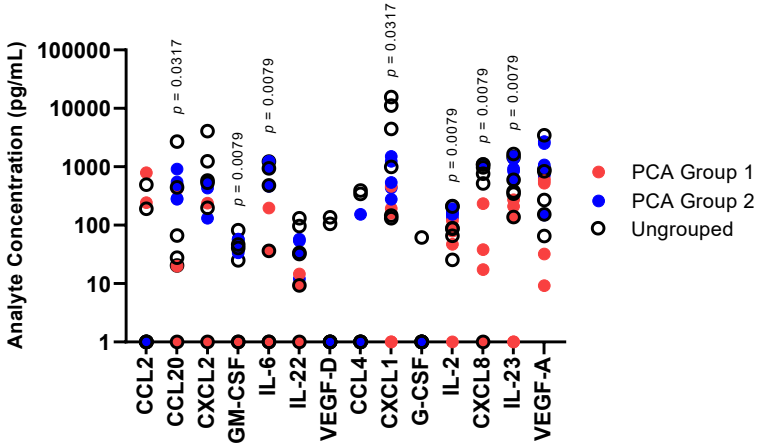
Analyte Quantification Coloured By PCA Group
Analyte Concentration (pg/mL)
p = 0.0317
p = 0.0079
p = 0.0079
p = 0.0317
p = 0.0079
p = 0.0079
p = 0.0079
CCL2
CCL20
CXCL2
GM-CSF
IL-6
IL-22
VEGF-D
CCL4
CXCL1
G-CSF
IL-2
CXCL8
IL-23
VEGF-A
PCA Group 1
PCA Group 2
Ungrouped

c)

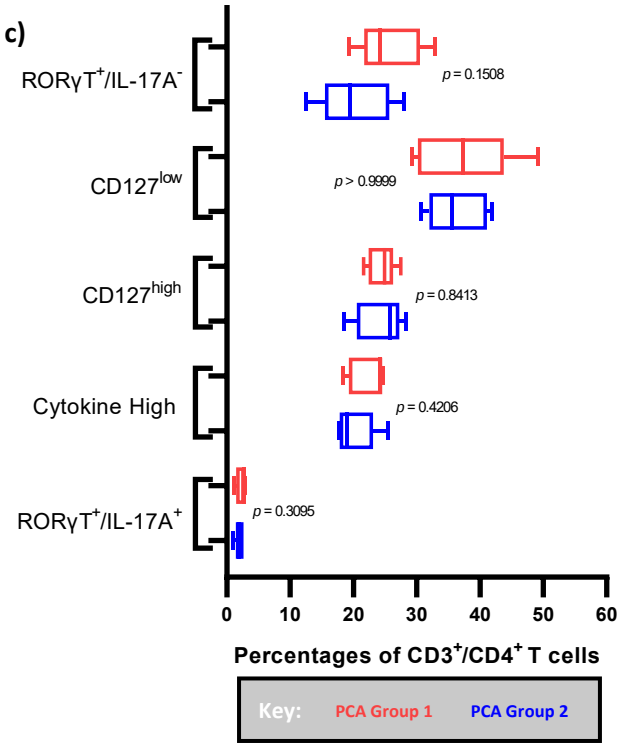
RORγT+/IL-17A-
CD127low
CD127high
Cytokine High
RORγT+/IL-17A+
p = 0.1508
p > 0.9999
p = 0.8413
p = 0.4206
p = 0.3095
Percentages of CD3+/CD4+ T cells
Key:
PCA Group 1
PCA Group 2

Figure 5.9 Grouping conditioned media by patterns of cytokine and chemokine expression and examining the T cell phenotypes associated with culturing in PCA groups of conditioned media

a) PCA generated from analyte concentrations from the Luminex experiment (Figure 5.8). Data from non-zero features (CCL2, CCL20, CXCL2, GM-CSF, IL-6, IL-22, VEGF-D, CCL4, CXCL1, G-CSF, IL-2, CXCL8, IL-23 and VEGF-A) were passed to the prcomp() function (*stats* package), then were centred and scaled to give a normal distribution (mean = 0, variance = 1) and PCA was performed. Loading plot arrows were shown. Conditioned media were coloured by cell line mutational subtype and two PCA groups were manually annotated. **b)** Analyte concentrations were plotted, and points were coloured by the two PCA groups defined in part **a)** (PCA Group 1 red, PCA Group 2 blue). Analyte concentrations were compared between the two PCA groups by unpaired two-sample Wilcoxon tests and *p* values were annotated if a difference was significant. **c)** Boxplots showing the flow cytometry data from the PBMCs cultured in different conditioned media that had been restimulated with PMA/iono ('Restimulated UMAP 2', processed as described in Figure 5.4b and gated as described in Figure 5.6b), grouped based on whether individual conditioned media from that cell line were classified as PCA Group 1 or PCA Group 2 in the Luminex PCA analysis from part **a)**. Differences in percentage gated $CD3^+/CD4^+$ T cells were statistically compared between the two PCA groups using unpaired two-sample Wilcoxon tests.

5.3 Discussion

Understanding the mechanisms that drive distinct immune microenvironments in tumours carrying different genetic mutations is important to inform the development of therapies that can manipulate these mechanisms to encourage anti-tumour responses and discourage pro-tumour responses.

In earlier work (Chapters 3 and 4) we demonstrated increased frequencies of RORγT^{+} lymphocytes in LUAD tumours with *KRAS* and/or *STK11* mutations compared to tumours without these mutations. T cell plasticity between the Th17/iTreg balance is known to be skewed by cytokines or secreted factors (215, 237-239, 246, 253, 260, 261). Chapter 4 also identified that ILC3s might be an important subset of RORγT^{+} lymphocytes in LUAD tumours, but we were unable to investigate ILC3s as our Th17 flow cytometry did not include all the required markers to gate lineage^{-} cells. To investigate ILC3s we would have to repeat these experiments with a revised flow cytometry panel. Concentrating on Th17s, we therefore developed an *in vitro* assay culturing PBMCs in conditioned media from NSCLC cell lines as a first step in investigating whether soluble factors preferentially released by tumour cells carrying mutations in the *KRAS* or *STK11* genes could cause T cell polarisation.

To our knowledge, studying how T cell phenotypes change after culture in TCM from NSCLC cell lines with different cancer mutations has not previously been examined in the literature.

5.3.1 Characterising UMAP Regions and Quantifying Populations of Cultured T Cells by *KRAS* and *STK11* Tumour Conditioned Media Mutational Subtypes

We firstly optimised a Th17 focused multicolour flow cytometry panel and validated a high dimensional approach to analyse the data, using *ex vivo* PBMCs stimulated with PMA/iono. This method clearly distinguished phenotypic differences between unstimulated and stimulated PBMCs, largely driven by induction of cytokine production.

This was then applied to PBMCs that had been previously stimulated with anti-CD3 and anti-CD28 and cultured for three days in conditioned media harvested from fifteen NSCLC cell lines of varied *KRAS* and *STK11* mutational status, one control epithelial cell line and control media. Although the anti-CD3 and anti-CD28 T cell activation cocktail has a substantial impact on T cell phenotype (488), its use was necessary for T cell survival during the three-day culture which was consistent across all conditions. We chose to culture PBMCs instead of a purified $CD3^+/CD4^+$ T cell population so not to exclude any interactions with APCs including DCs, monocytes or B cells that may be important for T cell polarisation. These PBMCs were then restimulated or not restimulated after the three-day culture.

It should noted that PMA/iono stimulation potently induces secretion of IFNγ, TNFα, IL-2, IL-6 and IL-17A, but not Treg cytokines such as IL-4 and IL-10 (489-491). Care should therefore be taken when comparing PMA/iono cytokine secretion findings to other stimulation systems.

Nevertheless, using this system, we found that $CD3^+/CD4^+$ T cells from PBMCs cultured for three days in TCM were phenotypically different to *ex vivo* $CD3^+/CD4^+$ T cells and to

$CD3^+/CD4^+$ T cells cultured in control media, both with and without restimulation with PMA/iono (Figure 5.3).

Changes in T cell phenotype were not unexpected as previous studies have shown that culturing leukocytes in TCM can induce T cell IFNγ secretion and TIM-3 expression and polarise macrophages to an M2 phenotype (492, 493). Voigt *et al* (213) showed that TCM from breast and NSCLC cell lines stimulated IL-22 release from T cells via AHR and RORγT.

Upon further analysis, we saw visual differences in the distributions of $CD3^+/CD4^+$ T cells on the UMAPs filtered into subgroups based on the *KRAS* and *STK11* mutational status of the NSCLC cell lines (Figure 5.4). This was independent of PMA/iono restimulation as differences were seen purely following culture in the 'Not Restimulated' cells.

To quantify these differences between mutational subgroups of NSCLC cell lines, we characterised the expression of markers from the Th17 flow cytometry panel within different regions of the UMAPs. Regions of marker expression were initially identified from the UMAPs of the total concatenated data from the three-day cultured cells (Figure 5.5).

We found that CD127 (IL-7R) expression was clearly differentially expressed between different regions of both UMAPs generated from cells that were either not restimulated (UMAP 1) or from cells that were restimulated with PMA/iono (UMAP 2) (Figure 5.5). As CD127 is negatively correlated with FoxP3 expression (266), this also provides an estimation of the position of Treg populations on the UMAP axes although inclusion of further markers such as CD25 and FoxP3 would be required to fully define Treg populations. Defining clear cut $ROR\gamma T^+$ T cell populations to allow comparison between

the two UMAPs was more difficult, largely because PMA/iono stimulation increased the expression of Th17 panel markers including RORγT.

With regard to cytokine expression, as expected, this was generally very low in the cultured $CD3^+/CD4^+$ T cells that had not been restimulated with PMA/iono shown in UMAP 1 (Figure 5.5a). The local marker scaling unfortunately exaggerates expression which is low across the board. Furthermore, it is likely that low level cytokine expression is a result of residual activation from the initial anti-CD3 and anti-CD28 T cell activation cocktail at the start of the experiment.

Considering cytokine and CD127 expression from the PMA/iono restimulated $CD3^+/CD4^+$ T cells, we defined three important regions within UMAP 2 (Figure 5.5b). This included a '$CD127^{low}$' region which might represent $FoxP3^+$ iTregs (265, 266, 494). We also defined a focused '$RORγT^+/IL\text{-}17A^+$' region encompassing cells that highly express RORγT and produce IL-17A, characteristic of the Th17 subset of $CD4^+$ T cells. These cells were also $CD127^+$, supporting a previously reported relationship between CD127 and the production of Th17-related cytokines, especially IL17A and TNFα (479-482, 495, 496). Interestingly we also identified another region of cells with weaker RORγT expression that did not express CD127 or produce IL-17A, termed '$RORγT^+/IL\text{-}17A^-$'.

This $RORγT^+/IL\text{-}17A^-$ population may represent suppressed Th17s which are unable to produce Th17 cytokines and do not express CD127 or could potentially be one of the novel $RORγT^+$ Treg populations described in the literature (217, 220-223, 226, 241, 486, 487). One such population are Tr17s that co-express FoxP3 and RORγT and express CCR6 have been observed in mice and humans, including in NSCLC patient blood (226). Tr17s secrete

lower quantities of IL-10 and have been suggested to be less immunosuppressive compared to conventional Tregs (221, 223, 226). However, Tr17 cells have also been reported to secrete IL-17A (221-223, 226). The other major FoxP3^{+}/RORγT^{+} Treg population RORγT^{+} Tregs are more suppressive than Tr17s. RORγT^{+} Tregs express CCR6 and are CD127^{low} but do not secrete IL-17A (217, 220, 241, 486, 487). This better matches our observed phenotype following TCM culture, however this experiment would need to be repeated to include FoxP3 profiling to make this conclusion.

We then applied these regions to the UMAPs filtered by *KRAS* and *STK11* mutational subtypes, to investigate differences in CD3^{+}/CD4^{+} T cell phenotypes following culture in TCM from NSCLC cell lines with different mutations. Although the results of these analyses were not statistically significant with the small number of cell lines available per group, we did see some interesting trends that warrant further investigation with larger numbers of cell lines.

The key observations were that culturing T cells in TCM from *KRAS/STK11* mutant cell lines was associated with higher percentages of CD3^{+}/CD4^{+} T cells in both the 'RORγT^{+}/IL-17A^{-}' and 'CD127^{low}' gates, with an associated decrease of 'CD127^{high}' T cells (Figure 5.7). This indicates that there is likely a greater fraction of suppressed or potentially regulatory Th17s and iTregs following culture in *KRAS/STK11* TCM. Single-cell RNA-Seq at different timepoints during T cell polarisation shows that it takes 5 days for full polarisation to Th17 or Treg phenotypes but that measurable transcriptional changes occur after 16 hours (488). Whether our three-day experiment is long enough for Th17/iTreg transdifferentiation to fully occur is not known. Alternatively, there could be better

maintenance of particular T cell subsets in *KRAS/STK11* TCM. Further investigations are required both to confirm these changes in T cell subsets and to formally identify the cell types involved.

With further confirmation, these findings would support a long-standing association of increased Tregs in tumours with *KRAS/STK11* mutations in studies on both humans and mice (115, 183, 189). Furthermore, mouse lung tumours with *KRAS* mutations have higher numbers of RORγT expressing Tregs compared to WT tumours, and depleting these cells reduced tumour burden, suppressed M2 macrophages, upregulated MHC class II and increased cytotoxic lymphocyte infiltrates (497). However, it is not clear whether the Tregs investigated in this previously mentioned study are RORγT$^+$ Tregs or Tr17s, which are also associated with *KRAS* driven lung cancer mouse models (498).

5.3.2 Profiling Tumour Conditioned Media-Derived Cytokines and Chemokines by *KRAS* and *STK11* Tumour Conditioned Media Mutational Subtypes

We next investigated the presence of soluble factors such as cytokines/chemokines in the NSCLC cell line derived TCM that may lead to CD3$^+$/CD4$^+$ T cell polarisation (157, 250, 260, 488).

We found that NSCLC TCM do not contain IL-1β, IL-10, IL-12p70, IL-17A, IL-21, TNFα and IFNγ (Figure 5.8), and contain variable concentrations of most other cytokines but with no link to *KRAS* and/or *STK11* mutational status.

Of interest, we found high concentrations of the Th17 polarising cytokine IL-6 and the neutrophil chemoattractant CXCL8 in TCM from most NSCLC cells lines, but especially in

TCM from cell lines with *STK11* and *KRAS/STK11* mutations (Figure 5.8). In the literature, constitutive secretion of IL-6 and CXLC8 has been reported from several different cancer cell lines, including NSCLC (492, 499, 500). However, this has not been previously linked to the genetic mutational profile of the cell lines. Regarding a potential mechanism, IL-6 and CXCL8 production might be regulated by STAT3 and MEK signalling driven by *KRAS/STK11* mutations. Dysregulated mTORC1 signalling resulting in STAT3 hyperactivation has been shown to induce *IL6* and *CXCL8* transcription, as has *KRAS* driven MEK pathway activation, and NF-κB signalling in the case of CXCL8 expression. Autocrine IL-6 signalling can further activate STAT3 and stimulate IL-6 production (98, 205, 421-427). Moreover, MEK signalling intermediates can cause IL-6R shedding, thereby allowing IL-6 trans-signalling in other cells via IL-6R complexing with the ubiquitously expressed glycoprotein 130 (422, 428-430). In addition to their roles in Th17 differentiation and neutrophil recruitment, IL-6 and CXCL8 autocrine signalling can induce IL-17RA expression, potentiating additional IL-17-mediated STAT3 activation and inflammatory effects (457, 501).

5.3.3 Uncovering Heterogeneity in the Secretion of Cytokines and Chemokines from Non-Small-Cell Lung Cancer Cell Lines with *KRAS* and *STK11* Mutations

Finally, we performed PCA on the TCM Luminex quantification data to further investigate any potential patterns of cytokine/chemokine expression that could link the cell lines. This gave two tight PCA groups both associated with *KRAS* and *STK11* mutations, whilst TCM from control cell lines without these mutations were distributed through the PCA plot (Figure 5.9). PCA Group 2 expressed significantly higher levels of type 17 immunity related

cytokines/chemokines compared to PCA Group 1. An interesting difference between these PCA groups is the nature of the specific *KRAS* mutations in the cell lines. This may provide a mechanism for the differential levels of cytokine/chemokine production seen. Smith *et al* (76) compared the transcriptional signatures of MEFs transfected with *KRAS* genes with different mutations, finding that G12 mutations and G13 mutations cluster differently. An explanation for this is that specific *KRAS* mutations have differences in KRAS GTPase kinetics (72).

We found that A549 cells with the G12S mutation group with A427 cells with the G12D mutation in PCA Group 1, whilst H1734 and H441 with G13C and G12V respectively fall in PCA Group 2. Although the grouping of H441 (G12V) with H1734 (G13C) rather than the other cell lines with G12 mutations initially appears unexpected, this may not be the case. Stolze *et al* (72) showed that G12V, G13C and G12C mutations all have a greater affinity for GTP compared to other codon 12 and 13 mutations, such as those found in A549 and A427. Interestingly, the two cell lines with *KRAS* mutations that do not group with either PCA Group 1 or 2, H460 and CALU-6, harbour Q61H and Q61K mutations. Q61 mutations were shown to have the highest GTP affinity and slowest hydrolysis speed, indicating high levels of KRAS signalling in cells with these mutations (68, 72). This suggests that differential KRAS GTPase signalling activity may influence NSCLC cell line cytokine/chemokine secretion.

Supporting this notion, the H441 and H1734 cell lines in PCA Group 2 are addicted to KRAS signalling and are dependent on KRAS for growth, whilst A549s and A427s (PCA Group 1) are not (53).

Rather, another study showed that *KRAS* mutant NSCLCs that are KRAS independent are instead dependent on *STK11* and *KEAP1* mutations and are reliant on antioxidative glucose rewiring (102, 502). These KRAS independent A549 and A427 cell lines are reliant on glutathione production via the TCA cycle from glutamine and α-ketoglutarate, and have undetectable expression of STING (15, 90, 119, 126). Despite this, LKB1 loss may not be the only delineating factor as 3/5 PCA Group 2 cell lines also have LKB1 loss compared to 4/5 PCA Group 1 cell lines.

Given the higher concentrations of Th17 polarising cytokines in the TCM from PCA Group 2 cell lines, it could be expected that increased '$ROR\gamma T^{+}$/IL-$17A^{+}$' Th17s would be present following PBMC culture. However, this was not the case. Interestingly, we did find increased '$ROR\gamma T^{+}$/IL-$17A^{-}$' Th17 cells following culture in conditioned media from PCA Group 1 cell lines compared to PCA Group 2, but this was not significant (Figure 5.9c).

A lack of type 17 immunity related cytokines and chemokines in the TCM from this group suggests that the presence of these '$ROR\gamma T^{+}$/IL-$17A^{-}$' Th17s is not due to any of our screened secreted factors. Alternatively, this could be due to different dosages of our profiled secreted factors, other unprofiled signalling molecules like TGFβ which we could not include into our Luminex panel, or an unmeasured metabolite.

5.3.4 Summary

Overall, in this Chapter we investigated whether soluble factors in TCM collected from NSCLC cell lines with *KRAS* and *STK11* mutations can induce T cell polarisation. Whilst we did not observe significant polarising differences in gated T cell populations cultured in

KRAS and *STK11* mutational subtypes of TCM, we found increases in RORγT^{+}/IL-17A^{-} T cells – which might represent suppressed Th17s or RORγT^{+} Tregs – and CD127^{low} putative iTregs associated with these mutations (216-220, 241, 486, 487).

Profiling type 17 immunity related cytokines/chemokines showed that IL-6 and CXCL8 are ubiquitously secreted at high concentrations by NSCLC cell lines, and PCA revealed two distinct groups both linked to *KRAS* and *STK11* mutations, differing in their concentrations of cytokines/chemokines revealing an added layer of complexity above mutational status alone. Re-grouping the data from the experiment culturing T cells by these PCA groups surprisingly showed no significant differences in T cell phenotypes between PCA groups, but a non-significant induction in RORγT^{+}/IL-17A^{-} T cells in the group with lower concentrations of the profiled cytokines/chemokines.

The mechanism behind the presence of these RORγT^{+}/IL-17A^{-} T cells remains unclear. Differences in cytokine/chemokine release, KRAS dependency and GTPase activity, and requirement for LKB1 loss indicates substantial signalling and metabolic differences between the PCA grouped cell lines. Therefore, it is possible that RORγT^{+}/IL-17A^{-} T cells are supported by an unprofiled metabolite found in TCM. Future work would confirm Treg statuses by FoxP3 staining and focus on uncovering the reason behind this immune phenotype by investigating unprofiled factors and metabolites.

6. Final Discussion

Ever since researchers recognised that solid tumour immunosurveillance occurs, it has been suggested that tumour cells – driven by oncogenic cancer gene alterations – can invoke immunomodulation by interacting with and manipulating intratumour immune cells. As these cancer gene alterations are the fundamental drivers of the aberrant cellular processes that define different tumour phenotypes, it is likely that specific cancer gene alterations are linked to distinct immune phenotypes. Thus, evidence from CRC showed that tumours with *POLE* mutations were associated with expression of immune genes that indicated high TILs, but that tumours with *KRAS* mutations had reduced expression of immune genes linked with $CD4^+$ T cell responses (197).

Here we examined the relationship between LUAD cancer gene mutations and immune gene expression, termed immune signatures. We showed similar high *HLA* expression in the immune signatures for cancer genes encoding RTKs, *MET* and *EGFR*, which are subject to gain of function mutations (11, 37). Yet, the opposite was true for *KRAS* mutations which also drives downstream RTK signalling in a ligand independent manner (38). Although it might be expected that different mutations that all ultimately activate RTK signal transduction would elicit similar immune signatures, there is an added layer of signalling heterogeneity. This is observed clinically, as although *EGFR* and *KRAS* mutations are typically mutually exclusive, tumours with *EGFR/KRAS* mutations do not respond to *EGFR* targeted therapies and inhibitors (11). These findings indicate differences in immune contextures and further highlight the need for mutational screening of LUAD tumours in

routine clinical practice to enable prescription of appropriate treatment regimens (360). Altogether, better knowledge of cancer gene associated immune signatures and understanding of the TME can inform rational immunotherapy stratification.

Like *KRAS* driven CRC, we provided evidence of a lack of immune gene expression in *KRAS* driven LUAD, as well as *STK11* mutant LUAD (49, 115, 126, 197, 316, 401, 403-405). LKB1 loss was particularly associated with a 'cold' immune microenvironment, and we found that tumours with *STK11* mutations have low expression of *HLA* genes and the genes encoding PD-1 and PD-L1. Clinically, tumours with *STK11* mutations do not benefit from immunotherapies including PD-1/PD-L1 blockade (115). Therapies that modulate epigenetic regulation could change this, as histone deacetylase inhibitors can restore HLA class II expression by upregulating *CIITA* expression (148, 503), and DNA methyltransferase inhibitors can stop LKB1-mediated STING silencing (126, 403). The literature suggests that these in combination with STING agnoists, would greatly increase PD-L1 expression and could re-sensitise these tumours to PD-L1 blockade (126, 403). These effects might be further augmented by chemokine therapies to increase the numbers of intratumoural T cells and by the depletion of TANs (189, 414).

We also uncovered evidence of the previously reported mutational synergy between *KRAS* and *STK11* in tumours with concomitant *KRAS/STK11* mutations (49, 115, 124, 125, 189, 316), regarding tumour immune infiltration and significantly increased expression of *RORC*. As *KEAP1* mutations can also co-occur with *KRAS/STK11* mutations, which further enhance tumour antioxidative properties and negatively regulate STING, future work

should assess RORγT mRNA and protein expression in *KRAS/STK11/KEAP1* mutant tumours (15, 49, 102, 116-118, 504).

Performing IHC staining for RORγT protein expression supported our findings at the transcriptional level, showing increased abundances of RORγT$^+$ lymphocytes in tumours with *KRAS* and *STK11* mutations. High RORγT$^+$ lymphocyte abundances were also found in tumours without whole genome duplications. As whole genome duplications occur in early-stage LUAD, RORγT$^+$ lymphocytes might be of an increased prevalence in very early-stage disease and Tregs might support a late-stage suppressive TME (246). Additional tumour resections from molecularly profiled patients with subclinical and stage III/IV LUAD would allow us to investigate this.

High RORγT$^+$ lymphocyte abundances were also specifically associated with poor patient OS. Evidence from the literature suggests that IL-17A secreted from RORγT$^+$ cells including Th17s, γδ17s and iNKT17s can result in reduced patient survival, by activating STAT3, inducing EMT as well as recruiting TANs and MDSCs (230, 231, 239, 276, 285, 287, 288, 291, 293, 294, 296, 297, 304, 432, 462). Furthermore, IL-22 is also linked to STAT3 activation, and IL-17A-induced CXCL8 also aids suppressive myeloid lineage recruitment (245, 275, 285, 298-302). We also found potential evidence of intratumoural RORγT$^+$ ILC3s. Whilst ILC3s are known for their LTi-like properties and their tumour localisation may indicate a role in TLS induction/maintenance, we did not observe any differences in TLS density in tumours with *KRAS* and *STK11* mutations. Instead, as ILC3s are a key subset of RORγT$^+$ lymphocytes that also secrete pathological IL-17A, IL-22 and CXCL8, it is possible that these cells contribute to poor patient prognosis (172, 174, 443, 467-470).

As RORγT$^+$ lymphocytes appear to perpetuate and potentially enhance hyperactive STAT3 signalling in patient tumours with *KRAS* and *STK11* mutations, using STAT3 inhibitors or neutralising IL-17A, IL-22 and CXCL8 may be appropriate strategies for these patients (213, 302, 505-508). RORγT antagonists are another therapeutic option, although these small molecules have not yet been rigorously tested in humans and may not inhibit IL-22 secretion (230, 509). Furthermore, we found that NSCLC cell lines secreted high concentrations of IL-6 which can further enhance STAT3 signalling by autocrine and paracrine mechanisms, as well as polarise naïve T cells to Th17s. Therefore, neutralising IL-6 directly or using tocilizumab to inhibit IL-6R could be another important intervention (189, 414, 510).

A key advantage of IHC phenotyping is the ability to pinpoint cellular localisations, albeit at the expense of a limited number of markers and variable qualities of fixed tissue. To improve this, new techniques such as imaging mass cytometry would offer more detailed phenotyping of RORγT$^+$ lymphocytes from tissue sections, however this approach remains expensive and low-quality tissue can still affect staining. An alternative approach that would retain tissue quality is analysis of dissociated fresh *ex vivo* NSCLC tumours. By designing multiple flow cytometry or cytometry by time of flight panels, future work could phenotype Th17s, ILC3s and Tregs from tumoural suspensions from tumours with different mutations. Whilst this was not possible in this thesis due to the lack of routine sequencing of LUAD tumours, it will become achievable when targeted mutational screening becomes a reality in the clinic. With reduced sequencing costs weighed against a growing need for stratification, the availability of fresh NSCLC tumours with biopsy confirmed *KRAS* and *STK11* mutations will increase.

In the absence of TCM from fresh tumours with *KRAS* and *STK11* mutations, we developed an *in vitro* system to study potential T cell polarisation in which we cultured PBMCs in TCM derived from NSCLC cell lines carrying alterations in different cancer genes. As Th17 cells display plasticity with Tregs, we were interested in whether Th17 phenotype is influenced by soluble factors in TCM.

After three-day culture in *KRAS* and *STK11* mutant TCM, we observed an increase in $CD127^{low}$ putative iTregs, although future staining for FoxP3 and other Treg markers is needed to formally confirm the identity of these cells. In previous literature, Tregs are associated with *KRAS* and *KRAS/STK11* driven murine models of NSCLC, but it is not known whether Tregs preferentially migrate into these tumours, are maintained in these tumours, or are a result of polarisation or plasticity (183, 189). This could be resolved by *in vivo* Treg tracking, and by performing similar *in vitro* culture experiments to our own using *ex vivo* mouse tumour tissue. We also observed increased $ROR\gamma T^{+}$/IL-$17A^{-}$ $CD3^{+}$/$CD4^{+}$ T cells associated with LKB1 cell line loss. These T cells could be suppressed Th17s unable to produce IL-17A, or $ROR\gamma T^{+}$ Tregs which might reflect Th17/iTreg plasticity (217, 220, 241, 486, 487), however again further characterisation is required. As it is not clear whether these T cells can produce other cytokines such as IL-22, IL-17F and IL-10, designing new flow cytometry panels and repeating these experiments using cell line and fresh tumour culture systems would enable us to assess phenotype and functionality.

There are many unprofiled soluble factors which might be mechanistically responsible for the differences in T cell phenotypes seen following culture with TCM. As the Th17/iTreg balance is responsive to metabolites, we would look to immunometabolically profile TCM

from fresh tumour and NSCLC cell lines (271). This future work would investigate the following with links to *KRAS/STK11* driven LUAD: glucose, glutamine, glutamate, branched-chained amino acids, phenylalanine, lipids, triglycerides, fatty acids, and phospholipids (15, 90, 102, 120, 123, 255, 439, 511-517).

It would also be interesting to investigate tumour-derived exosomes which contain a variety of instructional proteins, nucleic acids, and metabolites. Interestingly, *KRAS* mutated exosomal DNA from NSCLC patient sera can polarise Tregs (518), and CRC exosomes promoted Th17s and increased RORγT expression (519). Despite findings of reduced *TGFB1* expression in tumours with *STK11* mutations (520), which is supported by our own finding of a significant reduction in the *STK11* immune signature, we would also examine TGFβ which is an important in polarisation and plasticity in the Th17/iTreg axis (260, 263).

Together, this body of work demonstrates that RORγT^{+} lymphocytes are an important subset of TILs in LUADs (but not SqCCs) with *KRAS* and *STK11* mutations specifically and are associated with reduced patient survival. By adopting a novel stratified approach, this work enabled us to understand the immune contexture in tumours driven by different mutations, focusing on an important driver of LUAD, *KRAS*, and its concomitant pathological partner *STK11* which causes treatment resistant progressive disease. Molecular stratification will eventually need to become a clinical reality and the standard of care in order to improve patient outcomes through personalised medicine. This work is an important step forward in NSCLC tumour immunology research, which should now consider the mutational profile of the tumour. Ultimately, this will enable accurate

stratification of patients for immunotherapy regimens based on rational knowledge of how tumour genetics impact intratumoural immunity.

References

1. Wong MCS, Lao XQ, Ho KF, Goggins WB, Tse SLA. Incidence and mortality of lung cancer: global trends and association with socioeconomic status. Sci Rep. 2017;7(1):14300. 10.1038/s41598-017-14513-7
2. Office for National Statistics. Death registered in England and Wales. London: The United Kingdom Statistics Authority, Statistics OfN; 2019 2019.
3. Office for National Statistics. Cancer survival in England - adults diagnosed. London: The United Kingdom Statistics Authority, Statistics OfN; 2019 2019.
4. Pikor LA, Ramnarine VR, Lam S, Lam WL. Genetic alterations defining NSCLC subtypes and their therapeutic implications. Lung cancer. 2013;82(2):179-89. 10.1016/j.lungcan.2013.07.025
5. Sainz de Aja J, Dost AFM, Kim CF. Alveolar progenitor cells and the origin of lung cancer. J Intern Med. 2020. 10.1111/joim.13201
6. Schabath MB, Cote ML. Cancer Progress and Priorities: Lung Cancer. Cancer Epidemiol Biomarkers Prev. 2019;28(10):1563-79. 10.1158/1055-9965.EPI-19-0221
7. Dela Cruz CS, Tanoue LT, Matthay RA. Lung cancer: epidemiology, etiology, and prevention. Clin Chest Med. 2011;32(4):605-44. 10.1016/j.ccm.2011.09.001
8. Vaz M, Hwang SY, Kagiampakis I, Phallen J, Patil A, O'Hagan HM, et al. Chronic Cigarette Smoke-Induced Epigenomic Changes Precede Sensitization of Bronchial Epithelial Cells to Single-Step Transformation by KRAS Mutations. Cancer Cell. 2017;32(3):360-76 e6. 10.1016/j.ccell.2017.08.006
9. Park HY, Kang D, Shin SH, Yoo KH, Rhee CK, Suh GY, et al. Chronic obstructive pulmonary disease and lung cancer incidence in never smokers: a cohort study. Thorax. 2020;75(6):506-9. 10.1136/thoraxjnl-2019-213732
10. McCarthy WJ, Meza R, Jeon J, Moolgavkar SH. Chapter 6: Lung cancer in never smokers: epidemiology and risk prediction models. Risk Anal. 2012;32 Suppl 1:S69-84. 10.1111/j.1539-6924.2012.01768.x
11. Sharma SV, Bell DW, Settleman J, Haber DA. Epidermal growth factor receptor mutations in lung cancer. Nat Rev Cancer. 2007;7(3):169-81. 10.1038/nrc2088
12. Hanahan D, Weinberg RA. Hallmarks of cancer: the next generation. Cell. 2011;144(5):646-74. 10.1016/j.cell.2011.02.013
13. Jamal-Hanjani M, Wilson GA, McGranahan N, Birkbak NJ, Watkins TBK, Veeriah S, et al. Tracking the Evolution of Non-Small-Cell Lung Cancer. N Engl J Med. 2017;376(22):2109-21. 10.1056/NEJMoa1616288
14. Prabavathy D, Swarnalatha Y, Ramadoss N. Lung cancer stem cells-origin, characteristics and therapy. Stem Cell Investig. 2018;5:6. 10.21037/sci.2018.02.01
15. Kerr EM, Gaude E, Turrell FK, Frezza C, Martins CP. Mutant Kras copy number defines metabolic reprogramming and therapeutic susceptibilities. Nature. 2016;531(7592):110-3. 10.1038/nature16967
16. Vanhove K, Graulus GJ, Mesotten L, Thomeer M, Derveaux E, Noben JP, et al. The Metabolic Landscape of Lung Cancer: New Insights in a Disturbed Glucose Metabolism. Front Oncol. 2019;9:1215. 10.3389/fonc.2019.01215
17. Herbst RS, Heymach JV, Lippman SM. Lung cancer. N Engl J Med. 2008;359(13):1367-80. 10.1056/NEJMra0802714
18. De Palma M, Biziato D, Petrova TV. Microenvironmental regulation of tumour angiogenesis. Nat Rev Cancer. 2017;17(8):457-74. 10.1038/nrc.2017.51
19. Chen DS, Mellman I. Oncology meets immunology: the cancer-immunity cycle. Immunity. 2013;39(1):1-10. 10.1016/j.immuni.2013.07.012
20. Zhu T, Bao X, Chen M, Lin R, Zhuyan J, Zhen T, et al. Mechanisms and Future of Non-Small Cell Lung Cancer Metastasis. Front Oncol. 2020;10:585284. 10.3389/fonc.2020.585284
21. Lang-Lazdunski L. Surgery for nonsmall cell lung cancer. Eur Respir Rev. 2013;22(129):382-404. 10.1183/09059180.00003913
22. Nasser NJ, Gorenberg M, Agbarya A. First line Immunotherapy for Non-Small Cell Lung Cancer. Pharmaceuticals (Basel). 2020;13(11). 10.3390/ph13110373
23. Neal RD, Sun F, Emery JD, Callister ME. Lung cancer. Bmj. 2019;365:l1725. 10.1136/bmj.l1725

24. Dhamija S, Yang CM, Seiler J, Myacheva K, Caudron-Herger M, Wieland A, et al. A pan-cancer analysis reveals nonstop extension mutations causing SMAD4 tumour suppressor degradation. Nat Cell Biol. 2020;22(8):999-1010. 10.1038/s41556-020-0551-7
25. Anna A, Monika G. Splicing mutations in human genetic disorders: examples, detection, and confirmation. J Appl Genet. 2018;59(3):253-68. 10.1007/s13353-018-0444-7
26. Hastings PJ, Lupski JR, Rosenberg SM, Ira G. Mechanisms of change in gene copy number. Nat Rev Genet. 2009;10(8):551-64. 10.1038/nrg2593
27. Langevin SM, Kratzke RA, Kelsey KT. Epigenetics of lung cancer. Transl Res. 2015;165(1):74-90. 10.1016/j.trsl.2014.03.001
28. Soda M, Choi YL, Enomoto M, Takada S, Yamashita Y, Ishikawa S, et al. Identification of the transforming EML4-ALK fusion gene in non-small-cell lung cancer. Nature. 2007;448(7153):561-6. 10.1038/nature05945
29. Puig de la Bellacasa R, Karachaliou N, Estrada-Tejedor R, Teixido J, Costa C, Borrell JI. ALK and ROS1 as a joint target for the treatment of lung cancer: a review. Transl Lung Cancer Res. 2013;2(2):72-86. 10.3978/j.issn.2218-6751.2013.03.1
30. Choi M, Kipps T, Kurzrock R. ATM Mutations in Cancer: Therapeutic Implications. Mol Cancer Ther. 2016;15(8):1781-91. 10.1158/1535-7163.MCT-15-0945
31. Mantovani F, Collavin L, Del Sal G. Mutant p53 as a guardian of the cancer cell. Cell Death Differ. 2019;26(2):199-212. 10.1038/s41418-018-0246-9
32. Whibley C, Pharoah PD, Hollstein M. p53 polymorphisms: cancer implications. Nat Rev Cancer. 2009;9(2):95-107. 10.1038/nrc2584
33. Bencokova Z, Kaufmann MR, Pires IM, Lecane PS, Giaccia AJ, Hammond EM. ATM activation and signaling under hypoxic conditions. Mol Cell Biol. 2009;29(2):526-37. 10.1128/MCB.01301-08
34. Kanellou P, Zaravinos A, Zioga M, Spandidos DA. Deregulation of the tumour suppressor genes p14(ARF), p15(INK4b), p16(INK4a) and p53 in basal cell carcinoma. Br J Dermatol. 2009;160(6):1215-21. 10.1111/j.1365-2133.2009.09079.x
35. Lin JJ, Riely GJ, Shaw AT. Targeting ALK: Precision Medicine Takes on Drug Resistance. Cancer Discov. 2017;7(2):137-55. 10.1158/2159-8290.CD-16-1123
36. Sehgal K, Patell R, Rangachari D, Costa DB. Targeting ROS1 rearrangements in non-small cell lung cancer with crizotinib and other kinase inhibitors. Transl Cancer Res. 2018;7(Suppl 7):S779-S86. 10.21037/tcr.2018.08.11
37. Drilon A, Cappuzzo F, Ou SI, Camidge DR. Targeting MET in Lung Cancer: Will Expectations Finally Be MET? Journal of thoracic oncology : official publication of the International Association for the Study of Lung Cancer. 2017;12(1):15-26. 10.1016/j.jtho.2016.10.014
38. Buscail L, Bournet B, Cordelier P. Role of oncogenic KRAS in the diagnosis, prognosis and treatment of pancreatic cancer. Nat Rev Gastroenterol Hepatol. 2020;17(3):153-68. 10.1038/s41575-019-0245-4
39. Davidson SM, Papagiannakopoulos T, Olenchock BA, Heyman JE, Keibler MA, Luengo A, et al. Environment Impacts the Metabolic Dependencies of Ras-Driven Non-Small Cell Lung Cancer. Cell Metab. 2016;23(3):517-28. 10.1016/j.cmet.2016.01.007
40. Philpott C, Tovell H, Frayling IM, Cooper DN, Upadhyaya M. The NF1 somatic mutational landscape in sporadic human cancers. Hum Genomics. 2017;11(1):13. 10.1186/s40246-017-0109-3
41. Alvarez JGB, Otterson GA. Agents to treat BRAF-mutant lung cancer. Drugs Context. 2019;8:212566. 10.7573/dic.212566
42. Cargnello M, Roux PP. Activation and function of the MAPKs and their substrates, the MAPK-activated protein kinases. Microbiol Mol Biol Rev. 2011;75(1):50-83. 10.1128/MMBR.00031-10
43. Shackelford DB, Shaw RJ. The LKB1-AMPK pathway: metabolism and growth control in tumour suppression. Nat Rev Cancer. 2009;9(8):563-75. 10.1038/nrc2676
44. Laplante M, Sabatini DM. mTOR signaling in growth control and disease. Cell. 2012;149(2):274-93. 10.1016/j.cell.2012.03.017
45. Mihaylova MM, Shaw RJ. The AMPK signalling pathway coordinates cell growth, autophagy and metabolism. Nat Cell Biol. 2011;13(9):1016-23. 10.1038/ncb2329
46. Awad MM, Shaw AT. ALK inhibitors in non-small cell lung cancer: crizotinib and beyond. Clin Adv Hematol Oncol. 2014;12(7):429-39.
47. Zhao RX, Xu ZX. Targeting the LKB1 tumor suppressor. Curr Drug Targets. 2014;15(1):32-52. 10.2174/1389450114666140106095811

48. Middleton G, Fletcher P, Popat S, Savage J, Summers Y, Greystoke A, et al. The National Lung Matrix Trial of personalized therapy in lung cancer. Nature. 2020;583(7818):807-12. 10.1038/s41586-020-2481-8
49. Skoulidis F, Byers LA, Diao L, Papadimitrakopoulou VA, Tong P, Izzo J, et al. Co-occurring genomic alterations define major subsets of KRAS-mutant lung adenocarcinoma with distinct biology, immune profiles, and therapeutic vulnerabilities. Cancer Discov. 2015;5(8):860-77. 10.1158/2159-8290.CD-14-1236
50. Hallin J, Engstrom LD, Hargis L, Calinisan A, Aranda R, Briere DM, et al. The KRAS(G12C) Inhibitor MRTX849 Provides Insight toward Therapeutic Susceptibility of KRAS-Mutant Cancers in Mouse Models and Patients. Cancer Discov. 2020;10(1):54-71. 10.1158/2159-8290.CD-19-1167
51. Canon J, Rex K, Saiki AY, Mohr C, Cooke K, Bagal D, et al. The clinical KRAS(G12C) inhibitor AMG 510 drives anti-tumour immunity. Nature. 2019;575(7781):217-23. 10.1038/s41586-019-1694-1
52. Xue JY, Zhao Y, Aronowitz J, Mai TT, Vides A, Qeriqi B, et al. Rapid non-uniform adaptation to conformation-specific KRAS(G12C) inhibition. Nature. 2020;577(7790):421-5. 10.1038/s41586-019-1884-x
53. Singh A, Greninger P, Rhodes D, Koopman L, Violette S, Bardeesy N, et al. A gene expression signature associated with "K-Ras addiction" reveals regulators of EMT and tumor cell survival. Cancer Cell. 2009;15(6):489-500. 10.1016/j.ccr.2009.03.022
54. Reck M, Rodriguez-Abreu D, Robinson AG, Hui R, Csoszi T, Fulop A, et al. Pembrolizumab versus Chemotherapy for PD-L1-Positive Non-Small-Cell Lung Cancer. N Engl J Med. 2016;375(19):1823-33. 10.1056/NEJMoa1606774
55. Herbst RS, Baas P, Kim DW, Felip E, Perez-Gracia JL, Han JY, et al. Pembrolizumab versus docetaxel for previously treated, PD-L1-positive, advanced non-small-cell lung cancer (KEYNOTE-010): a randomised controlled trial. Lancet. 2016;387(10027):1540-50. 10.1016/S0140-6736(15)01281-7
56. Cheng B, Xiong S, Li C, Liang H, Zhao Y, Li J, et al. An annual review of the remarkable advances in lung cancer clinical research in 2019. Journal of thoracic disease. 2020;12(3):1056-69. 10.21037/jtd.2020.03.11
57. Qin S, Xu L, Yi M, Yu S, Wu K, Luo S. Novel immune checkpoint targets: moving beyond PD-1 and CTLA-4. Mol Cancer. 2019;18(1):155. 10.1186/s12943-019-1091-2
58. Leclerc M, Mezquita L, Guillebot De Nerville G, Tihy I, Malenica I, Chouaib S, et al. Recent Advances in Lung Cancer Immunotherapy: Input of T-Cell Epitopes Associated With Impaired Peptide Processing. Front Immunol. 2019;10:1505. 10.3389/fimmu.2019.01505
59. Wang JB, Huang X, Li FR. Impaired dendritic cell functions in lung cancer: a review of recent advances and future perspectives. Cancer Commun (Lond). 2019;39(1):43. 10.1186/s40880-019-0387-3
60. Robertson J, Salm M, Dangl M. Adoptive cell therapy with tumour-infiltrating lymphocytes: the emerging importance of clonal neoantigen targets for next-generation products in non-small cell lung cancer. IOTECH. 2019;3(1):1-7. https://doi.org/10.1016/j.iotech.2019.09.003
61. Zhong S, Cui Y, Liu Q, Chen S. CAR-T cell therapy for lung cancer: a promising but challenging future. Journal of thoracic disease. 2020;12(8):4516-21. 10.21037/jtd.2020.03.118
62. Marcus A, Eshhar Z. Allogeneic adoptive cell transfer therapy as a potent universal treatment for cancer. Oncotarget. 2011;2(7):525-6. 10.18632/oncotarget.300
63. Munoz-Maldonado C, Zimmer Y, Medova M. A Comparative Analysis of Individual RAS Mutations in Cancer Biology. Front Oncol. 2019;9:1088. 10.3389/fonc.2019.01088
64. Skoulidis F, Heymach JV. Co-occurring genomic alterations in non-small-cell lung cancer biology and therapy. Nat Rev Cancer. 2019;19(9):495-509. 10.1038/s41568-019-0179-8
65. Cancer Genome Atlas Research Network T. Comprehensive molecular profiling of lung adenocarcinoma. Nature. 2014;511(7511):543-50. 10.1038/nature13385
66. Pantsar T. The current understanding of KRAS protein structure and dynamics. Comput Struct Biotechnol J. 2020;18:189-98. 10.1016/j.csbj.2019.12.004
67. Vatansever S, Erman B, Gumus ZH. Oncogenic G12D mutation alters local conformations and dynamics of K-Ras. Sci Rep. 2019;9(1):11730. 10.1038/s41598-019-48029-z
68. Hunter JC, Manandhar A, Carrasco MA, Gurbani D, Gondi S, Westover KD. Biochemical and Structural Analysis of Common Cancer-Associated KRAS Mutations. Mol Cancer Res. 2015;13(9):1325-35. 10.1158/1541-7786.MCR-15-0203
69. Zhang X, Cao J, Miller SP, Jing H, Lin H. Comparative Nucleotide-Dependent Interactome Analysis Reveals Shared and Differential Properties of KRas4a and KRas4b. ACS Cent Sci. 2018;4(1):71-80. 10.1021/acscentsci.7b00440

70. Ihle NT, Byers LA, Kim ES, Saintigny P, Lee JJ, Blumenschein GR, et al. Effect of KRAS oncogene substitutions on protein behavior: implications for signaling and clinical outcome. J Natl Cancer Inst. 2012;104(3):228-39. 10.1093/jnci/djr523
71. Cespedes MV, Sancho FJ, Guerrero S, Parreno M, Casanova I, Pavon MA, et al. K-ras Asp12 mutant neither interacts with Raf, nor signals through Erk and is less tumorigenic than K-ras Val12. Carcinogenesis. 2006;27(11):2190-200. 10.1093/carcin/bgl063
72. Stolze B, Reinhart S, Bulllinger L, Frohling S, Scholl C. Comparative analysis of KRAS codon 12, 13, 18, 61, and 117 mutations using human MCF10A isogenic cell lines. Sci Rep. 2015;5:8535. 10.1038/srep08535
73. Walsh AB, Bar-Sagi D. Differential activation of the Rac pathway by Ha-Ras and K-Ras. J Biol Chem. 2001;276(19):15609-15. 10.1074/jbc.M010573200
74. Zhou ZW, Ambrogio C, Bera AK, Li Q, Li XX, Li L, et al. KRAS(Q61H) Preferentially Signals through MAPK in a RAF Dimer-Dependent Manner in Non-Small Cell Lung Cancer. Cancer Res. 2020;80(17):3719-31. 10.1158/0008-5472.CAN-20-0448
75. Akagi K, Uchibori R, Yamaguchi K, Kurosawa K, Tanaka Y, Kozu T. Characterization of a novel oncogenic K-ras mutation in colon cancer. Biochem Biophys Res Commun. 2007;352(3):728-32. 10.1016/j.bbrc.2006.11.091
76. Smith G, Bounds R, Wolf H, Steele RJ, Carey FA, Wolf CR. Activating K-Ras mutations outwith 'hotspot' codons in sporadic colorectal tumours - implications for personalised cancer medicine. British journal of cancer. 2010;102(4):693-703. 10.1038/sj.bjc.6605534
77. Poulin EJ, Bera AK, Lu J, Lin YJ, Strasser SD, Paulo JA, et al. Tissue-Specific Oncogenic Activity of KRAS(A146T). Cancer Discov. 2019;9(6):738-55. 10.1158/2159-8290.CD-18-1220
78. Renaud S, Guerrera F, Seitlinger J, Reeb J, Voegeli AC, Legrain M, et al. KRAS-specific Amino Acid Substitutions are Associated With Different Responses to Chemotherapy in Advanced Non-small-cell Lung Cancer. Clinical lung cancer. 2018;19(6):e919-e31. 10.1016/j.cllc.2018.08.005
79. Mellema WW, Masen-Poos L, Smit EF, Hendriks LE, Aerts JG, Termeer A, et al. Comparison of clinical outcome after first-line platinum-based chemotherapy in different types of KRAS mutated advanced non-small-cell lung cancer. Lung cancer. 2015;90(2):249-54. 10.1016/j.lungcan.2015.09.012
80. Iles KE, Dickinson DA, Wigley AF, Welty NE, Blank V, Forman HJ. HNE increases HO-1 through activation of the ERK pathway in pulmonary epithelial cells. Free Radic Biol Med. 2005;39(3):355-64. 10.1016/j.freeradbiomed.2005.03.026
81. Li T, Song T, Ni L, Yang G, Song X, Wu L, et al. The p-ERK-p-c-Jun-cyclinD1 pathway is involved in proliferation of smooth muscle cells after exposure to cigarette smoke extract. Biochem Biophys Res Commun. 2014;453(3):316-20. 10.1016/j.bbrc.2014.09.062
82. Xu X, Balsiger R, Tyrrell J, Boyaka PN, Tarran R, Cormet-Boyaka E. Cigarette smoke exposure reveals a novel role for the MEK/ERK1/2 MAPK pathway in regulation of CFTR. Biochim Biophys Acta. 2015;1850(6):1224-32. 10.1016/j.bbagen.2015.02.004
83. Kerr EM, Martins CP. Metabolic rewiring in mutant Kras lung cancer. FEBS J. 2017. 10.1111/febs.14125
84. Zheng J. Energy metabolism of cancer: Glycolysis versus oxidative phosphorylation (Review). Oncology letters. 2012;4(6):1151-7. 10.3892/ol.2012.928
85. Fan TW, Lane AN, Higashi RM, Farag MA, Gao H, Bousamra M, et al. Altered regulation of metabolic pathways in human lung cancer discerned by (13)C stable isotope-resolved metabolomics (SIRM). Mol Cancer. 2009;8:41. 10.1186/1476-4598-8-41
86. Weinberg F, Hamanaka R, Wheaton WW, Weinberg S, Joseph J, Lopez M, et al. Mitochondrial metabolism and ROS generation are essential for Kras-mediated tumorigenicity. Proc Natl Acad Sci U S A. 2010;107(19):8788-93. 10.1073/pnas.1003428107
87. DeNicola GM, Karreth FA, Humpton TJ, Gopinathan A, Wei C, Frese K, et al. Oncogene-induced Nrf2 transcription promotes ROS detoxification and tumorigenesis. Nature. 2011;475(7354):106-9. 10.1038/nature10189
88. Schafer ZT, Grassian AR, Song L, Jiang Z, Gerhart-Hines Z, Irie HY, et al. Antioxidant and oncogene rescue of metabolic defects caused by loss of matrix attachment. Nature. 2009;461(7260):109-13. 10.1038/nature08268
89. Ishikawa K, Takenaga K, Akimoto M, Koshikawa N, Yamaguchi A, Imanishi H, et al. ROS-generating mitochondrial DNA mutations can regulate tumor cell metastasis. Science. 2008;320(5876):661-4. 10.1126/science.1156906

90. Mayers JR, Torrence ME, Danai LV, Papagiannakopoulos T, Davidson SM, Bauer MR, et al. Tissue of origin dictates branched-chain amino acid metabolism in mutant Kras-driven cancers. Science. 2016;353(6304):1161-5. 10.1126/science.aaf5171
91. Facchinetti F, Bluthgen MV, Tergemina-Clain G, Faivre L, Pignon JP, Planchard D, et al. LKB1/STK11 mutations in non-small cell lung cancer patients: Descriptive analysis and prognostic value. Lung cancer. 2017;112:62-8. 10.1016/j.lungcan.2017.08.002
92. Gill RK, Yang SH, Meerzaman D, Mechanic LE, Bowman ED, Jeon HS, et al. Frequent homozygous deletion of the LKB1/STK11 gene in non-small cell lung cancer. Oncogene. 2011;30(35):3784-91. 10.1038/onc.2011.98
93. Momcilovic M, Shackelford DB. Targeting LKB1 in cancer - exposing and exploiting vulnerabilities. British journal of cancer. 2015;113(4):574-84. 10.1038/bjc.2015.261
94. Beggs AD, Latchford AR, Vasen HF, Moslein G, Alonso A, Aretz S, et al. Peutz-Jeghers syndrome: a systematic review and recommendations for management. Gut. 2010;59(7):975-86. 10.1136/gut.2009.198499
95. Lan F, Cacicedo JM, Ruderman N, Ido Y. SIRT1 modulation of the acetylation status, cytosolic localization, and activity of LKB1. Possible role in AMP-activated protein kinase activation. J Biol Chem. 2008;283(41):27628-35. 10.1074/jbc.M805711200
96. Gurumurthy S, Hezel AF, Sahin E, Berger JH, Bosenberg MW, Bardeesy N. LKB1 deficiency sensitizes mice to carcinogen-induced tumorigenesis. Cancer Res. 2008;68(1):55-63. 10.1158/0008-5472.CAN-07-3225
97. Shackelford DB, Vasquez DS, Corbeil J, Wu S, Leblanc M, Wu CL, et al. mTOR and HIF-1alpha-mediated tumor metabolism in an LKB1 mouse model of Peutz-Jeghers syndrome. Proc Natl Acad Sci U S A. 2009;106(27):11137-42. 10.1073/pnas.0900465106
98. Dodd KM, Yang J, Shen MH, Sampson JR, Tee AR. mTORC1 drives HIF-1alpha and VEGF-A signalling via multiple mechanisms involving 4E-BP1, S6K1 and STAT3. Oncogene. 2015;34(17):2239-50. 10.1038/onc.2014.164
99. Faubert B, Vincent EE, Griss T, Samborska B, Izreig S, Svensson RU, et al. Loss of the tumor suppressor LKB1 promotes metabolic reprogramming of cancer cells via HIF-1alpha. Proc Natl Acad Sci U S A. 2014;111(7):2554-9. 10.1073/pnas.1312570111
100. Koh HJ, Arnolds DE, Fujii N, Tran TT, Rogers MJ, Jessen N, et al. Skeletal muscle-selective knockout of LKB1 increases insulin sensitivity, improves glucose homeostasis, and decreases TRB3. Mol Cell Biol. 2006;26(22):8217-27. 10.1128/MCB.00979-06
101. Foretz M, Hebrard S, Leclerc J, Zarrinpashneh E, Soty M, Mithieux G, et al. Metformin inhibits hepatic gluconeogenesis in mice independently of the LKB1/AMPK pathway via a decrease in hepatic energy state. J Clin Invest. 2010;120(7):2355-69. 10.1172/JCI40671
102. Galan-Cobo A, Sitthideatphaiboon P, Qu X, Poteete A, Pisegna MA, Tong P, et al. LKB1 and KEAP1/NRF2 Pathways Cooperatively Promote Metabolic Reprogramming with Enhanced Glutamine Dependence in KRAS-Mutant Lung Adenocarcinoma. Cancer Res. 2019;79(13):3251-67. 10.1158/0008-5472.CAN-18-3527
103. Jones RG, Plas DR, Kubek S, Buzzai M, Mu J, Xu Y, et al. AMP-activated protein kinase induces a p53-dependent metabolic checkpoint. Mol Cell. 2005;18(3):283-93. 10.1016/j.molcel.2005.03.027
104. Karuman P, Gozani O, Odze RD, Zhou XC, Zhu H, Shaw R, et al. The Peutz-Jegher gene product LKB1 is a mediator of p53-dependent cell death. Mol Cell. 2001;7(6):1307-19. 10.1016/s1097-2765(01)00258-1
105. Tiainen M, Vaahtomeri K, Ylikorkala A, Makela TP. Growth arrest by the LKB1 tumor suppressor: induction of p21(WAF1/CIP1). Hum Mol Genet. 2002;11(13):1497-504. 10.1093/hmg/11.13.1497
106. Liang J, Shao SH, Xu ZX, Hennessy B, Ding Z, Larrea M, et al. The energy sensing LKB1-AMPK pathway regulates p27(kip1) phosphorylation mediating the decision to enter autophagy or apoptosis. Nat Cell Biol. 2007;9(2):218-24. 10.1038/ncb1537
107. Scott KD, Nath-Sain S, Agnew MD, Marignani PA. LKB1 catalytically deficient mutants enhance cyclin D1 expression. Cancer Res. 2007;67(12):5622-7. 10.1158/0008-5472.CAN-07-0762
108. Alexander A, Cai SL, Kim J, Nanez A, Sahin M, MacLean KH, et al. ATM signals to TSC2 in the cytoplasm to regulate mTORC1 in response to ROS. Proc Natl Acad Sci U S A. 2010;107(9):4153-8. 10.1073/pnas.0913860107
109. Luo L, Huang W, Tao R, Hu N, Xiao ZX, Luo Z. ATM and LKB1 dependent activation of AMPK sensitizes cancer cells to etoposide-induced apoptosis. Cancer Lett. 2013;328(1):114-9. 10.1016/j.canlet.2012.08.034

110. Shackelford DB, Abt E, Gerken L, Vasquez DS, Seki A, Leblanc M, et al. LKB1 inactivation dictates therapeutic response of non-small cell lung cancer to the metabolism drug phenformin. Cancer Cell. 2013;23(2):143-58. 10.1016/j.ccr.2012.12.008
111. Martin-Belmonte F, Perez-Moreno M. Epithelial cell polarity, stem cells and cancer. Nat Rev Cancer. 2011;12(1):23-38. 10.1038/nrc3169
112. Goodwin JM, Svensson RU, Lou HJ, Winslow MM, Turk BE, Shaw RJ. An AMPK-independent signaling pathway downstream of the LKB1 tumor suppressor controls Snail1 and metastatic potential. Mol Cell. 2014;55(3):436-50. 10.1016/j.molcel.2014.06.021
113. Mohseni M, Sun J, Lau A, Curtis S, Goldsmith J, Fox VL, et al. A genetic screen identifies an LKB1-MARK signalling axis controlling the Hippo-YAP pathway. Nat Cell Biol. 2014;16(1):108-17. 10.1038/ncb2884
114. Rodon L, Svensson RU, Wiater E, Chun MGH, Tsai WW, Eichner LJ, et al. The CREB coactivator CRTC2 promotes oncogenesis in LKB1-mutant non-small cell lung cancer. Sci Adv. 2019;5(7):eaaw6455. 10.1126/sciadv.aaw6455
115. Skoulidis F, Goldberg ME, Greenawalt DM, Hellmann MD, Awad MM, Gainor JF, et al. STK11/LKB1 Mutations and PD-1 Inhibitor Resistance in KRAS-Mutant Lung Adenocarcinoma. Cancer Discov. 2018;8(7):822-35. 10.1158/2159-8290.CD-18-0099
116. Romero R, Sayin VI, Davidson SM, Bauer MR, Singh SX, LeBoeuf SE, et al. Keap1 loss promotes Kras-driven lung cancer and results in dependence on glutaminolysis. Nat Med. 2017;23(11):1362-8. 10.1038/nm.4407
117. Li F, Han X, Li F, Wang R, Wang H, Gao Y, et al. LKB1 Inactivation Elicits a Redox Imbalance to Modulate Non-small Cell Lung Cancer Plasticity and Therapeutic Response. Cancer Cell. 2015;27(5):698-711. 10.1016/j.ccell.2015.04.001
118. Arbour KC, Jordan E, Kim HR, Dienstag J, Yu HA, Sanchez-Vega F, et al. Effects of Co-occurring Genomic Alterations on Outcomes in Patients with KRAS-Mutant Non-Small Cell Lung Cancer. Clin Cancer Res. 2018;24(2):334-40. 10.1158/1078-0432.CCR-17-1841
119. Zhang Y, Meng Q, Sun Q, Xu ZX, Zhou H, Wang Y. LKB1 deficiency-induced metabolic reprogramming in tumorigenesis and non-neoplastic diseases. Mol Metab. 2021;44:101131. 10.1016/j.molmet.2020.101131
120. Svensson RU, Parker SJ, Eichner LJ, Kolar MJ, Wallace M, Brun SN, et al. Inhibition of acetyl-CoA carboxylase suppresses fatty acid synthesis and tumor growth of non-small-cell lung cancer in preclinical models. Nat Med. 2016;22(10):1108-19. 10.1038/nm.4181
121. Li Y, Xu S, Mihaylova MM, Zheng B, Hou X, Jiang B, et al. AMPK phosphorylates and inhibits SREBP activity to attenuate hepatic steatosis and atherosclerosis in diet-induced insulin-resistant mice. Cell Metab. 2011;13(4):376-88. 10.1016/j.cmet.2011.03.009
122. Liu G, Kuang S, Cao R, Wang J, Peng Q, Sun C. Sorafenib kills liver cancer cells by disrupting SCD1-mediated synthesis of monounsaturated fatty acids via the ATP-AMPK-mTOR-SREBP1 signaling pathway. FASEB J. 2019;33(9):10089-103. 10.1096/fj.201802619RR
123. Bhatt V, Khayati K, Hu ZS, Lee A, Kamran W, Su X, et al. Autophagy modulates lipid metabolism to maintain metabolic flexibility for Lkb1-deficient Kras-driven lung tumorigenesis. Genes Dev. 2019;33(3-4):150-65. 10.1101/gad.320481.118
124. Kottakis F, Nicolay BN, Roumane A, Karnik R, Gu H, Nagle JM, et al. LKB1 loss links serine metabolism to DNA methylation and tumorigenesis. Nature. 2016;539(7629):390-5. 10.1038/nature20132
125. Kim J, Hu Z, Cai L, Li K, Choi E, Faubert B, et al. CPS1 maintains pyrimidine pools and DNA synthesis in KRAS/LKB1-mutant lung cancer cells. Nature. 2017;546(7656):168-72. 10.1038/nature22359
126. Kitajima S, Ivanova E, Guo S, Yoshida R, Campisi M, Sundararaman SK, et al. Suppression of STING Associated with LKB1 Loss in KRAS-Driven Lung Cancer. Cancer Discov. 2019;9(1):34-45. 10.1158/2159-8290.CD-18-0689
127. Kazyken D, Magnuson B, Bodur C, Acosta-Jaquez HA, Zhang D, Tong X, et al. AMPK directly activates mTORC2 to promote cell survival during acute energetic stress. Sci Signal. 2019;12(585). 10.1126/scisignal.aav3249
128. Chiang CT, Demetriou AN, Ung N, Choudhury N, Ghaffarian K, Ruderman DL, et al. mTORC2 contributes to the metabolic reprogramming in EGFR tyrosine-kinase inhibitor resistant cells in non-small cell lung cancer. Cancer Lett. 2018;434:152-9. 10.1016/j.canlet.2018.07.025

129. Srivastava RK, Li C, Khan J, Banerjee NS, Chow LT, Athar M. Combined mTORC1/mTORC2 inhibition blocks growth and induces catastrophic macropinocytosis in cancer cells. Proc Natl Acad Sci U S A. 2019;116(49):24583-92. 10.1073/pnas.1911393116
130. Acuto O, Michel F. CD28-mediated co-stimulation: a quantitative support for TCR signalling. Nat Rev Immunol. 2003;3(12):939-51. 10.1038/nri1248
131. Schumacher TN, Schreiber RD. Neoantigens in cancer immunotherapy. Science. 2015;348(6230):69-74. 10.1126/science.aaa4971
132. Rooney MS, Shukla SA, Wu CJ, Getz G, Hacohen N. Molecular and genetic properties of tumors associated with local immune cytolytic activity. Cell. 2015;160(1-2):48-61. 10.1016/j.cell.2014.12.033
133. Simoni Y, Becht E, Fehlings M, Loh CY, Koo SL, Teng KWW, et al. Bystander CD8(+) T cells are abundant and phenotypically distinct in human tumour infiltrates. Nature. 2018;557(7706):575-9. 10.1038/s41586-018-0130-2
134. Anagnostou V, Smith KN, Forde PM, Niknafs N, Bhattacharya R, White J, et al. Evolution of Neoantigen Landscape during Immune Checkpoint Blockade in Non-Small Cell Lung Cancer. Cancer Discov. 2017;7(3):264-76. 10.1158/2159-8290.CD-16-0828
135. Dunn GP, Bruce AT, Ikeda H, Old LJ, Schreiber RD. Cancer immunoediting: from immunosurveillance to tumor escape. Nat Immunol. 2002;3(11):991-8. 10.1038/ni1102-991
136. Mascaux C, Angelova M, Vasaturo A, Beane J, Hijazi K, Anthoine G, et al. Immune evasion before tumour invasion in early lung squamous carcinogenesis. Nature. 2019;571(7766):570-5. 10.1038/s41586-019-1330-0
137. Sivakumar S, Lucas FAS, McDowell TL, Lang W, Xu L, Fujimoto J, et al. Genomic Landscape of Atypical Adenomatous Hyperplasia Reveals Divergent Modes to Lung Adenocarcinoma. Cancer Res. 2017;77(22):6119-30. 10.1158/0008-5472.CAN-17-1605
138. Beane JE, Mazzilli SA, Campbell JD, Duclos G, Krysan K, Moy C, et al. Molecular subtyping reveals immune alterations associated with progression of bronchial premalignant lesions. Nat Commun. 2019;10(1):1856. 10.1038/s41467-019-09834-2
139. Lavin Y, Kobayashi S, Leader A, Amir ED, Elefant N, Bigenwald C, et al. Innate Immune Landscape in Early Lung Adenocarcinoma by Paired Single-Cell Analyses. Cell. 2017;169(4):750-65 e17. 10.1016/j.cell.2017.04.014
140. McGranahan N, Furness AJ, Rosenthal R, Ramskov S, Lyngaa R, Saini SK, et al. Clonal neoantigens elicit T cell immunoreactivity and sensitivity to immune checkpoint blockade. Science. 2016;351(6280):1463-9. 10.1126/science.aaf1490
141. Munn DH, Mellor AL. IDO in the Tumor Microenvironment: Inflammation, Counter-Regulation, and Tolerance. Trends Immunol. 2016;37(3):193-207. 10.1016/j.it.2016.01.002
142. Remark R, Becker C, Gomez JE, Damotte D, Dieu-Nosjean MC, Sautes-Fridman C, et al. The non-small cell lung cancer immune contexture. A major determinant of tumor characteristics and patient outcome. Am J Respir Crit Care Med. 2015;191(4):377-90. 10.1164/rccm.201409-1671PP
143. Akbay EA, Koyama S, Carretero J, Altabef A, Tchaicha JH, Christensen CL, et al. Activation of the PD-1 pathway contributes to immune escape in EGFR-driven lung tumors. Cancer Discov. 2013;3(12):1355-63. 10.1158/2159-8290.CD-13-0310
144. Platonova S, Cherfils-Vicini J, Damotte D, Crozet L, Vieillard V, Validire P, et al. Profound coordinated alterations of intratumoral NK cell phenotype and function in lung carcinoma. Cancer Res. 2011;71(16):5412-22. 10.1158/0008-5472.CAN-10-4179
145. Salih HR, Rammensee HG, Steinle A. Cutting edge: down-regulation of MICA on human tumors by proteolytic shedding. J Immunol. 2002;169(8):4098-102. 10.4049/jimmunol.169.8.4098
146. Perea F, Bernal M, Sanchez-Palencia A, Carretero J, Torres C, Bayarri C, et al. The absence of HLA class I expression in non-small cell lung cancer correlates with the tumor tissue structure and the pattern of T cell infiltration. Int J Cancer. 2017;140(4):888-99. 10.1002/ijc.30489
147. Cabrita R, Lauss M, Sanna A, Donia M, Skaarup Larsen M, Mitra S, et al. Tertiary lymphoid structures improve immunotherapy and survival in melanoma. Nature. 2020;577(7791):561-5. 10.1038/s41586-019-1914-8
148. Neuwelt AJ, Kimball AK, Johnson AM, Arnold BW, Bullock BL, Kaspar RE, et al. Cancer cell-intrinsic expression of MHC II in lung cancer cell lines is actively restricted by MEK/ERK signaling and epigenetic mechanisms. J Immunother Cancer. 2020;8(1). 10.1136/jitc-2019-000441

149. Marty R, Kaabinejadian S, Rossell D, Slifker MJ, van de Haar J, Engin HB, et al. MHC-I Genotype Restricts the Oncogenic Mutational Landscape. Cell. 2017;171(6):1272-83 e15. 10.1016/j.cell.2017.09.050
150. Marty Pyke R, Thompson WK, Salem RM, Font-Burgada J, Zanetti M, Carter H. Evolutionary Pressure against MHC Class II Binding Cancer Mutations. Cell. 2018;175(2):416-28 e13. 10.1016/j.cell.2018.08.048
151. Thorsson V, Gibbs DL, Brown SD, Wolf D, Bortone DS, Ou Yang TH, et al. The Immune Landscape of Cancer. Immunity. 2018;48(4):812-30 e14. 10.1016/j.immuni.2018.03.023
152. Worthylake RA, Burridge K. Leukocyte transendothelial migration: orchestrating the underlying molecular machinery. Curr Opin Cell Biol. 2001;13(5):569-77. 10.1016/s0955-0674(00)00253-2
153. Kroeger DR, Milne K, Nelson BH. Tumor-Infiltrating Plasma Cells Are Associated with Tertiary Lymphoid Structures, Cytolytic T-Cell Responses, and Superior Prognosis in Ovarian Cancer. Clin Cancer Res. 2016;22(12):3005-15. 10.1158/1078-0432.CCR-15-2762
154. Germain C, Gnjatic S, Tamzalit F, Knockaert S, Remark R, Goc J, et al. Presence of B cells in tertiary lymphoid structures is associated with a protective immunity in patients with lung cancer. Am J Respir Crit Care Med. 2014;189(7):832-44. 10.1164/rccm.201309-1611OC
155. Dieu-Nosjean MC, Giraldo NA, Kaplon H, Germain C, Fridman WH, Sautes-Fridman C. Tertiary lymphoid structures, drivers of the anti-tumor responses in human cancers. Immunol Rev. 2016;271(1):260-75. 10.1111/imr.12405
156. Stankovic B, Bjorhovde HAK, Skarshaug R, Aamodt H, Frafjord A, Muller E, et al. Immune Cell Composition in Human Non-small Cell Lung Cancer. Front Immunol. 2018;9:3101. 10.3389/fimmu.2018.03101
157. DuPage M, Bluestone JA. Harnessing the plasticity of CD4(+) T cells to treat immune-mediated disease. Nat Rev Immunol. 2016;16(3):149-63. 10.1038/nri.2015.18
158. Anichini A, Perotti VE, Sgambelluri F, Mortarini R. Immune Escape Mechanisms in Non Small Cell Lung Cancer. Cancers (Basel). 2020;12(12). 10.3390/cancers12123605
159. Oja AE, Piet B, van der Zwan D, Blaauwgeers H, Mensink M, de Kivit S, et al. Functional Heterogeneity of CD4(+) Tumor-Infiltrating Lymphocytes With a Resident Memory Phenotype in NSCLC. Front Immunol. 2018;9:2654. 10.3389/fimmu.2018.02654
160. Kim TS, Shin EC. The activation of bystander CD8(+) T cells and their roles in viral infection. Exp Mol Med. 2019;51(12):1-9. 10.1038/s12276-019-0316-1
161. Goc J, Germain C, Vo-Bourgais TK, Lupo A, Klein C, Knockaert S, et al. Dendritic cells in tumor-associated tertiary lymphoid structures signal a Th1 cytotoxic immune contexture and license the positive prognostic value of infiltrating CD8+ T cells. Cancer Res. 2014;74(3):705-15. 10.1158/0008-5472.CAN-13-1342
162. de Chaisemartin L, Goc J, Damotte D, Validire P, Magdeleinat P, Alifano M, et al. Characterization of chemokines and adhesion molecules associated with T cell presence in tertiary lymphoid structures in human lung cancer. Cancer Res. 2011;71(20):6391-9. 10.1158/0008-5472.CAN-11-0952
163. Petitprez F, de Reynies A, Keung EZ, Chen TW, Sun CM, Calderaro J, et al. B cells are associated with survival and immunotherapy response in sarcoma. Nature. 2020;577(7791):556-60. 10.1038/s41586-019-1906-8
164. Helmink BA, Reddy SM, Gao J, Zhang S, Basar R, Thakur R, et al. B cells and tertiary lymphoid structures promote immunotherapy response. Nature. 2020;577(7791):549-55. 10.1038/s41586-019-1922-8
165. De Groot R, Van Loenen MM, Guislain A, Nicolet BP, Freen-Van Heeren JJ, Verhagen O, et al. Polyfunctional tumor-reactive T cells are effectively expanded from non-small cell lung cancers, and correlate with an immune-engaged T cell profile. Oncoimmunology. 2019;8(11):e1648170. 10.1080/2162402X.2019.1648170
166. Ghorani E, Reading JL, Henry JY, de Massy MR, Rosenthal R, Turati V, et al. The T cell differentiation landscape is shaped by tumour mutations in lung cancer. Nat Cancer. 2020;1(5):546-61. 10.1038/s43018-020-0066-y
167. Russick J, Joubert PE, Gillard-Bocquet M, Torset C, Meylan M, Petitprez F, et al. Natural killer cells in the human lung tumor microenvironment display immune inhibitory functions. J Immunother Cancer. 2020;8(2). 10.1136/jitc-2020-001054
168. Cheng M, Hu S. Lung-resident gammadelta T cells and their roles in lung diseases. Immunology. 2017;151(4):375-84. 10.1111/imm.12764
169. Yoshida Y, Nakajima J, Wada H, Kakimi K. gammadelta T-cell immunotherapy for lung cancer. Surg Today. 2011;41(5):606-11. 10.1007/s00595-010-4478-7

170. Wolf MJ, Seleznik GM, Zeller N, Heikenwalder M. The unexpected role of lymphotoxin beta receptor signaling in carcinogenesis: from lymphoid tissue formation to liver and prostate cancer development. Oncogene. 2010;29(36):5006-18. 10.1038/onc.2010.260
171. ElKassar N, Gress RE. An overview of IL-7 biology and its use in immunotherapy. J Immunotoxicol. 2010;7(1):1-7. 10.3109/15476910903453296
172. Carrega P, Loiacono F, Di Carlo E, Scaramuccia A, Mora M, Conte R, et al. NCR(+)ILC3 concentrate in human lung cancer and associate with intratumoral lymphoid structures. Nat Commun. 2015;6:8280. 10.1038/ncomms9280
173. Hindley JP, Jones E, Smart K, Bridgeman H, Lauder SN, Ondondo B, et al. T-cell trafficking facilitated by high endothelial venules is required for tumor control after regulatory T-cell depletion. Cancer Res. 2012;72(21):5473-82. 10.1158/0008-5472.CAN-12-1912
174. Cupedo T, Crellin NK, Papazian N, Rombouts EJ, Weijer K, Grogan JL, et al. Human fetal lymphoid tissue-inducer cells are interleukin 17-producing precursors to RORC+ CD127+ natural killer-like cells. Nat Immunol. 2009;10(1):66-74. 10.1038/ni.1668
175. Lohr M, Edlund K, Botling J, Hammad S, Hellwig B, Othman A, et al. The prognostic relevance of tumour-infiltrating plasma cells and immunoglobulin kappa C indicates an important role of the humoral immune response in non-small cell lung cancer. Cancer Lett. 2013;333(2):222-8. 10.1016/j.canlet.2013.01.036
176. Altorki NK, Markowitz GJ, Gao D, Port JL, Saxena A, Stiles B, et al. The lung microenvironment: an important regulator of tumour growth and metastasis. Nat Rev Cancer. 2019;19(1):9-31. 10.1038/s41568-018-0081-9
177. Garrido-Martin EM, Mellows TWP, Clarke J, Ganesan AP, Wood O, Cazaly A, et al. M1(hot) tumor-associated macrophages boost tissue-resident memory T cells infiltration and survival in human lung cancer. J Immunother Cancer. 2020;8(2). 10.1136/jitc-2020-000778
178. Kunimasa K, Goto T. Immunosurveillance and Immunoediting of Lung Cancer: Current Perspectives and Challenges. Int J Mol Sci. 2020;21(2). 10.3390/ijms21020597
179. Chen W, Jin W, Hardegen N, Lei KJ, Li L, Marinos N, et al. Conversion of peripheral CD4+CD25- naive T cells to CD4+CD25+ regulatory T cells by TGF-beta induction of transcription factor Foxp3. J Exp Med. 2003;198(12):1875-86. 10.1084/jem.20030152
180. Sharma S, Yang SC, Zhu L, Reckamp K, Gardner B, Baratelli F, et al. Tumor cyclooxygenase-2/prostaglandin E2-dependent promotion of FOXP3 expression and CD4+ CD25+ T regulatory cell activities in lung cancer. Cancer Res. 2005;65(12):5211-20. 10.1158/0008-5472.CAN-05-0141
181. Setoguchi R, Hori S, Takahashi T, Sakaguchi S. Homeostatic maintenance of natural Foxp3(+) CD25(+) CD4(+) regulatory T cells by interleukin (IL)-2 and induction of autoimmune disease by IL-2 neutralization. J Exp Med. 2005;201(5):723-35. 10.1084/jem.20041982
182. Fallarino F, Grohmann U, Hwang KW, Orabona C, Vacca C, Bianchi R, et al. Modulation of tryptophan catabolism by regulatory T cells. Nat Immunol. 2003;4(12):1206-12. 10.1038/ni1003
183. Granville CA, Memmott RM, Balogh A, Mariotti J, Kawabata S, Han W, et al. A central role for Foxp3+ regulatory T cells in K-Ras-driven lung tumorigenesis. PloS one. 2009;4(3):e5061. 10.1371/journal.pone.0005061
184. Ganesan AP, Johansson M, Ruffell B, Yagui-Beltran A, Lau J, Jablons DM, et al. Tumor-infiltrating regulatory T cells inhibit endogenous cytotoxic T cell responses to lung adenocarcinoma. J Immunol. 2013;191(4):2009-17. 10.4049/jimmunol.1301317
185. Gabrilovich DI, Nagaraj S. Myeloid-derived suppressor cells as regulators of the immune system. Nat Rev Immunol. 2009;9(3):162-74. 10.1038/nri2506
186. Huang A, Zhang B, Wang B, Zhang F, Fan KX, Guo YJ. Increased CD14(+)HLA-DR (-/low) myeloid-derived suppressor cells correlate with extrathoracic metastasis and poor response to chemotherapy in non-small cell lung cancer patients. Cancer Immunol Immunother. 2013;62(9):1439-51. 10.1007/s00262-013-1450-6
187. Liu CY, Wang YM, Wang CL, Feng PH, Ko HW, Liu YH, et al. Population alterations of L-arginase- and inducible nitric oxide synthase-expressed CD11b+/CD14(-)/CD15+/CD33+ myeloid-derived suppressor cells and CD8+ T lymphocytes in patients with advanced-stage non-small cell lung cancer. J Cancer Res Clin Oncol. 2010;136(1):35-45. 10.1007/s00432-009-0634-0

188. Feng PH, Lee KY, Chang YL, Chan YF, Kuo LW, Lin TY, et al. CD14(+)S100A9(+) monocytic myeloid-derived suppressor cells and their clinical relevance in non-small cell lung cancer. Am J Respir Crit Care Med. 2012;186(10):1025-36. 10.1164/rccm.201204-0636OC
189. Koyama S, Akbay EA, Li YY, Aref AR, Skoulidis F, Herter-Sprie GS, et al. STK11/LKB1 Deficiency Promotes Neutrophil Recruitment and Proinflammatory Cytokine Production to Suppress T-cell Activity in the Lung Tumor Microenvironment. Cancer Res. 2016;76(5):999-1008. 10.1158/0008-5472.CAN-15-1439
190. Youn JI, Park SM, Park S, Kim G, Lee HJ, Son J, et al. Peripheral natural killer cells and myeloid-derived suppressor cells correlate with anti-PD-1 responses in non-small cell lung cancer. Sci Rep. 2020;10(1):9050. 10.1038/s41598-020-65666-x
191. Hickey MJ, Kubes P. Intravascular immunity: the host-pathogen encounter in blood vessels. Nat Rev Immunol. 2009;9(5):364-75. 10.1038/nri2532
192. Fridlender ZG, Sun J, Kim S, Kapoor V, Cheng G, Ling L, et al. Polarization of tumor-associated neutrophil phenotype by TGF-beta: "N1" versus "N2" TAN. Cancer Cell. 2009;16(3):183-94. 10.1016/j.ccr.2009.06.017
193. Singhal S, Bhojnagarwala PS, O'Brien S, Moon EK, Garfall AL, Rao AS, et al. Origin and Role of a Subset of Tumor-Associated Neutrophils with Antigen-Presenting Cell Features in Early-Stage Human Lung Cancer. Cancer Cell. 2016;30(1):120-35. 10.1016/j.ccell.2016.06.001
194. Rakaee M, Busund LT, Paulsen EE, Richardsen E, Al-Saad S, Andersen S, et al. Prognostic effect of intratumoral neutrophils across histological subtypes of non-small cell lung cancer. Oncotarget. 2016. 10.18632/oncotarget.12360
195. Lee V, Murphy A, Le DT, Diaz LA, Jr. Mismatch Repair Deficiency and Response to Immune Checkpoint Blockade. Oncologist. 2016;21(10):1200-11. 10.1634/theoncologist.2016-0046
196. Llosa NJ, Cruise M, Tam A, Wicks EC, Hechenbleikner EM, Taube JM, et al. The vigorous immune microenvironment of microsatellite instable colon cancer is balanced by multiple counter-inhibitory checkpoints. Cancer Discov. 2015;5(1):43-51. 10.1158/2159-8290.CD-14-0863
197. Lal N, Beggs AD, Willcox BE, Middleton GW. An immunogenomic stratification of colorectal cancer: Implications for development of targeted immunotherapy. Oncoimmunology. 2015;4(3):e976052. 10.4161/2162402X.2014.976052
198. Ling A, Lundberg IV, Eklof V, Wikberg ML, Oberg A, Edin S, et al. The infiltration, and prognostic importance, of Th1 lymphocytes vary in molecular subgroups of colorectal cancer. J Pathol Clin Res. 2016;2(1):21-31. 10.1002/cjp2.31
199. Sumimoto H, Imabayashi F, Iwata T, Kawakami Y. The BRAF-MAPK signaling pathway is essential for cancer-immune evasion in human melanoma cells. J Exp Med. 2006;203(7):1651-6. 10.1084/jem.20051848
200. van Gool IC, Eggink FA, Freeman-Mills L, Stelloo E, Marchi E, de Bruyn M, et al. POLE Proofreading Mutations Elicit an Antitumor Immune Response in Endometrial Cancer. Clin Cancer Res. 2015;21(14):3347-55. 10.1158/1078-0432.CCR-15-0057
201. Marzec M, Zhang Q, Goradia A, Raghunath PN, Liu X, Paessler M, et al. Oncogenic kinase NPM/ALK induces through STAT3 expression of immunosuppressive protein CD274 (PD-L1, B7-H1). Proc Natl Acad Sci U S A. 2008;105(52):20852-7. 10.1073/pnas.0810958105
202. Wang T, Niu G, Kortylewski M, Burdelya L, Shain K, Zhang S, et al. Regulation of the innate and adaptive immune responses by Stat-3 signaling in tumor cells. Nat Med. 2004;10(1):48-54. 10.1038/nm976
203. Kortylewski M, Kujawski M, Wang T, Wei S, Zhang S, Pilon-Thomas S, et al. Inhibiting Stat3 signaling in the hematopoietic system elicits multicomponent antitumor immunity. Nat Med. 2005;11(12):1314-21. 10.1038/nm1325
204. Kortylewski M, Xin H, Kujawski M, Lee H, Liu Y, Harris T, et al. Regulation of the IL-23 and IL-12 balance by Stat3 signaling in the tumor microenvironment. Cancer Cell. 2009;15(2):114-23. 10.1016/j.ccr.2008.12.018
205. Pardoll D. Cancer and the Immune System: Basic Concepts and Targets for Intervention. Seminars in oncology. 2015;42(4):523-38. 10.1053/j.seminoncol.2015.05.003
206. Hellmann MD, Rizvi NA, Goldman JW, Gettinger SN, Borghaei H, Brahmer JR, et al. Nivolumab plus ipilimumab as first-line treatment for advanced non-small-cell lung cancer (CheckMate 012): results of an open-label, phase 1, multicohort study. The Lancet Oncology. 2017;18(1):31-41. 10.1016/S1470-2045(16)30624-6
207. Chae YK, Arya A, Iams W, Cruz MR, Chandra S, Choi J, et al. Current landscape and future of dual anti-CTLA4 and PD-1/PD-L1 blockade immunotherapy in cancer; lessons learned from clinical trials with

melanoma and non-small cell lung cancer (NSCLC). J Immunother Cancer. 2018;6(1):39. 10.1186/s40425-018-0349-3
208. Latchman DS. Transcription factors: an overview. Int J Biochem Cell Biol. 1997;29(12):1305-12. 10.1016/s1357-2725(97)00085-x
209. Spitz F, Furlong EE. Transcription factors: from enhancer binding to developmental control. Nat Rev Genet. 2012;13(9):613-26. 10.1038/nrg3207
210. Hosokawa H, Rothenberg EV. How transcription factors drive choice of the T cell fate. Nat Rev Immunol. 2021;21(3):162-76. 10.1038/s41577-020-00426-6
211. Oestreich KJ, Weinmann AS. Master regulators or lineage-specifying? Changing views on CD4+ T cell transcription factors. Nat Rev Immunol. 2012;12(11):799-804. 10.1038/nri3321
212. Iwanaga N, Kolls JK. Updates on T helper type 17 immunity in respiratory disease. Immunology. 2019;156(1):3-8. 10.1111/imm.13006
213. Voigt C, May P, Gottschlich A, Markota A, Wenk D, Gerlach I, et al. Cancer cells induce interleukin-22 production from memory CD4(+) T cells via interleukin-1 to promote tumor growth. Proc Natl Acad Sci U S A. 2017;114(49):12994-9. 10.1073/pnas.1705165114
214. Plank MW, Kaiko GE, Maltby S, Weaver J, Tay HL, Shen W, et al. Th22 Cells Form a Distinct Th Lineage from Th17 Cells In Vitro with Unique Transcriptional Properties and Tbet-Dependent Th1 Plasticity. J Immunol. 2017;198(5):2182-90. 10.4049/jimmunol.1601480
215. Yeste A, Mascanfroni ID, Nadeau M, Burns EJ, Tukpah AM, Santiago A, et al. IL-21 induces IL-22 production in CD4+ T cells. Nat Commun. 2014;5:3753. 10.1038/ncomms4753
216. Mickael ME, Bhaumik S, Basu R. Retinoid-Related Orphan Receptor RORgammat in CD4(+) T-Cell-Mediated Intestinal Homeostasis and Inflammation. Am J Pathol. 2020;190(10):1984-99. 10.1016/j.ajpath.2020.07.010
217. Rizzo A, Di Giovangiulio M, Stolfi C, Franze E, Fehling HJ, Carsetti R, et al. RORgammat-Expressing Tregs Drive the Growth of Colitis-Associated Colorectal Cancer by Controlling IL6 in Dendritic Cells. Cancer Immunol Res. 2018;6(9):1082-92. 10.1158/2326-6066.CIR-17-0698
218. Ohnmacht C, Park JH, Cording S, Wing JB, Atarashi K, Obata Y, et al. MUCOSAL IMMUNOLOGY. The microbiota regulates type 2 immunity through RORgammat(+) T cells. Science. 2015;349(6251):989-93. 10.1126/science.aac4263
219. Sefik E, Geva-Zatorsky N, Oh S, Konnikova L, Zemmour D, McGuire AM, et al. MUCOSAL IMMUNOLOGY. Individual intestinal symbionts induce a distinct population of RORgamma(+) regulatory T cells. Science. 2015;349(6251):993-7. 10.1126/science.aaa9420
220. Yang BH, Hagemann S, Mamareli P, Lauer U, Hoffmann U, Beckstette M, et al. Foxp3(+) T cells expressing RORgammat represent a stable regulatory T-cell effector lineage with enhanced suppressive capacity during intestinal inflammation. Mucosal Immunol. 2016;9(2):444-57. 10.1038/mi.2015.74
221. Beriou G, Costantino CM, Ashley CW, Yang L, Kuchroo VK, Baecher-Allan C, et al. IL-17-producing human peripheral regulatory T cells retain suppressive function. Blood. 2009;113(18):4240-9. 10.1182/blood-2008-10-183251
222. Hovhannisyan Z, Treatman J, Littman DR, Mayer L. Characterization of interleukin-17-producing regulatory T cells in inflamed intestinal mucosa from patients with inflammatory bowel diseases. Gastroenterology. 2011;140(3):957-65. 10.1053/j.gastro.2010.12.002
223. Kim BS, Lu H, Ichiyama K, Chen X, Zhang YB, Mistry NA, et al. Generation of RORgammat(+) Antigen-Specific T Regulatory 17 Cells from Foxp3(+) Precursors in Autoimmunity. Cell Rep. 2017;21(1):195-207. 10.1016/j.celrep.2017.09.021
224. Kluger MA, Meyer MC, Nosko A, Goerke B, Luig M, Wegscheid C, et al. RORgammat(+)Foxp3(+) Cells are an Independent Bifunctional Regulatory T Cell Lineage and Mediate Crescentic GN. J Am Soc Nephrol. 2016;27(2):454-65. 10.1681/ASN.2014090880
225. Hussein H, Denanglaire S, Van Gool F, Azouz A, Ajouaou Y, El-Khatib H, et al. Multiple Environmental Signaling Pathways Control the Differentiation of RORgammat-Expressing Regulatory T Cells. Front Immunol. 2019;10:3007. 10.3389/fimmu.2019.03007
226. Phillips JD, Knab LM, Blatner NR, Haghi L, DeCamp MM, Meyerson SL, et al. Preferential expansion of pro-inflammatory Tregs in human non-small cell lung cancer. Cancer Immunol Immunother. 2015;64(9):1185-91. 10.1007/s00262-015-1725-1
227. Koizumi SI, Ishikawa H. Transcriptional Regulation of Differentiation and Functions of Effector T Regulatory Cells. Cells. 2019;8(8). 10.3390/cells8080939

228. Muranski P, Boni A, Antony PA, Cassard L, Irvine KR, Kaiser A, et al. Tumor-specific Th17-polarized cells eradicate large established melanoma. Blood. 2008;112(2):362-73. 10.1182/blood-2007-11-120998
229. Crowther MD, Dolton G, Legut M, Caillaud ME, Lloyd A, Attaf M, et al. Genome-wide CRISPR-Cas9 screening reveals ubiquitous T cell cancer targeting via the monomorphic MHC class I-related protein MR1. Nat Immunol. 2020;21(2):178-85. 10.1038/s41590-019-0578-8
230. Venken K, Jacques P, Mortier C, Labadia ME, Decruy T, Coudenys J, et al. RORgammat inhibition selectively targets IL-17 producing iNKT and gammadelta-T cells enriched in Spondyloarthritis patients. Nat Commun. 2019;10(1):9. 10.1038/s41467-018-07911-6
231. Sanos SL, Bui VL, Mortha A, Oberle K, Heners C, Johner C, et al. RORgammat and commensal microflora are required for the differentiation of mucosal interleukin 22-producing NKp46+ cells. Nat Immunol. 2009;10(1):83-91. 10.1038/ni.1684
232. Lamichhane R, Schneider M, de la Harpe SM, Harrop TWR, Hannaway RF, Dearden PK, et al. TCR- or Cytokine-Activated CD8(+) Mucosal-Associated Invariant T Cells Are Rapid Polyfunctional Effectors That Can Coordinate Immune Responses. Cell Rep. 2019;28(12):3061-76 e5. 10.1016/j.celrep.2019.08.054
233. Tan Z, Jiang R, Wang X, Wang Y, Lu L, Liu Q, et al. RORgammat+IL-17+ neutrophils play a critical role in hepatic ischemia-reperfusion injury. J Mol Cell Biol. 2013;5(2):143-6. 10.1093/jmcb/mjs065
234. Cai W, Chen X, Men X, Ruan H, Hu M, Liu S, et al. Gut microbiota from patients with arteriosclerotic CSVD induces higher IL-17A production in neutrophils via activating RORgammat. Sci Adv. 2021;7(4). 10.1126/sciadv.abe4827
235. Taylor PR, Roy S, Leal SM, Jr., Sun Y, Howell SJ, Cobb BA, et al. Activation of neutrophils by autocrine IL-17A-IL-17RC interactions during fungal infection is regulated by IL-6, IL-23, RORgammat and dectin-2. Nat Immunol. 2014;15(2):143-51. 10.1038/ni.2797
236. Chen Z, Laurence A, O'Shea JJ. Signal transduction pathways and transcriptional regulation in the control of Th17 differentiation. Semin Immunol. 2007;19(6):400-8. 10.1016/j.smim.2007.10.015
237. Mucida D, Park Y, Kim G, Turovskaya O, Scott I, Kronenberg M, et al. Reciprocal TH17 and regulatory T cell differentiation mediated by retinoic acid. Science. 2007;317(5835):256-60. 10.1126/science.1145697
238. Takahashi H, Kanno T, Nakayamada S, Hirahara K, Sciume G, Muljo SA, et al. TGF-beta and retinoic acid induce the microRNA miR-10a, which targets Bcl-6 and constrains the plasticity of helper T cells. Nat Immunol. 2012;13(6):587-95. 10.1038/ni.2286
239. Hoechst B, Gamrekelashvili J, Manns MP, Greten TF, Korangy F. Plasticity of human Th17 cells and iTregs is orchestrated by different subsets of myeloid cells. Blood. 2011;117(24):6532-41. 10.1182/blood-2010-11-317321
240. Bechtel S, Rosenfelder H, Duda A, Schmidt CP, Ernst U, Wellenreuther R, et al. The full-ORF clone resource of the German cDNA Consortium. BMC Genomics. 2007;8:399. 10.1186/1471-2164-8-399
241. Eberl G. RORgammat, a multitask nuclear receptor at mucosal surfaces. Mucosal Immunol. 2017;10(1):27-34. 10.1038/mi.2016.86
242. Spinner CA, Lazarevic V. Transcriptional regulation of adaptive and innate lymphoid lineage specification. Immunol Rev. 2020. 10.1111/imr.12935
243. Gaffen SL, Jain R, Garg AV, Cua DJ. The IL-23-IL-17 immune axis: from mechanisms to therapeutic testing. Nat Rev Immunol. 2014;14(9):585-600. 10.1038/nri3707
244. Muranski P, Restifo NP. Essentials of Th17 cell commitment and plasticity. Blood. 2013;121(13):2402-14. 10.1182/blood-2012-09-378653
245. Annunziato F, Cosmi L, Liotta F, Maggi E, Romagnani S. Main features of human T helper 17 cells. Ann N Y Acad Sci. 2013;1284:66-70. 10.1111/nyas.12075
246. Duan MC, Zhong XN, Liu GN, Wei JR. The Treg/Th17 paradigm in lung cancer. J Immunol Res. 2014;2014:730380. 10.1155/2014/730380
247. Akdis M, Burgler S, Crameri R, Eiwegger T, Fujita H, Gomez E, et al. Interleukins, from 1 to 37, and interferon-gamma: receptors, functions, and roles in diseases. J Allergy Clin Immunol. 2011;127(3):701-21 e1-70. 10.1016/j.jaci.2010.11.050
248. Wilson NJ, Boniface K, Chan JR, McKenzie BS, Blumenschein WM, Mattson JD, et al. Development, cytokine profile and function of human interleukin 17-producing helper T cells. Nat Immunol. 2007;8(9):950-7. 10.1038/ni1497
249. Vasquez-Dunddel D, Pan F, Zeng Q, Gorbounov M, Albesiano E, Fu J, et al. STAT3 regulates arginase-I in myeloid-derived suppressor cells from cancer patients. J Clin Invest. 2013;123(4):1580-9. 10.1172/JCI60083

250. Mathur AN, Chang HC, Zisoulis DG, Stritesky GL, Yu Q, O'Malley JT, et al. Stat3 and Stat4 direct development of IL-17-secreting Th cells. J Immunol. 2007;178(8):4901-7. 10.4049/jimmunol.178.8.4901
251. Dang EV, Barbi J, Yang HY, Jinasena D, Yu H, Zheng Y, et al. Control of T(H)17/T(reg) balance by hypoxia-inducible factor 1. Cell. 2011;146(5):772-84. 10.1016/j.cell.2011.07.033
252. Ciucci T, Vacchio MS, Bosselut R. A STAT3-dependent transcriptional circuitry inhibits cytotoxic gene expression in T cells. Proc Natl Acad Sci U S A. 2017;114(50):13236-41. 10.1073/pnas.1711160114
253. Veldhoen M, Hirota K, Christensen J, O'Garra A, Stockinger B. Natural agonists for aryl hydrocarbon receptor in culture medium are essential for optimal differentiation of Th17 T cells. J Exp Med. 2009;206(1):43-9. 10.1084/jem.20081438
254. Kryczek I, Zhao E, Liu Y, Wang Y, Vatan L, Szeliga W, et al. Human TH17 cells are long-lived effector memory cells. Sci Transl Med. 2011;3(104):104ra0. 10.1126/scitranslmed.3002949
255. Shi LZ, Wang R, Huang G, Vogel P, Neale G, Green DR, et al. HIF1alpha-dependent glycolytic pathway orchestrates a metabolic checkpoint for the differentiation of TH17 and Treg cells. J Exp Med. 2011;208(7):1367-76. 10.1084/jem.20110278
256. Babic M, Dimitropoulos C, Hammer Q, Stehle C, Heinrich F, Sarsenbayeva A, et al. NK cell receptor NKG2D enforces proinflammatory features and pathogenicity of Th1 and Th17 cells. J Exp Med. 2020;217(8). 10.1084/jem.20190133
257. Martin-Orozco N, Muranski P, Chung Y, Yang XO, Yamazaki T, Lu S, et al. T helper 17 cells promote cytotoxic T cell activation in tumor immunity. Immunity. 2009;31(5):787-98. 10.1016/j.immuni.2009.09.014
258. Yosef N, Shalek AK, Gaublomme JT, Jin H, Lee Y, Awasthi A, et al. Dynamic regulatory network controlling TH17 cell differentiation. Nature. 2013;496(7446):461-8. 10.1038/nature11981
259. Cosmi L, De Palma R, Santarlasci V, Maggi L, Capone M, Frosali F, et al. Human interleukin 17-producing cells originate from a CD161+CD4+ T cell precursor. J Exp Med. 2008;205(8):1903-16. 10.1084/jem.20080397
260. Zhou L, Lopes JE, Chong MM, Ivanov, II, Min R, Victora GD, et al. TGF-beta-induced Foxp3 inhibits T(H)17 cell differentiation by antagonizing RORgammat function. Nature. 2008;453(7192):236-40. 10.1038/nature06878
261. Zhang F, Meng G, Strober W. Interactions among the transcription factors Runx1, RORgammat and Foxp3 regulate the differentiation of interleukin 17-producing T cells. Nat Immunol. 2008;9(11):1297-306. 10.1038/ni.1663
262. Hill DG, Yu L, Gao H, Balic JJ, West A, Oshima H, et al. Hyperactive gp130/STAT3-driven gastric tumourigenesis promotes submucosal tertiary lymphoid structure development. Int J Cancer. 2018;143(1):167-78. 10.1002/ijc.31298
263. Fasching P, Stradner M, Graninger W, Dejaco C, Fessler J. Therapeutic Potential of Targeting the Th17/Treg Axis in Autoimmune Disorders. Molecules. 2017;22(1). 10.3390/molecules22010134
264. Koenen HJ, Smeets RL, Vink PM, van Rijssen E, Boots AM, Joosten I. Human CD25highFoxp3pos regulatory T cells differentiate into IL-17-producing cells. Blood. 2008;112(6):2340-52. 10.1182/blood-2008-01-133967
265. Zorn E, Nelson EA, Mohseni M, Porcheray F, Kim H, Litsa D, et al. IL-2 regulates FOXP3 expression in human CD4+CD25+ regulatory T cells through a STAT-dependent mechanism and induces the expansion of these cells in vivo. Blood. 2006;108(5):1571-9. 10.1182/blood-2006-02-004747
266. Liu W, Putnam AL, Xu-Yu Z, Szot GL, Lee MR, Zhu S, et al. CD127 expression inversely correlates with FoxP3 and suppressive function of human CD4+ T reg cells. J Exp Med. 2006;203(7):1701-11. 10.1084/jem.20060772
267. Shevach EM, Thornton AM. tTregs, pTregs, and iTregs: similarities and differences. Immunol Rev. 2014;259(1):88-102. 10.1111/imr.12160
268. Ziegler SF, Buckner JH. FOXP3 and the regulation of Treg/Th17 differentiation. Microbes Infect. 2009;11(5):594-8. 10.1016/j.micinf.2009.04.002
269. Duan MC, Han W, Jin PW, Wei YP, Wei Q, Zhang LM, et al. Disturbed Th17/Treg Balance in Patients with Non-small Cell Lung Cancer. Inflammation. 2015;38(6):2156-65. 10.1007/s10753-015-0198-x
270. Yang XO, Pappu BP, Nurieva R, Akimzhanov A, Kang HS, Chung Y, et al. T helper 17 lineage differentiation is programmed by orphan nuclear receptors ROR alpha and ROR gamma. Immunity. 2008;28(1):29-39. 10.1016/j.immuni.2007.11.016
271. Barbi J, Pardoll D, Pan F. Metabolic control of the Treg/Th17 axis. Immunol Rev. 2013;252(1):52-77. 10.1111/imr.12029

272. Blagih J, Krawczyk CM, Jones RG. LKB1 and AMPK: central regulators of lymphocyte metabolism and function. Immunol Rev. 2012;249(1):59-71. 10.1111/j.1600-065X.2012.01157.x
273. MacIver NJ, Blagih J, Saucillo DC, Tonelli L, Griss T, Rathmell JC, et al. The liver kinase B1 is a central regulator of T cell development, activation, and metabolism. J Immunol. 2011;187(8):4187-98. 10.4049/jimmunol.1100367
274. Amezcua Vesely MC, Pallis P, Bielecki P, Low JS, Zhao J, Harman CCD, et al. Effector TH17 Cells Give Rise to Long-Lived TRM Cells that Are Essential for an Immediate Response against Bacterial Infection. Cell. 2019;178(5):1176-88 e15. 10.1016/j.cell.2019.07.032
275. Moghaddam SJ, Li H, Cho SN, Dishop MK, Wistuba, II, Ji L, et al. Promotion of lung carcinogenesis by chronic obstructive pulmonary disease-like airway inflammation in a K-ras-induced mouse model. Am J Respir Cell Mol Biol. 2009;40(4):443-53. 10.1165/rcmb.2008-0198OC
276. He D, Li H, Yusuf N, Elmets CA, Li J, Mountz JD, et al. IL-17 promotes tumor development through the induction of tumor promoting microenvironments at tumor sites and myeloid-derived suppressor cells. J Immunol. 2010;184(5):2281-8. 10.4049/jimmunol.0902574
277. Kryczek I, Wei S, Szeliga W, Vatan L, Zou W. Endogenous IL-17 contributes to reduced tumor growth and metastasis. Blood. 2009;114(2):357-9. 10.1182/blood-2008-09-177360
278. Reppert S, Boross I, Koslowski M, Tureci O, Koch S, Lehr HA, et al. A role for T-bet-mediated tumour immune surveillance in anti-IL-17A treatment of lung cancer. Nat Commun. 2011;2:600. 10.1038/ncomms1609
279. Marshall EA, Ng KW, Kung SH, Conway EM, Martinez VD, Halvorsen EC, et al. Emerging roles of T helper 17 and regulatory T cells in lung cancer progression and metastasis. Mol Cancer. 2016;15(1):67. 10.1186/s12943-016-0551-1
280. Li Y, Cao ZY, Sun B, Wang GY, Fu Z, Liu YM, et al. Effects of IL-17A on the occurrence of lung adenocarcinoma. Cancer Biol Ther. 2011;12(7):610-6. 10.4161/cbt.12.7.16302
281. Zhao L, Yang J, Wang HP, Liu RY. Imbalance in the Th17/Treg and cytokine environment in peripheral blood of patients with adenocarcinoma and squamous cell carcinoma. Medical oncology. 2013;30(1):461. 10.1007/s12032-013-0461-7
282. Zhou H, Hua W, Jin Y, Zhang C, Che L, Xia L, et al. Tc17 cells are associated with cigarette smoke-induced lung inflammation and emphysema. Respirology. 2015;20(3):426-33. 10.1111/resp.12486
283. Liang Y, Shen Y, Kuang L, Zhou G, Zhang L, Zhong X, et al. Cigarette smoke exposure promotes differentiation of CD4(+) T cells toward Th17 cells by CD40-CD40L costimulatory pathway in mice. Int J Chron Obstruct Pulmon Dis. 2018;13:959-68. 10.2147/COPD.S155754
284. Le Rouzic O, Kone B, Kluza J, Marchetti P, Hennegrave F, Olivier C, et al. Cigarette smoke alters the ability of human dendritic cells to promote anti-Streptococcus pneumoniae Th17 response. Respir Res. 2016;17(1):94. 10.1186/s12931-016-0408-6
285. Lee KH, Lee CH, Woo J, Jeong J, Jang AH, Yoo CG. Cigarette Smoke Extract Enhances IL-17A-Induced IL-8 Production via Up-Regulation of IL-17R in Human Bronchial Epithelial Cells. Mol Cells. 2018;41(4):282-9. 10.14348/molcells.2018.2123
286. Montalbano AM, Riccobono L, Siena L, Chiappara G, Di Sano C, Anzalone G, et al. Cigarette smoke affects IL-17A, IL-17F and IL-17 receptor expression in the lung tissue: Ex vivo and in vitro studies. Cytokine. 2015;76(2):391-402. 10.1016/j.cyto.2015.07.013
287. Ma L, Jiang M, Zhao X, Sun J, Pan Q, Chu S. Cigarette and IL-17A synergistically induce bronchial epithelial-mesenchymal transition via activating IL-17R/NF-kappaB signaling. BMC Pulm Med. 2020;20(1):26. 10.1186/s12890-020-1057-6
288. Huang Q, Han J, Fan J, Duan L, Guo M, Lv Z, et al. IL-17 induces EMT via Stat3 in lung adenocarcinoma. Am J Cancer Res. 2016;6(2):440-51.
289. Bowers JS, Nelson MH, Majchrzak K, Bailey SR, Rohrer B, Kaiser AD, et al. Th17 cells are refractory to senescence and retain robust antitumor activity after long-term ex vivo expansion. JCI Insight. 2017;2(5):e90772. 10.1172/jci.insight.90772
290. Hamai A, Pignon P, Raimbaud I, Duperrier-Amouriaux K, Senellart H, Hiret S, et al. Human T(H)17 immune cells specific for the tumor antigen MAGE-A3 convert to IFN-gamma-secreting cells as they differentiate into effector T cells in vivo. Cancer Res. 2012;72(5):1059-63. 10.1158/0008-5472.CAN-11-3432
291. Salazar Y, Zheng X, Brunn D, Raifer H, Picard F, Zhang Y, et al. Microenvironmental Th9 and Th17 lymphocytes induce metastatic spreading in lung cancer. J Clin Invest. 2020;130(7):3560-75. 10.1172/JCI124037

292. Armstrong D, Chang CY, Lazarus DR, Corry D, Kheradmand F. Lung Cancer Heterogeneity in Modulation of Th17/IL17A Responses. Front Oncol. 2019;9:1384. 10.3389/fonc.2019.01384
293. Chen X, Wan J, Liu J, Xie W, Diao X, Xu J, et al. Increased IL-17-producing cells correlate with poor survival and lymphangiogenesis in NSCLC patients. Lung cancer. 2010;69(3):348-54. 10.1016/j.lungcan.2009.11.013
294. Bao Z, Lu G, Cui D, Yao Y, Yang G, Zhou J. IL-17A-producing T cells are associated with the progression of lung adenocarcinoma. Oncol Rep. 2016. 10.3892/or.2016.4837
295. Ye ZJ, Zhou Q, Gu YY, Qin SM, Ma WL, Xin JB, et al. Generation and differentiation of IL-17-producing CD4+ T cells in malignant pleural effusion. J Immunol. 2010;185(10):6348-54. 10.4049/jimmunol.1001728
296. Wang L, Yi T, Kortylewski M, Pardoll DM, Zeng D, Yu H. IL-17 can promote tumor growth through an IL-6-Stat3 signaling pathway. J Exp Med. 2009;206(7):1457-64. 10.1084/jem.20090207
297. Pan B, Shen J, Cao J, Zhou Y, Shang L, Jin S, et al. Interleukin-17 promotes angiogenesis by stimulating VEGF production of cancer cells via the STAT3/GIV signaling pathway in non-small-cell lung cancer. Sci Rep. 2015;5:16053. 10.1038/srep16053
298. Bi Y, Cao J, Jin S, Lv L, Qi L, Liu F, et al. Interleukin-22 promotes lung cancer cell proliferation and migration via the IL-22R1/STAT3 and IL-22R1/AKT signaling pathways. Mol Cell Biochem. 2016;415(1-2):1-11. 10.1007/s11010-016-2663-8
299. Khosravi N, Caetano MS, Cumpian AM, Unver N, De la Garza Ramos C, Noble O, et al. IL22 Promotes Kras-Mutant Lung Cancer by Induction of a Protumor Immune Response and Protection of Stemness Properties. Cancer Immunol Res. 2018;6(7):788-97. 10.1158/2326-6066.CIR-17-0655
300. Kobold S, Volk S, Clauditz T, Kupper NJ, Minner S, Tufman A, et al. Interleukin-22 is frequently expressed in small- and large-cell lung cancer and promotes growth in chemotherapy-resistant cancer cells. Journal of thoracic oncology : official publication of the International Association for the Study of Lung Cancer. 2013;8(8):1032-42. 10.1097/JTO.0b013e31829923c8
301. Ye ZJ, Zhou Q, Yin W, Yuan ML, Yang WB, Xiang F, et al. Interleukin 22-producing CD4+ T cells in malignant pleural effusion. Cancer Lett. 2012;326(1):23-32. 10.1016/j.canlet.2012.07.013
302. Weinberg FD, Ramnath N. Targeting IL22: a potential therapeutic approach for Kras mutant lung cancer? Transl Lung Cancer Res. 2018;7(Suppl 3):S243-S7. 10.21037/tlcr.2018.09.04
303. Carmi Y, Rinott G, Dotan S, Elkabets M, Rider P, Voronov E, et al. Microenvironment-derived IL-1 and IL-17 interact in the control of lung metastasis. J Immunol. 2011;186(6):3462-71. 10.4049/jimmunol.1002901
304. Wu Z, He D, Zhao S, Wang H. IL-17A/IL-17RA promotes invasion and activates MMP-2 and MMP-9 expression via p38 MAPK signaling pathway in non-small cell lung cancer. Mol Cell Biochem. 2019;455(1-2):195-206. 10.1007/s11010-018-3483-9
305. Ferreira N, Mesquita I, Baltazar F, Silvestre R, Granja S. IL-17A and IL-17F orchestrate macrophages to promote lung cancer. Cell Oncol (Dordr). 2020;43(4):643-54. 10.1007/s13402-020-00510-y
306. Kawano M, Mabuchi S, Matsumoto Y, Sasano T, Takahashi R, Kuroda H, et al. The significance of G-CSF expression and myeloid-derived suppressor cells in the chemoresistance of uterine cervical cancer. Sci Rep. 2015;5:18217. 10.1038/srep18217
307. Morales JK, Kmieciak M, Knutson KL, Bear HD, Manjili MH. GM-CSF is one of the main breast tumor-derived soluble factors involved in the differentiation of CD11b-Gr1- bone marrow progenitor cells into myeloid-derived suppressor cells. Breast Cancer Res Treat. 2010;123(1):39-49. 10.1007/s10549-009-0622-8
308. Chalmin F, Mignot G, Bruchard M, Chevriaux A, Vegran F, Hichami A, et al. Stat3 and Gfi-1 transcription factors control Th17 cell immunosuppressive activity via the regulation of ectonucleotidase expression. Immunity. 2012;36(3):362-73. 10.1016/j.immuni.2011.12.019
309. Li J, Wang L, Chen X, Li L, Li Y, Ping Y, et al. CD39/CD73 upregulation on myeloid-derived suppressor cells via TGF-beta-mTOR-HIF-1 signaling in patients with non-small cell lung cancer. Oncoimmunology. 2017;6(6):e1320011. 10.1080/2162402X.2017.1320011
310. Cancer Genome Atlas Research Network, Weinstein JN, Collisson EA, Mills GB, Shaw KR, Ozenberger BA, et al. The Cancer Genome Atlas Pan-Cancer analysis project. Nat Genet. 2013;45(10):1113-20. 10.1038/ng.2764
311. Gao J, Aksoy BA, Dogrusoz U, Dresdner G, Gross B, Sumer SO, et al. Integrative analysis of complex cancer genomics and clinical profiles using the cBioPortal. Sci Signal. 2013;6(269):pl1. 10.1126/scisignal.2004088

312. Mermel CH, Schumacher SE, Hill B, Meyerson ML, Beroukhim R, Getz G. GISTIC2.0 facilitates sensitive and confident localization of the targets of focal somatic copy-number alteration in human cancers. Genome Biol. 2011;12(4):R41. 10.1186/gb-2011-12-4-r41
313. Li B, Dewey CN. RSEM: accurate transcript quantification from RNA-Seq data with or without a reference genome. BMC Bioinformatics. 2011;12:323. 10.1186/1471-2105-12-323
314. R Core Team. R: A language and environment for statistical computing. 2020
315. RStudio Team. RStudio: Integrated Development for R. 2020
316. Schabath MB, Welsh EA, Fulp WJ, Chen L, Teer JK, Thompson ZJ, et al. Differential association of STK11 and TP53 with KRAS mutation-associated gene expression, proliferation and immune surveillance in lung adenocarcinoma. Oncogene. 2015. 10.1038/onc.2015.375
317. Edgar R, Domrachev M, Lash AE. Gene Expression Omnibus: NCBI gene expression and hybridization array data repository. Nucleic Acids Res. 2002;30(1):207-10.
318. Welsh EA, Eschrich SA, Berglund AE, Fenstermacher DA. Iterative rank-order normalization of gene expression microarray data. BMC Bioinformatics. 2013;14:153. 10.1186/1471-2105-14-153
319. Campbell JD, Alexandrov A, Kim J, Wala J, Berger AH, Pedamallu CS, et al. Distinct patterns of somatic genome alterations in lung adenocarcinomas and squamous cell carcinomas. Nat Genet. 2016;48(6):607-16. 10.1038/ng.3564
320. Ding L, Getz G, Wheeler DA, Mardis ER, McLellan MD, Cibulskis K, et al. Somatic mutations affect key pathways in lung adenocarcinoma. Nature. 2008;455(7216):1069-75. 10.1038/nature07423
321. Newman AM, Liu CL, Green MR, Gentles AJ, Feng W, Xu Y, et al. Robust enumeration of cell subsets from tissue expression profiles. Nat Methods. 2015;12(5):453-7. 10.1038/nmeth.3337
322. Becht E, Giraldo NA, Lacroix L, Buttard B, Elarouci N, Petitprez F, et al. Estimating the population abundance of tissue-infiltrating immune and stromal cell populations using gene expression. Genome Biol. 2016;17(1):218. 10.1186/s13059-016-1070-5
323. Irizarry RA, Hobbs B, Collin F, Beazer-Barclay YD, Antonellis KJ, Scherf U, et al. Exploration, normalization, and summaries of high density oligonucleotide array probe level data. Biostatistics. 2003;4(2):249-64. 10.1093/biostatistics/4.2.249
324. Barbie DA, Tamayo P, Boehm JS, Kim SY, Moody SE, Dunn IF, et al. Systematic RNA interference reveals that oncogenic KRAS-driven cancers require TBK1. Nature. 2009;462(7269):108-12. 10.1038/nature08460
325. Hanzelmann S, Castelo R, Guinney J. GSVA: gene set variation analysis for microarray and RNA-seq data. BMC Bioinformatics. 2013;14:7. 10.1186/1471-2105-14-7
326. Xu Q, Chen J, Ni S, Tan C, Xu M, Dong L, et al. Pan-cancer transcriptome analysis reveals a gene expression signature for the identification of tumor tissue origin. Mod Pathol. 2016;29(6):546-56. 10.1038/modpathol.2016.60
327. Chen J. cytofkit2: an integrated mass cytometry data analysis pipeline. 2020
328. Wickham H, Averick, M., Bryan, J., Chang, W., McGowan, L.D., Francois, R., Grolemund, G., Hayes, A., Henry, L., Hester, J., Kuhn, M., Pedersen, T.L., Miller, E., Bache, S.M., Muller, K., Ooms, J., Robinson, D., Seidel, D.P., Spinu, V., Takahashi, K., Vaughan, D., Wilke, C., Woo, K., Yutani, H.,. Welcome to the Tidyverse. J Open Source Softw. 2019;4(43). doi.org/10.21105/joss.01686
329. Vu VQ. A ggplot2 based biplot. 0.55 ed2011
330. Kassambara A. 'ggplot2' Based Publication Ready Plots. 0.4.0 ed2020
331. Warnes GR, Bolker, B., Bonebakker, L., Gentleman, R., Huber, W., Liaw, A., Lumley, T., Maechler, M., Magnusson, A., Moeller, S., Schwartz, M., Venables, B., Galili, T.,. Various R Programming Tools for Plotting Data. 3.1.0 ed2020
332. Diggins KE, Greenplate AR, Leelatian N, Wogsland CE, Irish JM. Characterizing cell subsets using marker enrichment modeling. Nat Methods. 2017;14(3):275-8. 10.1038/nmeth.4149
333. Johnson KS. phenoptr: inForm Helper Functions. R package version 0.2.7. 2020
334. Neuwirth E. ColorBrewer Palettes. 1.1.2 ed2015
335. R Core Team. Web Application Framework for R. 1.5.0 ed2020
336. Huber W, Carey VJ, Gentleman R, Anders S, Carlson M, Carvalho BS, et al. Orchestrating high-throughput genomic analysis with Bioconductor. Nat Methods. 2015;12(2):115-21. 10.1038/nmeth.3252
337. Fox J, Weisberg, S.,. An R Companion to Applied Regression. 2019
338. Wilke CO. Streamlined Plot Theme and Plot Annotations for 'ggplot2'. 1.1.0 ed2020
339. Dowle M, Scrinivasan, A.,. data.table: Extension of `data.frame`. 1.12.8 ed2019

340. Meyer D, Dimitriadou, E., Hornik, K., Weingessel, A., Leisch, F.,. Misc Functions of the Department of Statistics, Probability

Theory Group (Formerly: E1071). 1.7.3 ed2019
341. Kassambara A, Mundt, F.,. Extract and Visualize the Results of Multivariate Data Analyses. 1.0.7 ed2020
342. Hahne F, LeMeur N, Brinkman RR, Ellis B, Haaland P, Sarkar D, et al. flowCore: a Bioconductor package for high throughput flow cytometry. BMC Bioinformatics. 2009;10:106. 10.1186/1471-2105-10-106
343. Van Gassen S, Callebaut B, Van Helden MJ, Lambrecht BN, Demeester P, Dhaene T, et al. FlowSOM: Using self-organizing maps for visualization and interpretation of cytometry data. Cytometry A. 2015;87(7):636-45. 10.1002/cyto.a.22625
344. Gentleman R, Carey, V., Huber, W., Hahne, F.,. genefilter: methods for filtering genes from high-throughput

experiments. 1.66.0 ed2019
345. Auguie B. Miscellaneous Functions for "Grid" Graphics. 2.3 ed2017
346. Morgan M, Falcon, S., Gentleman, R.,. Gene set enrichment data structures and methods. 1.46.0 ed2019
347. Ritchie ME, Phipson B, Wu D, Hu Y, Law CW, Shi W, et al. limma powers differential expression analyses for RNA-sequencing and microarray studies. Nucleic Acids Res. 2015;43(7):e47. 10.1093/nar/gkv007
348. Bache SM, Wickham, H.,. A Forward-Pipe Operator for R. 2014
349. Schauberger P, Walker, A.,. Read, Write and Edit xlsx Files. 4.1.5 ed2020
350. Wickham H. The Split-Apply-Combine Strategy for Data Analysis. J Stat Softw. 2011;40(1). 10.18637/jss.v040.i01
351. Liaw A, Wiener, M.,. Classification and Regression by randomForest. 4.6.14 ed2002
352. Wickham H. Reshaping Data with the reshape Package. J Stat Softw. 2007;21(12). 10.18637/jss.v021.i12
353. Sing T, Sander O, Beerenwinkel N, Lengauer T. ROCR: visualizing classifier performance in R. Bioinformatics. 2005;21(20):3940-1. 10.1093/bioinformatics/bti623
354. Hunziker P. R-Trees for Point Data. 0.1.0 ed2020
355. Krijthe JH. Rtsne: T-Distributed Stochastic Neighbor Embedding using a Barnes-Hut Implementation. 2015
356. Wickham H. Scale Functions for Visulizations. 1.0.0 ed2018
357. Urbanek S, Johnson, K.,. Read and write TIFF images. 0.1.7 ed2020
358. Melville J. The Uniform Manifold Approximation and Projection (UMAP) Method for Dimensionality Reduction. 0.1.4 ed2019
359. Jamal-Hanjani M, Hackshaw A, Ngai Y, Shaw J, Dive C, Quezada S, et al. Tracking genomic cancer evolution for precision medicine: the lung TRACERx study. PLoS biology. 2014;12(7):e1001906. 10.1371/journal.pbio.1001906
360. Middleton G, Crack LR, Popat S, Swanton C, Hollingsworth SJ, Buller R, et al. The National Lung Matrix Trial: translating the biology of stratification in advanced non-small-cell lung cancer. Annals of oncology : official journal of the European Society for Medical Oncology / ESMO. 2015;26(12):2464-9. 10.1093/annonc/mdv394
361. Tate JG, Bamford S, Jubb HC, Sondka Z, Beare DM, Bindal N, et al. COSMIC: the Catalogue Of Somatic Mutations In Cancer. Nucleic Acids Res. 2019;47(D1):D941-D7. 10.1093/nar/gky1015
362. Coker EA, Mitsopoulos C, Tym JE, Komianou A, Kannas C, Di Micco P, et al. canSAR: update to the cancer translational research and drug discovery knowledgebase. Nucleic Acids Res. 2019;47(D1):D917-D22. 10.1093/nar/gky1129
363. Blanco R, Iwakawa R, Tang M, Kohno T, Angulo B, Pio R, et al. A gene-alteration profile of human lung cancer cell lines. Hum Mutat. 2009;30(8):1199-206. 10.1002/humu.21028
364. Mahoney CL, Choudhury B, Davies H, Edkins S, Greenman C, Haaften G, et al. LKB1/KRAS mutant lung cancers constitute a genetic subset of NSCLC with increased sensitivity to MAPK and mTOR signalling inhibition. British journal of cancer. 2009;100(2):370-5. 10.1038/sj.bjc.6604886

365. Furugaki K, Moriya Y, Iwai T, Yorozu K, Yanagisawa M, Kondoh K, et al. Erlotinib inhibits osteolytic bone invasion of human non-small-cell lung cancer cell line NCI-H292. Clin Exp Metastasis. 2011;28(7):649-59. 10.1007/s10585-011-9398-4
366. Livak KJ, Schmittgen TD. Analysis of relative gene expression data using real-time quantitative PCR and the 2(-Delta Delta C(T)) Method. Methods. 2001;25(4):402-8. 10.1006/meth.2001.1262
367. Parra ER, Uraoka N, Jiang M, Cook P, Gibbons D, Forget MA, et al. Validation of multiplex immunofluorescence panels using multispectral microscopy for immune-profiling of formalin-fixed and paraffin-embedded human tumor tissues. Sci Rep. 2017;7(1):13380. 10.1038/s41598-017-13942-8
368. Vasaturo A, Di Blasio S, Verweij D, Blokx WA, van Krieken JH, de Vries IJ, et al. Multispectral imaging for highly accurate analysis of tumour-infiltrating lymphocytes in primary melanoma. Histopathology. 2017;70(4):643-9. 10.1111/his.13070
369. Yang L, Liu Z, Tan J, Dong H, Zhang X. Multispectral imaging reveals hyper active TGF-beta signaling in colorectal cancer. Cancer Biol Ther. 2018;19(2):105-12. 10.1080/15384047.2017.1395116
370. Esbona K, Inman D, Saha S, Jeffery J, Schedin P, Wilke L, et al. COX-2 modulates mammary tumor progression in response to collagen density. Breast Cancer Res. 2016;18(1):35. 10.1186/s13058-016-0695-3
371. Chen H, Lau MC, Wong MT, Newell EW, Poidinger M, Chen J. Cytofkit: A Bioconductor Package for an Integrated Mass Cytometry Data Analysis Pipeline. PLoS Comput Biol. 2016;12(9):e1005112. 10.1371/journal.pcbi.1005112
372. Nowicka M, Krieg C, Crowell HL, Weber LM, Hartmann FJ, Guglietta S, et al. CyTOF workflow: differential discovery in high-throughput high-dimensional cytometry datasets. F1000Res. 2017;6:748. 10.12688/f1000research.11622.3
373. Kotecha N, Krutzik PO, Irish JM. Web-based analysis and publication of flow cytometry experiments. Curr Protoc Cytom. 2010;Chapter 10:Unit10 7. 10.1002/0471142956.cy1017s53
374. McInnes L, Healy, J., Saul, N., Großberger, L., . UMAP: Uniform Manifold Approximation and Projection. J Open Source Softw. 2018;3(29):861. 10.21105/joss.00861
375. Aredo JV, Padda SK, Kunder CA, Han SS, Neal JW, Shrager JB, et al. Impact of KRAS mutation subtype and concurrent pathogenic mutations on non-small cell lung cancer outcomes. Lung cancer. 2019;133:144-50. 10.1016/j.lungcan.2019.05.015
376. Calles A, Sholl LM, Rodig SJ, Pelton AK, Hornick JL, Butaney M, et al. Immunohistochemical Loss of LKB1 Is a Biomarker for More Aggressive Biology in KRAS-Mutant Lung Adenocarcinoma. Clin Cancer Res. 2015;21(12):2851-60. 10.1158/1078-0432.CCR-14-3112
377. Goh JY, Feng M, Wang W, Oguz G, Yatim S, Lee PL, et al. Chromosome 1q21.3 amplification is a trackable biomarker and actionable target for breast cancer recurrence. Nat Med. 2017;23(11):1319-30. 10.1038/nm.4405
378. Sanjmyatav J, Junker K, Matthes S, Muehr M, Sava D, Sternal M, et al. Identification of genomic alterations associated with metastasis and cancer specific survival in clear cell renal cell carcinoma. J Urol. 2011;186(5):2078-83. 10.1016/j.juro.2011.06.050
379. Maru DM, Luthra R, Correa AM, White-Cross J, Anandasabapathy S, Krishnan S, et al. Frequent loss of heterozygosity of chromosome 1q in esophageal adenocarcinoma: loss of chromosome 1q21.3 is associated with shorter overall survival. Cancer. 2009;115(7):1576-85. 10.1002/cncr.24122
380. Kou F, Wu L, Ren X, Yang L. Chromosome Abnormalities: New Insights into Their Clinical Significance in Cancer. Mol Ther Oncolytics. 2020;17:562-70. 10.1016/j.omto.2020.05.010
381. Devarakonda SHK, Waqar, S. N., Guebert, K., Maggi, L. B., Carpenter, D., Ozenberger, B., Govindan, R., Morgensztern, D.,. Characteristics of 1q amplification in adenocarcinoma of the lung (LUAD). J Clin Oncol. 2014;32(15). 10.1200/jco.2014.32.15_suppl.e22195
382. Kang J. High Level Amplifications of AKT3, SDCCAG8 and SLC35F3 Genes at Chromosomal 1q42.2-44 Region in Non-Small Cell Lung Cancer: Early and Prognostic Implications. Int J Cancer Res. 2017;13(1):1-8. 10.3923/ijcr.2017.1.8
383. Tan X, Banerjee P, Pham EA, Rutaganira FUN, Basu K, Bota-Rabassedas N, et al. PI4KIIIbeta is a therapeutic target in chromosome 1q-amplified lung adenocarcinoma. Sci Transl Med. 2020;12(527). 10.1126/scitranslmed.aax3772
384. Sy SM, Wong N, Lee TW, Tse G, Mok TS, Fan B, et al. Distinct patterns of genetic alterations in adenocarcinoma and squamous cell carcinoma of the lung. European journal of cancer. 2004;40(7):1082-94. 10.1016/j.ejca.2004.01.012

385. Zhang XC, Wang J, Shao GG, Wang Q, Qu X, Wang B, et al. Comprehensive genomic and immunological characterization of Chinese non-small cell lung cancer patients. Nat Commun. 2019;10(1):1772. 10.1038/s41467-019-09762-1
386. Chang SH, Reynolds JM, Pappu BP, Chen G, Martinez GJ, Dong C. Interleukin-17C promotes Th17 cell responses and autoimmune disease via interleukin-17 receptor E. Immunity. 2011;35(4):611-21. 10.1016/j.immuni.2011.09.010
387. Chakravarty D, Gao J, Phillips SM, Kundra R, Zhang H, Wang J, et al. OncoKB: A Precision Oncology Knowledge Base. JCO Precis Oncol. 2017;2017. 10.1200/PO.17.00011
388. Glodde N, Bald T, van den Boorn-Konijnenberg D, Nakamura K, O'Donnell JS, Szczepanski S, et al. Reactive Neutrophil Responses Dependent on the Receptor Tyrosine Kinase c-MET Limit Cancer Immunotherapy. Immunity. 2017;47(4):789-802 e9. 10.1016/j.immuni.2017.09.012
389. Benkhoucha M, Santiago-Raber ML, Schneiter G, Chofflon M, Funakoshi H, Nakamura T, et al. Hepatocyte growth factor inhibits CNS autoimmunity by inducing tolerogenic dendritic cells and CD25+Foxp3+ regulatory T cells. Proc Natl Acad Sci U S A. 2010;107(14):6424-9. 10.1073/pnas.0912437107
390. Saigi M, Alburquerque-Bejar JJ, Mc Leer-Florin A, Pereira C, Pros E, Romero OA, et al. MET-Oncogenic and JAK2-Inactivating Alterations Are Independent Factors That Affect Regulation of PD-L1 Expression in Lung Cancer. Clin Cancer Res. 2018;24(18):4579-87. 10.1158/1078-0432.CCR-18-0267
391. Albitar M, Sudarsanam S, Ma W, Jiang S, Chen W, Funari V, et al. Correlation of MET gene amplification and TP53 mutation with PD-L1 expression in non-small cell lung cancer. Oncotarget. 2018;9(17):13682-93. 10.18632/oncotarget.24455
392. Titmarsh HF, O'Connor R, Dhaliwal K, Akram AR. The Emerging Role of the c-MET-HGF Axis in Non-small Cell Lung Cancer Tumor Immunology and Immunotherapy. Front Oncol. 2020;10:54. 10.3389/fonc.2020.00054
393. Papaccio F, Della Corte CM, Viscardi G, Di Liello R, Esposito G, Sparano F, et al. HGF/MET and the Immune System: Relevance for Cancer Immunotherapy. Int J Mol Sci. 2018;19(11). 10.3390/ijms19113595
394. Nishimura T, Nakamura H, Yachie A, Hase T, Fujii K, Koizumi H, et al. Disease-related cellular protein networks differentially affected under different EGFR mutations in lung adenocarcinoma. Sci Rep. 2020;10(1):10881. 10.1038/s41598-020-67894-7
395. Gong K, Guo G, Panchani N, Bender ME, Gerber DE, Minna JD, et al. EGFR inhibition triggers an adaptive response by co-opting antiviral signaling pathways in lung cancer. Nat Cancer. 2020;1(4):394-409. 10.1038/s43018-020-0048-0
396. Lulli D, Carbone ML, Pastore S. Epidermal growth factor receptor inhibitors trigger a type I interferon response in human skin. Oncotarget. 2016;7(30):47777-93. 10.18632/oncotarget.10013
397. Lupberger J, Duong FH, Fofana I, Zona L, Xiao F, Thumann C, et al. Epidermal growth factor receptor signaling impairs the antiviral activity of interferon-alpha. Hepatology. 2013;58(4):1225-35. 10.1002/hep.26404
398. Venugopalan A, Lee MJ, Niu G, Medina-Echeverz J, Tomita Y, Lizak MJ, et al. EGFR-targeted therapy results in dramatic early lung tumor regression accompanied by imaging response and immune infiltration in EGFR mutant transgenic mouse models. Oncotarget. 2016. 10.18632/oncotarget.11021
399. Yang H, Chen H, Luo S, Li L, Zhou S, Shen R, et al. The correlation between programmed death-ligand 1 expression and driver gene mutations in NSCLC. Oncotarget. 2017;8(14):23517-28. 10.18632/oncotarget.15627
400. Schoenfeld AJ, Rizvi H, Bandlamudi C, Sauter JL, Travis WD, Rekhtman N, et al. Clinical and molecular correlates of PD-L1 expression in patients with lung adenocarcinomas. Annals of oncology : official journal of the European Society for Medical Oncology / ESMO. 2020;31(5):599-608. 10.1016/j.annonc.2020.01.065
401. Hamarsheh S, Gross O, Brummer T, Zeiser R. Immune modulatory effects of oncogenic KRAS in cancer. Nat Commun. 2020;11(1):5439. 10.1038/s41467-020-19288-6
402. Veatch JR, Jesernig BL, Kargl J, Fitzgibbon M, Lee SM, Baik C, et al. Endogenous CD4(+) T Cells Recognize Neoantigens in Lung Cancer Patients, Including Recurrent Oncogenic KRAS and ERBB2 (Her2) Driver Mutations. Cancer Immunol Res. 2019;7(6):910-22. 10.1158/2326-6066.CIR-18-0402
403. Della Corte CM, Sen T, Gay CM, Ramkumar K, Diao L, Cardnell RJ, et al. STING Pathway Expression Identifies NSCLC With an Immune-Responsive Phenotype. Journal of thoracic oncology : official publication of the International Association for the Study of Lung Cancer. 2020;15(5):777-91. 10.1016/j.jtho.2020.01.009

404. Wang H, Guo J, Shang X, Wang Z. Less immune cell infiltration and worse prognosis after immunotherapy for patients with lung adenocarcinoma who harbored STK11 mutation. Int Immunopharmacol. 2020;84:106574. 10.1016/j.intimp.2020.106574
405. Gillette MA, Satpathy S, Cao S, Dhanasekaran SM, Vasaikar SV, Krug K, et al. Proteogenomic Characterization Reveals Therapeutic Vulnerabilities in Lung Adenocarcinoma. Cell. 2020;182(1):200-25 e35. 10.1016/j.cell.2020.06.013
406. Biton J, Mansuet-Lupo A, Pecuchet N, Alifano M, Ouakrim H, Arrondeau J, et al. TP53, STK11 and EGFR Mutations Predict Tumor Immune Profile and the Response to anti-PD-1 in Lung Adenocarcinoma. Clin Cancer Res. 2018. 10.1158/1078-0432.CCR-18-0163
407. Sun H, Liu SY, Zhou JY, Xu JT, Zhang HK, Yan HH, et al. Specific TP53 subtype as biomarker for immune checkpoint inhibitors in lung adenocarcinoma. EBioMedicine. 2020;60:102990. 10.1016/j.ebiom.2020.102990
408. Gao G, Liao W, Ma Q, Zhang B, Chen Y, Wang Y. KRAS G12D mutation predicts lower TMB and drives immune suppression in lung adenocarcinoma. Lung cancer. 2020;149:41-5. 10.1016/j.lungcan.2020.09.004
409. Chen N, Fang W, Lin Z, Peng P, Wang J, Zhan J, et al. KRAS mutation-induced upregulation of PD-L1 mediates immune escape in human lung adenocarcinoma. Cancer Immunol Immunother. 2017. 10.1007/s00262-017-2005-z
410. Sumimoto H, Takano A, Teramoto K, Daigo Y. RAS-Mitogen-Activated Protein Kinase Signal Is Required for Enhanced PD-L1 Expression in Human Lung Cancers. PloS one. 2016;11(11):e0166626. 10.1371/journal.pone.0166626
411. Meylan E, Dooley AL, Feldser DM, Shen L, Turk E, Ouyang C, et al. Requirement for NF-kappaB signalling in a mouse model of lung adenocarcinoma. Nature. 2009;462(7269):104-7. 10.1038/nature08462
412. Saltz J, Gupta R, Hou L, Kurc T, Singh P, Nguyen V, et al. Spatial Organization and Molecular Correlation of Tumor-Infiltrating Lymphocytes Using Deep Learning on Pathology Images. Cell Rep. 2018;23(1):181-93 e7. 10.1016/j.celrep.2018.03.086
413. Kadara H, Choi M, Zhang J, Cuentas EP, Canales JR, Gaffney SG, et al. Whole-exome sequencing and immune profiling of early-stage lung adenocarcinoma with fully annotated clinical follow-up. Annals of oncology : official journal of the European Society for Medical Oncology / ESMO. 2016. 10.1093/annonc/mdw436
414. Akbay EA, Koyama S, Liu Y, Dries R, Bufe LE, Silkes M, et al. Interleukin-17A Promotes Lung Tumor Progression through Neutrophil Attraction to Tumor Sites and Mediating Resistance to PD-1 Blockade. Journal of thoracic oncology : official publication of the International Association for the Study of Lung Cancer. 2017;12(8):1268-79. 10.1016/j.jtho.2017.04.017
415. Tamminga M, Hiltermann TJN, Schuuring E, Timens W, Fehrmann RS, Groen HJ. Immune microenvironment composition in non-small cell lung cancer and its association with survival. Clin Transl Immunology. 2020;9(6):e1142. 10.1002/cti2.1142
416. Tai AL, Yan WS, Fang Y, Xie D, Sham JS, Guan XY. Recurrent chromosomal imbalances in nonsmall cell lung carcinoma: the association between 1q amplification and tumor recurrence. Cancer. 2004;100(9):1918-27. 10.1002/cncr.20190
417. Yakut T, Schulten HJ, Demir A, Frank D, Danner B, Egeli U, et al. Assessment of molecular events in squamous and non-squamous cell lung carcinoma. Lung cancer. 2006;54(3):293-301. 10.1016/j.lungcan.2006.08.011
418. Kim H, Yoon N, Woo HY, Lee EJ, Do SI, Na K, et al. Atypical Mesonephric Hyperplasia of the Uterus Harbors Pathogenic Mutation of Kirsten Rat Sarcoma 2 Viral Oncogene Homolog (KRAS) and Gain of Chromosome 1q. Cancer Genomics Proteomics. 2020;17(6):813-26. 10.21873/cgp.20235
419. Tan DS, Camilleri-Broet S, Tan EH, Alifano M, Lim WT, Bobbio A, et al. Intertumor heterogeneity of non-small-cell lung carcinomas revealed by multiplexed mutation profiling and integrative genomics. Int J Cancer. 2014;135(5):1092-100. 10.1002/ijc.28750
420. Mirkovic J, McFarland M, Garcia E, Sholl LM, Lindeman N, MacConaill L, et al. Targeted Genomic Profiling Reveals Recurrent KRAS Mutations in Mesonephric-like Adenocarcinomas of the Female Genital Tract. Am J Surg Pathol. 2018;42(2):227-33. 10.1097/PAS.0000000000000958
421. Greenhill CJ, Rose-John S, Lissilaa R, Ferlin W, Ernst M, Hertzog PJ, et al. IL-6 trans-signaling modulates TLR4-dependent inflammatory responses via STAT3. J Immunol. 2011;186(2):1199-208. 10.4049/jimmunol.1002971

422. Ancrile B, Lim KH, Counter CM. Oncogenic Ras-induced secretion of IL6 is required for tumorigenesis. Genes Dev. 2007;21(14):1714-9. 10.1101/gad.1549407
423. Lee MM, Chui RK, Tam IY, Lau AH, Wong YH. CCR1-mediated STAT3 tyrosine phosphorylation and CXCL8 expression in THP-1 macrophage-like cells involve pertussis toxin-insensitive Galpha(14/16) signaling and IL-6 release. J Immunol. 2012;189(11):5266-76. 10.4049/jimmunol.1103359
424. Yang B, Li X, Fu Y, Guo E, Ye Y, Li F, et al. MEK inhibition remodels the immune landscape of mutant KRAS tumors to overcome resistance to PARP and immune checkpoint inhibitors. Cancer Res. 2021. 10.1158/0008-5472.CAN-20-2370
425. Sparmann A, Bar-Sagi D. Ras-induced interleukin-8 expression plays a critical role in tumor growth and angiogenesis. Cancer Cell. 2004;6(5):447-58. 10.1016/j.ccr.2004.09.028
426. Sunaga N, Imai H, Shimizu K, Shames DS, Kakegawa S, Girard L, et al. Oncogenic KRAS-induced interleukin-8 overexpression promotes cell growth and migration and contributes to aggressive phenotypes of non-small cell lung cancer. Int J Cancer. 2012;130(8):1733-44. 10.1002/ijc.26164
427. Carneiro-Lobo TC, Scalabrini LC, Magalhaes LDS, Cardeal LB, Rodrigues FS, Dos Santos EO, et al. IKKbeta targeting reduces KRAS-induced lung cancer angiogenesis in vitro and in vivo: A potential anti-angiogenic therapeutic target. Lung cancer. 2019;130:169-78. 10.1016/j.lungcan.2019.02.027
428. Saad MI, Alhayyani S, McLeod L, Yu L, Alanazi M, Deswaerte V, et al. ADAM17 selectively activates the IL-6 trans-signaling/ERK MAPK axis in KRAS-addicted lung cancer. EMBO Mol Med. 2019;11(4). 10.15252/emmm.201809976
429. Brooks GD, McLeod L, Alhayyani S, Miller A, Russell PA, Ferlin W, et al. IL6 Trans-signaling Promotes KRAS-Driven Lung Carcinogenesis. Cancer Res. 2016;76(4):866-76. 10.1158/0008-5472.CAN-15-2388
430. Mihara M, Hashizume M, Yoshida H, Suzuki M, Shiina M. IL-6/IL-6 receptor system and its role in physiological and pathological conditions. Clin Sci (Lond). 2012;122(4):143-59. 10.1042/CS20110340
431. Wang H, Zhang Z, Li R, Ang KK, Zhang H, Caraway NP, et al. Overexpression of S100A2 protein as a prognostic marker for patients with stage I non small cell lung cancer. Int J Cancer. 2005;116(2):285-90. 10.1002/ijc.21035
432. Chang SH, Mirabolfathinejad SG, Katta H, Cumpian AM, Gong L, Caetano MS, et al. T helper 17 cells play a critical pathogenic role in lung cancer. Proc Natl Acad Sci U S A. 2014;111(15):5664-9. 10.1073/pnas.1319051111
433. Ritzmann F, Jungnickel C, Vella G, Kamyschnikow A, Herr C, Li D, et al. IL-17C-mediated innate inflammation decreases the response to PD-1 blockade in a model of Kras-driven lung cancer. Sci Rep. 2019;9(1):10353. 10.1038/s41598-019-46759-8
434. Rungsung I, Ramaswamy A. Effects of Peutz-Jeghers syndrome (PJS) causing missense mutations L67P, L182P, G242V and R297S on the structural dynamics of LKB1 (Liver kinase B1) protein. J Biomol Struct Dyn. 2019;37(3):796-810. 10.1080/07391102.2018.1441070
435. Liu Y, Beyer A, Aebersold R. On the Dependency of Cellular Protein Levels on mRNA Abundance. Cell. 2016;165(3):535-50. 10.1016/j.cell.2016.03.014
436. Koussounadis A, Langdon SP, Um IH, Harrison DJ, Smith VA. Relationship between differentially expressed mRNA and mRNA-protein correlations in a xenograft model system. Sci Rep. 2015;5:10775. 10.1038/srep10775
437. Huang Q, Fan J, Qian X, Lv Z, Zhang X, Han J, et al. Retinoic acid-related orphan receptor C isoform 2 expression and its prognostic significance for non-small cell lung cancer. J Cancer Res Clin Oncol. 2016;142(1):263-72. 10.1007/s00432-015-2040-0
438. Chen Z, Tato CM, Muul L, Laurence A, O'Shea JJ. Distinct regulation of interleukin-17 in human T helper lymphocytes. Arthritis Rheum. 2007;56(9):2936-46. 10.1002/art.22866
439. Cousin C, Aubatin A, Le Gouvello S, Apetoh L, Castellano F, Molinier-Frenkel V. The immunosuppressive enzyme IL4I1 promotes FoxP3(+) regulatory T lymphocyte differentiation. Eur J Immunol. 2015;45(6):1772-82. 10.1002/eji.201445000
440. Lu B, Liu M, Wang J, Fan H, Yang D, Zhang L, et al. IL-17 production by tissue-resident MAIT cells is locally induced in children with pneumonia. Mucosal Immunol. 2020;13(5):824-35. 10.1038/s41385-020-0273-y
441. Willing A, Jager J, Reinhardt S, Kursawe N, Friese MA. Production of IL-17 by MAIT Cells Is Increased in Multiple Sclerosis and Is Associated with IL-7 Receptor Expression. J Immunol. 2018;200(3):974-82. 10.4049/jimmunol.1701213

442. Yoshida N, Kinugasa T, Miyoshi H, Sato K, Yuge K, Ohchi T, et al. A High RORgammaT/CD3 Ratio is a Strong Prognostic Factor for Postoperative Survival in Advanced Colorectal Cancer: Analysis of Helper T Cell Lymphocytes (Th1, Th2, Th17 and Regulatory T Cells). Ann Surg Oncol. 2016;23(3):919-27. 10.1245/s10434-015-4923-3
443. Shikhagaie MM, Bjorklund AK, Mjosberg J, Erjefalt JS, Cornelissen AS, Ros XR, et al. Neuropilin-1 Is Expressed on Lymphoid Tissue Residing LTi-like Group 3 Innate Lymphoid Cells and Associated with Ectopic Lymphoid Aggregates. Cell Rep. 2017;18(7):1761-73. 10.1016/j.celrep.2017.01.063
444. Suzuki M, Sze MA, Campbell JD, Brothers JF, 2nd, Lenburg ME, McDonough JE, et al. The cellular and molecular determinants of emphysematous destruction in COPD. Sci Rep. 2017;7(1):9562. 10.1038/s41598-017-10126-2
445. Castro G, Liu X, Ngo K, De Leon-Tabaldo A, Zhao S, Luna-Roman R, et al. RORgammat and RORalpha signature genes in human Th17 cells. PloS one. 2017;12(8):e0181868. 10.1371/journal.pone.0181868
446. Bindea G, Mlecnik B, Tosolini M, Kirilovsky A, Waldner M, Obenauf AC, et al. Spatiotemporal dynamics of intratumoral immune cells reveal the immune landscape in human cancer. Immunity. 2013;39(4):782-95. 10.1016/j.immuni.2013.10.003
447. Chang WH, Lai AG. Timing gone awry: distinct tumour suppressive and oncogenic roles of the circadian clock and crosstalk with hypoxia signalling in diverse malignancies. J Transl Med. 2019;17(1):132. 10.1186/s12967-019-1880-9
448. Wu Y, Tao B, Zhang T, Fan Y, Mao R. Pan-Cancer Analysis Reveals Disrupted Circadian Clock Associates With T Cell Exhaustion. Front Immunol. 2019;10:2451. 10.3389/fimmu.2019.02451
449. Yao W, Maitra A. Hear Pancreatic Cancer Stem Cells ROR. Cell. 2019;177(3):516-8. 10.1016/j.cell.2019.04.002
450. Cao D, Qi Z, Pang Y, Li H, Xie H, Wu J, et al. Retinoic Acid-Related Orphan Receptor C Regulates Proliferation, Glycolysis, and Chemoresistance via the PD-L1/ITGB6/STAT3 Signaling Axis in Bladder Cancer. Cancer Res. 2019;79(10):2604-18. 10.1158/0008-5472.CAN-18-3842
451. Cunha LL, Morari EC, Nonogaki S, Bufalo NE, da Assumpcao LVM, Soares FA, et al. RORgammat may Influence the Microenvironment of Thyroid Cancer Predicting Favorable Prognosis. Sci Rep. 2020;10(1):4142. 10.1038/s41598-020-60280-3
452. Balabko L, Andreev K, Burmann N, Schubert M, Mathews M, Trufa DI, et al. Increased expression of the Th17-IL-6R/pSTAT3/BATF/RorgammaT-axis in the tumoural region of adenocarcinoma as compared to squamous cell carcinoma of the lung. Sci Rep. 2014;4:7396. 10.1038/srep07396
453. Chen G, Zhang PG, Li JS, Duan JJ, Su W, Guo SP, et al. Th17 cell frequency and IL-17A production in peripheral blood of patients with non-small-cell lung cancer. J Int Med Res. 2020;48(6):300060520925948. 10.1177/0300060520925948
454. Nagaraj AS, Lahtela J, Hemmes A, Pellinen T, Blom S, Devlin JR, et al. Cell of Origin Links Histotype Spectrum to Immune Microenvironment Diversity in Non-small-Cell Lung Cancer Driven by Mutant Kras and Loss of Lkb1. Cell Rep. 2017;18(3):673-84. 10.1016/j.celrep.2016.12.059
455. Lopez S, Lim EL, Horswell S, Haase K, Huebner A, Dietzen M, et al. Interplay between whole-genome doubling and the accumulation of deleterious alterations in cancer evolution. Nat Genet. 2020;52(3):283-93. 10.1038/s41588-020-0584-7
456. Davoli T, Uno H, Wooten EC, Elledge SJ. Tumor aneuploidy correlates with markers of immune evasion and with reduced response to immunotherapy. Science. 2017;355(6322). 10.1126/science.aaf8399
457. Huang Q, Du J, Fan J, Lv Z, Qian X, Zhang X, et al. The effect of proinflammatory cytokines on IL-17RA expression in NSCLC. Medical oncology. 2014;31(9):144. 10.1007/s12032-014-0144-z
458. van den Beucken T, Koritzinsky M, Niessen H, Dubois L, Savelkouls K, Mujcic H, et al. Hypoxia-induced expression of carbonic anhydrase 9 is dependent on the unfolded protein response. J Biol Chem. 2009;284(36):24204-12. 10.1074/jbc.M109.006510
459. Brustugun OT. Hypoxia as a cause of treatment failure in non-small cell carcinoma of the lung. Semin Radiat Oncol. 2015;25(2):87-92. 10.1016/j.semradonc.2014.11.006
460. Lin Z, Huang L, Li S, Gu J, Cui X, Zhou Y. Pan-cancer analysis of genomic properties and clinical outcome associated with tumor tertiary lymphoid structure. Sci Rep. 2020;10(1):21530. 10.1038/s41598-020-78560-3
461. Sheng SY, Gu Y, Lu CG, Tang YY, Zou JY, Zhang YQ, et al. The Characteristics of Naive-like T Cells in Tumor-infiltrating Lymphocytes From Human Lung Cancer. J Immunother. 2016. 10.1097/CJI.0000000000000147

462. Jin C, Lagoudas GK, Zhao C, Bullman S, Bhutkar A, Hu B, et al. Commensal Microbiota Promote Lung Cancer Development via gammadelta T Cells. Cell. 2019;176(5):998-1013 e16. 10.1016/j.cell.2018.12.040
463. Eddens T, Elsegeiny W, Garcia-Hernadez ML, Castillo P, Trevejo-Nunez G, Serody K, et al. Pneumocystis-Driven Inducible Bronchus-Associated Lymphoid Tissue Formation Requires Th2 and Th17 Immunity. Cell Rep. 2017;18(13):3078-90. 10.1016/j.celrep.2017.03.016
464. Caetano MS, Zhang H, Cumpian AM, Gong L, Unver N, Ostrin EJ, et al. IL6 Blockade Reprograms the Lung Tumor Microenvironment to Limit the Development and Progression of K-ras-Mutant Lung Cancer. Cancer Res. 2016;76(11):3189-99. 10.1158/0008-5472.CAN-15-2840
465. Busch SE, Hanke ML, Kargl J, Metz HE, MacPherson D, Houghton AM. Lung Cancer Subtypes Generate Unique Immune Responses. J Immunol. 2016;197(11):4493-503. 10.4049/jimmunol.1600576
466. McAllister F, Bailey JM, Alsina J, Nirschl CJ, Sharma R, Fan H, et al. Oncogenic Kras activates a hematopoietic-to-epithelial IL-17 signaling axis in preinvasive pancreatic neoplasia. Cancer Cell. 2014;25(5):621-37. 10.1016/j.ccr.2014.03.014
467. Koh J, Kim HY, Lee Y, Park IK, Kang CH, Kim YT, et al. IL23-Producing Human Lung Cancer Cells Promote Tumor Growth via Conversion of Innate Lymphoid Cell 1 (ILC1) into ILC3. Clin Cancer Res. 2019;25(13):4026-37. 10.1158/1078-0432.CCR-18-3458
468. Krabbendam L, Heesters BA, Kradolfer CMA, Spits H, Bernink JH. Identification of human cytotoxic ILC3s. Eur J Immunol. 2020. 10.1002/eji.202048696
469. Cella M, Fuchs A, Vermi W, Facchetti F, Otero K, Lennerz JK, et al. A human natural killer cell subset provides an innate source of IL-22 for mucosal immunity. Nature. 2009;457(7230):722-5. 10.1038/nature07537
470. Hoorweg K, Peters CP, Cornelissen F, Aparicio-Domingo P, Papazian N, Kazemier G, et al. Functional Differences between Human NKp44(-) and NKp44(+) RORC(+) Innate Lymphoid Cells. Front Immunol. 2012;3:72. 10.3389/fimmu.2012.00072
471. Vacca P, Montaldo E, Croxatto D, Loiacono F, Canegallo F, Venturini PL, et al. Identification of diverse innate lymphoid cells in human decidua. Mucosal Immunol. 2015;8(2):254-64. 10.1038/mi.2014.63
472. Irshad S, Flores-Borja F, Lawler K, Monypenny J, Evans R, Male V, et al. RORgammat(+) Innate Lymphoid Cells Promote Lymph Node Metastasis of Breast Cancers. Cancer Res. 2017;77(5):1083-96. 10.1158/0008-5472.CAN-16-0598
473. Wang W, Li Y, Hao J, He Y, Dong X, Fu YX, et al. The Interaction between Lymphoid Tissue Inducer-Like Cells and T Cells in the Mesenteric Lymph Node Restrains Intestinal Humoral Immunity. Cell Rep. 2020;32(3):107936. 10.1016/j.celrep.2020.107936
474. Withers DR. Innate lymphoid cell regulation of adaptive immunity. Immunology. 2016;149(2):123-30. 10.1111/imm.12639
475. Pascual-Reguant A, Kohler R, Mothes R, Bauherr S, Hernandez DC, Uecker R, et al. Multiplexed histology analyses for the phenotypic and spatial characterization of human innate lymphoid cells. Nat Commun. 2021;12(1):1737. 10.1038/s41467-021-21994-8
476. Magri G, Miyajima M, Bascones S, Mortha A, Puga I, Cassis L, et al. Innate lymphoid cells integrate stromal and immunological signals to enhance antibody production by splenic marginal zone B cells. Nat Immunol. 2014;15(4):354-64. 10.1038/ni.2830
477. Yamazaki T, Yang XO, Chung Y, Fukunaga A, Nurieva R, Pappu B, et al. CCR6 regulates the migration of inflammatory and regulatory T cells. J Immunol. 2008;181(12):8391-401. 10.4049/jimmunol.181.12.8391
478. Huster KM, Busch V, Schiemann M, Linkemann K, Kerksiek KM, Wagner H, et al. Selective expression of IL-7 receptor on memory T cells identifies early CD40L-dependent generation of distinct CD8+ memory T cell subsets. Proc Natl Acad Sci U S A. 2004;101(15):5610-5. 10.1073/pnas.0308054101
479. Boardman DA, Garcia RV, Ivison SM, Bressler B, Dhar TM, Zhao Q, et al. Pharmacological inhibition of RORC2 enhances human Th17-Treg stability and function. Eur J Immunol. 2020;50(9):1400-11. 10.1002/eji.201948435
480. Cai L, Xu H, Zhang H, Zhang L, Wang G, Nie H. Blockade of IL-7Ralpha alleviates collagen-induced arthritis via inhibiting Th1 cell differentiation and CD4(+) T cell migration. Mol Immunol. 2016;79:83-91. 10.1016/j.molimm.2016.09.017
481. Lee WW, Kang SW, Choi J, Lee SH, Shah K, Eynon EE, et al. Regulating human Th17 cells via differential expression of IL-1 receptor. Blood. 2010;115(3):530-40. 10.1182/blood-2009-08-236521

482. Bekiaris V, Sedy JR, Rossetti M, Spreafico R, Sharma S, Rhode-Kurnow A, et al. Human CD4+CD3- innate-like T cells provide a source of TNF and lymphotoxin-alphabeta and are elevated in rheumatoid arthritis. J Immunol. 2013;191(9):4611-8. 10.4049/jimmunol.1301672
483. Cerboni S, Gehrmann U, Preite S, Mitra S. Cytokine-regulated Th17 plasticity in human health and diseases. Immunology. 2020. 10.1111/imm.13280
484. Dunne MR, Ryan C, Nolan B, Tosetto M, Geraghty R, Winter DC, et al. Enrichment of Inflammatory IL-17 and TNF-alpha Secreting CD4(+) T Cells within Colorectal Tumors despite the Presence of Elevated CD39(+) T Regulatory Cells and Increased Expression of the Immune Checkpoint Molecule, PD-1. Front Oncol. 2016;6:50. 10.3389/fonc.2016.00050
485. Castro F, Cardoso AP, Goncalves RM, Serre K, Oliveira MJ. Interferon-Gamma at the Crossroads of Tumor Immune Surveillance or Evasion. Front Immunol. 2018;9:847. 10.3389/fimmu.2018.00847
486. Hagenstein J, Melderis S, Nosko A, Warkotsch MT, Richter JV, Ramcke T, et al. A Novel Role for IL-6 Receptor Classic Signaling: Induction of RORgammat(+)Foxp3(+) Tregs with Enhanced Suppressive Capacity. J Am Soc Nephrol. 2019;30(8):1439-53. 10.1681/ASN.2019020118
487. Ferreira RC, Rainbow DB, Rubio Garcia A, Pekalski ML, Porter L, Oliveira JJ, et al. Human IL-6R(hi)TIGIT(-) CD4(+)CD127(low)CD25(+) T cells display potent in vitro suppressive capacity and a distinct Th17 profile. Clin Immunol. 2017;179:25-39. 10.1016/j.clim.2017.03.002
488. Cano-Gamez E, Soskic B, Roumeliotis TI, So E, Smyth DJ, Baldrighi M, et al. Single-cell transcriptomics identifies an effectorness gradient shaping the response of CD4(+) T cells to cytokines. Nat Commun. 2020;11(1):1801. 10.1038/s41467-020-15543-y
489. Barten MJ, Rahmel A, Bocsi J, Boldt A, Garbade J, Dhein S, et al. Cytokine analysis to predict immunosuppression. Cytometry A. 2006;69(3):155-7. 10.1002/cyto.a.20215
490. Keski-Nisula L, Roponen M, Hirvonen MR, Heinonen S, Pekkanen J. Stimulated cytokine production correlates in umbilical arterial and venous blood at delivery. Eur Cytokine Netw. 2004;15(4):347-52.
491. Olsen I, Sollid LM. Pitfalls in determining the cytokine profile of human T cells. J Immunol Methods. 2013;390(1-2):106-12. 10.1016/j.jim.2013.01.015
492. Benner B, Scarberry L, Suarez-Kelly LP, Duggan MC, Campbell AR, Smith E, et al. Generation of monocyte-derived tumor-associated macrophages using tumor-conditioned media provides a novel method to study tumor-associated macrophages in vitro. J Immunother Cancer. 2019;7(1):140. 10.1186/s40425-019-0622-0
493. Yun SJ, Lee B, Komori K, Lee MJ, Lee BG, Kim K, et al. Regulation of TIM-3 expression in a human T cell line by tumor-conditioned media and cyclic AMP-dependent signaling. Mol Immunol. 2019;105:224-32. 10.1016/j.molimm.2018.12.006
494. Wang H, Daniel V, Sadeghi M, Opelz G. Plasticity and overlap of in vitro-induced regulatory T-cell markers in healthy humans. Transplant Proc. 2013;45(5):1816-21. 10.1016/j.transproceed.2012.10.060
495. Kudernatsch RF, Letsch A, Guerreiro M, Lobel M, Bauer S, Volk HD, et al. Human bone marrow contains a subset of quiescent early memory CD8(+) T cells characterized by high CD127 expression and efflux capacity. Eur J Immunol. 2014;44(12):3532-42. 10.1002/eji.201344180
496. Zhang B, Zhang Y, Xiong L, Li Y, Zhang Y, Zhao J, et al. CD127 imprints functional heterogeneity to diversify monocyte responses in human inflammatory diseases. bioRxiv. 2020. 10.1101/2020.11.10.376277
497. Kim BS, Clinton J, Wang Q, Chang SH. Targeting ST2 expressing activated regulatory T cells in Kras-mutant lung cancer. Oncoimmunology. 2020;9(1):1682380. 10.1080/2162402X.2019.1682380
498. Li A, Herbst RH, Canner D, Schenkel JM, Smith OC, Kim JY, et al. IL-33 Signaling Alters Regulatory T Cell Diversity in Support of Tumor Development. Cell Rep. 2019;29(10):2998-3008 e8. 10.1016/j.celrep.2019.10.120
499. Desai S, Kumar A, Laskar S, Pandey BN. Cytokine profile of conditioned medium from human tumor cell lines after acute and fractionated doses of gamma radiation and its effect on survival of bystander tumor cells. Cytokine. 2013;61(1):54-62. 10.1016/j.cyto.2012.08.022
500. Hsu YL, Hung JY, Ko YC, Hung CH, Huang MS, Kuo PL. Phospholipase D signaling pathway is involved in lung cancer-derived IL-8 increased osteoclastogenesis. Carcinogenesis. 2010;31(4):587-96. 10.1093/carcin/bgq030
501. Lindemann MJ, Hu Z, Benczik M, Liu KD, Gaffen SL. Differential regulation of the IL-17 receptor by gammac cytokines: inhibitory signaling by the phosphatidylinositol 3-kinase pathway. J Biol Chem. 2008;283(20):14100-8. 10.1074/jbc.M801357200

502. Liu K, Guo J, Liu K, Fan P, Zeng Y, Xu C, et al. Integrative analysis reveals distinct subtypes with therapeutic implications in KRAS-mutant lung adenocarcinoma. EBioMedicine. 2018;36:196-208. 10.1016/j.ebiom.2018.09.034
503. Londhe P, Zhu B, Abraham J, Keller C, Davie J. CIITA is silenced by epigenetic mechanisms that prevent the recruitment of transactivating factors in rhabdomyosarcoma cells. Int J Cancer. 2012;131(4):E437-48. 10.1002/ijc.26478
504. Gwinn DM, Lee AG, Briones-Martin-Del-Campo M, Conn CS, Simpson DR, Scott AI, et al. Oncogenic KRAS Regulates Amino Acid Homeostasis and Asparagine Biosynthesis via ATF4 and Alters Sensitivity to L-Asparaginase. Cancer Cell. 2018;33(1):91-107 e6. 10.1016/j.ccell.2017.12.003
505. Zou S, Tong Q, Liu B, Huang W, Tian Y, Fu X. Targeting STAT3 in Cancer Immunotherapy. Mol Cancer. 2020;19(1):145. 10.1186/s12943-020-01258-7
506. Zarogoulidis P, Katsikogianni F, Tsiouda T, Sakkas A, Katsikogiannis N, Zarogoulidis K. Interleukin-8 and interleukin-17 for cancer. Cancer Invest. 2014;32(5):197-205. 10.3109/07357907.2014.898156
507. Markota A, Endres S, Kobold S. Targeting interleukin-22 for cancer therapy. Hum Vaccin Immunother. 2018;14(8):2012-5. 10.1080/21645515.2018.1461300
508. Ha H, Debnath B, Neamati N. Role of the CXCL8-CXCR1/2 Axis in Cancer and Inflammatory Diseases. Theranostics. 2017;7(6):1543-88. 10.7150/thno.15625
509. Xiao S, Yosef N, Yang J, Wang Y, Zhou L, Zhu C, et al. Small-molecule RORgammat antagonists inhibit T helper 17 cell transcriptional network by divergent mechanisms. Immunity. 2014;40(4):477-89. 10.1016/j.immuni.2014.04.004
510. Deng S, Clowers MJ, Velasco WV, Ramos-Castaneda M, Moghaddam SJ. Understanding the Complexity of the Tumor Microenvironment in K-ras Mutant Lung Cancer: Finding an Alternative Path to Prevention and Treatment. Front Oncol. 2019;9:1556. 10.3389/fonc.2019.01556
511. Choi H, Na KJ. Integrative analysis of imaging and transcriptomic data of the immune landscape associated with tumor metabolism in lung adenocarcinoma: Clinical and prognostic implications. Theranostics. 2018;8(7):1956-65. 10.7150/thno.23767
512. Cluxton D, Petrasca A, Moran B, Fletcher JM. Differential Regulation of Human Treg and Th17 Cells by Fatty Acid Synthesis and Glycolysis. Front Immunol. 2019;10:115. 10.3389/fimmu.2019.00115
513. Jacobs SR, Michalek RD, Rathmell JC. IL-7 is essential for homeostatic control of T cell metabolism in vivo. J Immunol. 2010;184(7):3461-9. 10.4049/jimmunol.0902593
514. Johnson MO, Wolf MM, Madden MZ, Andrejeva G, Sugiura A, Contreras DC, et al. Distinct Regulation of Th17 and Th1 Cell Differentiation by Glutaminase-Dependent Metabolism. Cell. 2018;175(7):1780-95 e19. 10.1016/j.cell.2018.10.001
515. Cobbold SP, Adams E, Farquhar CA, Nolan KF, Howie D, Lui KO, et al. Infectious tolerance via the consumption of essential amino acids and mTOR signaling. Proc Natl Acad Sci U S A. 2009;106(29):12055-60. 10.1073/pnas.0903919106
516. Michalek RD, Gerriets VA, Jacobs SR, Macintyre AN, MacIver NJ, Mason EF, et al. Cutting edge: distinct glycolytic and lipid oxidative metabolic programs are essential for effector and regulatory CD4+ T cell subsets. J Immunol. 2011;186(6):3299-303. 10.4049/jimmunol.1003613
517. Howie D, Ten Bokum A, Cobbold SP, Yu Z, Kessler BM, Waldmann H. A Novel Role for Triglyceride Metabolism in Foxp3 Expression. Front Immunol. 2019;10:1860. 10.3389/fimmu.2019.01860
518. Kalvala A, Wallet P, Yang L, Wang C, Li H, Nam A, et al. Phenotypic Switching of Naive T Cells to Immune-Suppressive Treg-Like Cells by Mutant KRAS. J Clin Med. 2019;8(10). 10.3390/jcm8101726
519. Sun J, Jia H, Bao X, Wu Y, Zhu T, Li R, et al. Tumor exosome promotes Th17 cell differentiation by transmitting the lncRNA CRNDE-h in colorectal cancer. Cell Death Dis. 2021;12(1):123. 10.1038/s41419-020-03376-y
520. Gordian E, Welsh EA, Gimbrone N, Siegel EM, Shibata D, Creelan BC, et al. Transforming growth factor beta-induced epithelial-to-mesenchymal signature predicts metastasis-free survival in non-small cell lung cancer. Oncotarget. 2019;10(8):810-24. 10.18632/oncotarget.26574